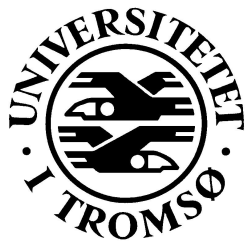

A DISSERTATION FOR THE DEGREE OF DOCTOR SCIENTIARUM

High Spatial and Temporal Resolution

Auroral Imaging

Trond S. Trondsen

November 1998

DEPARTMENT OF PHYSICS
Faculty of Science
University of Tromsø

High Spatial and Temporal Resolution

Auroral Imaging

Trond S. Trondsen

November 1998

University of Tromsø

1998

Abstract

High Spatial and Temporal Resolution

Auroral Imaging

by

Trond S. Trondsen
Dr. Scient. in Cosmic Geophysics

University of Tromsø

Professor Asgeir Brekke, Chair

A versatile auroral imaging system capable of high spatial and temporal resolution imaging at low light levels has been constructed and fielded. The Portable Auroral Imager (PAI) uses as primary detector a third-generation image intensified charge-coupled device (CCD) television camera. A secondary, wider field of view camera provides, along with resident all-sky cameras, important context measurements. Data are recorded onto high-resolution video tape at a rate of 30 frames per second, each individual video frame receiving an accurate time stamp immediately prior to recording. The field data is later digitized and analyzed in the laboratory using a personal computer based image digitizer and modern image processing workstations. The PAI system is designed primarily for narrow field auroral observations, although the modular design allows the system to be fully customized to meet changing scientific needs. The design, characterization, and operation of the instrument are described in some detail for the purpose of aiding others in emulating or improving upon the concept.

The PAI was fielded during two-week-long campaigns in the winters of 1994, 1995, and 1997. The resulting data contained impressive examples of the rich variety of evening and midnight sector short-scale auroral phenomena. Presented in this thesis are four separate phenomenological surveys pertaining to the small-scale aurora, namely, surveys of, (a) very thin auroral forms (less than 100 m widths), (b) “black” auroral forms, (c) “asymmetric” multiple arcs, and (d) auroral vortices, also known as “curls.” Some significant new findings are contained in these surveys. Throughout, it will also be demonstrated that the widely used concepts of “auroral forms,” “auroral arcs,” “diffuse aurora,” and “discrete aurora” are very dependent on the scale size involved, and thus also on the characteristics of the observer’s particular imaging instrumentation. Such terms should thus be used in the relevant fora only with extreme caution, especially when associating the terms with specific meanings in auroral theories.

Original photograph by Jan Curtis.

Fine-scale structures within auroral arcs are real and they are unexplained.

Joe Borovsky, 1995

To my wife Elizabeth.

Contents

List of Figures

List of Tables

Acknowledgements

I am grateful to my supervisors, Dr. Asgeir Brekke of the University of Tromsø and Dr. Leroy L. Cogger of the University of Calgary for their patience and invaluable support throughout the entire period of research. This work was performed in its entirety at the Institute for Space Research (ISR) at the University of Calgary, and I would like to sincerely thank Dr. J. Sandy Murphree and the rest of the ISR staff for their hospitality and support.

Significant assistance by the following personnel and institutions is acknowledged: Peter King, for much advice on the numerous technical aspects of auroral imager design; Cliff Marcellus for his untiring computer technical support; Rob Elphinstone, for fruitful scientific discussions; Dr. John Samson of the University of Alberta, for suggesting the inertial Alfvén wave as a possible cause of the asymmetric multiple auroral arcs of Chapter 9; Dr. Joe Borovsky of the Space and Atmospheric Sciences Group at the Los Alamos National Laboratory, for the frequent loan of their intensified video camera, which provided valuable support measurements; the Canadian Space Agency, and also Dr. Don McEwen of the University of Saskatchewan, for permission to use their research facilities at Rabbit Lake; and the Cameco Corporation and their personnel at Collins Bay for their hospitality and kind assistance. I am also grateful to the following individuals for their assistance in various ways up through the years: Noralv Bjørnå, Truls Lynne Hansen, and Ove Harang. Special thanks to Jan Curtis of Alaska for granting permission to use several of his beautiful color photographs of the *Aurora Borealis*, and to Achim Kopfmueller of Switzerland for expertly applying the jigsaw puzzle effect to the frontispiece. Last but not least, I would like to thank Titus Mathews, Jr. and Torsten Aslaksen for their valuable friendship and constant encouragement.

Significant financial assistance was provided by the Natural Sciences and Engineering Research Council of Canada (NSERC) and the Norwegian Research Council (NFR/NAVF). This help I gratefully acknowledge.

Chapter 1

Introduction

AND NOW MEN SEE NOT THE LIGHT AS IT GLEAMETH,
IT IS HIDDEN IN THE SKIES;
BUT THE WIND PASSETH BY AND CLEARETH THEM.
OUT OF THE NORTH COMETH GOLDEN SPLENDOR.
Book of Job, c. 1450 B.C.

The *Aurora Borealis* and *Australis* represent one of the most dynamic products of the Earth's electrodynamic relationship with the sun. Auroral phenomena can be described in terms of the electrodynamics of the ionosphere-magnetosphere-solar wind system, and auroral arcs may be considered a manifestation of the imperfect coupling state of the magnetosphere-ionosphere due to enhanced magnetospheric convection [Kan and Lee, 1981]. Auroral arcs are east-west oriented, magnetic-field-aligned sheets of airglow in the upper atmosphere. Energetic electrons precipitating into the atmosphere are observed above the arcs [McIlwain, 1960]. The energization of these electrons appears to take place in localized regions in the magnetosphere, at altitudes between 1 and 2 R_E [Gorney et al., 1981; Bennett et al., 1983]. Accelerated electrons leave these localized regions in narrow sheets and travel downward along the geomagnetic field lines, where they deposit their energy into the upper atmosphere in the polar regions. If the downward accelerated electrons acquire enough energy from the acceleration process, they may produce auroral emissions as they enter the atmosphere. The height profile of the auroral emissions is found to be consistent with energy deposition by precipitating electrons [Belon et al., 1966]. Typically, the lower border of the auroral curtain is located at about 95–110 km altitude [Currie, 1955; Störmer, 1955], it may be several hundred kilometers tall, and the arc may extend several thousand kilometers in the east-west direction. Arcs often have undulations and tight curls, the latter appearing as bright vertical rays in the curtains.

The term "auroral arc" is routinely used within the auroral research community to describe what appears to be a narrow linear auroral feature. However, terms like this are very subject to the scale size involved and there are enormous gaps between the scale sizes within a satellite image, an all-sky camera image, and an image acquired by a ground-based narrow-field imager. Indiscriminate use of the term should thus be avoided, especially when associating the term with specific meanings in auroral theories. Auroral

phenomena display an exceedingly rich phenomenology. There are the narrow, rapidly moving and metamorphosing breakup arcs, the quieter and somewhat thicker, slower-moving pre-breakup arcs, as well as the diffuse post-breakup arcs. Several latitudinal spatial scales can be associated with auroral arcs and the auroral zone. The most pertinent ones may be classified as, (1) the thickness of fine-scale auroral arcs ($\sim$100 m in the ionosphere), (2) the thickness of bright dynamic arc systems that are composed of several fine-scale arcs ($\sim$1 km), (3) the broad quiescent, homogeneous channel of diffuse airglow in which one or more such bright dynamic arc systems may be embedded (10–100 km), (4) the separation between such auroral arc systems ($\sim$100 km), and (5) the thickness of the auroral zone (200-700 km) [Borovsky, 1995; Hallinan and Davis, 1970]. The so-called "inverted V" electron precipitation corresponds to a latitudinal extent of up to 100 km in the ionosphere [Frank and Ackerson, 1971; Lin and Hoffman, 1979]. Thus, an assembly of much thinner arcs, involving a hierarchy of spatial scales, exists within the region believed to coincide with the "inverted V" precipitation. Satellite data indicate the presence of significant small-scale structure within the auroral zone [e.g., Bankov et al., 1986]. The "arcs" often observed from space correspond to those of class (3); simultaneous *in situ* E-field measurements often show smaller-scale electric field gradients within the boundaries of the generalized signature, suggestive of multiple current sheets associated with the apparent single arc [Johnson, 1996]. Arcs observed by time-lapse all-sky cameras also tend to correspond to those of class (3). However, in the case of all-sky television cameras, features belonging to class (2) may also be discerned, typically in the form of rays or beads of intensity that move along auroral curtains in waves.

The highly structured auroral arc is perhaps one of the most obvious features of the aurora, but it is also one of the least understood. The main purpose of this thesis is to make available to the research community experimentally obtained data describing spatial and temporal characteristics of auroral forms[1] belonging to the $\sim$0.1–1 km spatial scale regime, corresponding to classes (1) and (2) above. The work is done with a view towards equipping much abler minds with the information necessary to make inferences regarding the production mechanisms responsible for the formation of the smallest-scale auroral forms. Measurements of characteristics of auroral forms may provide information about the mechanisms that accelerate auroral electrons, about generator mechanisms that supply energy to auroral-arc field lines, and about the mechanisms that transfer energy electrodynamically between the magnetosphere and the ionosphere. Such measurements are also expected to yield information pertaining to gradient scale sizes in the nightside magnetosphere. While the auroral arc may not be very well understood, there certainly is not a lack of theories attempting its explanation. Borovsky [1993a] examined twenty-two of the most popular proposed theoretical mechanisms, all of which were found deficient in explaining the production of arcs of widths less than 1 km. This may be considered somewhat alarming in light of the result of a largely-ignored survey conducted by Maggs and Davis [1968]. These investigators systematically measured the thicknesses of auroral arcs using an image-orthicon television system that was pointed into the magnetic zenith. The obtained distribution of auroral-arc thicknesses is reproduced in Figure 1.1. As can be seen, the most probable thickness corresponded to the 70-

[1] We here again run into a problem of nomenclature. The aurora as seen by a high-resolution imager is significantly more dynamic and structured than is apparent to the visual observer or the all-sky camera. "Auroral structures" might be a more appropriate term than "auroral forms," as we in many cases will be describing the characteristics of structures within what might traditionally be referred to as "auroral forms."

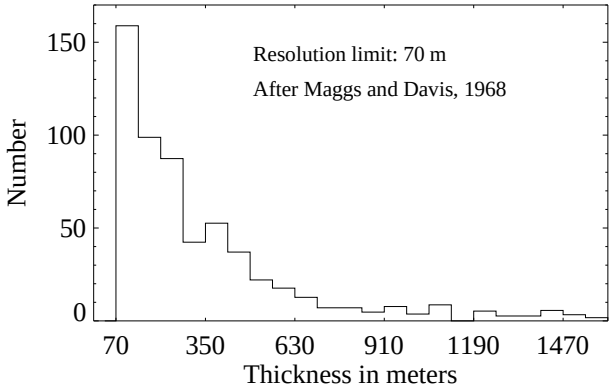

Figure 1.1: The distribution of auroral-arc thicknesses as measured by Maggs and Davis [1968].

m limiting resolution of their imaging system. This does not immediately disqualify the twenty-two theories examined by Borovsky [1993a], as some of these may indeed be applicable within the range of scale sizes that they do address ($\sim$1–100 km). However, due to the current lack of high-resolution optical auroral data one is largely prevented from making a critical assessment of many auroral arc theories, and consequently the advancement of new, improved theories is also impeded.

In order to fully understand the electrodynamics of auroral processes both microscopic and macroscopic plasma processes must be understood, as they both affect the electrodynamics and are coincident in time and space. In auroral physics, as in astronomy and particle physics, progress is closely tied to the development of better sensors, yielding higher sensitivity, higher resolution, larger statistical samples, and broader spectral response, as the observer effectively opens his eyes wider to the view offered by nature. Instrumentation employed in auroral studies has progressed from primarily large-scale studies to small-scale studies of the intricate workings of plasma processes, such as those involved in the formation of arcs. However, this general progression is only to a lesser extent reflected within the field of auroral imaging. Ground-based imaging instrumentation which has been used in the past include television cameras [Davis, 1966], scanning photometers [Sawchuk and Anger, 1972], and charge-coupled device (CCD) cameras [Ono et al., 1987]. However, it is the all-sky camera that has, albeit in increasingly sophisticated incarnations, been the mainstay of the field for close to half a century [Gartlein, 1947]. Instead of deploying increased temporal and spatial resolution ground-based imagers, the trend has rather been towards the deployment of space borne imagers. While these imagers have the significant advantage of being able to instantaneously image large portions of the auroral oval, their spatial and temporal resolutions at auroral heights are usually lower than, or at best comparable to, those of the all-sky camera. Another reason why high-resolution auroral imaging has not seen more widespread use may have its root in the fact that, while large-scale auroral systems are ultimately the result of the interaction of the solar wind with the magnetosphere, the sources of smaller-scale systems may be found in extremely short-lived plasma processes such as particle accelerations and plasma waves operating in the ionosphere, magnetosphere, or somewhere in between [e.g., Potemra, 1988; Borovsky, 1995]. Consequently, the auroral footprints of these processes are extremely dynamic with major spatial changes

occurring on temporal scales of milliseconds, as is amply demonstrated during the auroral breakup. The amount of data gathered during only one night of observation may thus easily become monumental, creating a logistical nightmare as data recording, reduction, and analysis are concerned. For this reason, high spatial and temporal resolution ground based imagers have only been employed on a very limited basis, e.g., to study the kinking and curling up of arcs [Hallinan and Davis, 1970; Oguti et al., 1988], the flickering of arcs [Beach et al., 1968], the multiplicity of arcs [Davis, 1978a], and as support instrumentation during individual case-studies [e.g., Lanchester et al., 1997]. No major organized surveys of small-scale auroral phenomena have been conducted, in spite of the fact that there has been, especially since the early 1980's, a growing interest in the microphysics of the aurora, as well as dramatic advances in the state-of-the-art of image sensors and computer technology.

This thesis is divided into two main parts. Part I (Chapters 2–5) deals with issues pertaining to instrumentation, while in Part II (Chapters 6–10) some observations of small-scale auroral phenomena are presented. Part I outlines the design, construction, and characterization of a functional high spatial and temporal resolution auroral imaging system, hereafter referred to as the Portable Auroral Imager, or PAI for short. This information is included so as to encourage other investigators to emulate or improve upon the concept. Much of the information pertaining to imager design is not readily available in any one textbook or review article. The information has been synthesised from a wide variety of sources, including reports of military origin. While there is a seemingly endless number of considerations involved in the design of a low-light-level imaging system, the material has here been laid out in a form easily accessible to the auroral scientist, hopefully giving him or her a good understanding of the often misunderstood concepts and trade-offs involved. Frequent bibliographical references to unclassified material are made to aid the future instrument designer in obtaining more in-depth information pertaining to the issues covered herein. The Portable Auroral Imager was first fielded in northern Canada in the winter of 1994. This campaign, along with subsequent campaigns in the winters of 1995 and 1997, provided footage of a wide range of auroral phenomena, imaged at heretofore unprecedented high signal-to-noise ratios. In Part II we present some of the scientific results that emerged from these campaigns. The results, which include some significant new findings, are presented in the form of four separate phenomenological surveys, namely:

– Observations of thin auroral arcs ($<$100 m)
– Observations of black aurora ($\sim$1–10 km)
– Observations of multiple arcs ($\sim$0.1–1 km)
– Observations of auroral vortices ($\sim$1–10 km)

Dimensions in brackets give an indication of the orders of magnitude of scale sizes involved. While seemingly pertaining to four unrelated issues, these surveys have as their common thread that they all relate to the smallest known, least explored, and least understood spatial scales in the aurora. Further, these phenomena are all interrelated. For example, the formation of vortices ("curls") along arcs is experienced by auroral arcs of all scale sizes considered here ($\sim$0.1–10 km), including by the black aurora. By definition, black and ordinary aurora co-exist. Thin ($<$100 m) auroral arcs, as well as multiple arcs, are seen in the black aurora as well as in the ordinary aurora. Further, constituent arcs within multiple arc systems (whether in black

or ordinary aurora) are frequently seen to exhibit vortex formation, resulting in entire arrays of vortices. All the phenomena surveyed here thus operate simultaneously, and a full understanding of the mechanisms responsible for small-scale auroral forms must of necessity take them all into account. The surveys presented here are considered an initial step toward such a fuller understanding.

Finally, the reader is again reminded that what will be dealt with here are the smallest-known spatial scales in the aurora, the so-called “breakup” forms of Goertz [1981]. We thus in many ways find ourselves within an entirely different paradigm as compared to when studying all-sky or satellite imagery. It is in this context pertinent to point out that the popular distinction between “discrete” and “diffuse” aurora must be rejected. Traditionally, the diffuse aurora is from an optical point of view considered to be a structureless background glow of low intensity, while discrete aurora, on the other hand, consists of structured arcs. As in the case of the “auroral arc,” the terms “discrete” and “diffuse” are very subject to the scale size, a fact not widely recognized. For example, what appears to an orbiting satellite to be a diffuse aurora may appear to the sensitive ground based high-resolution imager as an an assembly of discrete features and patches exhibiting rapid drift motions as well as considerable shear behavior. Conversely, what appears to the narrow-field imager as a completely structureless glow entirely filling the field of view may appear to the satellite imager to be a quiet, extremely well-defined discrete arc. Consequently, the term “diffuse” is in this work used in a more general sense to give an indication of relative emission intensities, whether it be of structured or structureless aurora. The term “discrete” is used to describe features exhibiting sharp intensity gradients (structure) within the context of the imager’s field of view, whether they be “bright” or “diffuse.”

Part I

Instrumentation

Chapter 2

The Portable Auroral Imager

The desire for a compact, transportable, campaign-mode auroral imager has existed within the Institute for Space Research, University of Calgary, since the end of the 1970s [L.L. Cogger, private communication, 1998]. The technology needed to realize such a concept became available during the 1980s, and when sufficient funds became available in the early 1990s it was decided to proceed with the implementation of such an imaging system. Towards this end, a major survey of the available technology was undertaken in the summer of 1992. The information thus gathered was considered along with science requirements and budgetary constraints, resulting in a final recommendation for a fully functional, compact imaging system [Trondsen, 1992]. Due to the inherent budgetary and time constraints it was decided that as far as possible only off-the-shelf modules be used in the implementation of the imager. Indeed, the above referenced survey revealed that the state-of-the-art of high-speed image acquisition had progressed to the point where little, if anything, could be gained in terms of performance from a potentially costly in-house development. The integration of the imager was essentially completed by the winter of 1994, and the complete system was fielded for the first time during a two-week campaign in March of that same year.

The Portable Auroral Imager (hereafter referred to as the PAI) is designed for manned, campaign based operations, with the camera head located either indoors or outdoors. As well, it is designed to function worldwide under a large variety of local mains voltages and frequencies. The imager, which might appropriately be described as an imaging *system*, consists of two main components: the *field component* and the *laboratory component*. The purpose of this chapter is to describe these two components of the PAI. In the interest of brevity, much technical detail is omitted; only detail considered necessary within the framework of the current thesis is included. The reader is referred to Trondsen [1992] for more exhaustive information. The various design considerations that resulted in this particular choice of imager are discussed in Chapters 3 and 4, while the actual imager characterization is treated in Chapter 5.

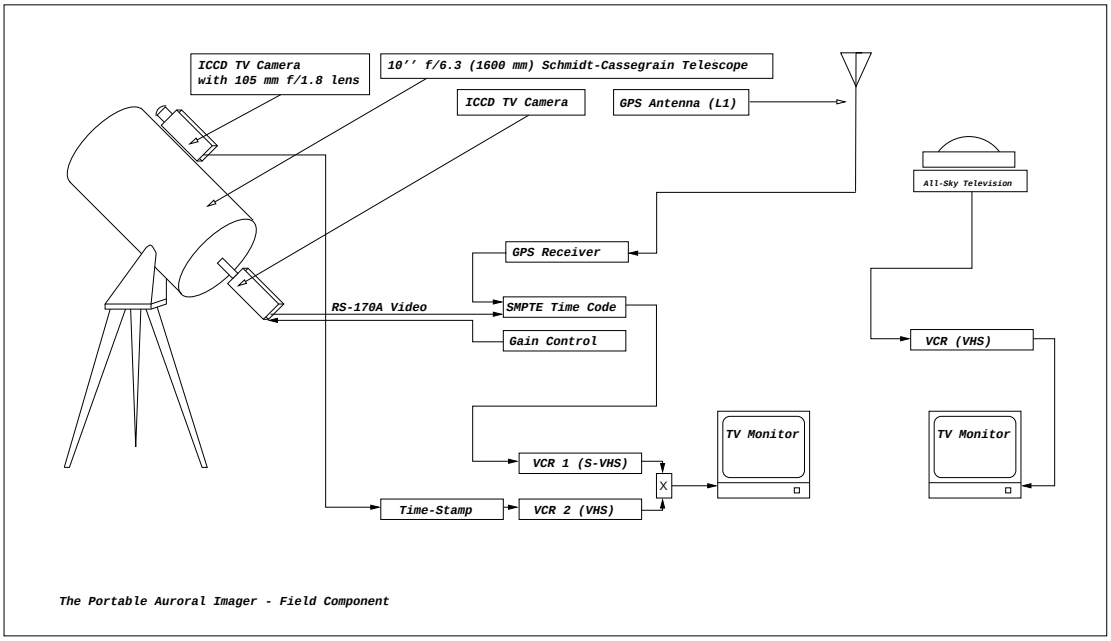

Figure 2.1: Schematic showing the field component of the PAI.

2.1 The Field Component

Figure 2.1 shows a schematic drawing of the setup of the imager in the field, while Table 2.1 gives a list of the various modules making up the PAI field component. Two fields of view are supplied: a primary and a secondary (supporting) field of view. The primary field of view is equipped with a high-sensitivity third-generation image-intensified charge-coupled device (ICCD) television camera with manual gain control, a high-resolution S-VHS video cassette recorder, and highly accurate time code equipment. These components constitute the core of the imaging system. Further, the secondary field of view is equipped with a somewhat lower-quality second-generation ICCD camera with automatic gain control, a VHS video cassette recorder, as well as somewhat less accurate time-stamp equipment. Thus, in the particular configuration depicted in Figure 2.1 the telescope field of view is considered primary and the 105 mm field of view (mounted piggy-back on the telescope) secondary. Which field of view is configured as primary and which one is designated secondary is entirely dependent upon the science objectives of the particular campaign. One major advantage of the PAI is that it can be easily reconfigured to accommodate changing science requirements. The main portion of the data analysis is performed on the high-quality primary field of view data, while the secondary field of view data are used as supporting context information only. The telescope/tripod subsystem actually serves a threefold purpose: (1) it provides a sturdy base on which to mount the ICCDs, (2) it provides a long focal-length objective lens for the PAI, and (3) it provides a means of closely aligning the imager's optic axis to the local geomagnetic field line by using stars seen through the telescope as reference points. If use of the telescope as an objective lens is not required, the camera can be furnished with an alternative objective lens

The PAI Field Component

Major Items
ITT F4588 Generation III Intensified CCD Camera
XYBION Generation II Intensified CCD Camera (backup camera, borrowed)
Hitachi VL-S100 S-VHS Professional Portable VCR *(Also part of lab component)*
Sony SVO-1450 Industrial VHS VCR *(Also part of lab component)*
JVC TM-63U 5” Compact Video Monitor *(Also part of lab component)*
Trimble Scout Hand-Held GPS Receiver
Trimble TRIMPACK III GPS Receiver
Trimble L1 GPS Antenna
Horita GPS-1/FP-50 SMPTE LTC Time Code Generator
Horita VG/FP-50 LTC–VITC Translator
Digi-Spec DTG-1000 Date/Time Generator
Lambda EWS15-15, 15V, 1.1A switched PSU (85–250VAC, 47–63 Hz)
Lambda EWS50-12, 12V, 4.4A switched PSU (85–250VAC, 47–63 Hz)
Minor Items
Silva 15TD-CL Sighting Compass
Camera Gain Control Box (home made)
Mini-Maglite Flashlight
Heating tapes (assorted) w/Selco OA-60 thermostats
Soldering iron, assorted screwdrivers, hex keys, and pliers
Fluke 21 Series II Digital Multimeter
Spare parts: batteries, fuses, plugs, test leads, electrical tape, etc.
Belden 9259 RG-59/U 75Ω co-axial cables (assorted lengths)
50’ camera gain control and PSU cable
Mains cords for Lambda PSUs, European and North American standards
Power supply cables and patch cords (RCA, banana, spade lug)
Full set of connector adapters/converters
Complete set of equipment Users’ Guides and Reference Manuals
Optics
Meade 2120 10”, f/6.3 SCT (incl. rigid tripod, equatorial mount, and accessories)
Nikon, 105 mm, f/1.8 35-mm objective lens, 100 lp mm^{-1}, multicoated, τ =90%
Cosmicar 50 mm, f/1.4 TV objective lens
Cosmicar 25 mm, f/1.4 TV objective lens
Celestron focal length reducer/corrector lens (#94175)
Glass Filter: Wratten 89B, infrared, cutoff 650 nm, AR coated
2” interference filters: 730.5 nm (BP15), 630.4 nm (NB2), 558.1 nm (NB2)
Lens adapters: Nikon–C, T, and T–C (16 mm)
Step-up rings for use of glass filter with Cosmicar/Nikon objectives
T-adapter with 2” interference-filter holder (home made)

Table 2.1: List of hardware comprising the field component of the PAI.

The PAI Field Component—Physical Characteristics

Case No.	Weight [kg]	Dimensions [m^3]	Contents
I	30	$.20 \times .55 \times .80$	VCR, camera, monitor, PSUs, cables,...
II	25	$.15 \times .55 \times .80$	GPS and SMPTE equipment, optics, tool,...
III	65	$.60 \times .85 \times .95$	Video tapes, secondary camera and VCR, extension cables,...
IV	30	$.45 \times .60 \times .90$	Meade 1600 mm Schmidt-Cassegrain telescope
V	15	$.30 \times .30 \times .90$	Tripod assembly for Meade SCT

Table 2.2: Physical characteristics of the PAI field component instrument cases.

Figure 2.2: Photograph of Instrument Case I of Table 2.2.

and mounted piggy-back under the front of the telescope. The telescope can in that case be equipped with an eyepiece and be used strictly for pointing purposes.

The field component of the PAI travels in five instrument cases. Some physical characteristics of these cases (numbered I–V), and their contents, are summarized in Table 2.2. Figure 2.2 is a photograph of Case I, which carries the important primary field (core) equipment. In cases where indoor operation is desired, and no telescope is required, smaller, ordinary camera tripods may be used (usually included in Case III), and there may thus be no need to ship Cases IV and V into the field.

Also shown in Figure 2.1 is an all-sky camera, not an integral part of the PAI. All campaigns thus far have been conducted at sites with pre-existing all-sky camera instrumentation. When performing high-resolution auroral imaging, larger-scale context information becomes crucial. By clever selection of optical focal lengths for the primary and seconday fields of view, and by the additional use of all-sky camera data, one can to a certain extent bridge the gaps between vastly different temporal and spatial scales, potentially gaining new information pertaining to auroral fractalization and the coupling between the various scale sizes within the aurora. Figure 2.3 shows an example of three very different magnetic-field aligned views of the

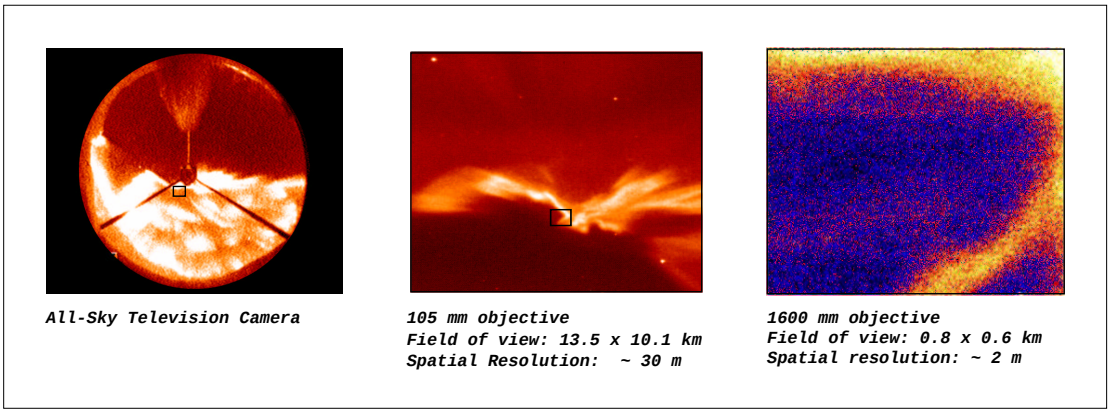

Figure 2.3: Three widely different fields of view of the same auroral scene. The small boxes indicate the field of view of the subsequent frame in the figure. Pseudo-colors have been added. *All-sky footage is courtesy of the Institute of Space and Atmospheric Studies, University of Saskatchewan.*

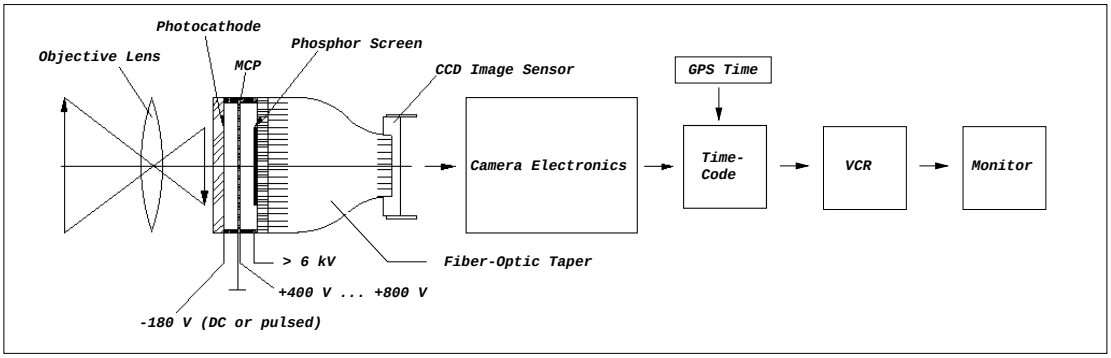

Figure 2.4: Schematic of the PAI field component primary channel signal chain.

same auroral scenario, as seen through the three fields of view of Figure 2.1.

Figure 2.4 illustrates the signal chain of the PAI primary video channel. Some of the individual units that together make up the PAI video chains are now discussed in somewhat more detail, with special emphasis on the primary field of view equipment.

2.1.1 Camera Head

The camera used with the PAI primary field of view is a third-generation image-intensified charge-coupled device (ICCD) video camera. It has an 18 mm diameter photocathode on a proximity-focused microchannel plate (MCP) image intensifier tube which is fiber-optically coupled to a charge-coupled device (CCD) sensor, as illustrated in Figure 2.4 [ITT Defense, 1993]. The merits of this kind of camera and the principles behind its design and engineering have been adequately covered elsewhere [e.g., Rougeot and Girard, 1988; Beauvais et al., 1985; Pollehn, 1985; Csorba, 1979, 1985]. Briefly, as an image is focused onto the photosensitive gallium arsenide (GaAs) cathode of the intensifier, photoelectrons are generated and im-

mediately accelerated away from the photocathode by a high voltage electric field. These photoelectrons are proximity focused onto the MCP, a thin disk containing millions of closely spaced, tiny holes, all parallel, passing through the plate from one face to the other. Each of these channels may be considered as the dynode chain of an ordinary photomultiplier. A voltage is applied across the faces of the plate and the incoming photoelectrons are accelerated and multiplied before hitting the output phosphor screen. From the 18 mm diameter phosphor screen the generated light is guided through a fiber-optic taper onto an 11 mm diagonal, $\frac{2}{3}$-inch format frame-transfer CCD array detector, a spatially coherent parallel transfer. The use of fiber-optic coupling instead of a set of optical lenses of appropriate magnification ensures a highly efficient coupling [Sandel and Broadfoot, 1976]. The phosphor-generated photons are converted back to photoelectrons again in the CCD pixel wells [Barbe and Campana, 1977]. The spectral responsivity of the CCD is closely matched to the wavelength of the light emitted by the phosphor. The CCD electrons are then clocked out and processed to give a composite video signal of 525 lines per frame with a 2:1 interlace, 15.75 kHz line scan rate, and 60 fields (30 frames) per second as specified by the RS-170A composite video standard [Benson, 1985]. Thus, each video frame, consisting of two interlaced fields, has been integrated for a total of $\frac{1}{60}$ s (16.7 ms) [Texas Instruments, 1990, 1993]. Under normal operation, a continually applied DC voltage is applied to the photocathode of the image tube, keeping the intensifier in the switched-on state. However, the intensifier also supports gated operation, wherein this voltage can be rapidly pulsed, effectively switching the image intensifier on and off at a given duty-cycle. This is similar in concept to a mechanical shutter in a conventional camera, except that it is capable of operating orders of magnitude faster than mechanical shutters, and is totally free of vibration. By gating the intensifier, effective exposure times in the range 150 ns – 16.7 ms may be realized. As will be shown in Chapter 4, the full 16.7 ms integration time is normally required for sufficient instrument sensitivity and spatial resolution at low light levels. However, in the case of very intense emissions, gating can be effectively used to avoid image overexposure, or to minimize spatial smearing of fast-moving bright features.

The particular photocathode selected for the PAI has an unusually high quantum efficiency (QE) across the green-red portion of the spectrum. The quantum efficiency of a detector may be interpreted as the probability of an impinging photon actually resulting in a primary photoelectron being emitted at the photocathode. Typical quantum efficiencies for second- and third-generation intensifier tubes are 15% and 20%, respectively. However, every photocathode manufactured has its own very unique spectral characteristics. In the case of the PAI, the vendor was requested to monitor the production line for photocathodes approaching a 30% quantum efficiency throughout the range 550–850 nm. This search lasted for about nine months, resulting in the identification of an exceptionally responsive intensifier tube whose manufacturer-measured spectral responsivity is shown in Figure 2.5a. Based on this data, the corresponding quantum efficiency may be calculated using the readily derived expression,

$$\text{Quantum efficiency [\%]} = \text{Responsivity [A/W]} \times \frac{hc}{\lambda e}, \tag{2.1}$$

where λ is the wavelength, h is Planck's constant, e is the electron charge, and c is the speed of light in vacuum. Figure 2.5b shows the resulting quantum efficiency curve. According to the manufacturer, the data

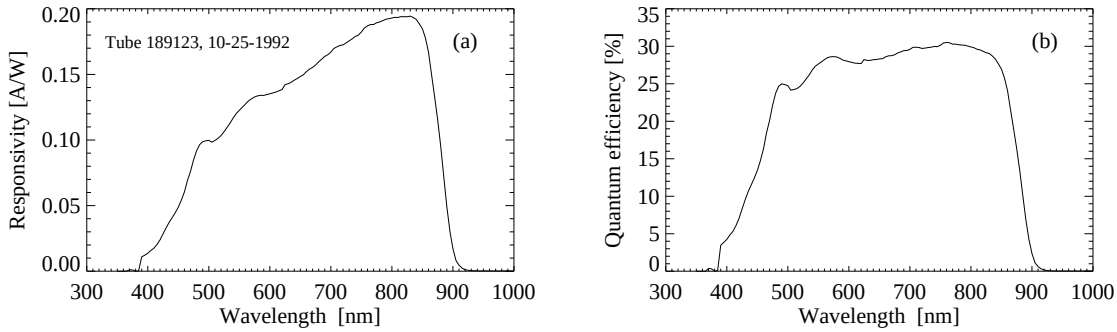

Figure 2.5: (a) PAI primary field of view intensifier tube responsivity. (b) Calculated quantum efficiency.

shown here refers to the actual "detective" quantum efficiency (DQE), meaning it takes into account effects such as the loss of photoelectrons impacting on the web of glass between the channels of the MCP.

Since image intensifiers have traditionally been aimed at the military marketplace, the "gain" of these devices is normally measured in a way appropriate for "night vision," not for scientific imaging. This is a fact not well understood by many users and thus deserves some treatment here. The nominal luminous gain quoted by the manufacturer in the case of the third-generation tube acquired for the PAI is an astounding 80,000. However, it is important to be aware that this number is determined in a way which produces a result both misleading and useless to the scientific user. Briefly put, the intensifier is illuminated with a tungsten filament lamp of color temperature 2854°K, and the input and output intensities are viewed with a photometer whose spectral response is similar to that of the human eye. The ratio of the measurements is given as the luminous gain. As can be see from the spectral responsivity curves of Figure 2.5, the intensifier is very sensitive to the near infra-red (incidentally, the dominant night-time illumination on the battle-field). The tungsten filament lamp emits most of its energy in the infra-red, with a large portion in the near infra-red, which the eye-corrected photometer cannot see or measure, but to which the intensifier responds very well. The photometer therefore accurately measures the output brightness of the intensifier under test (as observed at the green phosphor screen) but greatly underestimates the input because it is blind to the longer wavelengths that the intensifier itself sees very well. Consequently, the ratio of the numbers, i.e., the luminous gain, comes out as a very large number. However, the scientist generally needs to know the gain for applications where the light is not concentrated in the near infra-red but in a relatively narrow part of the visible spectrum. If intensifier tubes are re-measured as green-light-out for green-light-in, a number an order of magnitude smaller than the manufacturer-quoted luminous gain is usually obtained [Eather, 1982; Smith et al., 1983]. Upon request, the camera manufacturer estimated the true gain of the intensifier, taking into account factors such as MCP-voltage, phosphor efficiency, fiber-optic taper transmission, phosphor-to-CCD spectral matching, and CCD spectral responsivity, resulting in a calculated maximum true gain of about 3,600 CCD electrons per primary photoelectron. The manufacturer was unable to provide actual measured gain figures for their cameras. This estimated gain is quoted again in Table 2.3 along with several other important camera characteristics. These can be used—together with information on the other components comprising the PAI—for the purpose

ITT F4588 ICCD Camera Technical Specifications

Photocathode	GaAs
Photocathode diameter	18 mm
Intensifier resolution	36 lp mm^{-1}
Phosphor	P-22
Phosphor persistence to 10%	1.6–1.8 ms
Equivalent background illumination	4×10^{-18} W m^{-2}
Intensifier gating	150 ns to DC
FO minification	1.55 : 1
FO fiber diameter	6 μm
Intensifier gain	3,600 CCD electrons $photoelectron^{-1}$
Intensifier lifetime	20,000 hrs
Quantum efficiency	(See Figure 2.5b)
CCD	Texas Instruments TC241-40
CCD format	754(H) $\times$ 488(V) pixels image area
CCD optical fill-factor	100%
CCD image area	8.6365 mm $\times$ 6.5880 mm
CCD pixel size	11.5 μm $\times$ 27.0 μm
Pixel size projected onto photocathode	17.8 μm $\times$ 41.7 μm
CCD readout mode	Interlaced by centroid shifting
CCD full well capacity	200,000 electrons
Temporal resolution	30 frames s^{-1} (60 fields s^{-1})
Integration time	16.7 ms
CCD readout noise	80 electrons
Video resolution (maximum)	$>$600 lines, horizontal
Thermal requirements	-10° to +35° C (operating)
Power consumption	9.75 W (+15VDC)
Weight	2 kg

Table 2.3: PAI primary camera head technical specifications, as obtained from the camera manufacturer.

of modeling the imager's performance in order to assess its suitability for the scientific tasks at hand. Such modeling is the topic of Chapter 4.

2.1.2 Optics

As is often the case when developing solid-state imaging systems, off-the-shelf lenses were chosen rather than going to the expense of having lenses custom designed. The ICCD cameras used with the PAI are equipped with standard C-mount lens interfaces, causing a wide variety of commercially available 1-inch format TV lenses to be at our disposal. In addition, C-mount adapters for many non-C-mount objectives are readily available. This makes the PAI highly customizable from an optical point of view, permitting the use of objective lenses ranging from telescopes to fish-eye (all-sky) lenses. A main goal in selecting a particular set of objective lenses to be included with the PAI field component as standard equipment was to furnish the

imager with as fast optics as possible and with an as comprehensive set of fields of view as possible, within budgetary limits. As summarized in Table 2.1, the PAI currently includes the following objective lenses (as well as all necessary adapters):

- 25 mm, $f/1.4$ (TV lens)
- 50 mm, $f/1.4$ (TV lens)
- 105 mm, $f/1.8$ (35-mm camera lens)
- 1600 mm, $f/6.3$ (Schmidt-Cassegrain telescope)

The Schmidt-Cassegrain telescope has a frontal obscuration of 13.7% and is specified by the manufacturer as diffraction limited. A focal-length reducer was procured for this telescope; this is an optical device which threads directly onto the back of the telescope, between the telescope and the camera-head, and is designed to reduce the effective focal length of the telescope by 37.5%. The 1600 mm $f/6.3$ telescope is thus readily converted into a 1010 mm $f/3.9$ telescope if a slightly wider field of view and/or a faster telescope is needed.

A small selection of interference filters is also included (see, Table 2.1). Interference filters operate ideally in a beam of parallel light normal to its surface. The position of its transmission profile changes when illuminated under an oblique angle, as peak transmission decreases, bandwidth increases, and peak transmittance wavelength is shifted downward [Petitdidier, 1983]. The way around this problem is usually to utilize a telecentric optical assembly or in some cases simply to use broader-bandwidth filters. Due to budgetary restrictions a telecentric optical assembly was not procured for the PAI project. Accordingly, the included (fairly broad bandwidth) interference filters may only be used in combination with the telescope, where the maximum angle of divergence of a ray from the optic axis stays less than $5°$ through the telescope-to-camera adapter. A replacement telescope-to-camera adapter, doubling as a filter-holder, was designed and constructed for this purpose. In addition to interference filters, a Wratten 89B glass low-pass filter and a full set of step-up rings for the various objective lenses are included.

2.1.3 Time-Code Generator

When using the PAI to provide high temporal and spatial resolution support measurements for radar, rocket, or satellite experiments, accurate time-stamping of each video frame becomes crucial. For this purpose, the PAI takes advantage of the SMPTE time code standard [Benson, 1985]. Adopted in the late 1960s by the Society of Motion Picture and Television Engineers, SMPTE time code is an industry standard frame numbering system that assigns a specific number to each frame of video in the format of *hours:minutes:seconds;frames* (*hh:mm:ss;ff*). Other auxiliary information may be stored as well. There are two SMPTE formats for time code: Longitudinal Time Code (LTC) and Vertical Interval Time Code (VITC). LTC is an audible digital signal recorded on the audio channel of the video cassette recorder (VCR). VITC is a visual frame identification code recorded in the vertical blanking interval of each video field, thereby not obscuring any part of the visible video frame. Special decoding equipment is thus needed to recover the

recorded timing information. The advantage of VITC is that it can be accurately read and displayed even for still-frames, while in the case of LTC the video tape recorder must be in a continuous playback mode. The PAI records both LTC and VITC time codes in parallel, providing some redundancy (for reasons to be explained later). The main advantage of SMPTE time code is that it provides accuracy and repeatability. Every frame of video is given its own unique identifying number, and, once recorded, that time code/video frame relationship will be the same every time the tape is played. The SMPTE encoder plugs in between the camera and the VCR, as shown in Figures 2.1 and 2.4. An initial timing reference, accurate to within 1 μs, is provided to the SMPTE encoder by Global Positioning System (GPS) satellites through a GPS receiver acquired for this purpose.

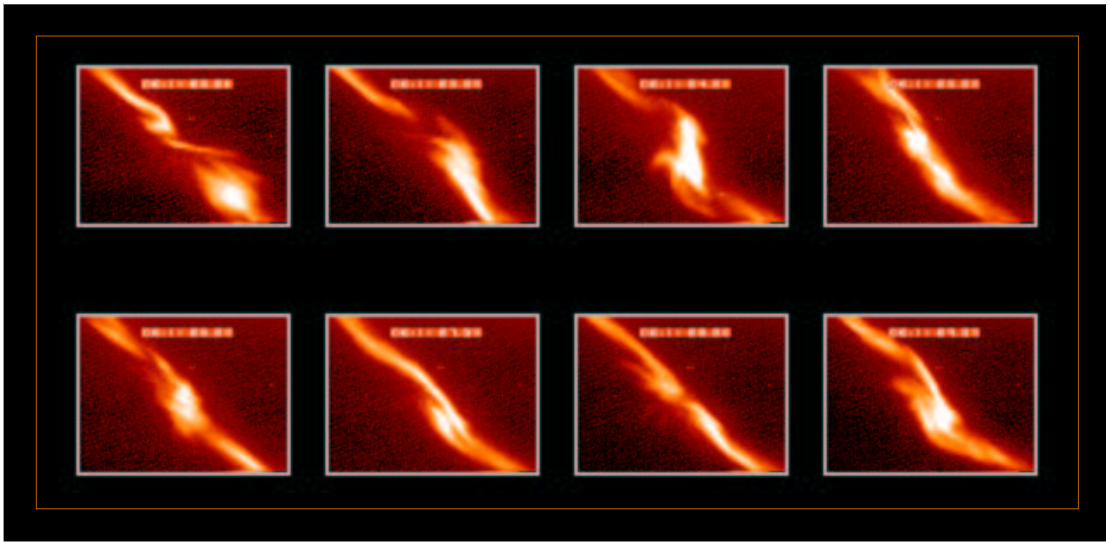

Figure 2.6: Data captured during a combined PAI and EISCAT Svalbard Radar (ESR) experiment at Longyearbyen, January 24, 1998. The SMPTE time code field has here been extracted and superimposed onto the frame. The image (subsampled) temporal resolution is here 1 s. Pseudo-colors have been added.

Using a so-called Window Generator, SMPTE time code (and auxiliary information) may be extracted from the recorded video footage and superimposed onto the footage as viewed on a TV monitor. An example of the SMPTE *hh:mm:ss;ff* format is shown in the snapshots of Figure 2.6. The *hh:mm:ss*-portion (06:11:02–06:11:09) is here Universal Time (UT). These images have a spatial resolution of about 100 m at 105 km altitude and clearly demonstrate the dynamic nature of the small-scale aurora. Significant topological changes are seen to take place within a time span of a few seconds. Changes occurring even on the order a fraction of a second are very common during auroral breakup conditions. The importance of accurate time-stamping of video frames is thus again underscored.

The frames field (*ff*) of the time code increments by one for each subsequent video frame. After reaching 29 it falls back to zero while the seconds field (*ss*) is incremented by one. A problem with using SMPTE time code with the RS-170A and NTSC video standards is that the actual frame rate of these standards is not precisely 30 frames per second, but rather 29.97 frames per second. This poses a problem as this small difference will cause SMPTE time and real time to differ increasingly over time. To compensate for this, the

PAI uses the so-called “drop-frame” compensation method. SMPTE drop-frame compensates exactly for the discrepancy between real-world time and SMPTE time by “dropping” frames from the sequence of SMPTE frames in order to catch up with real world time. What this means is that occasionally in the SMPTE sequence of time, the SMPTE time will jump forward by more than one frame. The time is adjusted forward by two frames on every minute boundary except at 00, 10, 20, 30, 40, and 50 minutes past the hour. Thus, when SMPTE time increments from 00:00:59;29, the next value will be 00:01:00;02 in drop-frame SMPTE rather than 00:01:00;00 in ordinary (uncompensated) SMPTE. In the case of drop-frame SMPTE time code, it must be remembered that certain codes no longer exist. For instance, there is no such time as 00:01:00;00—the time code is actually 00:01:00;02. A very simple computer program can be used to calculate the exact UT for any given drop-frame SMPTE time.

As indicated in Figure 2.1, also the secondary video channel receives a time-stamp. Due to budgetary constraints, this is simply done through an ordinary date-time generator which superimposes UT time and date information onto the video footage. It thus permanently obscures a portion of the signal, but it can be positioned discreetly off to the very top or bottom of the frame. Correct UT time is read off the GPS receiver’s front panel and manually set at the beginning of an observing session using push-buttons on the front of the the date-time generator. The time thus recorded is considered accurate to better than 0.5 s throughout that session.

2.1.4 Video Cassette Recorder

The video signal and attendant time code information are recorded in analog form on a Video Cassette Recorder (VCR) for later digitization and processing. The VCR is directly compatible with the RS-170A video standard, and is thus well matched to the dynamic range of the signal expected from the camera head. The video stream is always recorded at the full temporal resolution of 30 frames per second. The VCR is a professional unit utilizing the S-VHS recoding format, yielding a horizontal resolution of more than 400 lines [Hitachi, Ltd., 1989]. The VCR is equipped with playback-dedicated video heads separate from the standard record and playback video heads, allowing the “as-recorded” picture to be monitored in real-time in a separate window on the TV monitor during data gathering. In addition, the VCR is equipped with time-base correction (TBC) circuitry. The purpose of this particular functionality is explained in Chapter 3.2.

A maximum of two hours of continuous recording in the high-fidelity mode is possible before each change of tape. Shorter, 30-minute video tapes may be used for burst-mode data gathering, such as during individual satellite passes or rocket launches. In both cases, special broadcast-quality S-VHS tapes is the preferred medium.

2.2 The Laboratory Component

At the end of a campaign, equipment and data are shipped back to the laboratory. A preliminary assessment of the data is performed, and log sheets, as shown in Figure 2.7, are generated for each individual

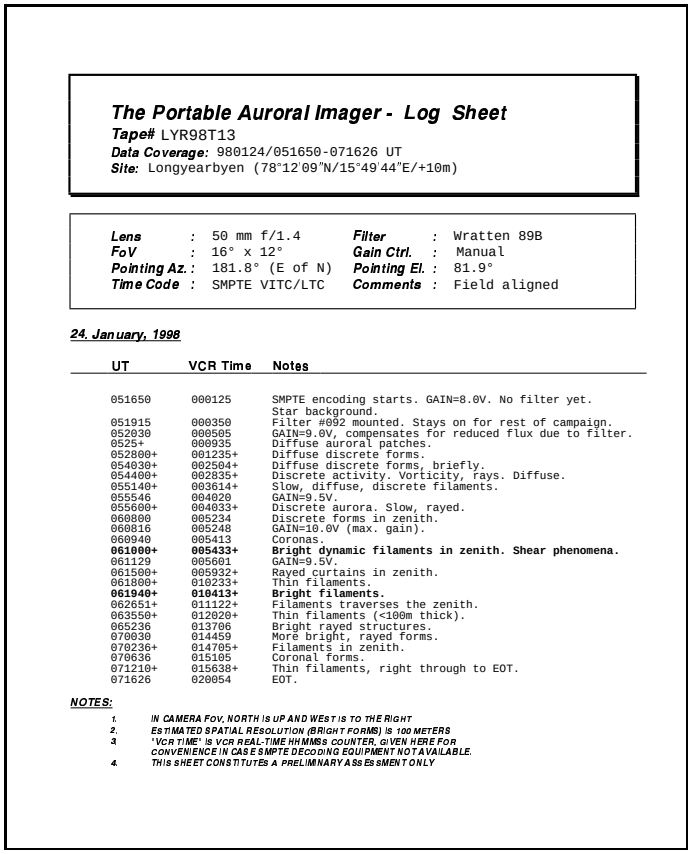

The Portable Auroral Imager - Log Sheet

Tape# LYR98T13
Data Coverage: 980124/051650-071626 UT
Site: Longyearbyen (78°12'09"N/15°49'44"E/+10m)

Lens :	50 mm f/1.4	***Filter*** :	Wratten 89B
FoV :	16° x 12°	***Gain Ctrl.*** :	Manual
Pointing Az. :	181.8° (E of N)	***Pointing El.*** :	81.9°
Time Code :	SMPTE VITC/LTC	***Comments*** :	Field aligned

24. January, 1998

UT	VCR Time	Notes
051650	000125	SMPTE encoding starts. GAIN=8.0V. No filter yet. Star background.
051915	000350	Filter #092 mounted. Stays on for rest of campaign.
052030	000505	GAIN=9.0V, compensates for reduced flux due to filter.
0525+	000935	Diffuse auroral patches.
052800+	001235+	Diffuse discrete forms.
054030+	002504+	Diffuse discrete forms, briefly.
054400+	002835+	Discrete activity. Vorticity, rays. Diffuse.
055140+	003614+	Slow, diffuse, discrete filaments.
055546	004020	GAIN=9.5V.
055600+	004033+	Discrete aurora. Slow, rayed.
060000	005234	Discrete forms in zenith.
060816	005248	GAIN=10.0V (max. gain).
060940	005413	Coronas.
061000+	**005433+**	**Bright dynamic filaments in zenith. Shear phenomena.**
061129	005601	GAIN=9.5V.
061500+	005932+	Rayed curtains in zenith.
061800+	010233+	Thin filaments.
061940+	**010413+**	**Bright filaments.**
062651+	011122+	Filaments traverses the zenith.
063550+	012020+	Thin filaments (<100m thick).
065236	013706	Bright rayed structures.
070030	014459	More bright, rayed forms.
070236+	014705+	Filaments in zenith.
070636	015105	Coronal forms.
071210+	015638+	Thin filaments, right through to EOT.
071626	020054	EOT.

NOTES:

1. *IN CAMERA FOV, NORTH IS UP AND WEST IS TO THE RIGHT*
2. *ESTIMATED SPATIAL RESOLUTION (BRIGHT FORMS) IS 100 METERS*
3. *'VCR TIME' IS VCR REAL-TIME HHMMSS COUNTER, GIVEN HERE FOR CONVENIENCE IN CASE SMPTE DECODING EQUIPMENT NOT AVAILABLE.*
4. *THIS SHEET CONSTITUTES A PRELIMINARY ASSESSMENT ONLY*

Figure 2.7: Facsimile of PAI log sheet.

video tape. These log sheets are used as a handy reference during the ensuing data analysis phase. A two-week campaign normally generates about 25 two-hour video tapes per video channel. The high-resolution VCR that is also part of the field component, along with a PC-based image digitizer and appropriate image processing and analysis software, form the basis of the PAI laboratory component. Table 2.4 gives a breakdown of the various hardware and software units that together comprise the laboratory part of the system, while Figure 2.8 illustrates the basic interrelationships between some of the major hardware components. Some important hardware and software issues are discussed next. Unless otherwise noted, all computer software were written by the author. No program listings are included here, as they alone could fill an entire volume. The reader is referred to Trondsen [1996] for a full set of program listings.

2.2.1 Hardware

The PAI laboratory component includes a fairly fast personal computer (PC) equipped with an image digitizer ("frame grabber") board. The image digitizer board accepts as input the RS-170A composite analog video signal fed to it from the VCR and is capable of digitizing video frames on-the-fly, i.e., at a rate of 30 frames per second, into an on-board memory buffer. The digitizer's analog-to-digital converter

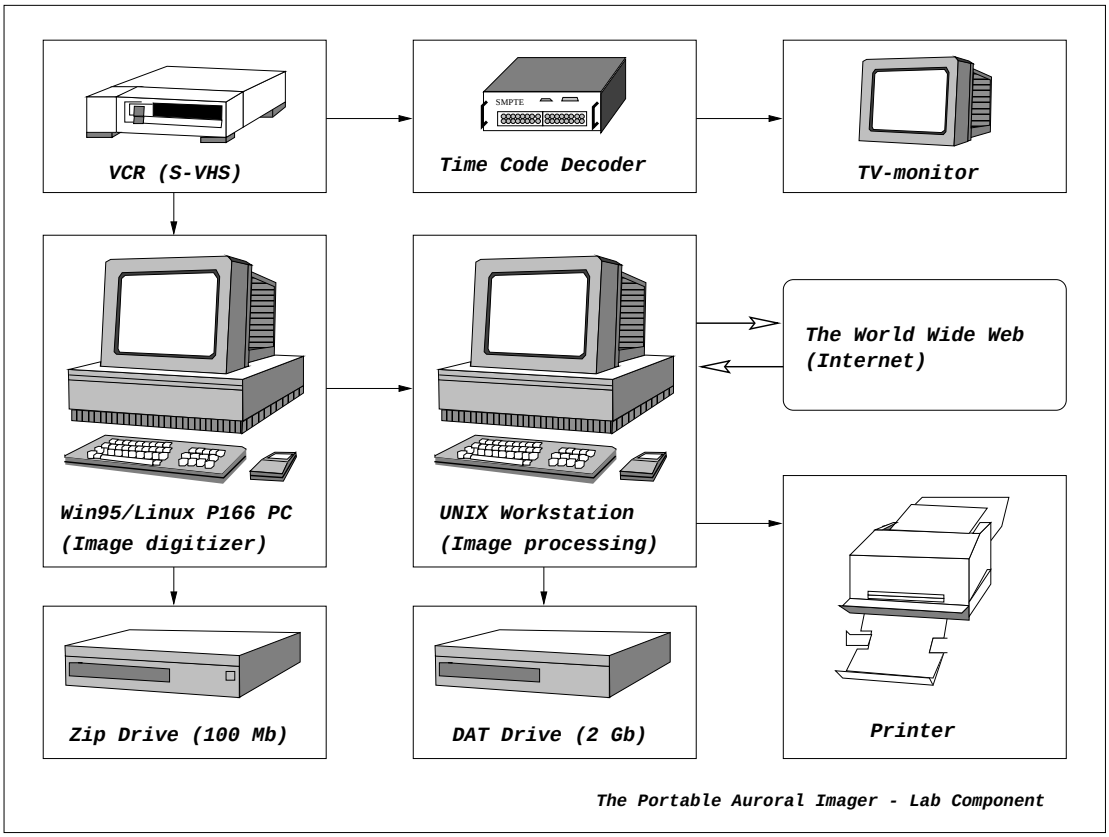

Figure 2.8: Schematic showing the PAI laboratory component.

(ADC) is 8 bits deep, resulting in $2^8 = 256$ gray-scale levels, a bit-depth generally considered sufficient for television bandwidth applications. Digitized video frames are stored on the computer's local hard-disk. A fast Ethernet card allows large sequences of digitized footage to be transferred from the PC to a more powerful image processing workstation, where they are subsequently analyzed and saved to digital audio tape (DAT). Publication-quality color or black & white hardcopies of image data are generated on a PostScript[1] laser printer.

As shown in Figure 2.8, a SMPTE time code decoder and a TV monitor are used with the VCR for locating desired data-intervals on a video tape prior to the commencement of the actual image digitization process. Once image digitization starts, the live real-time digitized footage can also be viewed in a window on the computer screen. The SMPTE decoder may be used between the VCR and the frame grabber as well, if digitization of an on-screen time stamp is desired. This was done when acquiring the data of Figure 2.6. This otherwise hidden time stamp, encoded within the video signal's vertical blanking interval, can always be detected by the frame grabber and used directly for file-naming purposes. Displaying the time stamp within the digitized frame is usually avoided for the purposes of preserving data integrity.

[1] PostScript is a registered trademark of Adobe Systems, Inc.

The PAI Laboratory Component

Hardware
Dell Pentium 166 MHz, 32 MB RAM, 2.1 Gb HD, 17" Monitor
MIPS Magnum, R3000 RISC Workstation
Hitachi VL-S100 S-VHS Professional Portable VCR *(Also part of field component)*
Sony SVO-1450 Industrial VHS VCR *(Also part of field component)*
JVC TM-63U 5" Compact Video Monitor *(Also part of field component)*
Horita VWG/FP-50 VITC Window Generator
Matrox IMAGE-LC Frame Grabber Card (IDE bus)
Iomega Zip 100 Mb disk drive (removable storage medium)
Archive Corporation 4 mm Digital Audio Tape (DAT) drive
100 Mbs Ethernet LAN adapter (PCI bus)
Radio Shack S/VHS Video Cassette Rewinder
Software
Operating Systems: Linux, RISC/os, and Windows 95
Image Analysis: Set of programs written in the Interactive Data Language (IDL)
General Image Manipulation: ImageMagick, xv, Gimp, pbmplus, bash, and Perl
Utilities: SatTrack (satellite tracking), Xephem (ephemerides)
Matrox Imaging Library (MIL: library of routines for programming the IMAGE-LC)
Borland C++ 3.1 (object oriented programming language)
Windows Application Programming Interface (API)
DimSum V1.0 (flexible image digitization program written in MIL/C++/Win API)

Table 2.4: A list of hardware and software units comprising the laboratory component of the PAI.

2.2.2 Software

Image Digitization

Operation of the image digitizer is controlled through a comprehensive set of computer programs running on the PC. This suite of programs controls all pertinent aspects of the digitization process and allows great flexibility in its customization. While the image digitizer is capable of digitizing images in real-time, i.e., at 30 frames per second, due to bandwidth limitations the PC is unable to actually write images to the hard-disk at the same high rate. Several workarounds to this problem have been implemented in the controlling software, all of which have their own unique merits. One approach is to write only a predefined region-of-interest (ROI) of the full video frame to the hard-disk. For example, if all the action takes place in only the lower half of the video frame, it may only be necessary to write this particular portion of the frame, thus speeding up the process of writing to disk as well as saving on memory usage. This approach still does not permit writing images to disk 30 times per second without making the ROI so small as to be practically useless, but has the advantage of permitting one to write several images per second, for prolonged periods of time. Arbitrary time delays can be introduced between the acquisition of individual images, in case periodic,

lower temporal resolution acquisition is sufficient. In case of idle periods of 1 s or more, the entire frame may comfortably be saved to the computer's hard-disk before the next frame is acquired. Another approach to the task of rapid image acquisition and storage is to create a so-called "virtual hard-disk" in the PC's Random Access Memory (RAM). The program then treats this area of RAM as an actual hard-disk, the difference being that since writing to RAM, rather than to a mechanical hard-disk, is an extremely fast process, it allows writing images or ROIs thereof in near real-time or real-time. The disadvantage to this approach is that since the size of the available RAM is limited, such burst-mode acquisition can only be performed for a few seconds at a time before acquisition has to be stopped and frames saved permanently to hard-disk. Further, binning of image pixels can be performed on-board the digitizer so as to increase the speed of writing images to the hard-disk, or for the purposes of matching the PAI's spatial resolution to that of supporting instrumentation operating in parallel with the PAI. Finally, if some temporal resolution can be sacrificed, video frames arriving from the VCR can be summed or averaged on-the-fly in special 16-bit deep frame buffers located on the image digitizer board, thus increasing the image "integration time," resulting in a corresponding improvement in the image signal-to-noise ratio. The resulting image may then be written to hard-disk in the background while the integration of the next frame is taking place.

The most important, and indeed the most difficult, aspect of the image acquisition process as a whole lies in carefully considering the characteristics of the data at hand, weighing these against the set down science objectives, and, based on that, designing an intelligent hybrid of the various acquisition modes just described. The controlling software has been designed to allow easy configuration and iterative re-configuration of the various parameters involved through a graphical user interface, thus allowing the image acquisition process to be fine-tuned as far as possible.

The gain and offset of the ADC are software controlled, permitting further optimization of the digitization process for any given data set. The ADC offset and camera video black level are set such that when digitizing video that was recorded with the camera lens-cap on and MCP voltage off, a few digitization units are obtained at the ADC output, thus establishing a known (i.e., positive) black reference. Further, when the RS-170A video signal is at its peak level (0.7 V above black level), digitized values of 255 are obtained.

The image digitizer pixel resolution (digitization timing) is software controlled. This resolution is in the case of the PAI project held constant at 640×480 pixels, as this particular timing choice leads to pixels having an exactly square geometry. At 8 bits per pixel, each full-sized image thus occupies 300 kilobytes of storage space, plus some header information. As already alluded to, the SMPTE VITC time code is extracted from each video frame and used in giving the corresponding digitized video frame a descriptive file name. Subsequent to a digitization session, digitized footage is transferred to a more powerful workstation for further processing and analysis.

Image Manipulation and Analysis

Before the digitized images are further analyzed, they must be corrected for instrument systematics, of both the additive and multiplicative kind. Such correction includes dark-frame subtraction, flat-field (fixed-

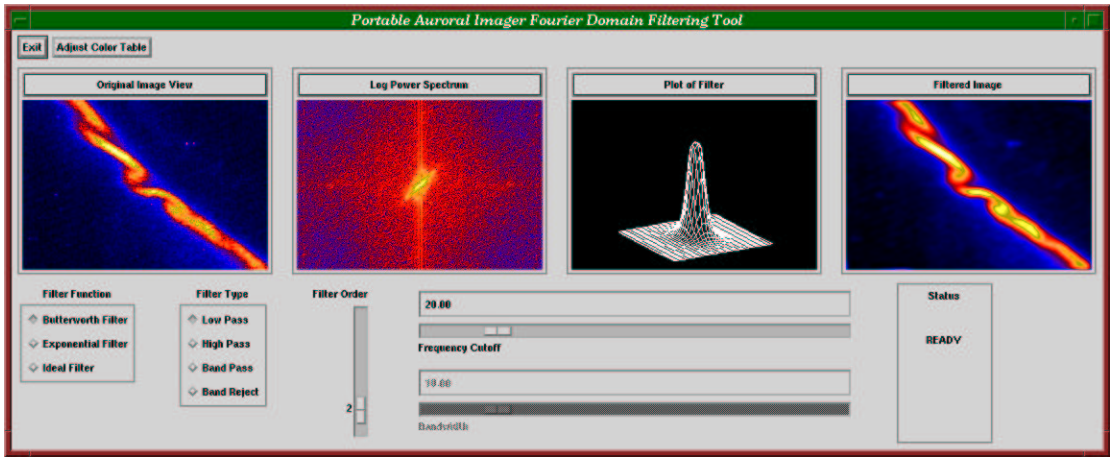

Figure 2.9: Sample output from the PAI Fourier domain analysis and filtering tool.

pattern) correction, and bad-pixel interpolation. There exist many excellent texts describing these concepts and the methods by which they are applied, see, e.g., Linde [1987] or Tyson [1986]. In the case of the third-generation ICCD acquired for the PAI project a certain price had to be paid in that, while the photocathode itself was exceptionally sensitive, the fiber optics taper exhibited a significant number of blemishes ("chicken-wire"). However, such blemishes only become apparent under high-light-level conditions, and can then be almost completely removed by performing a flat-field correction. Also, the PAI design is driven mainly by the requirement for low-light-level performance, in which case a sensitive photocathode becomes exceedingly more important than a cosmetically clean taper. A set of computer routines that perform corrections for instrument systematics has been written in the IDL[2] programming language. After these corrections are made, each pixel may be considered an independent photometer and the image is in a state ready for image analysis.

A large selection of image analysis routines has been written specifically for the PAI. There are routines for measuring the velocity of auroral features whose location change within the field of view from one frame to the next, the physical dimensions and lifetimes associated with a wide variety of auroral phenomena, and for measuring and fitting intensity profiles across auroral arcs. Furthermore, there are routines for performing Fourier analysis of the evolution of spatially periodic auroral distortions, and for Fourier domain filtering of auroral images, as shown in Figure 2.9. A set of routines designed for calibration purposes include programs for calculating image signal-to-noise ratios, and for measuring angular separations between sets of stars. The latter is used to verify the width of the field of view and to estimate the imager's angular resolution at a given distance away from the optic axis. These routined have all been written in the IDL programming language. By adopting IDL as the language of choice, additional routines may be written and integrated within the existing set with a minimum of effort.

General image manipulation, such as image cropping, binning, smoothing, histogram equalization, adding pseudo-colors, or performing conversions between different image formats, is mainly handled by

[2] IDL (Interactive Data Language) is a registered trademark of Research Systems, Inc.

software in the public domain and readily available over the Internet. Table 2.4 includes a list of the most frequently used image manipulation programs. These are particularly useful for automated processing of large amounts (e.g., several hundreds) of images, when identical sets of elementary operations are to be performed on each image.

Finally, software was developed for the purpose of superimposing geomagnetic latitude and longitude grid-lines onto auroral images. This procedure is performed by first determining the azimuth and elevation of each individual pixel in the image. These data are obtained by using stars as reference points. Figure 2.10a shows a star-background image obtained by the PAI. Figure 2.10b shows the corresponding scenario as output by an ephemerides program which was programmed for the same time, location, pointing, and field of view. The ephemerides program is here seen to output topocentric azimuth and elevation grid-lines. These are read by a computer program which subsequently calculates by interpolation the corresponding azimuth and elevation of each individual pixel in the image of Figure 2.10a. Calculated azimuth and elevation grid lines may then be superimposed onto the image, as shown in Figure 2.10c. Based on these data, the geographic latitude and longitude may be determined for each pixel, by assuming a certain altitude of emission. The method for calculating geographic latitude and longitude based on the azimuth and elevation data is described in detail in Appendix A. Once the geographic data have been obtained, they may be used as input to a model calculating the geomagnetic latitude and longitude for a given geographic position and altitude. The geomagnetic coordinates of each individual pixel in the frame may thus be obtained (see, e.g., Figure 8.1).

2.2.3 Public Outreach

Finally, an aspect of the PAI not to be undervalued is its Internet presence. Since its inception about 3 years ago, the Portable Auroral Imager Home Page on the World Wide Web (WWW) has seen approximately 15,000 hits from colleagues and other interested parties across the world. At this site, a variety of recent image data can be viewed. As well, reprints, preprints, conference handouts, and timely publication information can be retrieved. The Internet has a major advantage over the printed journal in that, while a journal can print a plate showing the temporal evolution of an auroral feature, the Internet may be used to show the reader an actual movie of the event. The PAI home page contains several movies that act as important complements to the corresponding published data. It is generally acknowledged that when dealing with dynamic phenomena, much information content is added when viewing a time series as a movie, as this permits essential phenomenological characteristics not otherwise obvious to leap out. By making auroral footage acquired in the field available on the WWW, other investigators, such as personnel devising theories for the generation and evolution of small-scale auroral phenomena, are allowed a (perhaps much-needed) sanity check.

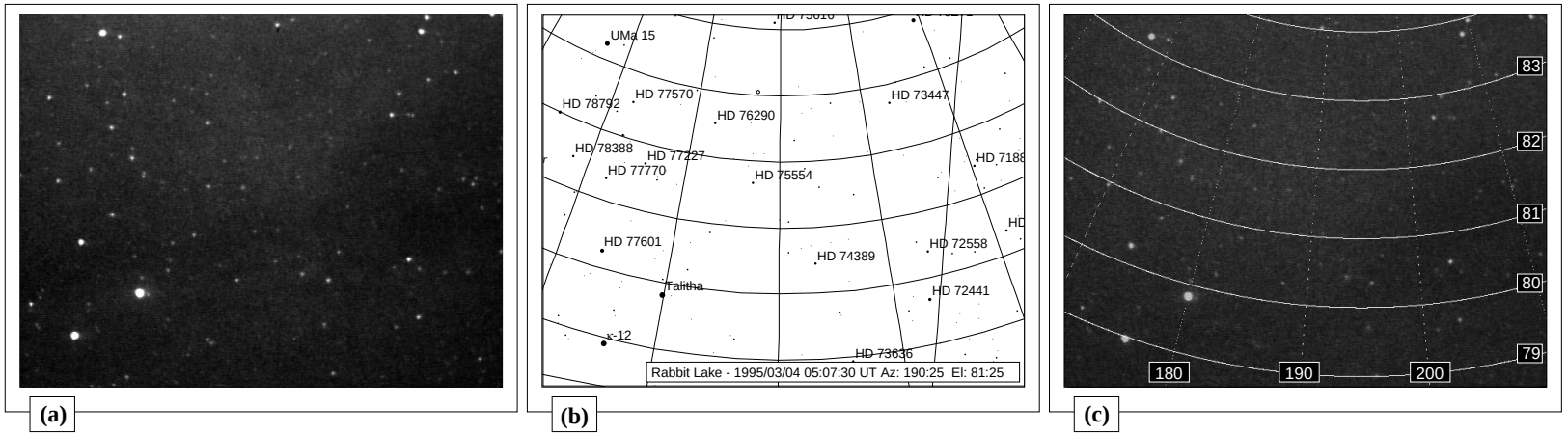

Figure 2.10: (a) Stellar field image acquired by the PAI. (b) Output from ephemerides program showing the same scenario, with superimposed azimuth and elevation grid-lines. (c) Stellar field image acquired by the PAI with azimuth and elevation grid-lines overlaid. Horizontally, topocentric azimuth (in degrees eastward of true north) is shown, while the topocentric elevation is shown vertically.

Chapter 3

Design Considerations

Designing any image sensing system is on a basic level a simple two-stage process. During Stage-1 one considers application constraints, requirements, and the desired results, while Stage-2 involves the actual design and selection of the optical system, detector, and data recording medium that will provide the system performance necessary to achieve the set down objectives. This latter stage is intrinsically iterative in nature, and can thus add a significant amount of complexity to the design process. The Portable Auroral Imager described in the preceding chapter was the end result of a design process wherein a variety of scientific and practical issues were carefully considered. In addition to cost, major design drivers were transportability, high temporal resolution, and a completely configurable spatial resolution with special emphasis on narrow field observations. This present chapter attempts to demonstrate that the system just described does indeed meet some set down application requirements, at least from a theoretical point of view. It must be remembered, however, that, as always when venturing into new and unexplored territory, the satisfaction of the various requirements will be largely by trial and error.

In designing a portable low-light-level imaging system with the intent to measure the wide range of characteristics of the small-scale aurora, both scientific and practical concerns must be addressed. In the first part of this chapter some issues with a bearing upon the scientific performance of the instrument are considered, while the latter part is devoted to a wide range of practical considerations. As well as giving the rationale behind the particular concept chosen for the PAI, this and the following chapter may serve as a guideline for future investigators who intend to design similar high-resolution, campaign-mode imaging instrumentation.

3.1 Scientific Considerations

The small-scale optical aurora, even more so than the “averaged” aurora seen through the eye of an all-sky camera, is an extremely dynamic phenomenon involving a wide range of spatio-temporal scale sizes and emission rates. Important issues to consider when designing any imaging system are those of angular and

temporal resolution, sensitivity, and dynamic range. These are the topic of the current section. The concepts of resolution and sensitivity are only briefly touched upon here; these are complex issues which are not very well understood by many researchers, and are thus treated in considerable more detail in Chapter 4.

3.1.1 Angular Resolution

A vast multitude of spatial scales are associated with auroral phenomena. Indeed, even within the very limited set of small-scale phenomena to be explored in this thesis, several orders of magnitude of spatial scales are involved (see, Chapter 1, page 4). In order to properly address any phenomenon within its native spatial regime, the imager's angular field of view must be tailored accordingly. Or, put another way, because the significant feature of an image is the variation of intensity over the field, the angular field of view must be selected to match the scale of the intensity variation to be measured. In the case of our investigation, there is thus the requirement of a highly configurable field of view.

The total angular field of view of the imager is a function of the focal length of the optics used in front of the detector and of the total detector size, while the angular resolution is determined by the focal length of the optics and the effective detector photosite ("pixel") size. Thus, for a given detector the field of view cannot be increased without derogating the spatial resolution. It is important to recognize that the photometry itself is completely independent of the size of the optical system. For example, although having widely different angular fields of view and angular resolutions, the 50 mm and 25 mm lenses included with the PAI system (see, Table 2.1) are exactly equivalent from a photometric standpoint. A proof of this fact is deferred to the next chapter. The minimum focal length is in general driven by spatial resolution requirements, while the maximum focal length is driven by requirements as to the angular field of view. Consequently, when selecting a field of view one must carefully consider how the spatial resolution is affected and make trade-offs appropriate to the spatial and temporal scale sizes of the particular auroral phenomenon under study. For the purposes of the present study of small-scale auroral forms, the imaging system includes a selection of lenses spanning several orders of magnitude of spatial resolution and angular field of view. Further, since the imaging system may employ simultaneous fields of view, the larger field of view may yield the context of events taking place within the smaller field of view.

The objective lenses selected for inclusion in the PAI were briefly described in Chapter 2.1.2. Some performance characteristics pertaining to each of the five selected objective lenses are presented in Table 3.1. First, the lens speed—defined as focal length divided by aperture diameter—is given. Next, the calculated angular field of view of each lens as applied to the PAI is given. More accurate figures, based on precise measurements of the angular separation between stars, are presented in Chapter 5. However, such measurements were not available at the time of the design phase, and manufacturer published technical specifications thus had to be relied upon. The angular field of view was calculated as follows. Referring to Table 2.3, the CCD photosensitive area is 8.6 mm (horizontal) by 6.6 mm (vertical). With a 1:1.55 fiber optic taper projecting this imaging area forward onto the photocathode, the dimensions of the photocathode imaging area is 13.4 mm by 10.2 mm. Referring to the simple geometry of Figure 3.1, for an objective lens of focal length f and a

Focal length	**1600 mm**	**1010 mm**	**105 mm**	**50 mm**	**25 mm**
***f*/#**	6.3	4.0	1.8	1.4	1.4
Field of view	.48° × .37°	.76° × .58°	7.3° × 5.6°	15° × 12°	30° × 23°
Linear coverage at 105 km altitude	880 m × 670 m	1390 m × 1060 m	13.4 km × 10.2 km	28 km × 21 km	56 km × 43 km
Angular resolution	.0012°	.0019°	.018°	.04°	.07°
Spatial Resolution at a zenith angle of half maximum	2.2 m	3.5 m	35 m	70 m	150 m

Table 3.1: Some important characteristics of the PAI objective lenses.

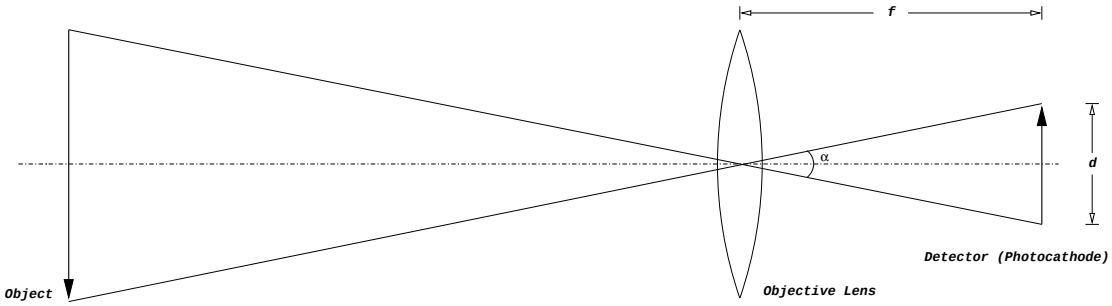

Figure 3.1: Simple objective lens geometry.

detector of dimension d, the angular field of view of view α, along that dimension is thus,

$$\alpha = 2 \times \arctan(\frac{d/2}{f}). \tag{3.1}$$

The corresponding mapped spatial coverage in zenith at 105 km altitude is given in the next line of Table 3.1. Next is given the maximum horizontal angular resolution of the instrument for each objective lens. As alluded to in Chapter 2.1.4, the VCR sets an upper limit to the imager's horizontal resolution of about 400 vertical TV lines. The PAI's horizontal resolution element is thus $dx = (13.4/400)$ mm $= 33.5$ μm, as projected forward onto the photocathode. Since we are in this case dealing with very small angles, the following expression suffices for determining the angular field of view of a single pixel of dimension dx located on the optic axis,

$$d\alpha = \frac{dx}{f} \quad \text{[radians]}. \tag{3.2}$$

This pixel angular resolution can then be mapped to a certain spatial resolution in the zenith ionosphere. In

the case of the linear projections offered by these relatively long focal length lenses, the ratio of the zenith ionospheric resolution element to the ionospheric altitude is equal to the ratio of the photocathode resolution element to the objective's focal length (law of similar triangles). However, due to spatial smearing the mapped spatial resolution degrades with increasing zenith angle. The last line of the table gives the spatial resolution at 105 km altitude for a zenith angle which is half of the maximum zenith angle offered by that lens. It is fairly easy to show that the spatial resolution R as a function of the zenith angle θ is,

$$R = \frac{105}{\cos^2(\theta)} \times \tan(d\alpha) \quad \text{[km]}, \tag{3.3}$$

for an ionospheric altitude of 105 km and a small pixel angular field of view of $d\alpha$. This is the expression that was used to derive the last line of Table 3.1. Of course, for a zenith angle of zero this reduces to the trivial result obtained by using Equation 3.2 and the law of similar triangles.

Only the imaging system's horizontal resolution was considered in the above discussion. Similar considerations may of course be applied along the detector's vertical dimension. The vertical resolution is the resolution transverse to the scanning lines of the television system. While the horizontal resolution, in our case about 400 TV lines, is limited by the bandwidth performance of the VCR's video processing circuitry, the vertical resolution is limited more directly by the number of scanning lines used in building the composite video signal. The television broadcast industry in North America utilizes 525 horizontal scanning lines per frame [Benson, 1985]. Due to the discrete nature of these raster lines, the number of picture elements that can be reproduced on a vertical line depends largely on the positioning of the elements with respect to the scan lines. Statistical surveys have shown that the effective vertical resolution is about 70% of the total number of available scan lines, resulting in a vertical resolution of about 370 TV lines. This factor of 0.7 is often referred to as the "Kell factor" [Fink, 1947].

In designing an auroral imaging system that is to fully resolve the thinnest auroral forms, a minimum scale size must be decided upon. As we have seen, the survey of Maggs and Davis [1968] showed that the auroral form of 70–100 m thickness appears to be the most common. It is thus imperative that our spatial resolution exceed the 70-m instrumental resolution of these investigators. This requirement is also suggested by the fact that the Larmor radius of electrons in the upper atmosphere is a mere 0–10 m. Borovsky et al. [1991] have performed a theoretical calculation wherein they consider the broadening of an infinitely thin sheet beam of electrons due to Coulomb scattering of electrons by upper atmosphere gas atoms and molecules. In the case of 5-keV electrons, a Gaussian full-width of the ionospheric energy-deposition of 9.5 m was obtained. A maximum spatial resolution design criterion can be derived based on this result. Assuming the light emission profile from the bottom edge of an auroral curtain has a Gaussian profile of 9.5 m full-width, then a spatial resolution of about a quarter of this, i.e., 2.4 m is needed to properly resolve the profile [Borovsky et al., 1991]. Assuming that the lower edge of the auroral curtain is found at about 105 km altitude [Currie, 1955; Störmer, 1955], the desired angular resolution of the imager, $d\alpha$, is,

$$d\alpha = (\frac{2.4 \text{ m}}{105000 \text{ m}}) = 2.3 \times 10^{-5} \text{ radians} = 0.0013^\circ. \tag{3.4}$$

It is not considered necessary here to construct an imager with a spatial resolution exceeding this figure. As

we have already seen, the horizontal resolution element at the PAI photocathode is 33.5 μm. To achieve the required angular resolution, the required objective lens focal length is thus,

$$f = \frac{33.5\ \mu\text{m}}{2.3 \times 10^{-5}\ \text{radians}} = 1480\ \text{mm}. \tag{3.5}$$

The 1600 mm focal length Schmidt-Cassegrain Telescope acquired for the PAI project is thus almost ideally suited for the purpose. As seen in Table 3.1, this objective lens exceeds the resolution requirement somewhat, an acceptable price to pay for not having to have optics custom made. The 1010 mm objective listed in the table can be used whenever spatial resolution can be sacrificed for faster optics and a somewhat wider field of view. As described in Chapter 2.1.2, this 1010 mm focal length lens is obtained simply by inserting a focal-length reducer into the 1600 mm telescope.

Any instrument observing auroral light necessarily integrates all the light emitted within a volume of space covered by the instrument's field of view along the line of sight of the instrument. Because auroral structures are aligned along the magnetic field, any aurora appearing away from magnetic zenith will be broadened due to perspective effects. It is therefore important that the imager be aligned with the local magnetic field line as precisely as possible. The importance of this is especially crucial (albeit practically difficult) in the case of the very small field of view associated with these highest spatial resolutions.

When studying multiple arcs and auroral vortices, whose gross features are expected to have dimensions in the range of several hundred meters to 10 km [Davis, 1978a; Hallinan and Davis, 1970], a spatial resolution in excess of 100 m, corresponding to an angular resolution of 0.05°, and a several tens of kilometers wide field of view may be considered sufficient. This yields a required focal length of about 40 mm. An off-the-shelf 50 mm objective lens suits the purpose quite well, as can be gleaned from Table 3.1. Its performance is nicely bracketed by that of the 105 mm and 25 mm objectives, obtained for the purposes of gaining some additional flexibility in studying these larger-scale phenomena.

It can thus be tentatively concluded that our spatial resolution requirements are indeed met by the PAI system described in Chapter 2, and that the current selection of objective lenses is suitable for studying a wide range of spatial scales existing within the small-scale aurora. However, the reader would do well to note that we have already made one crucial assumption. We have assumed that the imager is operating under high-light-level conditions, where there are sufficient photons available for the information content (and consequently, the spatial resolution) of the imagery to not be limited by the statistical nature of light itself. This (often unstated) assumption is indeed acceptable for purposes of gaining an idea of the maximum spatial performance obtainable from of the imager. However, the results are by no means representative of actual instrument performance under low-light-level conditions, as the lack of photons under such conditions have profound implications on the spatial resolution. The effective spatial resolution is thus very much a function of the image exposure time, which again is determined by requirements as to temporal resolution. An in-depth discussion of these important issues is found in Chapter 4. Fortunately, the small-scale aurora is typically associated with the auroral breakup, which itself is associated with an explosive release of energy into the upper atmosphere, resulting in the generation of extremely bright auroral forms [e.g., Elphinstone et al., 1996, and references therein].

3.1.2 Temporal Resolution

Auroral forms often exhibit rapid movements, and the image exposure time must thus be made short enough that the auroral feature does not get smeared significantly during the exposure, making it appear thicker than it really is. Moreover, since it is not practically possible to predict when such rapid small-scale forms are going to enter our field of view, it is desirable to obtain a new image every integration period. As pointed out in Chapter 2.1.1, the PAI detector operates at television-standard frame rates, a cost-effective solution from a system integration point of view. The standard television composite video format dictates that one full video frame be recorded every $\frac{1}{30}$ s. Each such frame is composed of two interlaced fields, with one field being captured each $\frac{1}{60}$-s interval. It is important to note that each of the two fields comprising a full video frame were integrated for $\frac{1}{60}$ s on the CCD, and that they were formed during two subsequent $\frac{1}{60}$-s intervals [Texas Instruments, 1993]. The image exposure time as well as the temporal resolution of the instrument is therefore 16.7 ms. To obtain a true 16.7 ms temporal resolution, one field (every second horizontal scan line) should be stripped away from the interlaced frame during image analysis. This will affect the vertical resolution, but horizontal resolution will remain the same. There is thus a trade-off between spatial and temporal resolution which will have to be assessed based on the characteristics of the data at hand. For many applications, such as the study of the slower-moving black aurora phenomenon [Royrvik, 1976], the full-frame 33.3 ms temporal "resolution" may be considered more than sufficient, thereby preserving the full vertical resolution.

When imaging features of thickness that approaches the theoretical limit discussed in the previous section, there is a requirement that the form should move through as small a fraction of the 2.4 m resolution element as possible. Auroral arcs moving in the north-south direction with speeds of up to 1 km s^{-1} have been observed [Omholt, 1971]. However, more typical velocities associated with auroral forms appear to be in the 100–200 m s^{-1} range [Evans, 1959; Frey et al., 1996a]. At 200 m s^{-1}, an arc will move through 2.4 m in about 12 ms. This is indeed comparable to the 16.7 ms integration time of the PAI, although it is obvious that fully resolved imaging of higher-velocity features at this spatial scale will be impossible without gating the intensifier. Decreasing the integration time by gating the intensifier into the off-state for portions of each 16.7 ms integration period may prevent smearing but will have an adverse effect both on the imager's sensitivity and spatial resolution, as will be shown in Chapter 4.

In addition to such very thin forms we shall survey small-scale features with ionospheric dimensions of $\sim$1 km, such as auroral curls. These are distortions appearing along auroral curtains and are reported to have diameters of $\sim$1 km and typical speeds of around 5–25 km s^{-1} [Hallinan and Davis, 1970; Haerendel et al., 1996]. A sufficiently-sized field of view must be allowed for such fast-moving features, and a reasonable spatial resolution would be on the order of a few hundred meters. This corresponds, again, to a required temporal resolution of on the order of 10–20 ms, which is satisfied by the PAI. In the case of the 50 mm objective lens, the field of view is about 30 km in the horizontal direction, allowing even very rapidly moving features to stay within the field of view for several seconds, permitting the study of the evolution of small-scale distortions at an acceptable temporal resolution. Lifetimes of auroral curls are on the order of a

Source	Wavelength [nm]	Rel. Intens.	Lifetime
O^1S	557.7	100	0.7 s
O^1D	630.0	2–100	110 s
O^2P	732.0	1–10	5 s
N_2 1P	596–1887	880	6 μs
N_2^+ 1N	391–522	150	70 ns
N_2^+ M	612–1585	630	14 μs
N_2^+ 2P	296–380	110	50 ns
N_2 VK	246–343	55	2 s
O_2^+ 1N	527–682	26	1 μs

Table 3.2: The most prominent emission lines and bands in the electron aurora. Emission intensities are relative to a 100 kR 557.7 nm aurora (IBC III); after Vallance Jones [1974].

second [Hallinan and Davis, 1970], thus further strengthening the case for the very short exposure times of the PAI. Speeds of features with velocities approaching as much as 100 km s^{-1} may be estimated in spite of significant smearing by considering the movement of the center of gravity of the smeared feature from one frame to the next.

A natural blurring of small-scale curtains due to the nonzero lifetime of some excited states has to be expected. An air atom may spend seconds in an excited state after having been excited by an auroral electron before it de-excites and emits a photon. The sheet of electrons that caused the excitation in the first place may in the meantime have moved through a considerable distance, leaving the recorded image of the electron sheet with an afterglow associated with it. The region of afterglow will typically be dimmer than the arc itself, often making it possible to distinguish between them provided the image is not overexposed and the scene not too turbulent [Borovsky, 1993b]. However, in the case of breakup aurora, metamorphosing small-scale features, such as auroral vortices within which there can be much fine structure, tend to sweep across the across the field of view at speeds of several tens of kilometers per second. Unless much of the afterglow is eliminated, any embedded fine structure is completely lost to the recorded image due to the associated reduction in contrast. Afterglow can be eliminated by using optical filters, i.e., by filtering through only wavelengths corresponding to very fast de-excitation of gas atoms. Such filtering, while certainly making the PAI's temporal resolution of 16.7 ms more meaningful, will cause fewer image-forming photons to be available at the detector, potentially having a dramatic impact on the final image signal-to-noise ratio.

Table 3.2 gives a summary of the most prominent emission lines and bands within the electron stimulated aurora, along with their lifetimes and relative intensities, as referred to an IBC III type aurora [Chamberlain, 1961; Vallance Jones, 1974]. IBC refers to the International Brightness Coefficient [Vallance Jones, 1974]. In a scenario of rapidly moving auroral features, blurring would in large part be caused by the intense emissions associated with the long-lifetime O^1S (557.7 nm) and O^1D (630.0 nm) states. For this reason, a Wratten 89B filter is included as part of the PAI instrument standard accessories. This glass low-pass filter has a cut-off wavelength of about 650 nm, and thus absorbs these long-lived emissions while passing through the more prompt emissions associated with the N_2^+ Meinel and N_2 1P bands to produce sharp, well-defined

images. In spite of filtering away some very bright emissions, considerable photon flux is still retained [Frey et al., 1996b]. This filter was applied to the imager during a recent field trip to the Adventdalen site, near Longyearbyen, Norway, where it was confirmed that the high intensity of the bands that are still passed through the filter, combined with the favorable spectral sensitivity of the GaAs photocathode (as shown in Figure 2.5) does indeed provide sufficient sensitivity for real-time observation of the aurora with a minimum of blurring. Some examples of the imagery thus acquired may be seen in Figure 2.6.

It is well-known that spatial smearing due to scene movement during image exposure can to a certain extent be corrected for by using sophisticated deconvolution techniques, assuming the overall topology of the feature does not change significantly during the exposure. However, the process cannot be automated in the case of the oftentimes chaotic or turbulent, high bandwidth data to be obtained by the PAI. Such deblurring techniques were thus not baselined on grounds that their implementation and application would become far too work-intensive.

3.1.3 Sensitivity and Dynamic Range

The sensitivity of the imager is adversely affected by the short exposure time that is required and by any optical filtering employed. For a photocathode of given quantum efficiency, the system sensitivity at the given exposure time may only be maximized by adopting a filter with more favorable transmission characteristics and a faster lens, subject to budgetary constraints. (The cost of a very fast, custom made lens can quickly exceed the total cost of the rest of the imaging system.) Further, contrary to popular opinion, turning up the gain of the image intensifier does not affect the imager's sensitivity. During the design process, the imager's sensitivity performance must be modeled for various electro-optical parameter alternatives. Such a model must take into account the various contributing sources of noise along the signal path. The output of the model would typically be a plot of image signal-to-noise ratio as a function of the rayleigh emission rate. The minimum detectable signal (the "threshold of detection") is often taken to be that resulting in a signal-to-noise ratio of 2:1 [Eather, 1982]. This kind of modeling may be used to answer questions such as whether an intensified or an unintensified CCD detector would suffice for detecting a given auroral emission at a given exposure time. A model of the sensitivity of the PAI, based on the vendor supplied specifications presented in Table 2.3, is presented in Chapter 4. Based on this model, the choice of an intensified CCD over a bare CCD will be justified.

For adequate modeling one needs access to information pertaining to expected scene intensities and scene contrast. However, there is currently a definite lack of information in literature regarding the brightnesses of small-scale auroral features; only rarely have reliable measurements been reported for specific auroral forms. One difficulty associated with intensity measurements on breakup forms is that the rapid movement and geometrical distortions involved often precludes a proper interpretation. Due to this general lack of information from the field regarding actual auroral emission rates, we resort to the results of Vallance Jones [1974] who presented calculated absolute band intensities for the most prominent auroral emissions. His calculations were done for IBC III aurora and might therefore be considered appropriate for

our purposes, as forms seen during breakup are typically very bright. Using Table 3.2 as a starting point, the calculations of Vallance Jones [1974] are used to estimate the fraction of these band intensities that fall within our limited passband. For modeling purposes, we make the simplifying assumption that the PAI photocathode has a 25% detective quantum efficiency throughout the wavelength range 480–850 nm and zero responsivity outside this band. This is a reasonable approximation, *cf.*, Figure 2.5. Using the tables of Vallance Jones [1974], the total auroral emission within this band can be estimated at approximately 750 kR. By mounting the Wratten 89B IR filter in front of the photocathode, a passband of 650–850 nm is introduced. The flux available within this window is estimated to be about 550 kR. This flux is still subject to a 5% transmission loss in the filter. Interference filters may be used to select individual emissions. The available photon flux will in that case suffer due to the typically 30–40% transmission loss associated with such filters.

A design aim in the case of the PAI was to implement an imager yielding a signal-to-noise ratio of no less than 2 for the 557.7 nm emission line per 16.7 ms exposure for breakup IBC III auroral intensities (100 kR). As will be shown in Chapter 4, this requirement is indeed satisfied by the PAI, from the modeling point of view. This theoretical result may or may not correspond to actual performance, but these kinds of calculations are nevertheless of great value during the initial stages of the imager design process as they furnish the designer with a valuable sanity-check.

Further, during the design process it was recognized that the signal-to-noise ratio of the data can later—during the data processing stage—be improved by averaging successive video frames during the image digitization process. It is widely recognized that whenever n video frames are averaged, the pixel signal-to-noise ratio improves by a factor $\sqrt{n}$. (Perhaps less widely recognized is the fact that there actually exists a general proof of this; see, Boyd [1983], page 117.) When performing such post-integration, there will always be a trade-off between temporal resolution and signal-to-noise ratio. For example, in the case of studying the black aurora the surrounding emission is expected to be relatively weak [Royrvik, 1976], but because the associated drifts are also typically quite slow the image signal-to-noise ratio may safely be improved by post-integration. Note, however, that although areas with identifiable intensity structure will improve in signal-to-noise ratio, it is unlikely that the summation of samples with a signal-to-noise ratio of unity or less will result in any recognizable improvement in the threshold of detection.

The dynamic range of an imager is in general limited at the low end by the minimum operating illumination as determined by the condition that the signal-to-noise ratio be no less than 2 and on the high end by the full-well capacity (saturation level) of the CCD. In our case, due to the high gain of the ICCD detector, each pixel can be considered as a photon counting device that preserves the Poisson statistics of the arriving photons. At an intermediate gain setting the intensifier generates approximately 1,500 electrons per photoevent in a CCD pixel. This implies an intrascene dynamic range of about 130, i.e., 7 bits, for a full-well capacity of 200,000 electrons. This can to a certain extent be improved upon by reducing the gain of the intensifier. Note that the analog-to-digital converter used by the PAI image digitization equipment is 8 bits—it is thus well matched to the full-well capacity of the CCD. Further, if temporal resolution is not of crucial importance, and if conditions permit, the intensifier may be gated and images be digitized and accumulated in the image digitizer's on-board 16-bit memory. This has the effect of shifting the responsibility of the

dynamic range limitation away from the detector and onto the bit-depth of the external digital memory. The ability to adjust the image intensifier's gain, and to subject it to rapid gating schemes, as well as the ability to integrate image data digitally, enables the imager to work under more than eight orders of magnitude of illumination levels [Lynch, 1989]. In comparison, the rather vast range stretching from nightglow to IBC IV aurora corresponds to only three or four orders of magnitude.

3.2 Practical Considerations

There is currently a very broad range of equipment available in the imaging marketplace. The numerous competing industry standards can make the task of selecting the individual building blocks of an imaging system somewhat confusing. On the other hand, the fact that such standards exist is a great boon as regards system integration, as the amount of in-house development may be minimized considerably. When selecting the building blocks of an imaging system, the type of operation in which the imaging system is to be deployed becomes an important consideration. The PAI may be considered a purely tactical instrument, and should thus be light, compact, robust, and simple to deploy and operate in the field. Strategic installations, on the other hand, such as all-sky cameras, have fewer constraints, and size, mass, and user-friendliness may be compromised for the purposes of gaining certain instrumental advantages. Some design considerations pertaining to practical aspects of the PAI are now briefly discussed, and should serve as a guideline for future investigators wishing to pursue a similar concept. The issues discussed all affect the ease with which the system is stored, transported, deployed, configured, and utilized. It must be remembered that the solution that was chosen in the case of the PAI reflects trade-offs between scientific, practical, as well as budgetary requirements. Note that it was from the beginning the intention that the PAI be a campaign mode instrument, to be set up and operated in the field by one person. With the enormous amount of data generated (30 Gigabytes per hour), unmanned, long-term operational modes are, given the current state-of-the-art of data storage and telecommunication, considered unfeasible.

The issues to be touched upon in the following sections include those of data recording convenience, interface requirements, environmental requirements, as well as transportability requirements.

3.2.1 Data Recording Convenience

There are several advantages to storing auroral footage on video tape. Modern video tape recorders are directly compatible with the industry standard NTSC/RS-170A composite video signal output by many solid-state video cameras. Further, one two-hour S-VHS format video tape can store the equivalent of about 60 Gigabytes of digital image data (without any error detection or correction facilities). An average two-week field trip may result in the recording of about 25 such tapes, i.e., a total of 1.5 Terabytes. There currently does not exist a viable digital alternative to storing such vast amounts of data. In addition, the video signal provides a fairly accurate time base for events recorded on tape. Using standard video equipment, the 30 frames per second (actually, 29.97 frames per second) capture rate allows studies of auroral dynamics of features with

a reasonable range of velocities, as shown in an earlier section. The extraction of information from video tape can be done using reasonably priced, commercially available components for image digitization and time code recovery. Digitized images may be transferred across local area networks and accessed from image processing workstations for further image processing and analysis. There are certain constraints on the technique, which all have to be taken into account as they affect the overall system design. The following paragraphs are devoted to a brief discussion of some of the most important issues in this regard. Some of these issues have been touched upon already in some way or another. The fact that they are touched upon again, here in the context of selecting a PAI data recording medium, merely reflects the iterative nature of the entire design process.

Spatial and contrast resolution in the recovered image. When using video tape to store scientific data, the spatial resolution of the overall imaging system will usually be limited by the video recorder itself. This is certainly the case for the PAI. However, the S-VHS storage format was at the time of designing the PAI found to be the only format that offered acceptable performance at an affordable price. By chosing the S-VHS video format, which has a luminance signal bandwidth of 5 MHz, a horizontal resolution of about 440 lines is achieved [Benson, 1985]. While this resolution is much better than that of the conventional VHS standard, it is still significantly below the 650 lines of resolution of the original signal arriving down the line from the camera head. Thus, by recording the video signal on the analog S-VHS medium, the spatial resolution is expected to degrade considerably as the VCR sets the upper limit to the achievable resolution. The resulting system resolution is actually a convolution of the camera's resolution with the VCR's resolution, yielding a useful resolution of no more than about 400 lines. The contrast in the recorded footage, on the other hand, is related not to the VCR but mainly to the video camera used, as well as to the actual contrast within the scene being observed [Johnston et al., 1991]. Aurora superimposed onto an airglow background might contribute to such low-contrast images.

Velocity of the feature of interest as compared to video frame rates. In order to use standard video equipment, the velocity of the object under study must be such that the movement in $\frac{1}{30}$s is not significant. If the per frame movement is greater than the equivalent of a few pixels in the digitized image then noticeable blurring will occur. As shown in the Chapter 3.1.1, an intelligent choice of objective lens must be made for any particular scientific investigation. Image smearing may be decreased by gating the image intensifier, thereby decreasing the effective exposure time. This of course causes a corresponding reduction in the amount of available image-forming photons, potentially impacting the resulting image signal-to-noise ratio and spatial resolution.

Requirement for frame accuracy. When performing coordinated measurements with other high temporal resolution instrumentation, single-frame accuracy becomes important. In order to recover specific video frames from the from video tape it is necessary to have unique identifiers for each frame. As described in Chapter 2.1.3, this may be accomplished by writing a SMPTE time code precisely synchronized with each video frame. SMPTE time code is a serial collection of bits that encode a unique number for each frame. The time code and the corresponding video frame are always written on tape simultaneously in order to achieve the necessary precision of correspondence. The time code sequence may be written into the video frame's

vertical blanking area. It can be recorded onto the audio track as well, provided the audio track is not used for other purposes, such as for simultaneous recording of digital magnetometer data, riometer data, or perhaps audible "whistler" data. In the case of the PAI VCR, which is a professional, lightweight field-unit, there is a dedicated time code audio input, allowing the recording of other audio signals in addition to the time code data.

Establishing correspondence between the video record and related real-time events. It is important to provide correspondence between the images being recorded and other aspects of the experimental environment. In addition to the important issue just discussed of labeling each frame with a Universal Time, such other aspects might include the pointing of the optic axis (azimuth, elevation), intensifier gain and/or gating pulse-width, as well as information on what filter is mounted on the objective lens. A portion of the SMPTE time code bitstream, known as the "user bits," is available for storing auxiliary data. A personal computer could thus be used as a controller of many external parameters, and the instantaneous status of these could be conveniently encoded in the form of bitwise flags into the SMPTE user bits of each video frame. In the case of the PAI, however, the inclusion of a personal computer was not built into the design, mainly for purposes of system portability, compactness, robustness, and reliability. The main advantage of including a personal computer into the PAI system would have been the ability to digitize images in the field, avoiding the resolution-degrading intermediate step of an analog VCR. However, this was not considered feasible due to the extreme data bandwidth involved (300 kbytes frame^{-1} $\times$ 30 frames s^{-1} = 70 Megabits s^{-1}) and attendant data storage problems. For this reason, the PAI takes advantage of the "log-book principle" to establish any relevant correspondence between the video record and real-time events. This ancient and proven method relies on the experimenter manually entering any changes to the experimental environment into a log-book for future reference. While far from frame accurate, this approach nevertheless provides a cost-effective and compact alternative to the more sophisticated approach. Recently, fairly powerful "palmtop" computers with credit-card sized frame grabbers have become available on the market. Their size and weight might very well justify their inclusion into a future upgraded version of the PAI. Such a small computer could then be used to control the image intensifier gain and gating duty-cycle, as well as to insert pertinent information into each video frame's SMPTE user's bits. The communication between computer and SMPTE encoder would take place through the standard RS-422/232 serial interface of the SMPTE encoder. Additionally, a small frame grabber residing on the computer could be used to subsample the analog TV signal in selectable time intervals (e.g., 1 minute intervals) and store these images on the local hard disk. These digitally stored images could later be used in the laboratory to correct the images derived from the analog video recorder for quality and intensity loss during recording and playback.

Digitization issues. As already noted in Chapter 2.2.2, it is not generally possible to digitize a continuous stream of video frames from the VCR. The image digitizer itself is certainly fast enough for this to be done, but the problem arises because most current computer equipment cannot deal with the resulting data rate. As described earlier, the PAI personal computer based image digitizer is a monochrome unit operating at eight bits per pixel. Images are digitized into a 640 $\times$ 480 pixels format according to the VGA industry standard. At the given RS-170A video rate of 30 frames per second, 9 Megabytes of digital data are thus

generated *each second.* This is a rate that most current personal computers or workstations cannot even move in memory, much less write to an external storage device. Some of the methods used to get around this serious inherent limitation were described in Chapter 2.2.2. Another issue related to digitization of prerecorded video is that of synchronization signal integrity. VCRs are infamous for reproducing noisy and inaccurate composite video synchronization signals. The result of bad synchronization information from a VCR is that an image digitizer may fail to correctly digitize video frames [Johnston et al., 1991]. To alleviate this potential problem, the VCR includes a so-called time-base corrector (TBC). The TBC circuitry strips off the synchronization information from the video signal during playback and inserts restored, correctly generated synchronization information. The TBC is meant to ensure a stabilized playback picture with reduced jitter. The VCR's TBC functionality has indeed proven itself to be of great value when digitizing PAI data. However, when the TBC function is enabled, any recorded SMPTE VITC time code information (see, Chapter 2.1.3) is lost. It is for this reason that both VITC and LTC time code are recorded during PAI campaigns. The LTC time code resides on the video tape's audio track and is thus unaffected by the TBC.

Storage and processing issues. An average campaign yields video data that would occupy several Terabytes of storage space if digitized. It is thus necessary that only selected sequences of particular scientific interest be digitized at a time. In the case of the PAI, digitized video images are immediately transferred via a local-area network to image processing workstations, where typically a set of preprocessing operations are immediately executed, such as rotation and reflection operations to give a standard orientation, and conversion of the image data to a different image storage format that takes advantage of modern data compression techniques. Images may be compressed a factor of two or three losslessly, and a factor of 10 by slightly lossy techniques. Compressed images are finally saved onto DAT tape, each tape holding approximately 2 Gigabytes of compressed image data. Recall again that one two-hour video tape contains an equivalent of 60 Gigabytes of data. The capacity of a single DAT tape thus only becomes comparable by introducing lossy compression methods (e.g., Fourier transform methods which remove from the image spatial information to which the human eye is not generally sensitive).

3.2.2 Interface Requirements

When integrating a complete imaging system, one must consider all the various interfaces involved, so as to ensure compatibility, flexibility, and expandability. Interfaces that had to be considered during the PAI design process were optical, electrical, mechanic, and electronic in nature.

Opto-mechanical interfaces

Opto-mechanically, the interface problem was solved by adopting the C-mount standard for lens mounting. Since adapters are available for converting from many other common formats to this format, this choice ensured a flexible, optically configurable instrument. C-mount compatible telecentric optical assemblies for use with interference filters are commercially available, although not yet adopted as an integral part of the PAI.

A C-mount compatible lens has a flange focal distance of 17.526 mm (0.690”). The flange focal distance is the distance from the lens mounting flange to the convergence point of all parallel rays entering the lens when the lens is focused at infinity. The C-mount lens convention dictates that the camera mating threads be according to specification 1.00–32 UN-2B. It should be noted that not all C-mount type lenses will work adequately with the PAI ICCDs. A majority of C-mount lenses on the market are designed for closed circuit TV (CCTV) cameras. Historically, these cameras have had one of three different sized image sensors: $\frac{1}{2}$-inch, $\frac{2}{3}$-inch, and 1-inch. The actual sizes of the photosensitive areas for these three standards (i.e., the diagonal measure of the 4:3 aspect ratio video field of view) are 8 mm, 11 mm, and 15.3 mm, respectively. Since the PAI camera has a photosensitive area diagonal of approximately 17 mm, care must in general be exercised in selecting lenses. Only commercial C-mount lenses listed for use with 1-inch formats should be used with the PAI camera heads. Use of lenses which were designed for the $\frac{1}{2}$-inch or $\frac{2}{3}$-inch formats will result in vignetting of the image.

The Nikon 105 mm, $f/1.8$ lens that is included in the PAI system was originally manufactured for use with ordinary 35-mm film cameras. A Nikon-to-C adapter is used to mount this lens on the PAI camera heads. Since only the center portion of the field of view is used, no vignetting is experienced with this long focal length objective, in spite of its high speed.

Electronic interfaces

When designing any imaging system, the variety of associated electronic interfaces must be considered carefully. By clever selection of interface standards, system integration may be simplified considerably. Important interfaces to consider are those related to camera video output, data recording and digitization, time code equipment, gain and gating control, and housekeeping.

In the case of the PAI, system integration was considerably simplified by adopting the RS-170A standard, an analog composite video signal standard [Benson, 1985]. During the design process, an important consideration was whether or not to employ a digital or an analog camera. Digital cameras combine the ICCD, its drive circuitry, and an ADC into one unit, providing a digital signal out of the camera. Using digital imaging reduces analog noise and signal deterioration in the interconnecting cables. As has already been pointed out, however, the high data bandwidth required for high temporal and spatial resolution imaging prohibits the implementation of a digital camera of sufficient flexibility. Another disadvantage to digital imaging is that these cameras tend to output data in parallel form, requiring one to work in the field with numerous data, synchronization, and control lines. This is especially problematic during outdoor operations under arctic winter conditions where it is imperative that the number of parts that may fail be minimized. Expensive, proprietary cables usually have to be purchased for these systems, as there is no truly standard connector. Further, these cables have to be of limited length to preserve the integrity of the digital data. Analog imaging (RS-170A) was thus chosen for reasons of off-the-shelf availability, affordability, transportability, and ease of data storage. The 16.7 ms temporal resolution of the PAI was to a large extent driven by this choice. The choice of composite video allows the video signal to be carried by a single 75 Ω RG-59/U coaxial cable

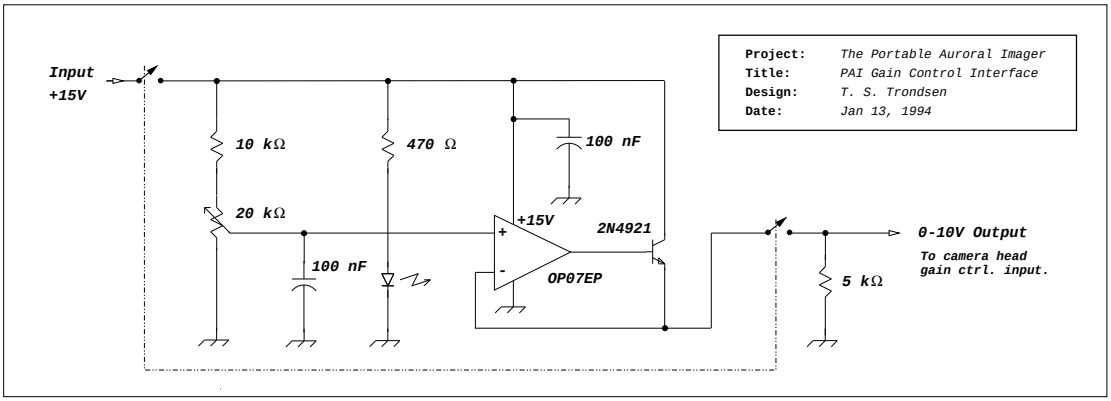

Figure 3.2: Schematic of the homemade PAI gain control interface electronics.

and viewed instantaneously. The composite video is directly compatible with a variety of off-the-shelf time code equipment, VCRs, TV monitors, and video printers. Back in the laboratory, the field VCR plugs directly into PC-based image digitization equipment without the necessity of converting the video signal into another format prior to digitization, significantly streamlining the data reduction process. The PAI cameras, VCRs, SMPTE time code equipment, TV monitors, and the image digitizer are all implemented with standard BNC-type connectors, allowing these components to be interconnected through RG-59/U coaxial cables. This again allows the system to be easily reconfigured according to changing needs. Since the camera head is often to be operated outdoors with all data recording and time code equipment residing indoors, some care has to be taken to avoid visible degradation of the video signal through signal losses in the coaxial cable. Low-loss coaxial cables have been adopted throughout the PAI system. These have a nominal attenuation of 3 dB per 100 m at video frequencies. During PAI field trips where the camera head was operated outdoors, cables were fed out of the building through cable ports and strung along the ground to a nearby spot of level ground where the system tripod was set up. Cable lengths of 15 m were generally found sufficient, resulting in no noticeable degradation of the video signal.

In addition to a BNC-type connector for the video signal, the PAI cameras are equipped with 15-pin subminiature connectors for power supply and camera control purposes. Extra connectors were procured separately, and 15 m long extension cables were built in-house. The camera control port is used to control the intensifier gain or gating characteristics through standard TTL-level signals. As well, a variety of synchronization pulses are output. When manual gain control is enabled, the MCP gain is controlled by subjecting a control input to a voltage in the range of 0–10 V (DC). The corresponding gain is zero for a 0 V signal and maximum for a 10 V signal. There is a known relationship between this control voltage and the corresponding MCP voltage. Unfortunately, the impedance of this gain control input is only about 100 Ω, acknowledged by the camera manufacturer to be a design flaw. Due to this low input impedance the input had to be buffered. The voltage follower circuit shown in Figure 3.2 was designed for this purpose. The principle behind voltage followers is described in more detail in, e.g., Horowitz and Hill [1989].

The VCR unit procured for the PAI primary channel is aimed at the professional/industrial market. In addition to unusual features like the digital time-base correction circuitry described above, it is also equipped with an RS-422 serial port interface, allowing its operation to be remotely controlled via the serial port of any personal computer through a standard RS-232 to RS-422 converter. As mentioned earlier, a small "palmtop" computer might in the future be integrated into the PAI system—possibly allowing the PAI to also be used in an unmanned operational mode on a limited basis.

Electrical interfaces

When designing a portable imager, local mains power characteristics at potential sites must be considered. The imager's power supplies must be able to handle a sufficient range of AC voltages and frequencies. Primary target areas for PAI were North America and Northern Scandinavia. Therefore, switched power supplies compatible with the European 220 V, 50 Hz as well as the North American 110 V, 60 Hz were procured. Special attention had to be paid to local grounding requirements. Class I application mains cords were procured with NEMA 5-15 type mains plugs for operations in the U.S. and Canada, and CEE 7/7 type plugs for operations in Scandinavia. The power requirements of the imager must also be considered before installing the imager at a new site. The total PAI power consumption (two fields of view, and including heating tapes) is about 500 W.

Mechanical interfaces

Mechanically, the main problem was to find a way of mounting the camera heads onto a sturdy yet pointable base during field operations. The solution found was to use a telescope, with its very sturdy tripod and fork mount, as a base. The tripod assembly has an altitude-azimuth mount which permits easy pointing of the optic axis prior to using reference stars for fine-tuning the pointing. Leveling of the tripod is accomplished using a spirit-level. The requirement of a rigid base arises from the fact that at the high angular resolution and narrow field of view of the telescope, mechanical, wind-induced vibrations of the telescope optical assembly tend to become very apparent in the recorded data.

Adapters for mounting cameras onto the telescope's optical assembly tube were available from the telescope manufacturer. These are compatible with the standard 1/4-20 TPI threaded holes found in the base of most video and still cameras today, including the PAI camera heads.

3.2.3 EMI Requirements

Electromagnetic interference and susceptibility (EMI) issues must also be considered. As the PAI is intended for deployment in the vicinity of permanently installed instrumentation, a sensitive shortwave receiver was used to confirm that no part of the PAI was radiating in the vicinity of 30 MHz, a frequency range to which sensitive riometers are often tuned. The PAI was found to be somewhat susceptible to interference from other instrumentation, however. When operating within research trailers packed with other instrumentation, a subtle, intermittent diagonal interference pattern appeared across the recorded video frames. This

pattern was, however, so weak as to be barely noticeable. The interference could generally be minimized through shielding the indoor components of the imager using aluminum foil.

3.2.4 Environmental Requirements

The manufacturer-specified operational temperature range of the camera head is -10°C to +35°C, and the storage temperature range is -30°C to +65°C. While the storage temperature permits safe commercial transportation into the arctic, the operational temperature does not permit outdoor operations under typical arctic winter conditions. This problem was solved by including a set of thermostatically controlled heating tapes with the PAI. Using these heating tapes, the temperature of the camera electronics was maintained at about +10°C, even at ambient temperatures of -40°C. Heating tapes were wrapped around the camera body itself, somewhat behind the intensifier tube so as to avoid heating the detector itself, thus reducing the amount of detector dark current. Since the characteristics of interference filters are temperature sensitive, thermostatically controlled heating tapes are applied to the interference filter holder device as well.

Cooling of the detector is in the case of the PAI not considered necessary, in view of the mere 17 ms on-chip integration time which makes dark current negligible, even at room temperatures. During normal use, the total photocathode lifetime is 20,000 hours. A field trip averages 50 hours, and the photocathode lifetime is thus satisfactory for these kinds of tactical applications.

The primary lens of the telescope constitutes a fairly large glass surface pointed at outer space, a cold place indeed. This results in the formation of dew and ice on the telescope's correcting plate, quickly reducing visibility through the telescope to zero. This problem was completely eliminated by applying two revolutions of a $\frac{1}{2}$-inch, 100 W heating wire around the primary lens mount ring.

The PAI is operated outdoors whenever the highest-resolution measurements are required. The telescope would most likely not fit indoors, and even if it did, convection bubbles rising above the dome would probably severely affect the effective angular resolution of the instrument. If the telescope field of view is not required, the ICCD cameras may be run indoors with shorter focal length objectives, and comfortably pointed out through an observing dome in the roof of the building. Since wind shake is not a concern in this case, ordinary light-weight camera tripods may be used for such operations.

Whenever possible, especially rugged components were deliberately chosen for the PAI. For example, the VCR is a very compact unit especially designed for broadcast industry field work. Also, the TV monitor is a very compact unit of the type often used for helicopter-mounted operations. Rugged construction permits the equipment to withstand hostile environmental conditions, and decreases the risk of equipment damage during shipping.

3.2.5 Transportability Requirements

Finally, another major design driver in the case of the PAI was transportability. A rugged and compact instrument allows for easy deployability during short campaign operations, such as coordinated studies involving radar, rocket, or satellite footprint support. Referring to Table 2.2, the PAI package consists

of a total of five shipping/storage cases. Cases I–III are ruggedized foam-fitted aluminum cases especially designed for the PAI project. The total weight of these is 120 kg, and they contain all the equipment needed in the case where the highest-resolution measurements are not required. This is true in the case of most coordinated studies where fields of view corresponding to that of 50–105 mm focal length lenses are usually the most meaningful choices. During surveys of the thinnest of auroral arcs, however, the telescope and tripod (Cases IV-V) need to be included as well, bringing the total PAI weight up to approximately 170 kg. In both modes the total weight and physical dimensions are well within what international couriers are able to deliver anywhere in the world within days.

Chapter 4

Sensitivity and Resolution: A Closer Look

4.1 Some Radiometric Concepts

We here define certain radiometric quantities to be used in subsequent sections. In particular, the unit of rayleigh (R) which is widely used in auroral and airglow research is defined, and its relationship to source radiance is made clear. A relationship between source radiance and detector irradiance as a function of optical parameters, such as focal length and aperture diameter, is also derived. The laws of traditional radiometry are used. These laws assume incoherent sources, an assumption well justified in the case of auroral phenomena.

4.1.1 Source Radiance

Radiance, L_w, is defined as the radiant power, in a given direction, per unit solid angle per unit of projected area of the source, as viewed from the given direction. Radiance is usually expressed in units of W m^{-2} sr^{-1}. Radiance is also frequently expressed in quantum units, as photons m^{-2} s^{-1} sr^{-1}. The relationship between radiance expressed in power units, L_w, and radiance expressed in quantum units, L_γ, is thus,

$$L_\gamma = \frac{L_w}{h\,\nu} = \frac{L_w\,\lambda}{h\,c}, \tag{4.1}$$

where h is Planck's constant, c the speed of light, and ν and λ the frequency and wavelength, respectively, of the radiation under study. Note that radiance is not the same as surface brightness, as brightness is a perception sensation involving certain characteristics of the human eye. We will in general make a point of avoiding terms that relate to the visual effectiveness of light, such as lumens and candela.

In auroral research, where results are often interpreted in terms of physical processes, the important physical quantity is volume emission rate, ϵ, in photons m^{-3} s^{-1}. This emission rate cannot be found

directly by measuring surface radiance. However, consider a cylindrical column of cross-sectional area of 1 m^2 extending away from the detector into an extended, isotropic emission source with no significant self-absorption. The emission rate from a volume element of length dl at a distance l is $\epsilon(l)$ photons m^{-3} s^{-1}. This volume element contributes to L_γ an amount,

$$dL_\gamma = \epsilon(l)\ dl/4\pi. \tag{4.2}$$

Integrating along the line of sight gives,

$$4\pi L_\gamma = \int_0^\infty \epsilon(l)\ dl. \tag{4.3}$$

This quantity is simply the rate of emission from a 1 m^2 column along the line of sight, measured in units of photons m^{-2} (column)$^{-1}$ s^{-1}. The word "column" is intended to convey the concept of emission from a column of unspecified length. So, although the volume emission rate ϵ cannot be found directly by measuring the surface radiance, the column emission rate $4\pi L_\gamma$ is easily obtained.

The rayleigh is defined as a column emission rate of 10^{10} photons m^{-2} (column)$^{-1}$ s^{-1} [Hunten et al., 1956],

$$1 \text{ rayleigh} \equiv 1 \text{ R} = 10^{10} \text{ photons m}^{-2} \text{ (column)}^{-1} \text{ s}^{-1}. \tag{4.4}$$

Note that the rayleigh is an apparent emission rate, as no allowance has been made for scattering or absorption. The relationship between L_γ in photons m^{-2} s^{-1} sr^{-1} and I in rayleighs is now simply [Baker, 1974],

$$L_\gamma = I \times \frac{1}{4\pi} \times 10^{10}. \tag{4.5}$$

4.1.2 Detector Irradiance

Irradiance, E_w, is defined as radiant power incident per unit area upon a surface, and is usually expressed in W m^{-2}. Dividing this by the photon energy $h\nu$ yields E_γ, the irradiance expressed in units of photons m^{-2} s^{-1}.

We proceed to determine the irradiance E_γ onto a detector's faceplate in the case where a source of given emission rate I expressed in rayleighs is imaged onto the detector through an optical system. We represent the optical system by a single lens in front of a detector as depicted in Figure 4.1. The lens has a focal length of f and an aperture diameter of D. In the case of ground-based imaging of small-scale auroral features, source and lens dimensions may be considered small compared to the distance between source and lens. The source radiance in quantum units, L_γ, is given by Equation 4.5. In the figure, let A_o be the area of the source. The rate of photon arrival P_γ, in photons s^{-1}, at the lens subtending a solid angle $\Omega(\alpha)$ is proportional to the solid angle as well as the area of the source, with the constant of proportionality being of course the radiance,

$$P_\gamma = L_\gamma A_o \Omega(\alpha) = L_\gamma A_o \frac{\pi D^2}{4p^2}, \tag{4.6}$$

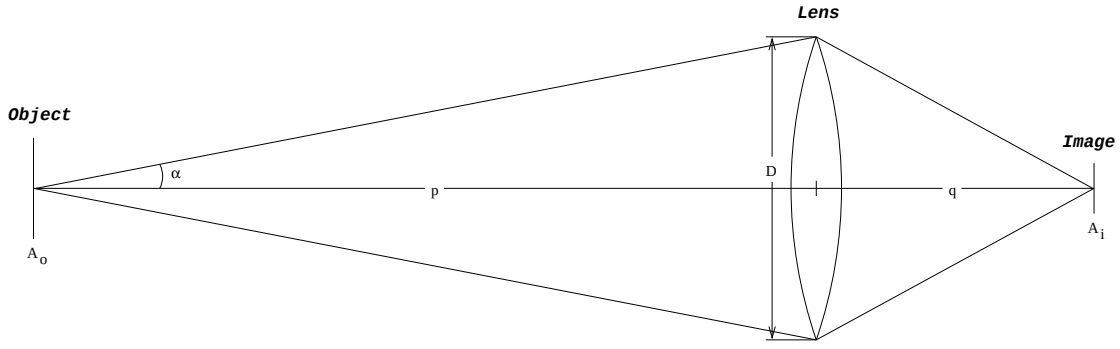

Figure 4.1: Optical system represented by a single lens in front of a detector.

where $\Omega(\alpha) = \frac{\pi}{p^2}(\frac{D}{2})^2 = \frac{\pi D^2}{4p^2}$ is used as an acceptable approximation for the solid angle subtended by the lens. By thermodynamic equilibrium of flow, the irradiance E_γ onto the detector of area A_i is therefore,

$$E_\gamma = \frac{P_\gamma \tau}{A_i} = \frac{A_o}{A_i} L_\gamma \tau \frac{\pi D^2}{4p^2}, \tag{4.7}$$

where τ represents lens transmission losses. By the simple lens magnification concept,

$$\frac{A_o}{A_i} = \frac{p^2}{q^2} = \frac{p^2}{f^2}, \tag{4.8}$$

since we have assume a very distant object, making $f = q$. Thus,

$$E_\gamma = \frac{p^2}{f^2} L_\gamma \tau \pi \frac{D^2}{4p^2} = L_\gamma \tau \pi \frac{D^2}{4f^2} = \frac{\pi L_\gamma}{4\,(f\text{-}no)^2}\tau, \tag{4.9}$$

where the lens' speed ("f-number"), $f\text{-}no = \frac{f}{D}$. Expressing E_γ in terms of the apparent emission rate I in rayleighs, we obtain finally,

$$E_\gamma = I \times \frac{\tau}{16\,(f\text{-}no)^2} \times 10^{10} \quad (\frac{\text{photons}}{\text{m}^2\ \text{s}}). \tag{4.10}$$

This equation yields the number of photons hitting the detector faceplate per second per square meter for a source of column emission rate I expressed in units of rayleighs. By multiplying E_γ by the detector pixel dimensions, the integration time, and detector quantum efficiency, the number of photoelectrons generated per pixel per exposure may be obtained.

Finally, note that Equation 4.10 yields the irradiance at a point on the optic axis. The detector irradiance will vary as a function of field position. In general, the irradiance for a corner position will be somewhat less than that obtained on-axis. This results from the fact that at an off-axis position corresponding to an angle θ off the optic axis, the exit pupil of the lens is diminished and the solid angle subtended by the exit pupil at the off-axis point is reduced accordingly. The flux falling on the image surface is at an oblique angle θ and the area which the flux covers is correspondingly larger. These factors together contribute to a reduction of the off-axis radiation proportional to $\cos^4\theta$ [Lavin, 1971]. This constitutes what is frequently called the natural vignetting. Additional vignetting may be introduced by a given lens assembly. For example, the transmittance through the optical surfaces may depend on the off-axis angle θ because of internal reflections.

4.2 Sensitivity

Needless to say, the choice of detector will have a profound impact on the resulting system performance. The most recent image detector development has been in the family of solid-state arrays, which includes the charge-coupled device (CCD). During the past couple of decades the CCD sensor has gradually replaced the tube type sensors, such as the vidicon, due to its advantages in size, weight, power consumption, noise characteristics, linearity, dynamic range, photometric accuracy, spectral responsivity, geometric stability, reliability, and durability [Janesick et al., 1987]. During the past decade, the CCD and the intensified CCD (ICCD) have slowly become the imaging detectors of choice within the astronomy and aurora/airglow research communities [Broadfoot and Sandel, 1992; Reynolds, 1989].

In selecting between using the bare, i.e. unintensified, CCD or the ICCD for our particular application, a primary consideration was their thresholds of detection, i.e., sensitivity, for the integration time chosen for the PAI. We will in the following sections consider the most prominent sources of noise in the CCD and ICCD detectors [Janesick et al., 1987; Csorba, 1985], and construct a simple model for the resulting signal-to-noise ratio. This model will serve for comparing the threshold of detection of the CCD to that of the ICCD detector. It will be shown that, in our particular case, an ICCD is indeed the appropriate detector, despite the fact that its photocathode quantum efficiency is lower by a factor of three than the quantum efficiency of the bare CCD (550 nm).

4.2.1 Photon Noise

The quantum nature of light places the ultimate limit on the achievable signal-to-noise ratio and threshold of detection of any low-light-level imaging instrumentation. The noise intrinsic to the emission of photons by a "steady" source is a stochastic process governed by Poisson statistics. The resulting root-mean-square (rms) variation in the signal is often called photon noise and is of course exhibited even by a perfect photon detector.

Both the bare CCD and the ICCD are sensitive enough to be evaluated by single-photon statistics. During an exposure, each element in the scene illuminates the detector with a certain number of photons. The number of photons, N, arriving at a detector pixel during a given exposure interval is distributed according to the well-known Poisson distribution,

$$p(N) = \frac{\overline{N}^N}{N!} e^{-\overline{N}}. \tag{4.11}$$

The Poisson distribution has a variance equal to its mean, $\overline{N}$.

While the number of photons arriving at a detector pixel during each exposure is governed by Poisson statistics, the conversion of photons into electrons in the photosensitive material of the detector is subject to a Bernoulli process. It can be shown that the Poisson statistics of the incoming photons is transferred to the photoelectrons [Albrecht, 1965]. This results in a photoelectron distribution with a mean (and variance) of $\eta\overline{N}$, where η is the Bernoulli distribution mean, i.e., the probability that a photon is successfully converted into a photoelectron. The factor η is of course better known as the detector's quantum efficiency (QE). Let us

now treat the two cases (the CCD and the ICCD) separately.

Photon noise — The bare CCD

Photons impinging onto the CCD's photosensitive surface generate photoelectrons at an average rate of 1 photoelectron per $1/\eta_{\text{CCD}}$ photons, where η_{CCD} is the CCD's quantum efficiency. If an average of $\overline{N}_{\text{CCD}}$ photons arrive at a pixel per exposure, the resulting average signal, in units of CCD electrons per pixel per exposure, is,

$$\overline{s}_{\text{CCD}} = \eta_{\text{CCD}}\,\overline{N}_{\text{CCD}}, \tag{4.12}$$

with a corresponding variance of,

$$\sigma^2_{\gamma(\text{CCD})} = \overline{s}_{\text{CCD}} = \eta_{\text{CCD}}\,\overline{N}_{\text{CCD}}, \tag{4.13}$$

where the suffix γ is meant to convey the fact that the variance is due to the statistical nature of the incoming photons. Upper case letters are used for symbols referring to photons and lower case letters are used to refer to photoelectrons, a convention that will be adhered to throughout.

The quantity $\overline{N}_{\text{CCD}}$ in the above equations is found in terms of the detector photon irradiance E_γ as follows,

$$\overline{N}_{\text{CCD}} = E_\gamma\, t\, dx\, dy, \tag{4.14}$$

where dx and dy are the CCD pixel's horizontal and vertical dimension, respectively, and t is the image exposure time. The detector irradiance E_γ is a function of source radiance and of the optics used, as defined by Equation 4.10.

Photon noise — The ICCD

The ICCD utilizes a microchannel plate (MCP) to produce a burst of on the order of 10^3 CCD electrons for each primary photoelectron released from the photocathode (see, Chapter 2.1.1). The emission of photoelectrons from the intensifier's photocathode is governed by Poisson as well as Bernoulli statistics, just as in the case of photoelectron production in the bare CCD. The resulting mean, i.e., the average number of photoelectrons emitted from the photocathode per pixel per exposure, is given by,

$$\overline{n}_{\text{ICCD}} = \eta_{\text{ICCD}}\,\overline{N}_{\text{ICCD}}, \tag{4.15}$$

where η_{ICCD} is the image intensifier photocathode's quantum efficiency, and $\overline{N}_{\text{ICCD}}$ the average number of photons to arrive at the photocathode pixel per exposure. The corresponding variance is,

$$\sigma^2_{\gamma(\text{ICCD})} = \overline{n}_{\text{ICCD}} = \eta_{\text{ICCD}}\,\overline{N}_{\text{ICCD}}, \tag{4.16}$$

where the suffix γ again indicates that this variance is due only to the Poisson characteristics of photoelectron emission. Note that the symbol $\overline{n}$ is used for primary photoelectrons, while, as before, the symbol $\overline{s}$ will be used for the number of electrons eventually deposited in the CCD well.

$\overline{N}_{\text{ICCD}}$ is a function of source emission rate, optics, as well as pixel size and integration time, and may be written,

$$\overline{N}_{\text{ICCD}} = E_\gamma \, M^2 \, t \, dx \, dy, \tag{4.17}$$

where E_γ is the detector photon irradiance given by Equation 4.10, and M is the fiber optic taper minification factor ($M > 1$). The factor M^2 projects the CCD pixel area $dx \times dy$ forward onto the photocathode.

4.2.2 Electron Multiplication Noise

This source of noise is unique to the ICCD. The ICCD's electron gain, i.e., the number of CCD electrons produced per photoelectron, has its own statistical distribution. The statistics of this spread in gain is governed by the statistics of the intensifier's microchannel plate (MCP), as the exceptionally high gain of the MCP effectively reduces the significance of noise introduced by succeeding elements such as the phosphor screen. MCPs typically exhibit an exponential gain distribution [Sackinger, 1971], in which case the variance is equal to the square of the mean. Assume in our case a mean gain of $\overline{g}$ and therefore a variance of $\overline{g}^2$, both measured in terms of CCD electrons per primary photoelectron.

In general, for a serial combination of two statistical processes, A and B, with means $\overline{n}_A$ and $\overline{n}_B$ and variances σ_A and σ_B, the mean and variance for the entire combination are [Albrecht, 1965; Engstrom, 1985],

$$\overline{n}_{AB} = \overline{n}_A \overline{n}_B, \tag{4.18}$$

$$\sigma^2_{AB} = \overline{n}^2_B \sigma^2_A + \overline{n}_A \sigma^2_B. \tag{4.19}$$

With this in mind, and using the results from the previous section, we conclude that the average number of CCD electrons per pixel per exposure in the case of the ICCD is,

$$\overline{s}_{\text{ICCD}} = \overline{g} \, \overline{n}_{\text{ICCD}}, \tag{4.20}$$

and for the corresponding variance we get,

$$\sigma^2_{\gamma,\text{mcp(ICCD)}} = 2 \, \overline{g}^2 \, \overline{n}_{\text{ICCD}}, \tag{4.21}$$

where $\overline{n}_{\text{ICCD}}$ is obtained by combining Equations 4.15 and 4.17. The suffix "γ, mcp" indicates that this variance is due to the statistics of the incoming photons as well as of the MCP's gain characteristics.

4.2.3 Dark Noise

There will be a dark current contribution of $\overline{d}_{\text{CCD}}$ CCD electrons per pixel per exposure from the CCD. This is due to random emission or production of electrons owing to thermal effects within the photosensitive material. While this average dark level can be subtracted from the final signal, thermal noise remains. Assuming Poisson statistics, the corresponding variance introduced is,

$$\sigma^2_{\text{dark(CCD)}} = \overline{d}_{\text{CCD}}, \tag{4.22}$$

in units of CCD electrons pixel^{-1} exposure^{-1}.

In the case of the ICCD, there is, in addition, an image intensifier (II) dark current contribution of $\overline{d}_{\text{II}}$ photoelectrons per pixel per exposure. Assuming again a combination of Poisson and Exponential distributions in the intensifier, we write down the corresponding variance,

$$\sigma^2_{\text{dark(II)}} = 2\overline{g}^2\overline{d}_{\text{II}}, \tag{4.23}$$

also in units of CCD electrons pixel^{-1} exposure^{-1}.

Dark noise becomes significant when long integration times are involved, and is then usually minimized by cooling the photocathode and the CCD. Thermal noise goes down by a factor of two for every 7–8°C reduction in temperature. However, in our particular case integration times are extremely short and dark current is not expected to pose a serious threat.

4.2.4 Read Noise

Both in the case of the bare CCD and the ICCD detector, the photoelectrons eventually deposited in the CCD well must be sensed by some process which will introduce an rms noise of its own, r. This noise is for convenience often expressed in units of CCD electrons pixel^{-1} exposure^{-1}. The corresponding variance is,

$$\sigma^2_{\text{read(CCD)}} = r^2. \tag{4.24}$$

This noise can be minimized by decreasing the readout frequency. However, in our case there is a requirement for a new image every integration period, dictating a fairly high readout frequency, resulting in a significant amount of read noise.

As will be seen, the high read noise level will only have a noticeable degrading effect in the case of the bare CCD. For each photoelectron created, the ICCD deposits a burst of on the order of 10^3 electrons into the CCD, overwhelming the lower level of noise associated with CCD readout. So in essence, the presence of an image intensifier transfers the problem of detectivity and noise from the CCD detector to the image intensifier.

4.2.5 Threshold of Detection

We are now ready to compare the resulting pixel signal-to-noise ratios of the bare CCD to those of the ICCD for various levels of photon flux. The individual contributions to the total variance of the signal that is eventually read out of the CCD pixel well are considered statistically independent. The total variance can then be obtained by summing the individual variance components. The resulting total rms noise is the square root of this sum.

For the bare CCD we obtain a signal-to-noise ratio (SNR) of,

$$\text{SNR}_{\text{CCD}} = \frac{\overline{s}_{\text{CCD}}}{\sqrt{\sigma^2_{\gamma\text{(CCD)}} + \sigma^2_{\text{dark(CCD)}} + \sigma^2_{\text{read(CCD)}}}} = \frac{\overline{s}_{\text{CCD}}}{\sqrt{\overline{s}_{\text{CCD}} + \overline{d}_{\text{CCD}} + r^2}}, \tag{4.25}$$

where all parameters are to be specified in units of CCD electrons pixel^{-1} exposure^{-1}. The average number of CCD electrons produced per pixel per exposure, $\overline{s}_{\mathrm{CCD}}$, is a function of the rayleigh auroral column emission rate and is obtained by using Equations 4.12 and 4.14 along with Equation 4.10. We see that for a given dark current and read noise contribution, the signal-to-noise ratio may be improved only by increasing $\overline{s}_{\mathrm{CCD}}$. For a given detector quantum efficiency, $\overline{s}_{\mathrm{CCD}}$ can be increased by using faster optics or by increasing the integration time. CCD read noise is proportional to the CCD signal readout frequency, and can be decreased only by reading out the CCD signal more slowly. In our case, however, where the desire for high temporal resolution and a standard video rate of 30 frames per second are driving factors, there is not the option of increasing the on-chip integration time, nor of reading out the CCD at a slower rate. High-transmittance filters, and the fastest possible objective lens that still provides the desired field of view for the given detector size have to be used.

In the case of the ICCD we obtain,

$$\begin{aligned} \mathrm{SNR}_{\mathrm{ICCD}} &= \frac{\overline{s}_{\mathrm{ICCD}}}{\sqrt{\sigma^2_{\gamma,\mathrm{mcp(ICCD)}} + \sigma^2_{\mathrm{dark(II)}} + \sigma^2_{\mathrm{dark(CCD)}} + \sigma^2_{\mathrm{read(CCD)}}}} \\ &= \frac{\overline{g}\,\overline{n}_{\mathrm{ICCD}}}{\sqrt{2\overline{g}^2\overline{n}_{\mathrm{ICCD}} + 2\overline{g}^2\overline{d}_{\mathrm{II}} + \overline{d}_{\mathrm{CCD}} + r^2}}. \end{aligned} \tag{4.26}$$

The average number of photoelectrons produced per pixel per exposure, $\overline{n}_{\mathrm{ICCD}}$, is obtained through Equations 4.15 and 4.17 together with Equation 4.10. Just as in the case of the bare CCD, the signal-to-noise ratio can be improved by increasing the incoming signal $\overline{s}_{\mathrm{ICCD}}$. In addition to utilizing faster optics and/or increasing the integration time, this is usually done by selecting a photocathode material that has a high quantum efficiency at the desired frequencies, and also by using a larger-diameter photocathode, thus increasing the fiber optic taper minification factor M of Equation 4.17. It is obvious from the above equation that increasing the intensifier's gain $\overline{g}$ does not contribute to an increase in the imager signal-to-noise ratio (sensitivity). The effect of the high gain of image intensifier tubes is simply to cause all CCD-related noise sources to become negligible in comparison with intensifier and photon noise. Once the gain is set to a point where individual photoelectron events are detected, nothing is gained by further increasing the MCP voltage. On the contrary, image definition is expected to deteriorate rapidly with increasing gain, as single photoelectrons may cause rather large blotches of light on the phosphor screen, thus lowering the CCD's effective dynamic range and spatial resolution.

A major decision when designing a low-light-level imaging system has to do with whether to employ a bare or an intensified CCD as a detector. As should be clear by now, the answer is found only by considering the wide variety of constraints and requirements in effect. In the case of the PAI, Equations 4.25 and 4.26 were used to compare the theoretical thresholds of detection of the bare CCD *vs.* the intensified CCD. Table 4.1 lists the vendor-supplied technical characteristics that were used in this effort. (These numbers are representative of similar devices from other vendors as well.) By plotting the resulting signal-to-noise ratio of the bare CCD imager and the ICCD imager as a function of rayleigh signal level for a given optical system, the imagers' sensitivities can be determined. In accordance with convention, the threshold of detection (i.e.,

PAI Detector Technical Specifications

Parameter	Symbol	Typ. Value	Unit
Photocathode QE	η_{ICCD}	28	% (557.7 nm)
FO minification ratio	M	1.55 (17:11)	–
Photocathode dark current	$\overline{d}_{\text{II}}$	0.1	nA m^{-2} (27° C)
ICCD mean gain (medium)	$\overline{g}$	1,500	CCD electrons photoelectron^{-1}
CCD QE	η_{CCD}	67	% (557.7 nm)
CCD horizontal pixel dim.	dx	11.5	μm
CCD vertical pixel dim.	dy	27.0	μm
CCD dark current	$\overline{d}_{\text{CCD}}$	0.1	mA m^{-2} (27° C)
CCD read noise	r	80	electrons
Image integration time	t	16.7	ms
Transmission, Nikon lens	τ_{Nikon}	0.9	–
Transmission, Cosmicar lenses	τ_{Cosmicar}	0.7	–
Transmission, Meade SCT	τ_{Meade}	0.72	–
Transmission, Interference filter	$\tau_{\text{interf.}}$	0.7	–
Transmission, Wrattan 89B filter	τ_{Meade}	0.95	–

Table 4.1: Published technical specifications of the PAI primary detector.

sensitivity) is defined to be that signal which yields a pixel signal-to-noise ratio of SNR $= 2$ at the given integration time. Considering the 557.7 nm (green line) auroral emission as an example, the plots of Figure 4.2 result. The optical system here is the Schmidt-Cassegrain Telescope in the $f/3.9$ and $f/6.3$ configuration, respectively, since, as was explained in Chapter 2.1.2 this is currently the only PAI optics that facilitate the mounting of interference filters. The dotted line depicts the signal-to-noise ratio of a bare CCD detector, the dashed line that of the ICCD, and the continuous line shows the signal-to-noise ratio of a perfect photon counter. It is clear from these plots that the ICCD, with its 100 kR threshold of detection is indeed the better imager for observing breakup auroral emissions at the extremely high temporal resolution desired for the PAI project. While it is true that at the high end of the range of light levels the bare CCD yields a better signal-to-noise ratio than the ICCD, notice that this crossover occurs at light levels beyond those expected even from very intense auroral emissions. The data is plotted out to the outrageous emission rate of 10 Giga-rayleighs solely for the purpose of showing the typical behavior of CCD performance with increasing light level. Notice how the CCD curve has a "knee" and rapidly deviates from the ideal curve as photon flux decreases, causing the ICCD to yield a far better signal-to-noise ratio than the bare CCD across most of the range of light levels being considered. This deviation from the straight line characteristic is a direct result of read and dark noise becoming increasingly significant compared to photon noise. At light levels even lower than those plotted, it turns out that also the ICCD curve has a "knee." As in the case of the bare CCD, this happens at light levels where read noise and dark current effects increase in significance relative to photon noise. It is due to the high electron gain of the image intensifier that this "knee" occurs at light levels far below the range currently of interest to us (SNR ≥ 2).

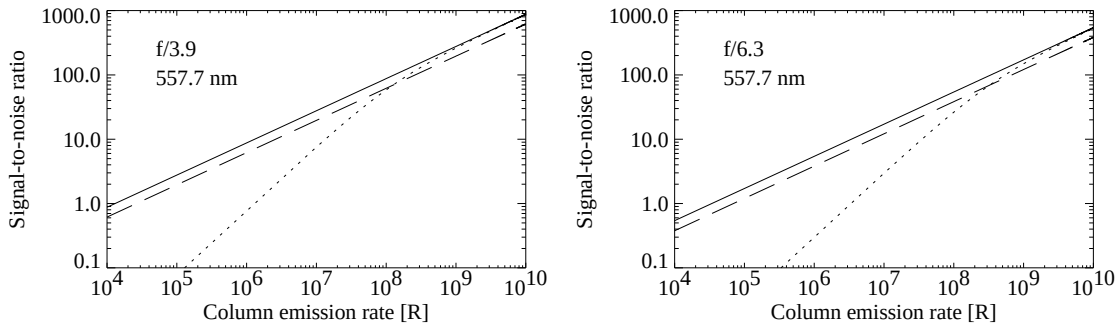

Figure 4.2: Calculated SNR *vs.* emission rate for the CCD (dotted), ICCD (dashed), and ideal (continuous line) detector. The optics is the PAI Schmidt-Cassegrain Telescope in the $f/3.9$ and $f/6.3$ configuration, respectively, with 70% transmission interference filters.

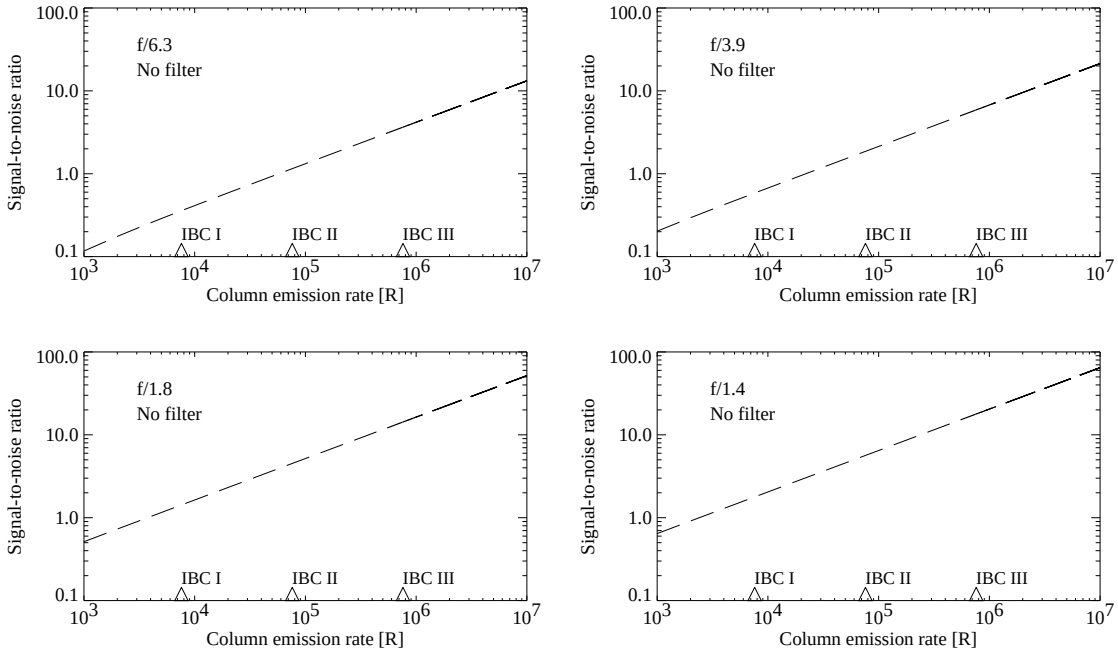

Figure 4.3: Calculated SNR *vs.* emission rate for the ICCD for various optics, assuming no filters. Estimated continuum emission rates corresponding to IBC I, II, and III aurora are indicated. The responsivity is in this case determined by the continuum characteristics of the photocathode, allowing acceptable SNR even at IBC I aurora.

Removing the narrow-band interference filter causes a continuum of emissions determined by the photocathode spectral responsivity to be detected. Figure 4.3 depicts the resulting ICCD signal-to-noise ratio for the various speeds of lenses obtained for the PAI. As suggested in Chapter 3.1.3, for a continuum emission whose spectral passband is determined by the photocathode responsivity, IBC III aurora would correspond to a signal of about 750 kR. (Note that we have assumed a flat photocathode spectral responsivity of 25% across the wavelength range 450–850 nm.) According to the figure, the telescope optics has a sensitivity limit of about 100 kR, while the shorter focal length optics have a useful sensitivity down to about 10 kR. Detection of IBC I continuum emission is thus considered possible using the faster optics. These curves are also representative of the performance expected with the Wrattan 89B glass low-pass filter mounted, due to its very high transmittivity. In that case, however, IBC III aurora corresponds to about 550 kR on the abscissa, as indicated in Chapter 3.1.3.

Notice that the ICCD curve appears as a straight line across the range of emission rates considered in the plot. It is is parallel to the line representing the signal-to-noise ratio of an ideal sensor, having a slope of $\frac{1}{2}$ in the logarithmic plot. This straight-line relationship is not simply a consequence of our idealized model, but is consistent with reality, as demonstrated by, e.g., Baumgardner et al. [1992] and Richard et al. [1988]. The simpler equation for this straight line representing the signal-to-noise ratio of the ICCD across the plotted range of light levels is obtained from Equation 4.26 by assuming a noise free CCD and negligible intensifier dark noise, yielding,

$$\mathrm{SNR}_{\mathrm{ICCD}} = \sqrt{\frac{\overline{n}_{\mathrm{ICCD}}}{2}}. \tag{4.27}$$

The signal-to-noise ratio is thus in this simple model down by a factor $\sqrt{2}$ as compared to the ideal detector.

4.2.6 Intensifier Noise Factor

In view of the above, it is safe to say that the problem of detectivity has been transferred from the CCD to the image intensifier. We can therefore for all practical purposes assume an ideal (noiseless) CCD. The non-idealness of the intensifier itself is characterized by its noise factor Γ, defined as [Hertel, 1989],

$$\Gamma = \frac{\mathrm{SNR}_{\mathrm{in}}^2}{\mathrm{SNR}_{\mathrm{out}}^2}, \tag{4.28}$$

where $\mathrm{SNR}_{\mathrm{in}}$, the input signal-to-noise ratio, is in our case simply the signal-to-noise ratio associated with the Poisson statistics of photoelectron emission. If the MCP exponential statistics were the only source of noise in the intensifier, the intensifier's total noise factor would indeed be $\Gamma = 2$, as suggested by Equation 4.27. However, there are several other sources of noise in an image intensifier, such as the MCP ion-barrier film [Pollehn, 1985] as well as sources that are currently not very well understood [Csorba, 1985]. Such factors were not included in the simple, idealized model constructed in the previous section as this would have added complexity, hiding essential features. In fact, the noise factor of the intensifier is best found by measurement rather than analysis. We adopt a value of $\Gamma \simeq 3$, a noise factor typically measured on third-generation image intensifiers operating at TV bandwidths [Rougeot and Girard, 1988]. A reasonably accurate expression for

Intensifier Tube	*427.8 nm*		*557.7 nm*	
	η	$\sqrt{\eta/\Gamma}$	η	$\sqrt{\eta/\Gamma}$
Gen II	.04	.13	.07	.17
Super Gen II	.07	.17	.12	.22
Gen III	.00	.00	.25	.29
Extended Blue Gen III	.10	.18	.28	.31

Table 4.2: Sensitivity compared between second- and third-generation intensifiers at two different wavelengths, assuming noise factors of 2.5 for the second-generation and 3.0 for the third-generation tubes.

the signal-to-noise ratio of a third-generation ICCD detector is then,

$$\text{SNR}_{\text{ICCD}} = \sqrt{\frac{\overline{n}_{\text{ICCD}}}{\Gamma}} \simeq \sqrt{\frac{\overline{n}_{\text{ICCD}}}{3}}. \tag{4.29}$$

This equation may from now on be used instead of Equations 4.26 or 4.27. The signal-to-noise ratio curves of Figures 4.2 and 4.3 can still be used to determine the imager's sensitivity if the definition of the limiting signal-to-noise ratio is increased slightly, from 2.0 to approximately 2.4. Equation 4.29 implies that the lower illumination limit for operation may be extended by raising the photocathode quantum efficiency, increasing the minification ratio $M(M > 1)$, and by obtaining a tube with as low a noise factor as possible.

It is a well-known fact that the first- and second-generation intensifier tubes have considerably lower noise factors than third-generation tubes. The question therefore arises whether or not a first- or a second-generation tube would have been a better choice than a third-generation tube. The first-generation image intensifier does not employ an MCP and thus has a noise factor close to unity. However, this intensifier has a very low gain, and as a result CCD read noise and dark noise become significant, degrading the total signal-to-noise ratio considerably [Van Geest and Stoop, 1985; Rougeot and Girard, 1988; Richard et al., 1988]. Total gain can be improved by cascading several first-generation intensifiers, but, in addition to having an adverse impact on the total system spatial resolution, this would as well impact PAI weight, physical dimensions, and thus portability. In contrast, the double proximity-focused second- and third-generation intensifiers are very compact. The second-generation intensifier has a typical noise factor of $\Gamma = 2.5$ [Pollehn, 1985]. We deduce from Equation 4.29 that tube sensitivity is proportional to the tube's quantum efficiency and the noise factor in the following way,

$$\text{SNR}_{\text{ICCD}} \propto \sqrt{\frac{\eta}{\Gamma}}. \tag{4.30}$$

The quantity on the right hand side of this expression has been calculated for currently available second- and third-generation intensifiers at two different wavelengths, with the results presented in Table 4.2. Quantum efficiencies are typical values. Table 4.2 does indeed reveal that the "Extended Blue" third-generation intensifier chosen for the PAI has a sensitivity superior to that of the second-generation intensifiers. We conclude that its lower noise factor is more than compensated for by its superior detective quantum efficiency.

4.3 Spatial Resolution

The spatial resolution of any imager is limited by two main factors. Firstly, there is an optical resolution limit, independent of light level, as described by the imager's modulation transfer function. Secondly, resolution is limited by photon noise due to the statistical nature of light itself, causing image resolution to decrease with decreasing light level. We will examine each of these two aspects individually before proceeding to construct a model that takes them both into account.

4.3.1 The Modulation Transfer Function

Horizontal and vertical spatial resolution of an imaging instrument is usually measured by imaging a test chart that contain sets of bars of increasing spatial frequency. Vertically and horizontally aligned bars are used for measuring horizontal and vertical resolution, respectively. Traditionally, imager resolution is characterized by one number only, namely, the resolution corresponding to the highest spatial frequency at which the bar pattern was still just discernable in the image. A much more useful concept, however, is the imager's modulation transfer function (MTF). The MTF of an imaging system fully characterizes its performance at high light levels (i.e., at high signal-to-noise ratios). Specifically, the MTF is the sine-wave spatial frequency amplitude response of a given lens, system element, or system. The MTF can also be described as the ability to transfer object contrast to the image as a function of object spatial frequency [Lavin, 1971]. It is usually specified by means of a graph depicting the ratio of modulation in the image to the corresponding modulation in the object *vs.* the spatial frequency in the sinusoidally modulated test chart. The MTF varies from 0 to 100 percent modulation; a modulation of 100% indicates that there is no distortion or loss of data from the image source to the displayed image, while at 0% modulation there is no recognizable image. It can be shown that the MTF of a system element is the amplitude, along a given radius, of the two-dimensional Fourier transform of the system element's point spread function (PSF) [Williams and Becklund, 1989]. The MTF of the total system is simply the product, frequency by frequency, of the properly scaled MTFs of its individual system elements. Note, however, that an exception to this cascading rule exists in the case of dealing with combinations of optical lenses. MTFs can then only be legitimately multiplied when a set of quite restrictive technical conditions are satisfied [Lavin, 1971].

The contrast transfer function (CTF) is similar to the MTF. The difference is that instead of using a purely sinusoidal test pattern, which has traditionally been hard to manufacture, a black/white square-wave pattern is used. The CTF thus describes the ability of an imaging system to respond to spatial step functions of increasing frequency. CTF step-response data can be used to approximate the system's MTF by employing a simple correction formula given by Coltman [1954].

In the case of an ICCD camera, system elements contributing to the total camera MTF are, the intensifier tube, fiber optics coupling, CCD, and signal processing electronics [Beauvais et al., 1985]. The total MTF of the third-generation ICCD camera procured for the PAI was not specified by the manufacturer. Due to a lack of proper equipment, the camera MTF could not be determined in-house. For the purposes of

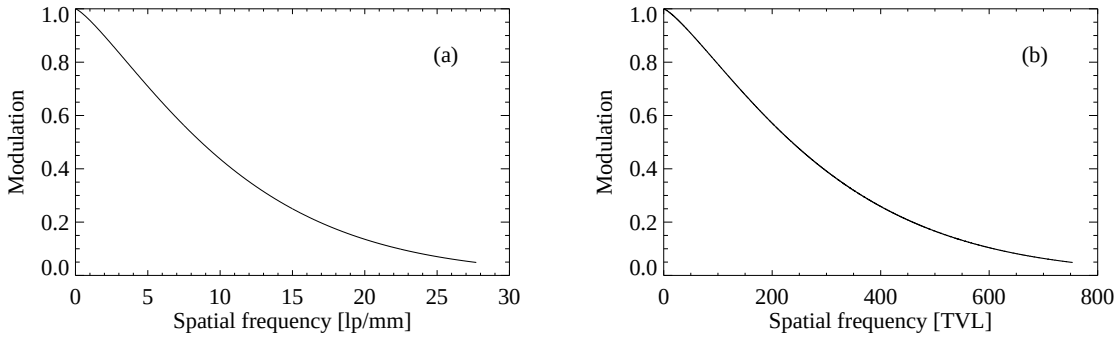

Figure 4.4: (a) Modeled horizontal MTF for the ITT F4588 ICCD camera, with the spatial frequency expressed in units of linepairs per millimeter on the photocathode. (b) The same MTF, with frequency expressed in units of TV lines.

modeling we thus construct an approximate MTF based on available data. Typical MTFs of third-generation intensifier tubes are sketched in most intensifier tube specifications sheets [e.g., ITT Defense, 1990]. Further, Allen [1989] has shown that the MTF of the intensifier tube itself typically dominates the MTF of the entire system, far surpassing the effect of the MTFs of the fiber optics taper, fiber optics coupler, CCD, and video processing circuitry. It is well-known that MTFs can be approximated by an analytical expression on the form [Johnson et al., 1991],

$$\mathrm{MTF}(r) = e^{-(r/a)^b}, \tag{4.31}$$

where r is the spatial resolution in units of linepairs per millimeter (lp mm^{-1}), and a and b are constants. a and b are sometimes referred to as the "frequency constant" and the "MTF index," respectively. By treating a and b as curve-fitting parameters, one can obtain an MTF curve very similar to that indicated in the tube manufacturer's technical literature. By further adjusting a and b, the MTF can be lowered slightly to account for the degrading effect of finite-bandwidth system components following the intensifier tube. This results in the modeled horizontal MTF for the entire camera as plotted in Figure 4.4, a curve which is very consistent with the results of Allen [1989]. For this curve, values of $a = 11.6$ and $b = 1.27$ were used. The MTF is plotted both in terms of lp mm^{-1} on the photocathode and in terms of TV lines (TVL). The MTF has in Figure 4.4 been plotted out to a spatial resolution corresponding to the imager's Nyquist limit of 28 lp mm^{-1}. The Nyquist frequency is of course ultimately determined by the CCD, not by the image intensifier.

It is common within the imaging industry to determine an imager's limiting resolution based on its MTF alone. It is important to be aware of the fact that the assumption implicitly being made then is that light levels are so high that photon noise is of negligible significance. In the case of the third-generation ICCD camera acquired for the PAI, specification sheets boast "greater than 600 TV lines limiting resolution." As will be shown in the next section, the resolution is expected to be much worse under actual low-light-level conditions. Even during high-light-level conditions, the MTF alone is not sufficient to determine the imager's limiting resolution. In addition to the MTF, the "threshold of detectability" (TOD) curve is needed [Lavin, 1971]. This curve is determined experimentally and describes, for a given set of operating conditions, how the modulation demanded by the observer for just discerning the test pattern varies as a function of

spatial frequency. Whereas the MTF is a decreasing function with frequency, the TOD curve is of course an increasing function. The limiting resolution of a system is then determined by the intersection of the MTF and TOD curves. When the TOD curve is not known, which is most often the case, a rough limit for an acceptable resolution is often taken to be where the MTF is down to about 10%. Using this approach on the MTF of Figure 4.4, we may conclude that the camera has a useful horizontal resolution of better than 600 TV lines under well-lit conditions, quite consistent with the camera's technical specifications sheet.

In the above modeled camera MTF we did not incorporate or consider the impact of the camera's lens on total system MTF. The 600 lines high-light-level resolution just deduced would not be of much practical use if the point spread function of the lens being used with the imager is inferior. Let us evaluate the effect of the telescope in its 1600 mm focal length configuration on the total system MTF at the Nyquist limit. At the Nyquist limit, two pixels cover one period on the target. Using a photocathode horizontal pixel dimension of 17.8 μm (see, Table 2.3), we arrive at a corresponding angular resolution of,

$$\alpha_{\text{Nyquist}} = 2\,\frac{17.8\times10^{-6}\ \text{m}}{1600\times10^{-3}\ \text{m}} = .00002\ \text{ radians period}^{-1} = 4.6\ \text{ arcsec period}^{-1}. \tag{4.32}$$

This corresponds to about 0.2 periods per arcsecond. For the vertical resolution case, as well as the shorter focal length case, the number is even less. The theoretical MTF of a diffraction limited Schmidt-Cassegrain telescope is found in Zmek [1993]. By scaling the horizontal axis to account for our particular aperture (taking into account the 13.7% frontal obscuration), it is seen that we are here, relatively speaking, located in the very-low-frequency regime, wherein the MTF is practically unity. We therefore conclude that the MTF of the diffraction limited telescope does not alter the total system MTF significantly. As a matter of fact, the MTF of the atmosphere through which the camera is looking may be considered to have a more adverse effect on the imager's performance than the lens.

Unfortunately, the MTF of the VCR is not known. The manufacturer merely states that it has a useful horizontal resolution of about 440 lines [Hitachi, Ltd., 1989]. When convolving this limiting resolution by the more than 600 lines limiting resolution of the camera/lens system, we essentially end up with a system resolution of no more than 400 lines [Caudle, 1990]. An improvement in resolution would be obtained by using the image digitizer directly in conjunction with the camera without going via a VCR, as the resolution of the image digitizer more closely matches the resolution of the camera itself.

The definition of limiting resolution used here is in our case not very useful. At best, it gives us a feel for the imager's performance under ideal conditions. When operating under less-than-ideal conditions, such as at the kind of light levels often associated with auroral emissions, we expect the statistical nature of light itself to play an important role in limiting spatial resolution. This is the topic of the following section.

4.3.2 Photon Noise

We have explained how at high light levels, where system noise can be ignored and the shot noise limited signal-to-noise ratio is high, resolution is limited by total system MTF. As light level decreases, however, limiting resolution is decreasingly determined by system MTF and increasingly determined by the

decrease in signal-to-noise ratio that is due to the paucity of photons. As photon flux decreases, the area of a detail of a given contrast and shape that is required for it to still be resolved will increase correspondingly. In the case of the PAI we may assume the following scenario. The camera is sitting outdoors, pointed along the local geomagnetic field line. Its video output is fed into a video cassette recorder located indoors, for example, in a research trailer. An observer sits inside the trailer, watching a black and white monitor that shows the camera video output. Every time the observer detects the passage of an auroral arc (or some other interesting feature) through the camera's field of view, he writes down the time of the event. With the enormous amount of data being collected during a campaign, this is a sensible way of ensuring that interesting events are rapidly located during later data assessment and analysis.

In this section we construct a simple model for how resolution is governed by the statistics of light, ignoring MTF effects. This model can be used to determine the smallest auroral structures just detectable by the observer, for a given set of electro-optical parameters. One of the most common ways of estimating the resolution performance of an electro-optical system at very low light levels is to use the signal-to-noise ratio concept, whose early foundation was based on theoretical and experimental work by, among others, Rose [1948] and deVries [1943]. The concept assumes a simple object/background scenario and is often considered sufficient as a first-order approach to evaluating the resolution of an imaging system.

A quantitative relationship between image definition, contrast, and detector irradiance may be derived by considering the image area subdivided into picture elements and by assuming that the image sensing device can do no better than count the photoelectrons from the various picture elements. If the device is to be able to recognize an image, it must be able to distinguish differences in the number of photoelectrons between one picture element A and another picture element B. Now, if the statistical fluctuation in the number of photoelectrons in these two elements is greater than the difference of the average numbers, it is impossible to say with certainty that one element is brighter than the other. The degree of certainty with which one can say that there is a meaningful difference in intensity between two elements depends on the factor k by which the difference of the mean values exceeds the root-mean-square deviation. The factor k is frequently called the "threshold signal-to-noise ratio" or the "certainty coefficient," and it reflects the random nature of the photon distribution and the need to avoid false alarms, i.e., observing a signal that is merely a result of random photon fluctuation. The value of k depends on the pattern to be observed. For isolated disk patterns, k has been experimentally determined by Rose [1948] to be approximately 5. For a bar pattern, Coltman [1954] gives a value of $k = 1.7$. This lower threshold signal-to-noise ratio reflects the fact that the eye tends to integrate over the entire length of an elongated structure in determining its presence in the image. These values of k correspond to a probability of detection of 50%, and have been found to be valid for a very wide range of viewing distances and display illumination levels [Legault, 1971].

There is no literature describing corresponding results within the field of auroral imaging, where objects may be thin auroral arcs or perhaps elliptically shaped auroral curls. We may assume that the criterion for just detectable auroral features lies somewhere in the range between the two above values. Recognizing that auroral features tend to be elongated across the field of view, we choose a value of $k = 3.5$. The auroral arc being recorded may, assuming a moonless, clear night sky, be superimposed on a several hundred

rayleighs nightglow background and/or embedded in an auroral surrounding radiating at the order of a kilorayleigh. Typical continuum background from nightglow is in the range of a few rayleighs per ångström [Broadfoot and Kendall, 1968]. Thus, for narrow-band filters nightglow continuum contributes typically no more than 10–100 R. Further, we will assume that the only sources of noise are the image intensifier and the random nature of photoelectron emission, an assumption that was justified in Chapter 4.2. The noise introduced by the image intensifier is described by the intensifier's noise factor Γ, as defined by Equation 4.28. Finally, we assume that the display's luminance is high enough that the human eye is eliminated as a degrading factor, i.e., the eye itself is not resolution light-level limited. This is easily accomodated by adjusting the luminance controls on the TV monitor.

Consider now the two adjacent resolution elements A and B having average photoelectron rates of $\dot{n}_{\max}$ and $\dot{n}_{\min}$, respectively. In line with the above discussion, define the *signal* during the detector's integration time t to be the difference of the average numbers, i.e., $(\dot{n}_{\max} - \dot{n}_{\min})\, t$. The corresponding rms noise will be the square root of the sum of the mean-square noises from the pair of resolution elements, $\sqrt{(\dot{n}_{\max} + \dot{n}_{\min})\, t}$. If we now assume that the threshold of detectability is a scene peak-to-peak signal of approximately k times the rms noise introduced by the surrounding background and the MCP, we have for detectability,

$$\frac{(\dot{n}_{\max} - \dot{n}_{\min})\, t}{\sqrt{\Gamma \times (\dot{n}_{\max} + \dot{n}_{\min})\, t}} \geq k, \tag{4.33}$$

where we have assumed that the only noise sources present are the Poisson noise associated with photoelectron emission and intensifier noise as described by the intensifier noise factor, Γ.

Now define $\dot{n}_s$ and $\dot{n}_b$ to be the number of photoelectrons produced per area on the photocathode per unit time as a result of object and background emissions, respectively. We assume a transparent auroral arc on a uniform background, in which case Equation 4.33 becomes,

$$\frac{\dot{n}_s\, t}{\sqrt{\Gamma \times (\dot{n}_s + 2\dot{n}_b)\, t}} \geq k. \tag{4.34}$$

The foreground $\dot{n}_s$ and background $\dot{n}_b$ will now have to be mapped back to corresponding auroral column emission rates, I_s and I_b, expressed in rayleighs. For given optics and source column emission rate I in rayleighs, photoelectron production rate in an area a^2 on the photocathode is given by Equation 4.10,

$$\dot{n} = I\, \frac{\tau}{16(f\text{-}no)^2}\, 10^{10}\, \eta\, a^2. \tag{4.35}$$

Inserting this into Equation 4.34, we obtain as our criterion,

$$\frac{I_s\, \frac{10^{10}}{16(f\text{-}no)^2}\, \eta\, \tau\, a^2\, t}{\sqrt{\Gamma\, \frac{10^{10}}{16(f\text{-}no)^2}\, \eta\, \tau\, a^2\, (I_s + 2I_b)\, t}} \geq k. \tag{4.36}$$

Note that in keeping with convention, we assume that the "soft" photocathode pixels being considered here are square, with area a^2. The underlying "hard" photocathode pixels have, of course, an aspect ratio dictated by the dimensions of the CCD pixels as projected onto the photocathode.

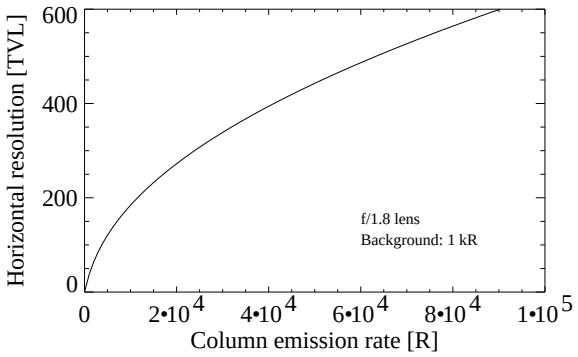

Figure 4.5: Photon limited resolution as a function of column emission rate.

We may now solve for the smallest detectable horizontal structure at the intensifier photocathode,

$$a = \sqrt{\frac{\Gamma\, k^2\, 16\, (f\text{-}no)^2\, (I_s + 2I_b)}{I_s^2\, 10^{10}\, \eta\, \tau\, t}}. \tag{4.37}$$

As source emission rate increases, the picture element area a^2 required for a satisfactory signal-to-noise ratio decreases. Converting now a into a corresponding number of TV lines across the horizontal dimension of the photocathode, we can plot horizontal resolution as a function of rayleigh light level, as done in Figure 4.5 for the $f/1.8$ lens. The figure shows a resolution that increases without bounds as light level increases. However, we know that due to effects such as diffraction in the lens and a finite CCD pixel size, there must be some upper limit on resolution. All such effects are taken into account by somehow including the imager's modulation transfer function or contrast transfer function into the above equations. This is the topic of the next section.

4.3.3 Limiting Low Light Level Resolution

A model taking both the imager's contrast transfer function and the statistical nature of light into account has been derived by Whitby [1972]. According to this model, Equation 4.33 needs to be changed to,

$$\frac{(\dot{n}_{\max} - \dot{n}_{\min})\, t}{\sqrt{\Gamma \times (\dot{n}_{\max} + \dot{n}_{\min})\, t}} \times \text{CTF} \geq k, \tag{4.38}$$

where CTF denotes the imager's contrast transfer function. Equation 4.37 now takes the form,

$$a \times \text{CTF}(a) = \sqrt{\frac{\Gamma\, k^2\, 16\, (f\text{-}no)^2\, (I_s + 2I_b)}{I_s^2\, 10^{10}\, \eta\, \tau\, t}}, \tag{4.39}$$

where CTF(a) indicates that the CTF is to be taken at the spatial frequency corresponding to the linear distance a. As pointed out earlier, the MTF of a system may be deduced from knowledge of the system's CTF. When plotting the CTF and the deduced MTF in the same co-ordinate system, it is seen that the CTF is similar to, but a bit higher than the MTF [Richard et al., 1988]. Since the models we are dealing with are only approximations in the first place, it will suffice to use the MTF of Chapter 4.3.1 as a substitute for the corresponding CTF. This way we will at least err on the side of safety in our modeling efforts.

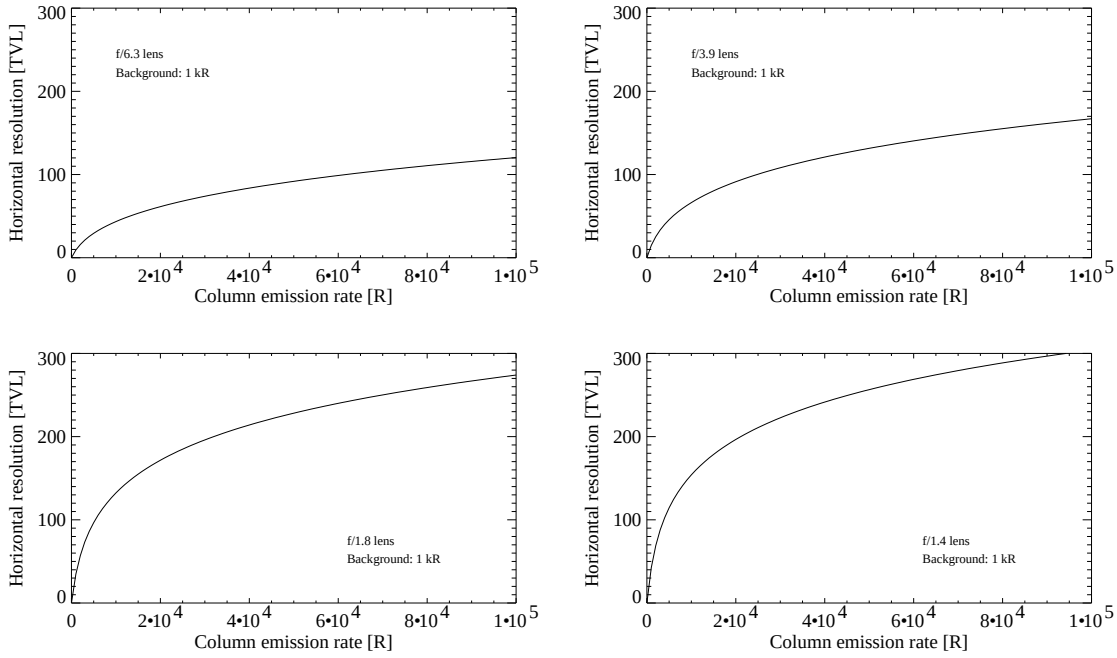

Figure 4.6: Modeled spatial resolution as a function of column emission rate, taking MTF as well as photon statistics into account.

Equation 4.39 may now be solved numerically to find how resolution varies with light level. It can be shown that the resulting resolution converges towards the finite limiting resolution determined by the CTF as light level increases. As light level decreases, however, resolution will more and more closely match that given by the curve of Figure 4.5. Figure 4.6 shows plots resulting from solving Equation 4.39 for different objective lenses assuming unfiltered operations. We see that in all cases horizontal resolution is well below 400 TV lines, the resolution of the VCR. Hence, the VCR is not expected to degrade resolution seriously beyond what is shown in these plots, assuming that the MTF of the VCR is reasonably good out to its specified limiting resolution.

The distance a on the photocathode can now be mapped to auroral altitudes to obtain the corresponding smallest detectable structure at the source, $\delta = (h \times a)/f$, where h is the altitude of the aurora, and f is the focal length of the lens measured in the same units as h. Assuming an auroral altitude of 105 km, and the various optics described in Chapter 2.1.2, without any filters, we may plot the resulting zenith spatial resolution as a function of auroral column emission rate. Assuming a continuum airglow background emission of 1 kR, the plots of Figures 4.7, 4.8, and 4.9 results. It can be seen from these plots that in the case of the telescope optics, the spatial resolution at auroral heights is about 10 m at the 100 kR sensitivity limit derived in the previous section. For more intense emissions, spatial resolution may reach $\sim$5 m. This is somewhat worse than the original 2.4 m criterion, set down in Chapter 3.1.1, but is still considered acceptable. In the case of the f/1.8 lens, limiting resolution is about 100 m, quickly improving to a few tens of meters as the (continuum) emission rate increases from that corresponding to IBC I aurora to that of IBC II and III aurora.

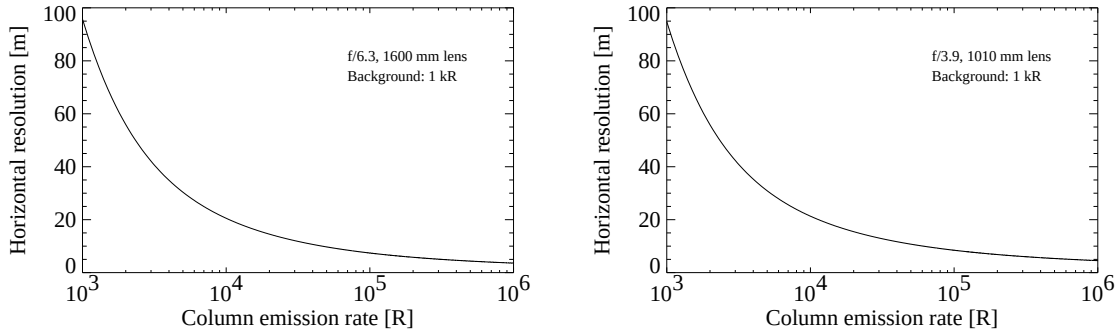

Figure 4.7: Limiting spatial resolution at auroral altitudes using the telescope in its two different focal-length configurations.

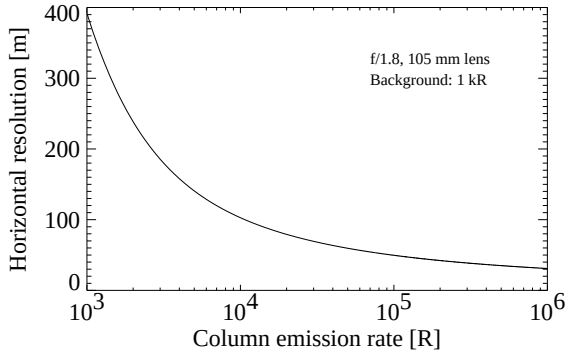

Figure 4.8: Limiting spatial resolution at auroral altitudes using the $f/1.8$ lens.

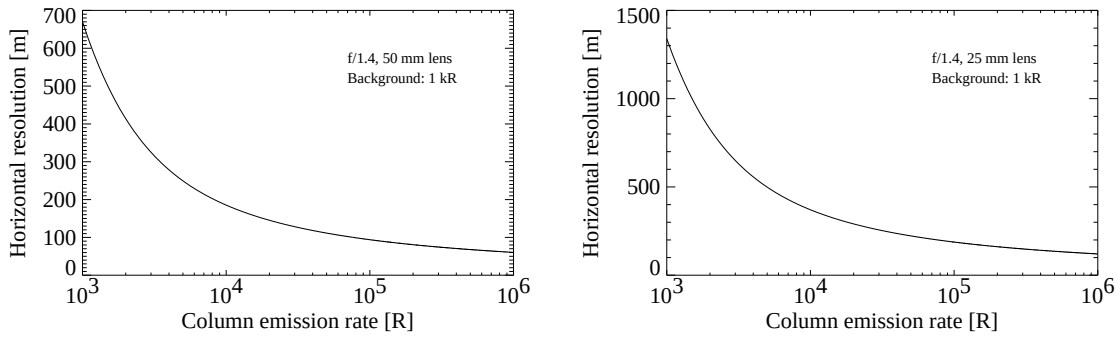

Figure 4.9: Limiting spatial resolution at auroral altitudes using the two $f/1.4$ lenses included with the PAI.

Chapter 5

Imager Characterization

The Portable Auroral Imager was designed mainly with qualitative morphological studies in view. Accurate photometric measurements were not originally a requirement, and thus not a driving factor during its design process. Rather, the PAI was meant to constitute an initial foray into the largely unexplored territory of short-scale auroral imaging, with the intent of obtaining knowledge useful in planning future photometric instrumentation and constructive campaign modes. Another important purpose of the PAI project was to obtain expertise when it comes to the logistics of handling, assessing, and analyzing very large amounts of data. Although designed mainly for qualitative studies, the PAI was quantitatively characterized in a variety of ways, so as to confirm or confute its predicted performance. It is shown that the performance predictions of the previous two chapters do indeed provide a very good estimate of actual imager performance.

5.1 Field of View

The general validity of many models of auroral arc generation may be successfully tested using purely morphological considerations applying basic metrics such as linear distance, velocity, and multiplicity. The video signal from the camera provides a highly accurate time base, as already mentioned in Chapter 3.2.1. However, the angular field of view of each pixel in the final, digitized image still needs to be established. This is crucial information that will enable us to determine the relationship between pixel dimensions in the digitized image and actual linear dimensions at auroral altitudes. The actual auroral altitude must in the case of a single, stand-alone imager of course remain within the realm of speculation. An altitude of 105 km will be assumed throughout, in accordance with the results of some attempts at triangulating the auroral lower border [Currie, 1955; Störmer, 1955].

Observations of point sources of known angular separation within the field of view may yield accurate information as to the angular extent of the field of view. Stars may be considered excellent point sources, easily accessible, and conveniently arranged in the sky. Figure 5.1a shows a star background image obtained using the PAI's 50 mm focal length lens. The image was acquired in the absence of detectable

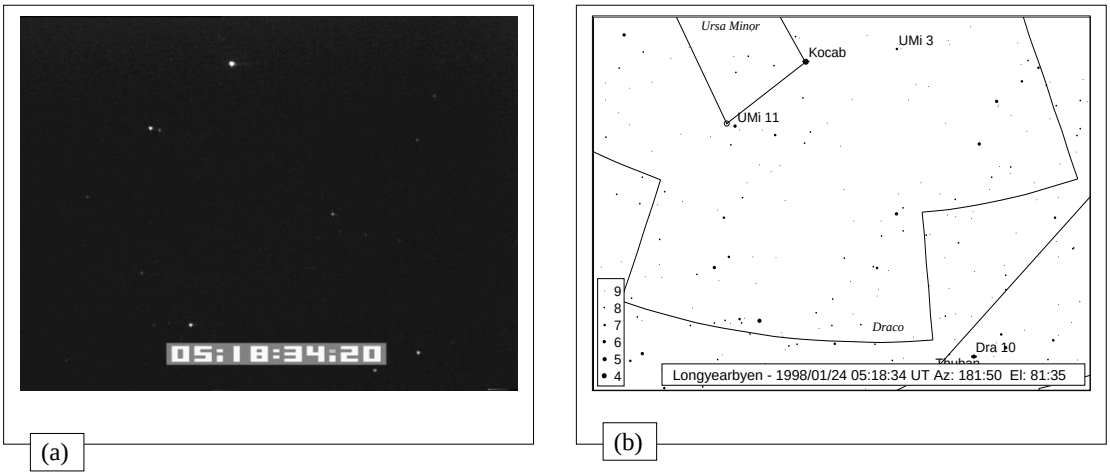

Figure 5.1: (a) Star background image acquired by the PAI. (b) Output from ephemerides program, using settings appropriate for direct comparison with the star background image of part (a).

Lens	Angular pixel fov	Total angular fov	Pixel coverage	Total coverage
1600 mm	0.00075° × 0.00075°	0.48° × 0.36°	1.4 m × 1.4 m	880 m × 660 m
1010 mm	0.00119° × 0.00119°	0.77° × 0.57°	2.2 m × 2.2 m	1.4 km × 1.0 km
105 mm	0.0115° × 0.0115°	7.36° × 5.52°	21 m × 21 m	13.5 km × 10.1 km
50 mm	0.024° × 0.024°	15.5° × 11.6°	44 m × 44 m	28.4 km × 21.2 km
25 mm	0.048° × 0.048°	30.9° × 23.2°	88 m × 88 m	56.7 km × 42.4 km

Table 5.1: Angular and linear fields of view characteristics for the different PAI lenses. The total angular fields of view are considered accurate to within 0.5%. An altitude of 105 km has been assumed.

aurora, using no optical filtering, and with the imager running at a fairly low gain setting. Using a low gain setting permitted only the the brightest stars within the field to be seen, facilitating their subsequent easy identification on star charts. Figure 5.1b shows a star chart obtained by using an ephemerides computer program (identified in Table 2.4). The field of view of the chart window was set to $16° \times 12°$, and the azimuth and elevation pointing was set identical to that of the PAI (in this case, parallel to the local geomagnetic field line). By comparing the figures, bright stars seen in the PAI field of view are readily identified. By overlaying star background images with such star charts, it was established that the objective lenses acquired for the PAI do not introduce significant spatial distortion within the image. Further, the ephemerides program may be queried for the the right ascension and declination of each celestial body within the field of view. Based on these data, the angular separation d between two stars may be calculated as,

$$\cos d = \sin\delta_1 \sin\delta_2 + cos\delta_1 \cos\delta_2 \cos(\alpha_1 - \alpha_2), \tag{5.1}$$

where α_1 and δ_1 are the right ascension and declination of one star, and α_2 and δ_2 those of the other star [e.g., Meeus, 1991].

A computer program was written for the purpose of tracking two stars within the field of view for several hundred consecutive digitized frames, centroiding their location. The resulting separation was mea-

sured within each frame and averaged over time, allowing a fairly accurate determination of their separation in units of pixels. These data were then used together with the actual angular separation calculated using Equation 5.1 to obtain quantities such as the total angular field of view of the imager as well as the angular field of view of a single pixel within the digitized image. The results of such star field measurements using different optics is presented in Table 5.1. These fairly accurate measurements permitted the fiber optic taper minification ratio to be determined. The manufacturer specification is 1.55 ± 0.05. Based on these experimental measurements, a value of about 1.54 is found. Note that the PAI image digitization process is carefully timed and synchronized so as to obtain digitized pixels having a square geometry. Such square pixels permit easy measurements of linear distances across the field of view. These imposed timing constraints are among the factors that dictate the resulting image size of 640 pixels by 480 pixels. Note that the mapped pixel dimension of 20 m, as in the case of the 105 mm focal length lens, does not imply a spatial resolution of 20 m at auroral altitudes. As will be seen shortly, the imager has a finite point spread function, and a certain amount of care thus has to be exercised when trying to measure linear distances having dimensions of only a few pixels.

5.2 Sensitivity

Imager sensitivity was measured using a monochromator as well as a low brightness blackbody source (LBS) with interference filters. The full details of the calibration session may be found in a separate report [Trondsen, 1993], but some main results are summarized here. Note that in the case of GaAs photocathodes the spectral responsivity tends to change somewhat over time due to ion poisoning of the photocathode. Spectral performance measurements should thus be repeated at regular intervals if quantitative measurements are intended.

A monochromator was first used to verify the general shape of the imager's spectral responsivity curve. Relative imager response was sampled at 20 nm intervals throughout the range 400–900 nm. This confirmed that the spectral range to which the imager is sensitive is as specified by the manufacturer, and that the overall shape of the curve given in Figure 2.5 is indeed representative of actual imager performance.

LBS measurements were made for the purpose of studying the behavior of the imager's signal-to-noise ratio as a function of source radiance around the threshold of detection for some selected wavelengths. The LBS, calibrated at the National Research Council (NRC) in Ottawa, has a known spectral output, a function of wavelength, given in units of kR/Å. A baffle unit of known length and aperture was mounted in front of the bare photocathode of the imager, and narrow-bandwidth interference filters were in turn mounted at the front of the baffle unit. The LBS and the sensor were aligned so that the opal screen of the LBS completely filled the field of view of the imager, as viewed through the baffle unit. Since the geometry of the setup and the filter transmission characteristics were completely known, the optic axis solid angle of acceptance could be calculated, and the corresponding irradiance onto the photocathode could be determined [e.g., Smith, 1981]. The photocathode's responsivity may be assumed constant over the bandwidth of the filter. Using the three

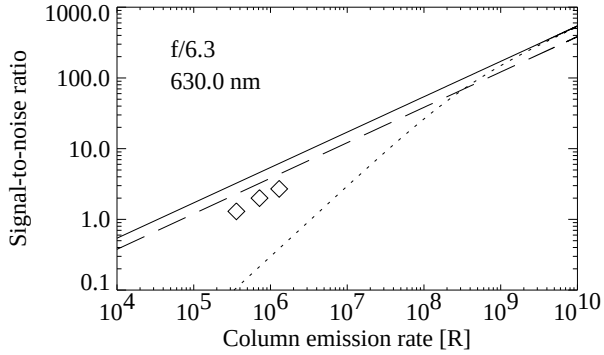

Figure 5.2: Calculated SNR *vs.* emission rate for the CCD (dotted), ICCD (dashed), and ideal (continuous line) detector. The three diamonds indicate actual measured values, using a low brightness source (LBS). The optics assumed is the PAI Schmidt-Cassegrain Telescope in the $f/6.3$ configuration, with a 70% transmission 630.0 nm interference filter.

largest LBS aperture disc settings, the LBS signal was recorded onto video tape and subsequently digitized. The calculated signal-to-noise ratios thus include the effects of the camera video processing circuitry and the VCR, and also the effect of the image digitizer analog-to-digital converter (ADC) noise. The camera gain was during these measurements set sufficiently high so as to enable individual photoevents to be discerned, thus relegating all CCD-related sources of noise (see, Chapter 4.2). This gain was about one-third of the maximum available gain. The signal-to-noise ratio was calculated as follows. For each interference filter used, 60 consecutive video images were digitized, each constituting the central 12 pixels by 12 pixels region of the full 640 pixels by 480 pixels field of view. The standard deviation and mean of each of these 144 pixels were calculated along the axis of time. The mean of the 144 thusly generated standard deviations and means were then used to estimate the signal-to-noise ratio of the imager at the level of irradiance defined by the LBS aperture disc setting. The irradiance produced onto the photocathode by the LBS was referenced to a corresponding auroral column emission rate, as seen through a specific objective lens and filter, so as to be able to directly compare the result with that obtained by using the model of Chapter 4.2. Figure 5.2 shows the result of measurements using a 2 nm bandwidth, 630.0 nm wavelength interference filter. The three points corresponding to the three LBS aperture disc settings appear as diamonds, located in the vicinity of the threshold of detection of the sensor as defined in Chapter 4.2.5. Just like in Figure 4.2, the predicted signal-to-noise ratio of an ideal detector (continuous line), a CCD (dotted line), and an ICCD (dashed line), are also shown. The fact that the measured values are situated somewhat below the dashed line corresponding to an ICCD is simply an indication of the fact that we are here dealing with a non-ideal ICCD detector. In such cases, the noise factor of the ICCD has to be taken into account, as explained in Chapter 4.2.6. In fact, the three points plotted in Figure 5.2 may be fitted by a line corresponding to a noise factor of about 3.5, i.e., somewhat worse than the value of 3.0 assumed previously. The explanation for this higher value may lie in part in the high ambient temperature of $\sim$30°C measured in the laboratory during the LBS measurements. Third-generation photocathodes are optimized for infra-red response, and are thus inherently noisy unless actively cooled [Csorba, 1985]. For this reason, outdoor operation of the camera head is preferred in the

field, thereby keeping the photocathode relatively cold (0–15°C). Other reasons for the discrepancy may be that the measured values incorporate noise introduced by the VCR (the same physical video frame digitized repeatedly always shows some variance), as well as quantization noise originating with the image digitizer's merely 8-bit-deep ADC.

By experimenting with real-time averaging operations during the digitization of LBS footage it was confirmed that the signal-to-noise ratio indeed increases as the square root of the number of frames averaged, as already suggested in Chapter 3.1.3. It is interesting to note that viewing auroral footage as a movie sequence instead of as a series of still frames (whether printed, on a computer monitor, or on a TV screen) has a certain merit in and of itself in that the apparent signal-to-noise ratio is significantly enhanced. This comes about as a result of the fact that the "storage time" of the human eye-brain sensor system is about 0.2 s [Rose, 1973]. Since the duration of one television frame is only 33 ms, the eye is in effect looking at a superposition of some 7 successive frames, thus achieving a signal-to-noise ratio larger than that of the single frame by a factor of $\sqrt{7}$. Anyone who has looked at a still frame of low-light-level footage will be aware that it is noisier than the visual impression gained from the moving footage in normal projection.

The "sensitivity" of auroral imagers is often stated in units of R ADU^{-1} s^{-1}, where the unit of ADU is the number output by the image digitizer's ADC. By summing 60 consecutive frames within the image digitizer's 16-bit deep frame store memory, an effective pixel integration time of 1 s may be obtained. Using this method on the 630.0 nm LBS measurements referred to above, where one-third of maximum gain was used, the sensitivity was found to be 1.2 kR ADU^{-1} s^{-1}. For a gain of about half the maximum available gain, a value of 10 R ADU^{-1} s^{-1} was obtained. These results were found to be independent of the actual LBS aperture disc setting, bearing testimony to the linear response of the imager. A representative dark frame was subtracted from the data prior to calculating the rayleigh-to-ADU ratios. This rayleigh-to-ADU sensitivity was only measured for two different gain settings. If the PAI is to be used for accurate photometric measurements in the future, these quantities will probably need to be measured again, and mapped out more accurately as a function of MCP voltage.

5.3 Spatial Resolution

In the language of *system analysis*, an optical imaging system may often be considered a two-dimensional, space-invariant, fixed-parameter linear system. Linear, space invariant systems may be described by linear differential equations with constant coefficients, causing, for example, an image of a sinusoidal pattern to remain sinusoidal. Such a system is completely characterized by its *impulse response*, which in the case of an imaging system is its point spread function (PSF) [Williams and Becklund, 1989]. The dependence of the image on the object may be expressed as a convolution integral, where the convolving function is the imaging system's PSF [Bracewell, 1995]. One may regard a point source as being composed equally of sinusoidal components with all possible wavelengths. Therefore, if the image of the point source is decomposed into its individual frequency components by a spatial Fourier analysis, the result is the imaging

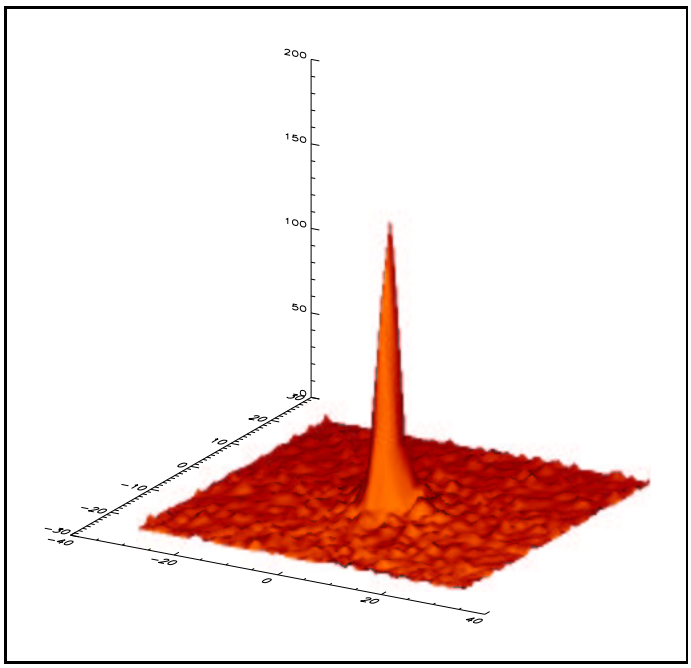

Figure 5.3: Three-dimensional plot of the imager's point spread function. The vertical axis represents relative image pixel intensities. Only a small central portion of the much larger original frame is shown.

system's *transfer function* [e.g., Scott and Frauenhofer, 1971]. As the attentive reader may already have surmised based on the discussion of Chapter 4.3.1, the magnitude of the Fourier transform of the PSF is exactly the imager's modulation transfer function (MTF).

The image of a point source can never be as precise as the point source itself. Several factors cause a spreading of the radiant energy reaching the image plane of an imaging system. Within the optics there are factors such as dust particles on optical surfaces and scratches in these surfaces, foreign particles such as bubbles within lens material, irregularities on the edge of apertures stops, and aberrations (including defocusing). Within the rest of the system, factors such as a finite CCD pixel size, impurities within the fiber optic taper, and the finite bandwidth of the video processing circuitry cause the signal to further scatter and spread out about the point where the image would otherwise be formed. The imaging system's PSF is an excellent tool for characterizing the total impact of all these factors.

A source of appreciable size (in our case, a monochromator) was made to function as a point source by forming an image of the source on a small hole in a metallic screen. The illuminated hole was found to function as a point source. The hole was small enough that further small adjustments of the hole diameter did not influence the width of the image of the point source as viewed by feeding the RS-170A video signal into a high-frequency oscilloscope. Further, the intensity of the point source was adjusted to somewhat below the point where the video signal started saturating, thus ensuring that the digitized image would be fully resolved. Figure 5.3 shows a three-dimensional plot of the image of the point source, wherein the vertical dimension represents image intensity. Only the central 64 pixels by 48 pixels portion of the full 640 pixels

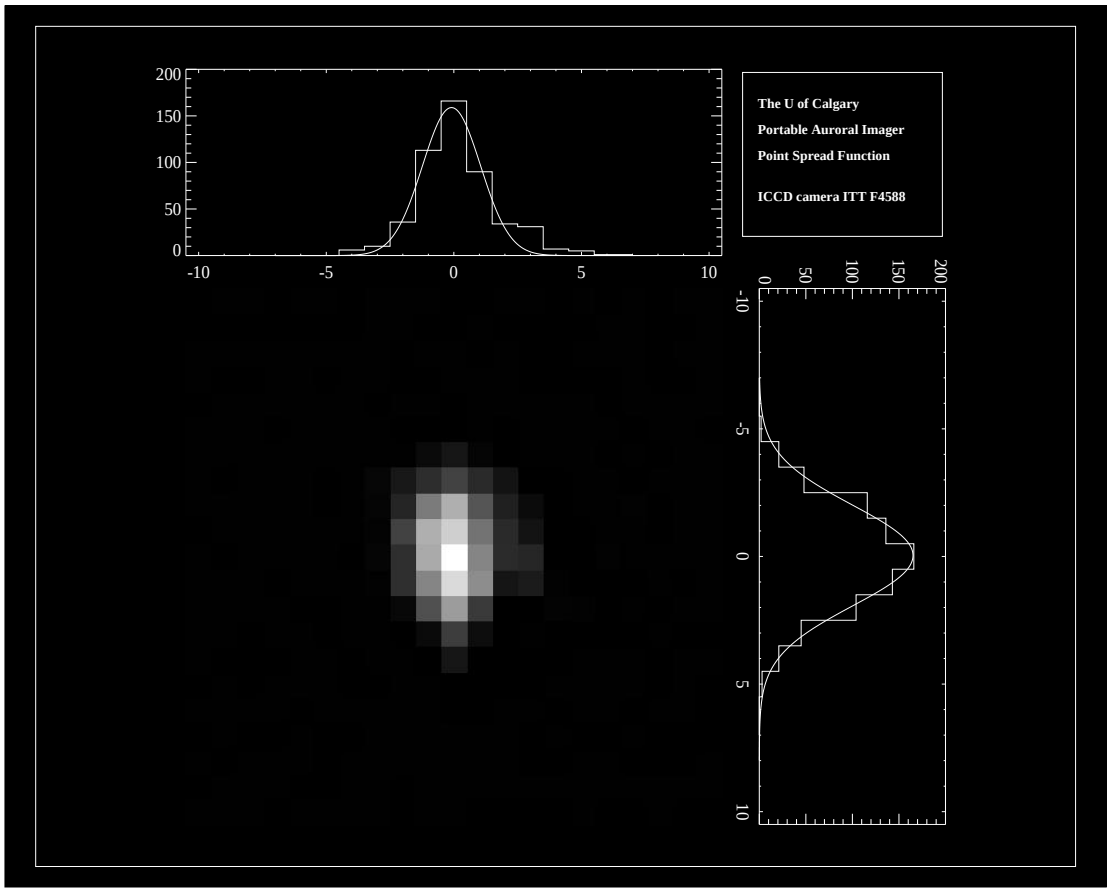

Figure 5.4: The PAI ICCD point spread function.

by 480 pixels frame is shown. The PAI's PSF is shown in the more conventional representation in Figure 5.4. It can be seen that the PSF is approximately Gaussian, with a full width at half maximum (FWHM) of 2.75 pixels, horizontally. The fact that the PSF is asymmetric is ultimately a reflection of the fact that the CCD pixels are not square. This gives the appearance of an elongated spot owing to the small number of pixels involved. (The image digitizer itself outputs pixels that are exactly square.) This PSF may now be used to estimate the imager's MTF. The Gaussian curve fitted to the horizontal PSF in Figure 5.4 is plotted again in Figure 5.5a, here within the context of the full 640 columns of the digitized frame. Figure 5.5b shows the Fourier transform of this fitted PSF, plotted out to the Nyquist limit. This may now be considered a rough estimate of the system's overall MTF, an estimate which includes the degrading effects of video processing circuitry, VCR, and image digitizer ADC. The MTF is down to about 10% at a frequency of just above 0.3 linepairs per pixel. For a total of 640 pixels across the full frame, this corresponds to a limiting (high-light-level) horizontal resolution of about 400 lines, a result that is in good agreement with the assumption made in Chapter 3.1.1 that the resolution is limited by the VCR's own horizontal resolution. It is worth noting that the MTF curve of Figure 5.5b has a qualitatively different shape that that of Figure 4.4. The somewhat

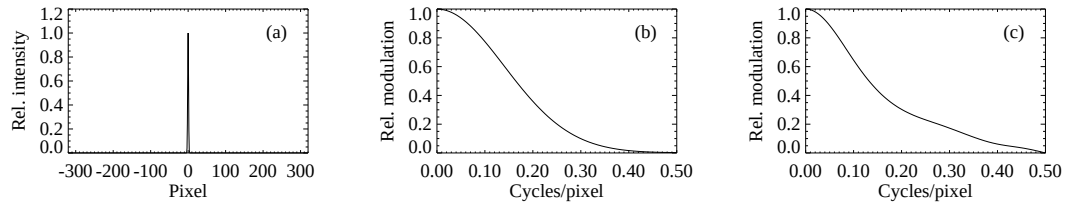

Figure 5.5: (a) The fitted Gaussian horizontal point spread function. (b) The modulation transfer function obtained by taking the Fourier transform of the fitted point spread function. (c) The modulation transfer function obtained by taking the Fourier transform of the actually measured point spread function. The units along the frequency axes are linepairs per pixel within the image digitizer's frame store.

convex shape of the former (a quality normally aimed for during any imager design process) is unfortunately only due to the fact that fitted values for the PSF were used in generating the MTF. As seen in Figure 5.5c, where the actually measured PSF values are used, a considerably less convex shape emerges. Curiously, the cutoff frequency is now higher. However, recognizing the uncertainties involved in this exercise, it is best to take the conservative approach and adopt the 400 lines resolution-limit suggested by Figure 5.5b. One such uncertainty involves the fact that the CCD has discrete pixels, and that the image of the point source is thus very much a function of the relative alignment of the point source with respect to the actual CCD pixel as projected onto the photocathode. No accurate alignment of the point source to pixel centers was attempted.

Note that it is less than straightforward to compare these result with the results of Chapter 4.3, as we in the present case are dealing with a point source, for which the concept of radiance is no longer meaningful since there is no extended source area to which throughput (etendue) considerations can be properly applied [Nicodemus, 1963]. However, the result obtained here may be considered a useful sanity-check, in that our assumption of Chapter 4.3.3, that the results obtained there would not be significantly altered by the VCR's own high-light-level limiting resolution, has now been partially justified. We have thus obtained much valuable information from a simple point-source observation, thus avoiding a complete MTF characterization, a process which is typically both complicated and time consuming [e.g., Reichenbach et al., 1991, and references therein].

An imager's spatial resolution may be estimated at various light levels using resolution test charts, such as the standard Electronic Industries Association (EIA) test chart. Such a test chart, of the back-illuminated type, was placed in front of the opal screen of the LBS, and the resolving ability of the imager was estimated by viewing the test chart bar-pattern on a large TV monitor and through an oscilloscope. To obtain sufficient light intensity, the LBS had to be operated at its three largest aperture settings, without any interference filters. Using the modeled LBS spectrum of a 2970°K blackbody source, together with the known imager photocathode response, the corresponding total rayleigh brightness could be estimated [Trondsen, 1993]. A $f/1.5$ lens (belonging to the laboratory) was used for imaging the test target. The geometry of the setup of imager and test target was such that a lateral magnification of 2 resulted. Snapshots of the test target, as observed using the three largest LBS aperture disc settings, are shown in Figure 5.6. (The images

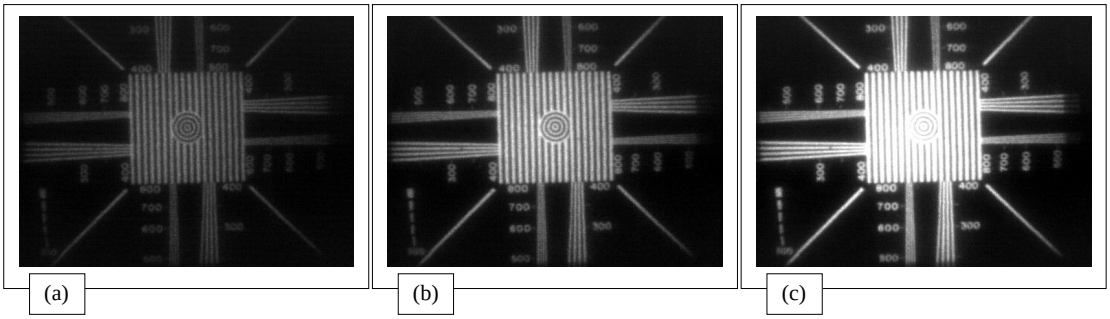

Figure 5.6: EIA-type test chart at three different levels of irradiance. Corresponding column emission rates are estimated at, (a) 250 kR, (b) 500 kR, and (c) 1 MR.

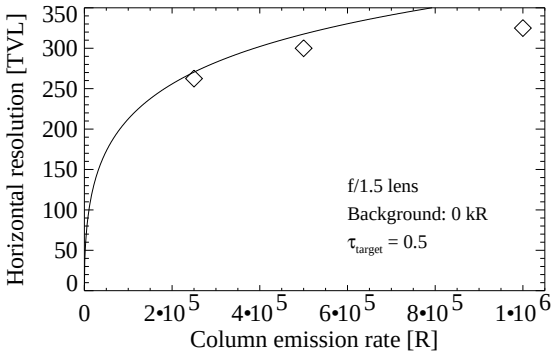

Figure 5.7: Modeled (continuous line) and measured (diamonds) spatial resolution as a function of source emission rate.

as presented here have been shrunk considerably for the purposes of saving space, and are thus not very well suited for accurate determination of bar-pattern resolution.) Taking the magnification factor into account, and studying the bar-patterns at the different settings of the LBS aperture disc, the three data points shown as diamonds in Figure 5.7 resulted. The continuous line represents the performance as modeled using the model of Chapter 4.3. Note that the model appears to overestimate the resolution somewhat, especially at the higher light levels. The discrepancy may be in part due to the fact that at high light levels such as in Figure 5.6c, which in this case actually caused CCD pixel wells to saturate, the spots on the phosphor screen of the image intensifier resulting from each primary photoelectron tend to become large enough to have an adverse effect on the overall spatial resolution. A fairly low MCP gain was used so as to minimize these effects over the measured range. The act of deciding which bar pattern frequencies are resolved and which ones are not, is, even when using an oscilloscope, a somewhat subjective process. The method was thus not considered accurate enough to generate reliable results for the very lowest light levels of Figure 5.7, where the slope of the modeled curve becomes extremely steep. Specialized MTF-measurement instrumentation, not available in the laboratory that was used during the PAI characterization, is usually employed for such tasks.

Finally, the point source measurements were used to study the imager's inter-frame horizontal pixel stability, i.e., its "jitter" characteristics. For accurate measurements of linear dimensions within an image

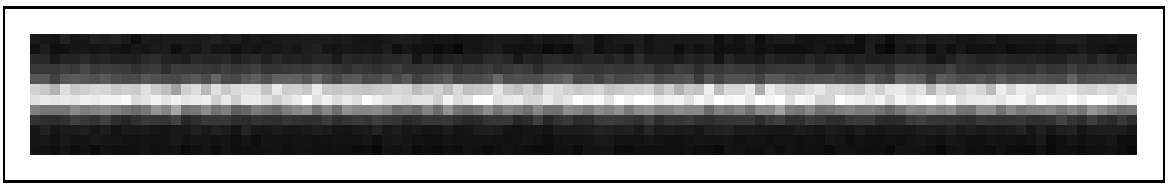

Figure 5.8: Slice through the center of the image of the point source (vertical dimension) showing pixel jitter as a function of time (horizontal dimension). The centroided locations are quantified in Figure 5.9.

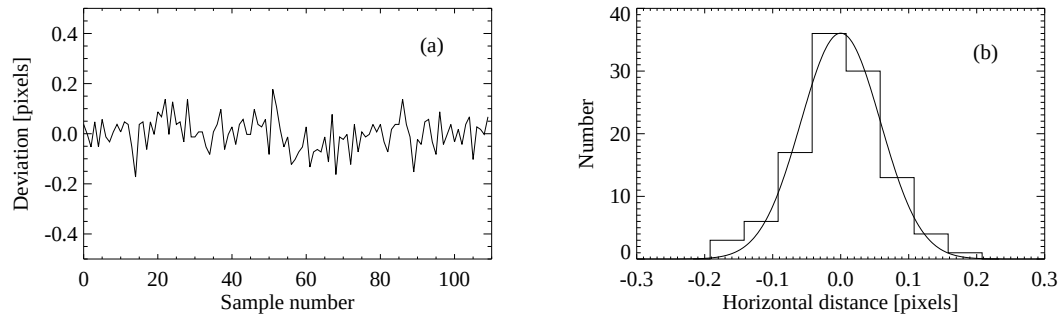

Figure 5.9: (a) The inter-frame movement of centroided point source locations. (b) The corresponding distribution of centroided point source locations. A Gaussian curve has been fitted to the data.

there needs to be good geometric stability. Inaccuracies are in the case of the PAI expected to have their origin mainly with the VCR and the image digitizer. However, the VCR employs time-base correction circuitry to minimize pixel jitter, as described in Chapter 3.2.1. Further, the image digitizer is especially designed to minimize pixel jitter, given proper synchronization information from its video source. Figure 5.8 shows a stack of 12-pixel-wide horizontal slices through the center of a point source image (along the vertical dimension of the figure) as a function of time for 110 consecutive video frames (along the horizontal dimension). By measuring how the centroided point source location wanders from frame to frame one may gain an impression of the imager's overall pixel stability. Figure 5.9a shows quantitatively how the centroided location of the point source data of Figure 5.8 wanders with time, while Figure 5.9b shows the resulting distribution of centroided locations. Fitting a Gaussian through this distribution yields a jitter FWHM value of only $\frac{1}{7}$th of a pixel, clearly acceptable in view of the system's 400-line spatial resolution. Note that it is not meaningful to measure pixel jitter vertically, as none of the small timing inaccuracies involved here could possibly introduce the full 64 μs deviation needed to cause a pixel to jump an entire scan line.

Part II

Observations

Chapter 6

Introduction to Observations

6.1 The Observing Site

The observations that are the subject of the following chapters were made during the first three field trips made with the Portable Auroral Imager. The imager was during these three campaigns fielded at Rabbit Lake, in the northern part of the province of Saskatchewan, Canada. The Rabbit Lake site was considered a well-suited test site for the PAI, as it is located within the auroral zone and is permanently equipped with an all-sky camera, a magnetometer, as well as a variety of other scientific instrumentation. Figure 6.1 shows

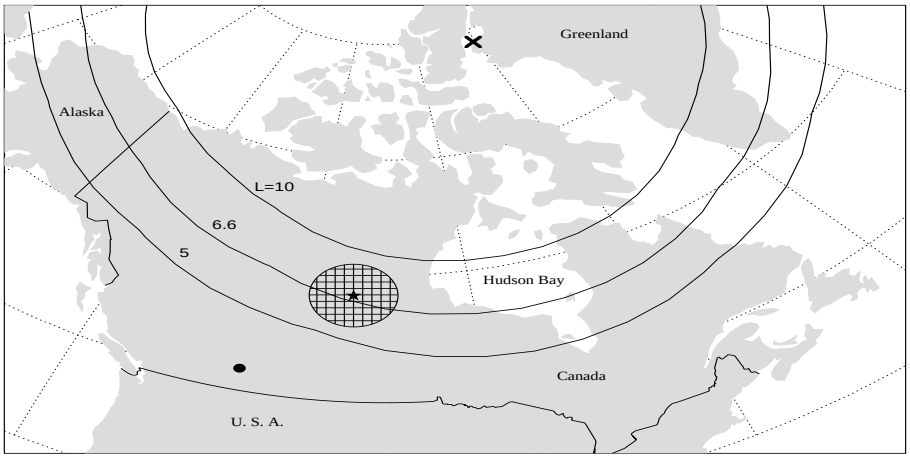

Figure 6.1: Map centered on the northern regions of Canada. The location of Rabbit Lake is marked with a star in the middle of a larger circle representing the all-sky camera coverage at 105 km altitude. The geomagnetic north pole is marked with a cross; the location of Calgary is indicated with a dot. Also suggested here are the northern and southern borders of the auroral distribution.

a plot of northern Canada, with the Rabbit Lake observing site indicated. The meshed area corresponds to the coverage of the Rabbit Lake all-sky camera at 105 km altitude. According to GPS measurements, the site is located at 58°13′36″N and 103°40′35″W, at an altitude of about 410 meters above sea level. Using a

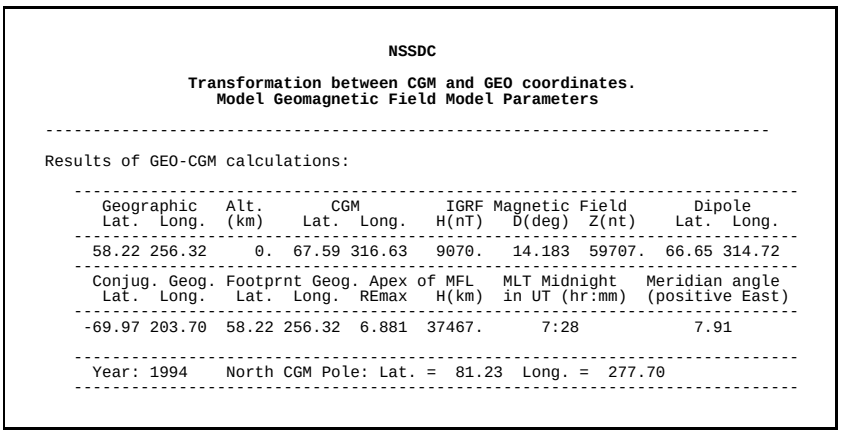

```
                                    NSSDC

                Transformation between CGM and GEO coordinates.
                   Model Geomagnetic Field Model Parameters

-------------------------------------------------------------------------

Results of GEO-CGM calculations:

   ---------------------------------------------------------------------------
      Geographic   Alt.       CGM         IGRF Magnetic Field       Dipole
      Lat.  Long.  (km)    Lat.  Long.   H(nT)   D(deg)  Z(nt)    Lat.  Long.
   ---------------------------------------------------------------------------
     58.22 256.32     0.  67.59 316.63   9070.   14.183  59707.  66.65 314.72
   ---------------------------------------------------------------------------
     Conjug. Geog. Footprnt Geog. Apex of MFL   MLT Midnight   Meridian angle
      Lat.  Long.   Lat.  Long.  REmax   H(km)  in UT (hr:mm)  (positive East)
   ---------------------------------------------------------------------------
    -69.97 203.70  58.22 256.32  6.881  37467.      7:28            7.91

   ---------------------------------------------------------------------------
     Year: 1994    North CGM Pole: Lat. =  81.23  Long. =  277.70
   ---------------------------------------------------------------------------
```

Figure 6.2: Output of an NSSDC computer program, giving the CGM location and other data relevant to the Rabbit Lake observing site.

computer program which employs an algorithm based on DGRF/IGRF geomagnetic field models [Gustafsson et al., 1992], a corresponding corrected geomagnetic (CGM) location of 67°36′N, 316°43′E is obtained. These coordinates, and some additional information pertinent to the site, are found in Figure 6.2 which constitutes the output of the computer program, which is freely available from the National Space Science Data Center (NSSDC). As can be seen, magnetic midnight at this site occurs at 0728 UT. It can also be shown that Rabbit Lake is located somewhat below the 7th L-shell (see, Figure 6.1).

6.2 Instrument Pointing

During observations of the thinnest auroral structures using the longest focal length objective lenses, an accurate alignment of the optic axis of the instrument to the local geomagnetic field line is crucial. Using computer models, one can estimate the magnitude of the various components of the local magnetic field. These components may in turn be used to calculate the azimuth and elevation pointing of the field line. The components of the geomagnetic field are readily obtained through the Internet; Figure 6.3 shows the output of an empirical model accessible through an NSSDC Internet site. The dip angle α will be calculated first. Using the values of Figure 6.3, we obtain,

$$\alpha = \arctan\left(\frac{B_{\text{down}}}{\sqrt{B_{\text{north}}^2 + B_{\text{east}}^2}}\right) = 81.4^\circ, \tag{6.1}$$

corresponding to a zenith angle of 8.6°. Further, the azimuth pointing Φ is,

$$\Phi = 180^\circ - \arctan\left(\frac{B_{\text{east}}}{B_{\text{north}}}\right) = 165.8^\circ \text{ west of north.} \tag{6.2}$$

The imager may now be pointed in the appropriate direction by using stars as reference points. For this purpose, an ephemerides computer program is normally used. This program outputs tables of azimuth and elevation data for a set of stars as a function of time, for any given observing point on the surface of the Earth.

```
                                    NSSDC

      External (T96_01) and Internal Geomagnetic Field Model Parameters

------------------------------------------------------------------------------

Results of MODEL calculations:

Year= 1994   Day =  67   Hour =  7  Min = 30  Sec =  0  Alt.=     0 km

Starting point:       Geographic      Dipole     Corr.geomagn.
                      Lat.  Long.   Lat.  Long.   Lat.  Long.
                      58.22 256.32  66.65 314.72  67.59 316.63

Internal Geom. Field Comp. H (nT) =  9071.5  D(deg) =  14.185  Z (nT) = 59719.0
                           X (nT) =  8794.9  Y (nT) =  2223.0  Z (nT) = 59719.0

------------------------------------------------------------------------------
```

Figure 6.3: Geomagnetic field components for the Rabbit Lake observing site, as output by an NSSDC computer program.

6.3 Data Coverage

The observing campaigns that form the basis of the following sections were conducted during the winters of 1994, 1995, and 1997. The campaigns were centered around new-moon periods in the early part of March of these years. In terms of the number of clear days, spring is superior to fall for the entire North American auroral zone. The PAI was for the duration of these three initial campaigns run strictly in the unfiltered ("white light") and ungated (16.7 ms integration time) mode, so as to ensure the availability of sufficient photon flux. Experience and confidence gained during these early campaigns in turn provided a foundation for later campaigns where optical filtering modes were experimented with, with good results. The data obtained during such later campaigns are not discussed in this thesis.

Tables 6.1 to 6.3 give an overview of the total data coverage resulting from the three field trips. The objective lenses that constituted the primary and secondary fields of view are also indicated in the tables. As can be seen, a secondary camera was not always available. The PAI's secondary camera is normally borrowed from other projects. In the case of the 1997 campaign, no secondary camera was available for loan. In the second half of the 1994 campaign, the borrowed camera malfunctioned due to the extremely low ambient temperatures. It is worth noting that the third-generation primary field of view ICCD camera acquired especially for the PAI project has thus far functioned without any problems whatsoever, even under the most hostile of conditions. Note finally that during the 1997 campaign the need for an intermediary field of view was alleviated somewhat by the availability of 30 frames per second all-sky camera video footage. During the other campaigns, only time-lapse all-sky imagery was available (nominally one new image approximately every 5–10 s). As pointed out in Chapter 2, all PAI data are recorded onto high-resolution, analog video tape, and interesting periods are digitized and studied later in the laboratory. A variety of digitization modes were applied during these studies, the mode being dependent of the particular characteristics of the phenomenon under study, and the set down science objectives. Unless otherwise stated, dark frames were subtracted from the digitized images, and a flat field correction applied by dividing each image by a previously acquired flat-field frame, thus eliminating fixed-pattern noise (see, Chapter 2.2.2).

The following four sections consist of four separate phenomenological surveys done on these sets

Day	Date	Coverage, UT	*Fields of View*		
			Primary	Secondary	Other
064	05-03-94	02.35.00 – 08.23.30	1600 mm	50 mm	ASC (time lapse)
067	08-03-94	02.02.00 – 08.21.00	1600 mm	50 mm	ASC (time lapse)
068	09-03-94	02.20.00 – 07.40.00	1600 mm	–	ASC (time lapse)
069	10-03-94	01.56.00 – 07.50.00	1600 mm	–	ASC (time lapse)

Table 6.1: Portable Auroral Imager data coverage, Rabbit Lake, March 5 – 10, 1994.

Day	Date	Coverage, UT	*Fields of View*		
			Primary	Secondary	Other
058	27-02-95	00.50.00 – 07.54.30	105 mm	–	ASC (time lapse)
059	28-02-95	02.36.00 – 07.33.00	105 mm	1600 mm	ASC (time lapse)
060	01-03-95	01.45.00 – 08.25.00	105 mm	1600 mm	ASC (time lapse)
062	03-03-95	01.55.00 – 08.00.00	105 mm	1600 mm	ASC (time lapse)
063	04-03-95	02.00.00 – 08.03.00	105 mm	1600 mm	ASC (time lapse)
064	05-03-95	01.55.00 – 08.20.00	105 mm	1600 mm	ASC (time lapse)
065	06-03-95	02.00.00 – 07.55.00	105 mm	1600 mm	ASC (time lapse)
066	07-03-95	02.00.00 – 07.42.00	105 mm	1600 mm	ASC (time lapse)

Table 6.2: Portable Auroral Imager data coverage, Rabbit Lake, February 27 – March 7, 1995.

Day	Date	Coverage, UT	*Fields of View*		
			Primary	Secondary	Other
065	06-03-97	02.55.00 – 08.15.00	105 mm	–	–
066	07-03-97	02.05.00 – 07.35.00	105 mm	–	ASC (30 fps video)
067	08-03-97	02.25.00 – 03.15.00	105 mm	–	ASC (30 fps video)
070	11-03-97	02.00.00 – 07.35.00	105 mm	–	ASC (30 fps video)
071	12-03-97	02.45.00 – 07.10.00	105 mm	–	ASC (30 fps video)
072	13-03-97	02.00.00 – 07.55.00	105 mm	–	ASC (30 fps video)
073	14-03-97	03.00.00 – 07.20.00	105 mm	–	ASC (30 fps video)
074	15-03-97	02.00.00 – 07.50.00	50 mm	–	ASC (30 fps video)
075	16-03-07	02.35.00 – 07.10.00	50 mm	–	ASC (30 fps video)
076	17-03-97	03.00.00 – 05.20.00	50 mm	–	ASC (30 fps video)

Table 6.3: Portable Auroral Imager data coverage, Rabbit Lake, March 6 – 17, 1997.

of data. These surveys of small-scale auroral forms pertain to, in order of appearance,

Chapter 7: Observations of thin auroral forms ($<$100 m)

Chapter 8: Observations of black aurora ($\sim$1–10 km)

Chapter 9: Observations of multiple auroral arcs ($\sim$0.1–1 km)

Chapter 10: Observations of auroral vortices ($\sim$1–10 km)

We shall thus be dealing with some of the smallest known, and possibly least explored, features of the aurora.

Chapter 7

Thin Auroral Forms

7.1 Introduction

A fraction of the energy transferred from the solar wind to the Earth's magnetosphere goes into energizing the electrons that produce auroral arcs. While many theories have been put forth, the mechanisms by which energy is transferred to the electrons are still largely shrouded in mystery. The aurora, especially during the breakup phase, tends to contain much fine structure, as is evident from Figure 7.1. Since the auroral arc is the glowing footprint of a sheet of energetic electrons, measurements of the thickness of auroral arcs may be compared with predictions about the thickness of the electron-energization zone. Such measurements may thus provide direct tests of the competing theories for the generation of arcs. Most of the models currently in fashion predict thicknesses ranging from about a kilometer to several tens of kilometers [Borovsky, 1993a]. This is in stark contrast to observational evidence suggesting a most common thickness of 70–100 m or less (see, Figure 1.1). The presence of fine structure within the aurora alone does not disqualify any of the proposed theories of auroral arc generation; there is a hierarchy of spatial scales within the auroral zone, and some of the proposed theories may indeed be adequately addressing some of the larger scales.

As inferred from Chapter 1, auroral arcs may be considered to be characterized by at least three (usually latitudinal) spatial scales: (1) a broad diffuse 10 km wide channel, (2) a 1 km wide bright dynamic sheet of emission residing within the broader channel, and (3) the narrow, dynamic structures with thickness of on the order of 100 m, residing within the bright 1-km-wide feature. These narrow 100-m wide structures are the auroral-arc fine structures that are the topic of this chapter. The Portable Auroral Imager was especially designed to resolve auroral fine structure on the order of 10–100 m. The many design considerations that formed the basis for the final design were discussed in-depth in Chapters 3 and 4. Since the region of airglow of an arc appears as a magnetic-field aligned sheet, the arc must be imaged in the magnetic zenith to be properly resolved. Figure 7.2 shows several examples of auroral arcs observed edge-on by the PAI using its 105 mm focal length objective lens. Arcs with thicknesses on the order of several hundred meters to a few kilometers are seen in this figure. It can be seen that in some cases smaller-scale fine-structure exists within

Figure 7.1: Photographs of the *Aurora Borealis*. Note its laminar appearance and the very thin sheets of which it is comprised. *Photographs are ©Jan Curtis, and are used with permission.*

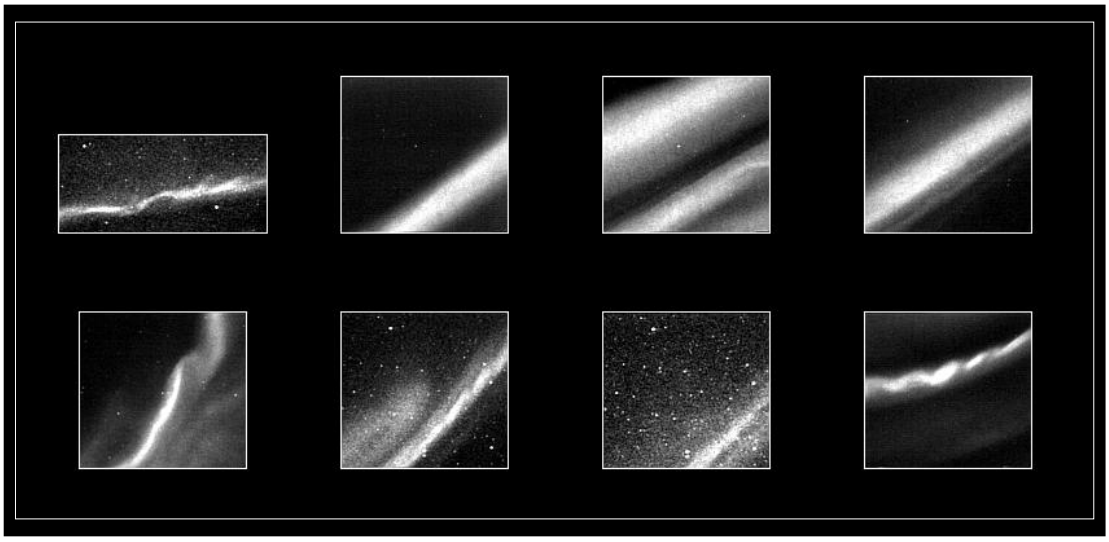

Figure 7.2: Snap-shots of auroral arcs, as observed in the zenith by the Portable Auroral Imager using a 105 mm focal length objective lens and no optical filtering. The field of view depicted corresponds to 10.8 km by 10.1 km at the location of the arc, with the exception of the first frame, which field of view corresponds to 13.5 km by 5.4 km.

the broader structure. The curl-like distortions (seen in the lower right hand side frame of the panel) are often the cause of what appears as long vertical rays when the aurora is observed off-zenith. Examples of such rays may be seen in Figure 7.1. The focus of the current investigation is on the smallest spatial scales, namely, the largely unexplored territory of the sub-100-m wide auroral-arc fine structure. To preserve photon flux and spatial resolution, the imager was during these observations run in the unfiltered ("white light") mode. This was partly motivated by the results of Borovsky [1993b], who used a fairly sophisticated computer model to show that any blurring of the image of a moving arc by nonzero lifetime emission lines will not normally obscure the main arc itself. The blurring can, according to this model, often be distinguished as an exponential decay in the wake of the causative arc. This permits (1) the estimation of the main arc's thickness, e.g., by the fitting of the data to a Gaussian curve, and (2) the lifetime of the slow emission to be estimated based on the time constant of the wake decay. A requirement for this afterglow to be properly distinguished from the main arc itself is that the image not be overexposed.

7.2 Observations and Discussion

The highest-quality footage of sub-100-m auroral arcs were obtained during the 1994 campaign, when the 1600 mm telescope lens was assigned to the primary field of view of the imager (see, Table 6.1). Some further data suitable for thickness measurements were also obtained during the 1995 campaign, when this lens was mounted on the secondary field of view (see, Table 6.2). As already pointed out, owing to the thinness of many auroral structures, it is necessary to measure the thickness only when the structure is exactly in the magnetic zenith. Accurate alignment to the local geomagnetic field is crucial, as the total angular field of view itself is very small, on the order of $\sim$0.5° (see, Table 5.1). Using stars as reference objects, the telescope pointing was locked at the beginning of each campaign to the predicted azimuth and elevation of the local magnetic zenith. However, the predicted (Φ, α)-pointing, as calculated in Chapter 6.2, is only as good as the model employed. Further, the instantaneous magnetic zenith may move around by as much as 8° during an observing session due to ionospheric currents [Maggs and Davis, 1968; Velichko et al., 1985]. The peak-to-peak magnitude of this deviation is, unfortunately, larger than the total field of view of the imager in this high-resolution configuration. Note that an infinitely-thin sheet of aurora with lower border at 105 km and vertical extent 30 km observed only 0.5° out of the magnetic zenith at Rabbit Lake will appear to have a thickness of 200 m. Owing to these difficulties, only 12 events of arcs whose thicknesses could be properly resolved were observed throughout the two campaigns. In addition to the problem associated with the magnetic-field alignment of the imager, another factor contributing to the sparseness of data was the very low probability of an auroral form of appropriate dimensions entering the miniscule field of view (880 m by 660 m at 105 km altitude) at the right time, and with a low enough speed. Further, in some cases intense arcs entering the field of view were overexposed, making the data useless.

The recorded data were surveyed for auroral arcs with thicknesses that could be properly resolved within the boundaries of the imager's field of view. This would include arcs of thickness in the range $\sim$10–

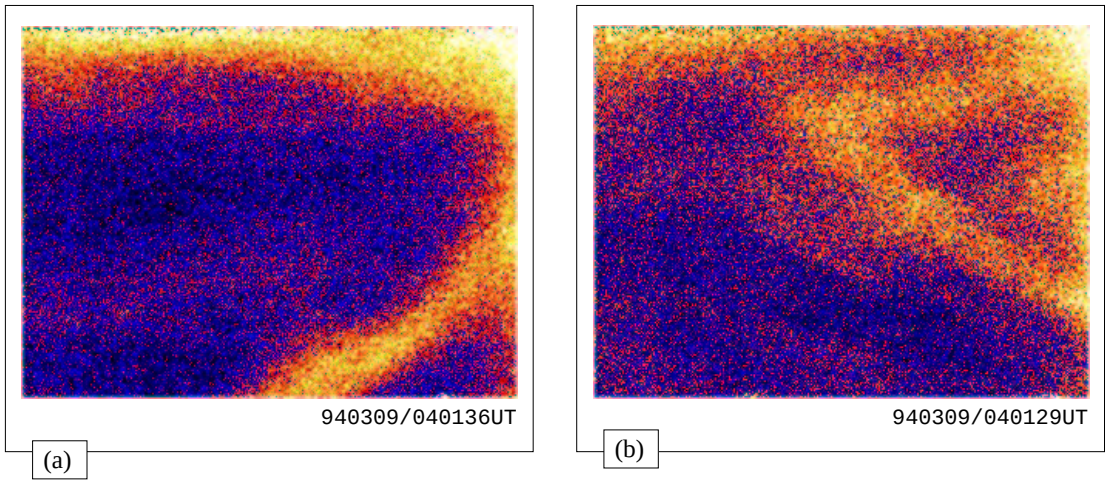

Figure 7.3: (a), (b) Examples of auroral forms of thickness less than 100 m, as seen through the 1600 mm objective lens. The effective exposure time is about 17 ms, i.e., no frame averaging was employed.

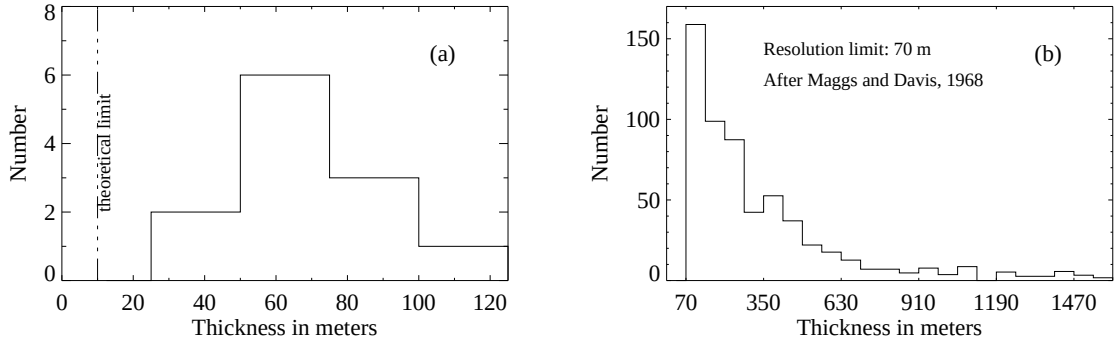

Figure 7.4: (a) The distribution of auroral arc thicknesses for the 12 events observed by the Portable Auroral Imager. The spatial resolution limit is about 10 m, close to the theoretical arc thickness limit. (b) The distribution of auroral arc thicknesses for the 581 events observed in the zenith by Maggs and Davis [1968], with a spatial resolution of 70 m. An 105 km altitude is assumed.

500 m. Only 12 events were identified, all of which actually had thicknesses of less than 120 m. Figure 7.3 shows two examples such auroral forms. The 12 observed forms were all traveling across the field of view, often at a considerable speed—typically 1–2 km s^{-1}. At a 17 ms integration time, this causes a 50 m wide arc to be broadened by about 30–60% due to smear. While sophisticated deblurring techniques do exist[1], results accurate enough for the present purposes were found to result from simply subtracting from the estimated full-width a quantity representative of the estimated speed of the arc feature. When measuring arc thicknesses, only the even (or odd) field of the interlaced video signal was used, thusly ensuring a true 17 ms exposure time (see, Chapter 3.1.2). Figure 7.4a shows a histogram of the resulting thicknesses measured for the 12 events observed. The theoretical arc-thickness limit of Borovsky et al. [1991] is also indicated in the plot. The

[1] These techniques are based on the fact that the corresponding image motion may be described by its own transfer function, that when multiplied with the imager's own total modulation transfer function gives the function for the combination of the two. Alternatively, this process might be viewed in terms of a convolution, and the deblurring process in terms of a deconvolution [Gonzales and Wintz, 1987].

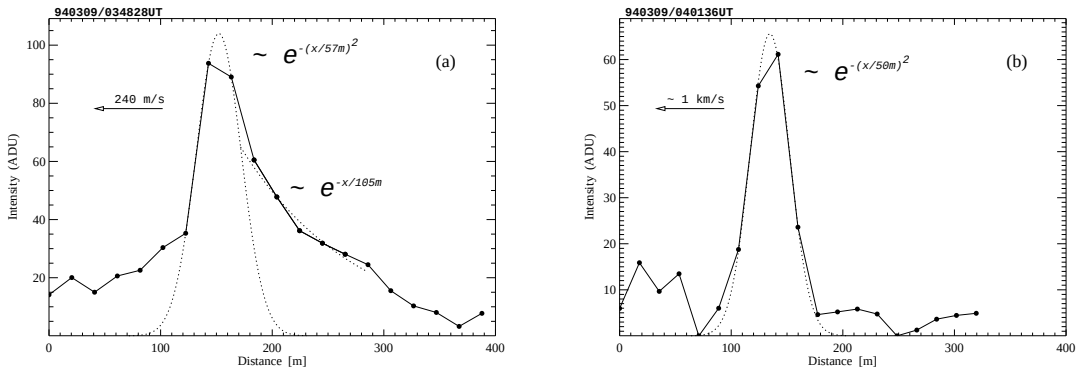

Figure 7.5: (a) Intensity profile through a slow-moving arc. The main arc is fit to a Gaussian curve, and the afterglow is fit to an exponential curve. The exponential is very close to being $\sim \exp(-x/(v_{\rm arc}\,0.7\,{\rm s}))$, indicative of the 557.7 nm emission from atomic oxygen. (b) Similar profile through a much faster-moving arc segment. No attached afterglow is detected in this case, in agreement with the model of Borovsky [1993b].

imager's estimated spatial resolution is about 10 m (see, Chapter 4.3.3), i.e., fairly close to the theoretical thickness limit. Figure 7.4b shows again the distribution obtained by Maggs and Davis [1968], who were constrained by a spatial resolution of 70 m in the zenith. Although 12 events are far too little data on which to base any definitive statements, it is still interesting to note that we are perhaps now starting to discern the shape of the distribution below the original 70-m instrumental resolution limit of Maggs and Davis [1968]. Obviously, significant errors may result from the assumption that all the auroras measured were at the same 105 km altitude. There is definitely a need for more data, but the current data set do suggest a most frequently occurring arc thickness of 50–70 m. Measured velocities were distributed in the range 200–3000 m s^{-1}, with a mean of about 2 km s^{-1}. These measured velocities of small-scale auroral filaments were much larger than those initially expected based on previously reported results (see, Chapter 3.1.2). The total length of the structures could not be determined because of the limited extent of the field of view.

Figure 7.5 shows the intensity profile through two different small-scale arc structures. The distance axis is defined to be normal to the linear extent of the structure. The structure of Figure 7.5a had a drift of 240 m s^{-1} in the direction indicated by the arrow. The structure was drifting through a background emission, as also suggested by the appreciable intensity ahead of the structure in this plot. The intensity profile of the main arc was fit to a Gaussian having a full-width of 115 m, and an exponential curve was fit to the trailing side. This particular structure was the widest (and slowest-moving) structure observed. It was found embedded within a wider, east-west aligned quiet-time diffuse channel that drifted northward. Comparing this emission profile to the modeling results of Borovsky [1993b], it appears that the Gaussian portion of the emission may have its origin in the very fast auroral emissions (see, e.g., Table 3.2). Further, the afterglow, fit by $\exp(-x/105\,m)$, corresponds to a temporal exponential decay in intensity of 0.5 s for a structure moving at 240 m s^{-1}. This value is close to the value of 0.7 s expected for the 557.7 nm line of atomic oxygen. For an arc structure of similar properties, Borovsky [1993b] obtained a value of 0.9 s.

Figure 7.5b shows the intensity profile of a somewhat thinner and faster-traveling structure. (In-

cidentally, this is the structure depicted in Figure 7.3a.) Borovsky [1993b] predicted that at speeds on the order of 1 km s^{-1}, no attached afterglow is expected. However, he was only able to observe structures with velocities in the range 100–200 m s^{-1} and could thus not support his prediction by observational evidence. It appears that Figure 7.5b does indeed furnish such evidence. This arc structure had a speed of about 1 km s^{-1}, and there was no detectable afterglow. After compensating for smearing due to arc velocity, a full width of about 80 m is obtained. This is the nearly instantaneous emission from the atmosphere as it is being bombarded by energetic electrons. It is thus also a measure of the width of the electron sheet beam in the upper atmosphere. Since the sheet beam is expected to broaden only by 10–20 m [Borovsky, 1993b], the true width of the energetic electron beams is in this case only about 70 m. These kinds of observations must of necessity be accounted for by any future theory that wishes to explain the existence of thin auroral arcs.

As already pointed out, Borovsky [1993b] observed only arc structures with velocities in the range 100–200 m s^{-1}. Structures were in that case found to be east-west aligned, with a north-south movement. He presented no statistical data, but did depict the intensity profile through one 100 m wide arc, and stated that the thinnest feature seen during their campaigns was about 40 m wide. In the present survey, only one of the 12 events studied had such a low speed, an east-west alignment, and a north-south movement. This may be due to the fact that the current survey is focused on features within the breakup aurora, while that of Borovsky [1993b] appears to have been centered around the quiet-time aurora. The features observed in breakup aurora were in general found to be thinner, brighter, more dynamic and contorted than those of the quiet-phase auroral structures. Intense, often multiple, dynamic structures were usually contorted with kinks, as in the case of the features shown in Figure 7.3, and were found to pass through the field of view in a variety of ways (east-west, north-south, as well as intermediate bearings). A common feature was that all arcs were highly robust, with the arc intensity often an order of magnitude higher than the intensity ahead of the arc. This demonstrates that these features are not merely a few-percent increase in intensity within a broader feature, but that they may be considered a significant increase in intensity. A main criticism leveled towards the study of Maggs and Davis [1968] was that their 70–100 m wide small-scale structures may have been mere instrumental artifacts associated with very small brightenings of much wider arcs. It should, however, be clear by now that these investigators were indeed reporting a new, important, and still largely unexplained class of auroral phenomena.

This study has been very preliminary in nature, but has offered some very useful insight into the nature of the hitherto largely unexplored auroral small-scale structure. The numbers of Figure 7.4 should not be taken too literally, due to the difficulties in ensuring that the form was indeed exactly in the zenith when the thickness was measured. Curvature of geomagnetic field lines may also have contributed to spatial smearing errors. One lesson learned from this survey is that the smallest-scale structures can be extremely dynamic, and that at the high angular resolution required to resolve them, a very high temporal resolution is needed. 200 frames per second may very well be needed (this is technology which is currently readily available), in which case much faster optics is required. A supporting field of view provided by a 500 mm objective lens (in the case of a 18 mm diameter photocathode) as well as a 100 mm lens might also be invaluable, based on current experience. A telescope jig that provides automatic alignment of the telescope optic axis

to the the instantaneous direction of the local magnetic zenith might also prove to be helpful, albeit difficult to implement. Further, intensifier gating with a dutycyle instantaneously adjusted by the output current of a nearby zenith-pointing photometer might help minimize the amount of overexposed image data.

Chapter 8

Black Aurora

In view of a recent revival of interest in the black aurora and related phenomena, and a striking lack of information on the phenomenon in the literature, we present in this chapter some fairly unique high spatial and temporal resolution optical observations of the black aurora made by the Portable Auroral Imager. A variety of black auroral phenomena, such as black vortex streets (black curls), black arcs, black streaming, and eastward drifting black auroral patches and arc segments, were observed in the evening and midnight sector diffuse (postbreakup, early recovery phase) auroral oval during a field trip to Rabbit Lake, Saskatchewan, from February 25 to March 7, 1995. The data are reviewed here with an emphasis on observed spatial and temporal characteristics. This study indicates that the midnight sector diffuse auroral oval at times may be layered, with a high-altitude aurora containing eastward drifting features and a lower-altitude aurora consisting of patches, veils, and arc segments drifting westward before midnight. Black aurora has been found in both layers. The data presented in this chapter should aid in testing future theories of the diffuse aurora and the black aurora, as well as in interpreting data returned by satellite instrumentation.

8.1 Introduction

According to the definitions of Royrvik [1976] and Davis [1978b], "black aurora" is a lack of emission in a small, well-defined region within an otherwise uniform, diffuse background or within auroras exhibiting a degree of shear behavior intermediate between that of diffuse and discrete aurora. Black auroras appear to be a common feature of the late recovery phase of an auroral substorm. However, to date, very little information on the phenomenon is contained in the literature. Oguti [1975], using a 60° field of view intensified TV camera, observed the formation of "dark holes" in midnight sector auroral surfaces after auroral expansions. Using a 20° field of view intensified TV camera, Royrvik [1976] observed eastward drifting black "spots," arc segments, and vortex structures in the midnight sector but presented very little quantitative information. The phenomenon has been observed as much as 30° off-zenith [Davis, 1978a], an indication that the emission in which the black aurora occurs tends to have a limited height extent.

Large, radially divergent fine-scale electric fields associated with a fallout in electron precipitation have been observed by the Freja satellite double-probe electric field instrument. These have been associated with black arc structures and black vortex street arrays [Marklund et al., 1994, 1995], an association made in the absence of supporting ground-based optical observations. The lack of readily available statistical data on geometrical scale sizes of black auroral structures, and the separation between them, makes it difficult to test such hypotheses.

During a winter 1995 field trip the Portable Auroral Imager performed a survey of the midnight sector black aurora in its various manifestations. These observations will be reviewed in this chapter, and basic quantitative information will be presented in the form of histograms. With stars used as reference points the outdoor-mounted camera head was pointed toward the local magnetic zenith. A 105 mm, $f/1.8$ Nikon lens provided a viewing angle of about 7.4° by 5.5°, yielding a field of view of 13.5 km by 10.1 km at 105 km altitude during this campaign. The imager's spatial resolution is limited by the video recorder's own horizontal resolution of approximately 400 lines, yielding a maximum resolution of about 35 m at 105 km altitude. However, as explained in Chapter 4, in the case of low-light-level phenomena, such as those being reviewed in this chapter, scene contrast and photon statistics play a more prominent role in limiting spatial resolution than does the imager's own modulation transfer function. In practice, therefore, a limiting resolution in the diffuse aurora of $\sim$100 m was more often experienced. Image intensifier gain was manually controlled and recorded. No optical filtering was performed during the experiment so as to maximize the amount of light available to form an image. The spectral response of the imager was thus determined by the photocathode, which has better than 10% quantum efficiency in the range 420–880 nm, with 30% quantum efficiency at 557.7 nm, as shown in Figure 2.5. Consequently, the absolute brightnesses of auroral emissions were not determined.

All times given in this and the following chapters are universal time (UT). Saskatchewan standard time lags UT by 6 hours. Whenever the terms "evening" and "midnight" are used, they refer to the concept of magnetic local time (MLT). Local geomagnetic midnight occurred at about 0730 UT, as indicated in the computer model output presented in Figure 6.2. In all images presented here the magnetic zenith is close to the center of the frame, with the top and right being to the north and west, respectively, as shown in Figure 8.1. This is the natural perspective of an observer facing south, looking upward along the geomagnetic field line. All images were digitized from the original videotapes. Typically, four successive video frames were averaged, effectively doubling the pixel signal-to-noise ratio (see, Chapter 3.1.3). Images have been contrast enhanced by using a linear (unless otherwise specified) transformation. The single-pixel angular field of view was determined by using the angular separation between stars as reference, as explained in Chapter 5. The total field of view of images reproduced here is 7.4° by 5.5° unless otherwise specified. Note again that an altitude of auroral emissions of 105 km is assumed throughout this thesis.

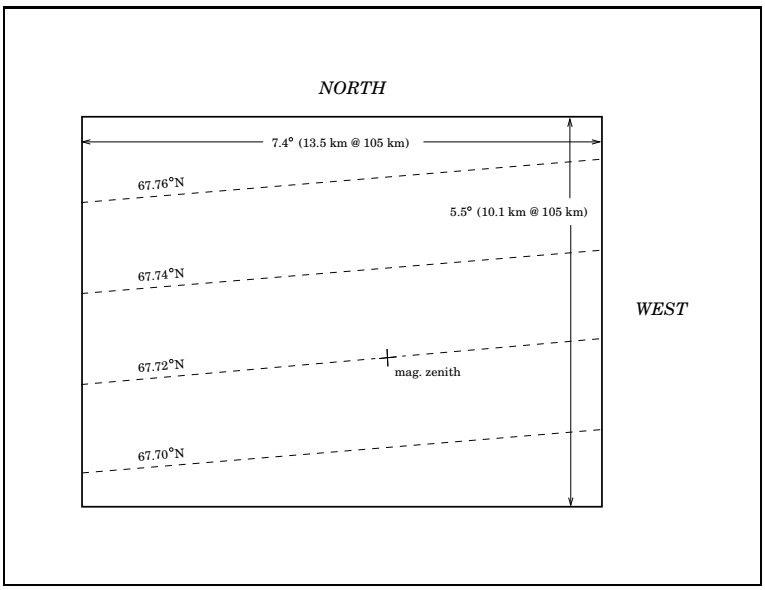

Figure 8.1: Characteristics of the Portable Auroral Imager's field of view during the winter 1995 field trip to Rabbit Lake. Note that west is to the right. Magnetic latitudes have been indicated, using CGM (1980) coordinates. The cross marks the location of the local geomagnetic zenith. In all images to be presented the field of view is 7.4° by 5.5° unless otherwise stated.

8.2 Observations

During the 1995 campaign at Rabbit Lake the nights of February 27 to March 1 and March 3 to March 7 provided unhindered observations of the night sky, with observations commencing at 0200 UT and camera shutdown taking place at about 0800 UT due to concerns related to the rapidly dropping ambient temperature. The result was about 50 hours of video recordings, much of which contained impressive examples of the rich variety of evening and midnight sector short-scale auroral phenomena.

The scope of this chapter, however, will be limited to the various "black" auroral phenomena that were found embedded in the midnight sector diffuse, often pulsating, aurora. Outwardly convex black shapes, corresponding to the "black spots" of Royrvik [1976], and probably also to the "black holes" of Oguti [1975], will be referred to from now on as black patches. Black patches and arc segments will be treated together, since they appear to have many features in common and since one type is occasionally seen to evolve into another. Together they will often be referred to simply as "black objects." Black objects, black arcs, and black vortices will be treated separately in the following three sections.

8.2.1 Eastward Drifting Black Patches and Arc Segments

A striking phenomenon of the midnight sector diffuse auroral oval, otherwise largely characterized by westward drifting features before midnight, was the occurrence of eastward drifting black patches and arc segments embedded in homogeneous diffuse auroral surfaces. No westward drifting black objects of this kind

were observed. By referring to simultaneous all-sky camera observations, it was found that these eastward drifting black objects normally resided poleward of the main (normally westward drifting, diffuse) auroral distribution.

Figure 8.2 depicts a portion of an event that occurred on March 1, wherein an approximately 1–1.5-km-thick arc segment was seen drifting eastward at a speed of about 600 m s^{-1}. Ripples of wavelength 1.5–2.5 km could be seen drifting westward along the edges. A small separate patch of ordinary aurora appeared trapped within the black arc segment, as seen from 0502:00 UT. Whereas the arc segment of Figure 8.2 was oriented roughly parallel to its drift velocity, arc segments would frequently be oriented at an angle to this direction. In a few cases this angle was close to 90°, with the concave end facing west.

Black objects generally had sharply defined boundaries, and the error in the distance over which the velocity was measured is estimated to be less than 200 m, regardless of location within the field of view. Velocities were estimated by averaging such measured displacements in multiple pairs of images separated by 9 s, 6 s, or 3 s, the longer intervals being used for slower moving objects. Measured drifts are relative to the ground. Apparent motion, because of a corotating Earth fixed imager situated below the auroral oval, has not been compensated for. Because of the absence of discrete features in the surrounding emission it was not possible to determine whether or not structures drifted with respect to the ambient plasma.

Figure 8.3 shows a series of arc segments and elliptical patches that drifted through the imager's field of view on March 3. It was not uncommon for black objects to have a southward component to their drift, as seen both here and in the event of Figure 8.2. The drift speed was about 1.3 km s^{-1}, and patch diameters were approximately 2 km. Where patches occurred in a cluster-like formation, the center-to-center patch separation was about 5 km. Patches were seen to undergo identical deformations at the same point in space, indicating that they may have been drifting with respect to some stationary field. This phenomenon is particularly evident when the imagery is viewed as a film sequence.

The majority of patches and arc segments maintained a fairly constant geometry and drift velocity for the duration of their stay within the imager's field of view. Drift speed and geometrical data were measured for 31 such objects, with the resulting distributions shown in Figure 8.4. The 31 observed objects appeared during seven distinct events. Table 8.1 lists mean quantities for each event.

As seen in Figure 8.4a, the eastward drift speed of the observed objects was mainly concentrated in the range 0.6–1.5 km s^{-1}. Note that the one patch event reported by Royrvik [1976], also observed in the premidnight region, had an eastward drift speed of about 3 km s^{-1}. It is possible that our somewhat limited sample size has biased results so as to indicate a lower than average speed distribution. (Note in this context that almost half of the 31 observed objects transpired during one 4-min-duration event). No vorticity was apparent in any of the black objects observed. Figure 8.4b shows that the areal extent of black objects was distributed around 2 km^2, i.e., below what is resolved by most conventional all-sky cameras. A scatterplot of drift speed versus size, shown in Figure 8.4c, suggests that the smallest objects were typically also the fastest. Object thickness was typically in the range 0.5–1.5 km, and the preferred length appears to have been 2.5–3 km, as shown in Figures 8.4d and 8.4e, respectively. Finally, the distribution of the thickness-to-length ratio is plotted in Figure 8.4f, showing that a $\sim$1:4 ratio was the most common. This was also the

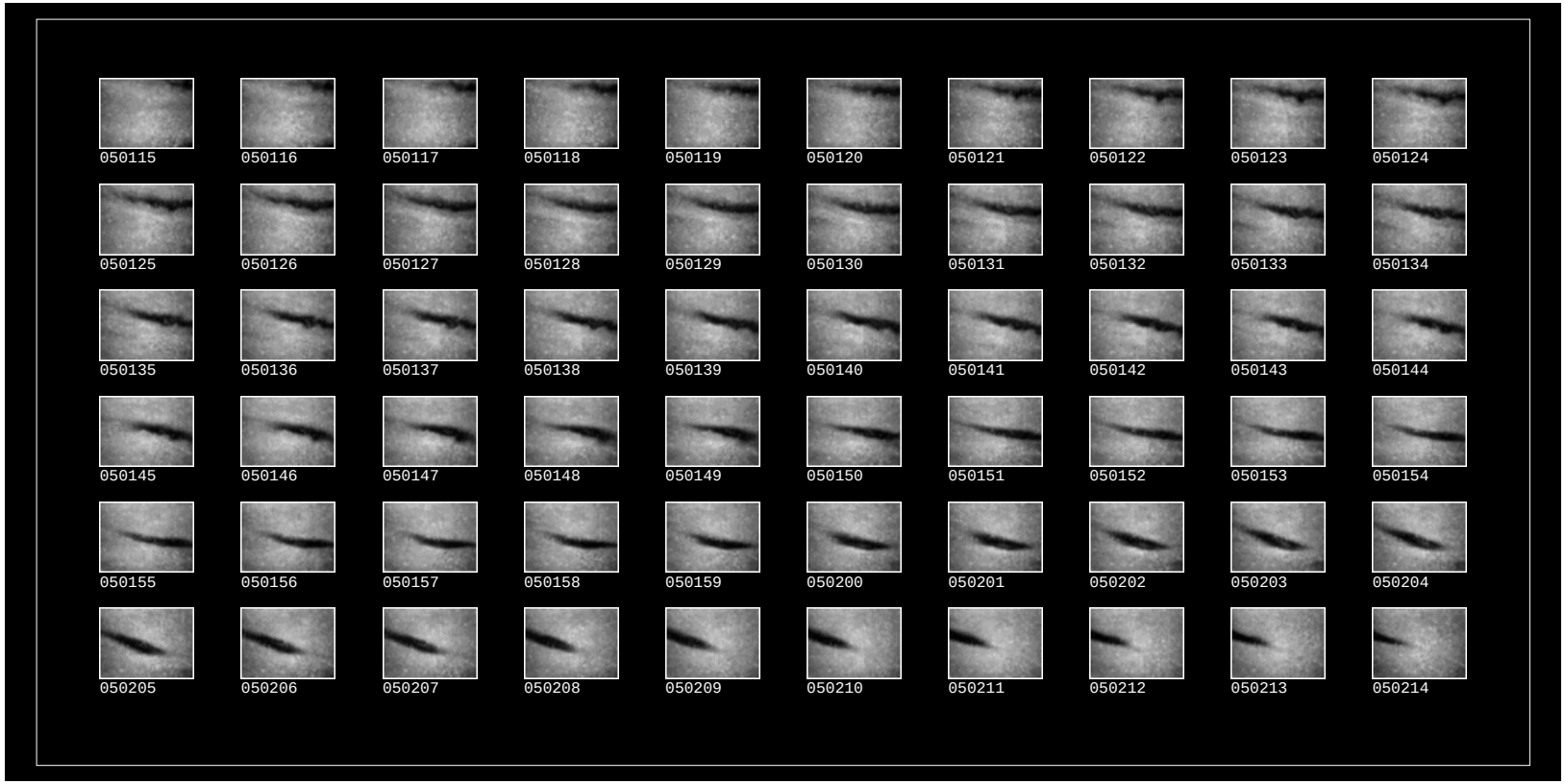

Figure 8.2: Eastward drifting arc segment, March 1, 1995, 0501:15–0502:14 UT. Decreased brightness toward image edges/corners and the faint, near-vertical striations seen in these and some of the following images are due to imager "fixed-pattern" noise that, because of scene dimness, was not successfully removed in the flat-fielding process.

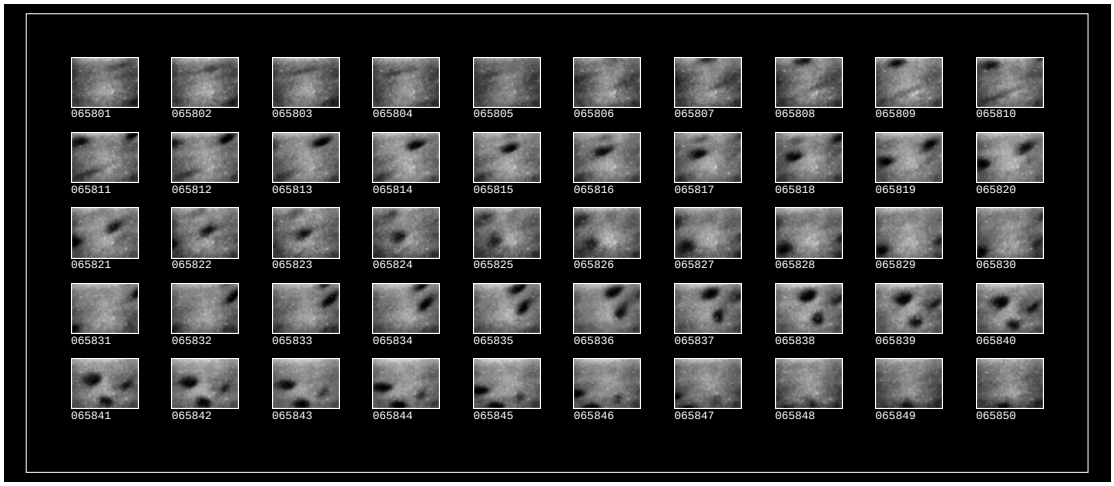

Figure 8.3: Black patches observed on March 3, 1995, 0658:01–0658:50 UT.

Date	Time, UT	Number	$\bar{v}$, km s^{-1}	$\bar{A}$, km^2	$\bar{d}$, km	$\bar{l}$, km
February 28, 1995	0728:55–0731:30	6	1.0 (0.3)	4.5 (1.8)	1.2 (0.3)	5.7 (2.7)
March 1, 1995	0456:10–0504:05	4	0.3 (0.3)	13.7 (3.7)	2.6 (1.2)	8.1 (2.7)
March 3, 1995	0616:05	1	0.6	2.3	1.0	3.0
March 3, 1995	0655:55–0659:45	14	1.4 (0.3)	2.8 (1.8)	1.3 (0.7)	2.7 (0.8)
March 3, 1995	0707:15–0707:25	2	2.7 (0.1)	1.8 (0.1)	0.8 (0.2)	2.7 (0.3)
March 3, 1995	0732:15–0735:25	3	1.6 (0.9)	3.4 (3.6)	0.8 (0.5)	4.8 (2.6)
March 3, 1995	0757:30	1	1.4	3.1	1.2	3.2

Table 8.1: Observed characteristics of seven events of eastward drifting black objects. Columns are date, range of time during which objects constituting the event entered the field of view, the number of objects contained within the event, mean speed $\bar{v}$, mean area $\bar{A}$, mean thickness $\bar{d}$, and mean length $\bar{l}$ of objects within each event. The numbers in parentheses are the sample standard deviations. The assumed altitude is 105 km.

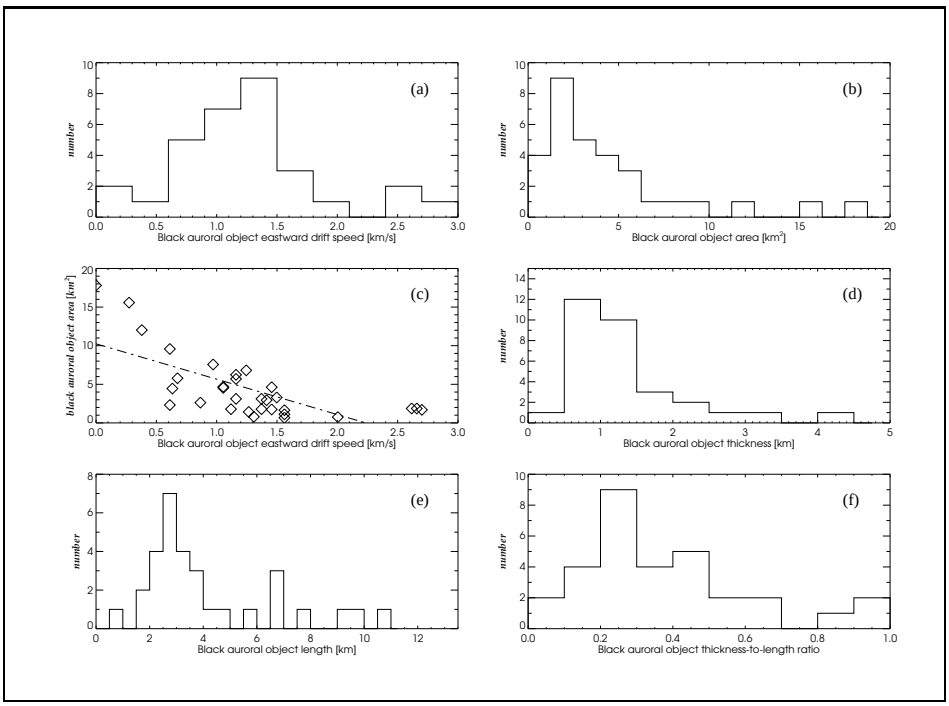

Figure 8.4: (a) Distribution of the drift speed of 31 eastward drifting black patches and arc segments. (b) Distribution of area contained within eastward drifting black objects. (c) Scatterplot of eastward drift speed versus area contained by black object. (d,e) Distribution of the thickness and length, respectively, of eastward drifting black objects. (f) Thickness-to-length ratio of the 31 black objects observed. An altitude of 105 km has been assumed throughout.

thickness-to-length ratio of the event reported by Royrvik [1976].

Instrumental cutoff has been ruled out as the cause of the low-end falloff in the histograms depicting linear extent. The small size of the field of view also imposed no limitation, as there were no signs of eastward drifting black objects having a linear extent comparable to, or larger than, the field of view. The emission originating from dark areas was found to have a magnitude likely consistent with that of continuum airglow and scattered starlight. A contrast with respect to the surrounding diffuse emission of up to 70% was observed.

Less well behaved patches were also encountered, as exemplified in Figure 8.5. This March 1 event started out as a region of decreased emission streaming at an apparent speed of several kilometers per second along what was seemingly some underlying dark arc structure. It rapidly assumed a patch shape and began to drift about more slowly and freely, exhibiting a behavior reminiscent to that of a water-filled balloon, constantly deformed as ripples bounced back and forth along its walls. The patch (or arc segment) eventually drifted off equatorward at a speed of a few hundred meters per second.

Another example of this black streaming phenomenon was seen on February 28 and is depicted in Figure 8.6 with a temporal resolution of 0.5 s. A dark area could be seen propagating roughly equatorward at an apparent speed of about 4 km s^{-1} along what again seemed to be an underlying dark arc structure, until it came to a sudden halt at the bottom of the "V" shape. The resulting patch, seen in the last frame, subsequently

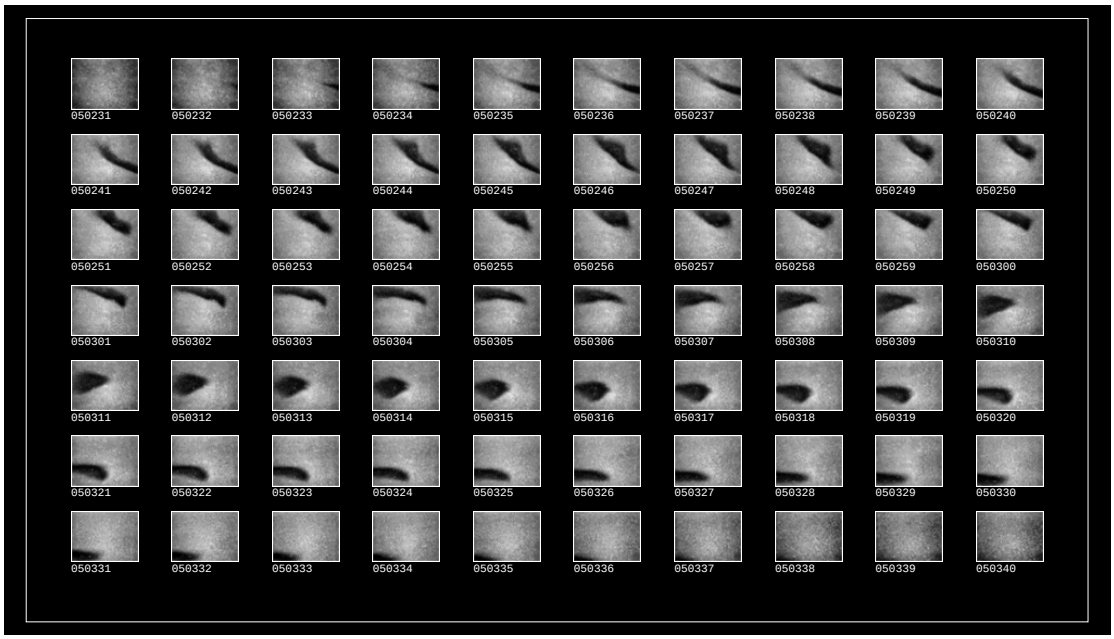

Figure 8.5: Metamorphosing black patch or arc segment, as observed on March 1, 1995, 0502:31–0503:40 UT.

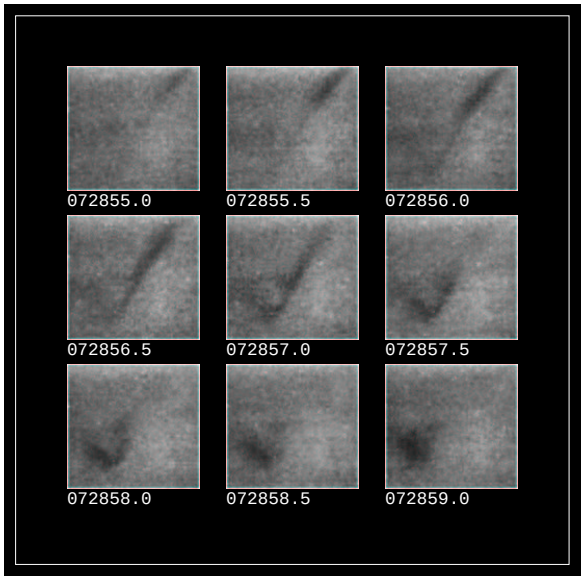

Figure 8.6: Dark region streaming equatorward along underlying dark arc structure, resulting in the formation of a black patch (February 28, 1995, 0728:55–0728:59 UT). The (cropped) field of view is 5.9° by 5.5°.

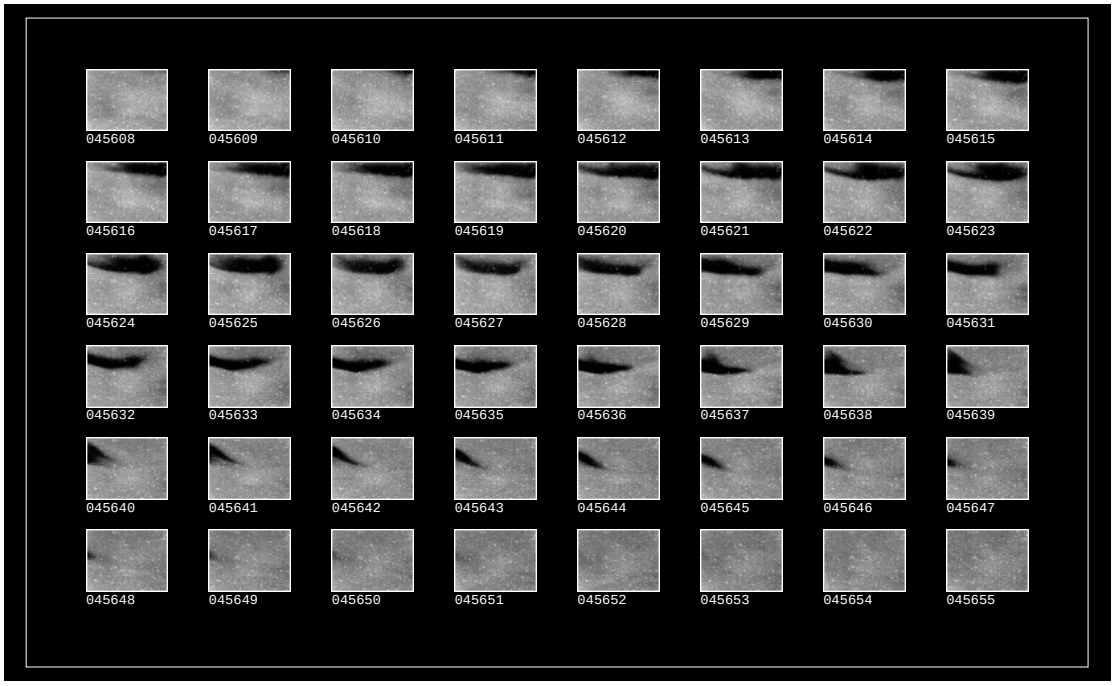

Figure 8.7: Eastward drifting black arc segment seen on March 1, 1995, 0456:08–0456:55 UT.

drifted off toward the northeast, along the opposite arm of the V, at a speed of about 600 m s^{-1}. This change in velocity is particularly impressive when viewed directly from the original videotape.

Figure 8.7 shows a patch or arc segment that drifted slowly in an eastward direction. Its northern and southern edges were sharply defined, while the eastern and western edges were less so, as the object appeared to be associated with an underlying east-west oriented black arc structure. As the patch disappeared out of the field of view, it underwent rapid streaming along this underlying dark arc structure, recognizable as a subtle dark arc spanning almost the entire field of view at about 0456:48 UT.

All patches and arc segments discussed in this section occurred in aurora associated with dual-layer pulsations [Royrvik, 1976]. Figure 8.8 shows an example of such a pulsation which took place on March 3, wherein a foreground diffuse aurora apparently was "switched off," revealing a structured "background" that might itself be called black aurora. The structure in this "background" aurora subsequently faded away. Note the 0.2 s time interval between frames in the figure. This event was followed 45 s later by the series of patches depicted in Figure 8.3. The drift direction of these patches was roughly aligned with the general direction of the discrete features seen during the brief pulsation. No such features could be seen "through" these patches, suggesting that the patches may have been embedded in the "background" aurora. This point will be discussed more fully later.

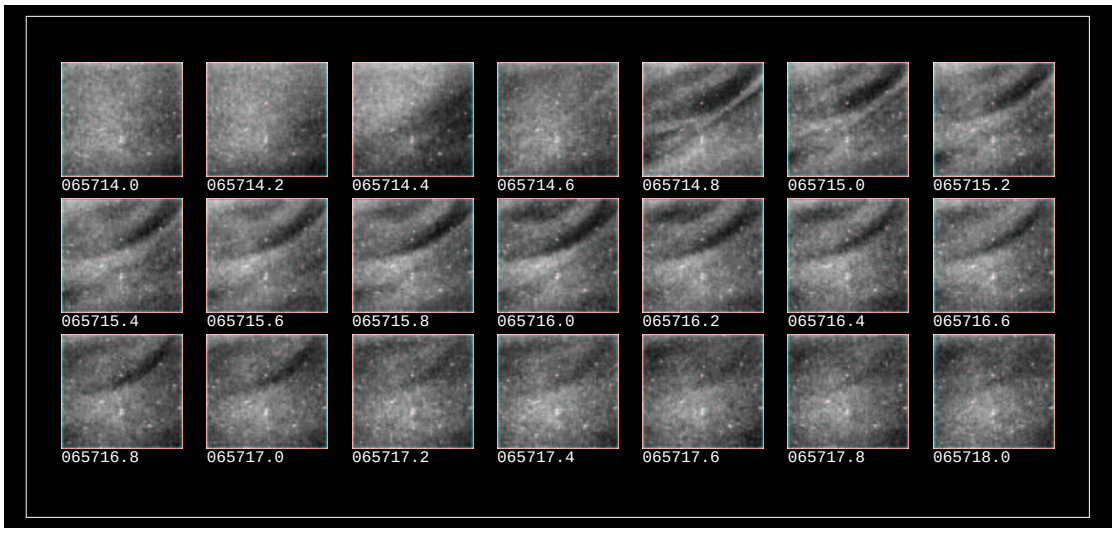

Figure 8.8: Brief dual-layer pulsation observed ∼45 s prior to the event of Figure 8.3 (March 3, 1995, 0657:14–0657:18 UT). The (cropped) field of view is 5.9° by 5.5°. The white spots are stars.

8.2.2 Black Arcs

East-west aligned, often multiple, black arcs were frequently found embedded within the midnight sector diffuse aurora. Examples of such arcs, which typically had an equatorward drift of a few hundred meters per second and occasionally were seen to be pulsating, are found in Figures 8.9a through 8.9h. Figure 8.9i shows a multiple black arc structure that was oriented roughly north-south, presumably due to rotational distortions of east-west aligned black forms. Note that the spacing between ordinary discrete auroral forms, such as the north-south aligned arcs depicted in Figure 8.9j, does not fit the definition of black aurora and is thus not counted as such in this study. Occasionally, limiting cases would occur wherein it became a matter of opinion whether arcs were black arcs on a bright background or bright arcs on a dark background, such as in Figures 8.9g and 8.9h. In Figure 8.9g, only the arc that was considerably darker than the background existing over a broader region is considered black. Figure 8.10 shows an example of narrow-scale multiple black filaments embedded in westward drifting diffuse aurora. Such semiparallel black filaments were frequently observed in westward drifting patches and veils before midnight. The westward drift speed was usually in the range of a few hundred meters per second to more than 1 km s^{-1}.

Arc thickness was estimated for 135 black arcs observed on March 1, March 3, March 4, and March 6. Because of the limited height extent of the surrounding diffuse aurora, observationally defining the arc thickness was a relatively straightforward task. The resulting distribution, seen in Figure 8.11a, indicates a preferred thickness of 400–500 m. The average thickness of these 135 structures was 615 m, comparable to the 740 m average thickness of ordinary (i.e., not black) IBC I/II auroral fine-scale arcs measured by Maggs and Davis [1968]. Note that any error due to the vertical extent of out-of-zenith forms has the effect of increasing the measured width of normal auroras and decreasing the apparent width of black auroras. Instrumental cutoff occurred somewhere in the range 100–200 m, depending on the emission rate of the

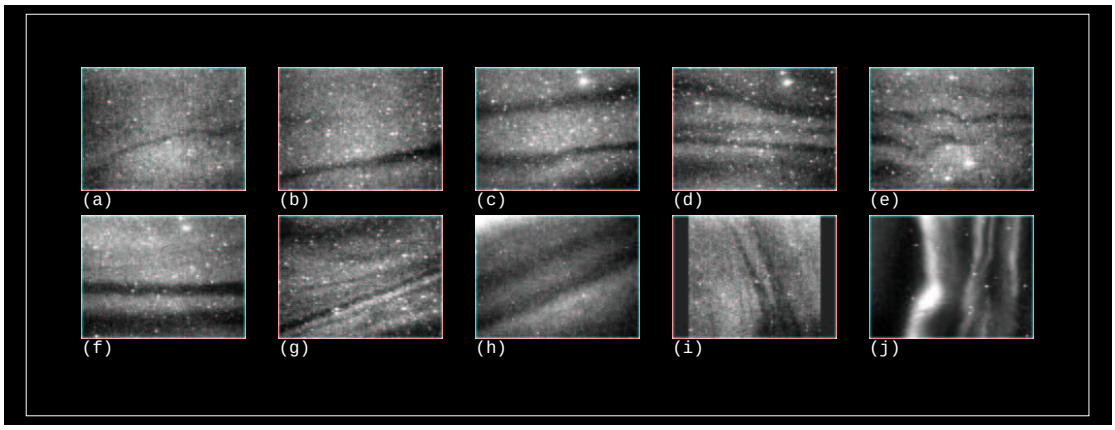

Figure 8.9: (a)–(i) Examples of black auroral arcs. (j) North-south oriented discrete auroral arcs. The gaps between such discrete auroral arcs are not classified as black aurora in this study. The white spots are stars.

surrounding diffuse aurora. The decrease in the number of arcs with thickness less than 400 m thus appears to be real. Because of the limited field of view there was generally no way of determining the length of these arcs.

The spacing between black auroral arcs may provide information on the scale sizes of phenomena leading to such arc formation. The widths of 92 emitting surfaces separating black arcs were measured, and the resulting distribution, relevant in the range ∼200 m to 5 km, is shown in Figure 8.11b. The data are suggestive of a preferred spacing in the range 0.5–1.2 km. The mean spacing was 1 km. Finally, the arc spacing-to-thickness ratio for spacings less than 5 km is plotted in Figure 8.11c. These are distributed on both sides of 1.

In addition to such stable black arcs, more active and transient black auroral arcs were observed. The filamentary black arc structure of Figure 8.12 is a case in point. Observed on March 1, this very dynamic black arc structure was embedded in a westward drifting diffuse auroral surface. Note in particular the presence of cuspidate forms, of which good examples are seen at 0516:56 UT. Adopting the terminology of Oguti [1975] also for the black aurora, one here witnesses the phenomena of arc disruption and reconnection, shear folding, and "folding over." (Similar activity is also seen in Figure 8.10, for example, near 0452:06 UT.) It is interesting to note that the apparent "folding over" observed from 0517:05 UT had a clockwise vorticity, opposite of that exhibited by "folding over" of ordinary auroral forms. Note also the multiple-arc structure seen at around 0517:08 UT. The widths of these black arcs were less than 100 m, and the arc spacings were about 500 m. Fine-scale structures of the order of 100 m are, even in the case of ordinary auroral forms, a still unexplained phenomenon [Borovsky, 1995]. In view of these incredibly small and dynamic features, it is somewhat amazing to discover that from the all-sky camera's perspective, shown in Figure 8.13, the sky is filled with a largely uniform diffuse glow with no discernable dynamics. The uniformity is disrupted only by the presence of some larger-scale black auroral forms appearing a bit south of the PAI's field of view, which is indicated in the frame by a white box. This highlights the point made earlier in Chapter 1 that the classic

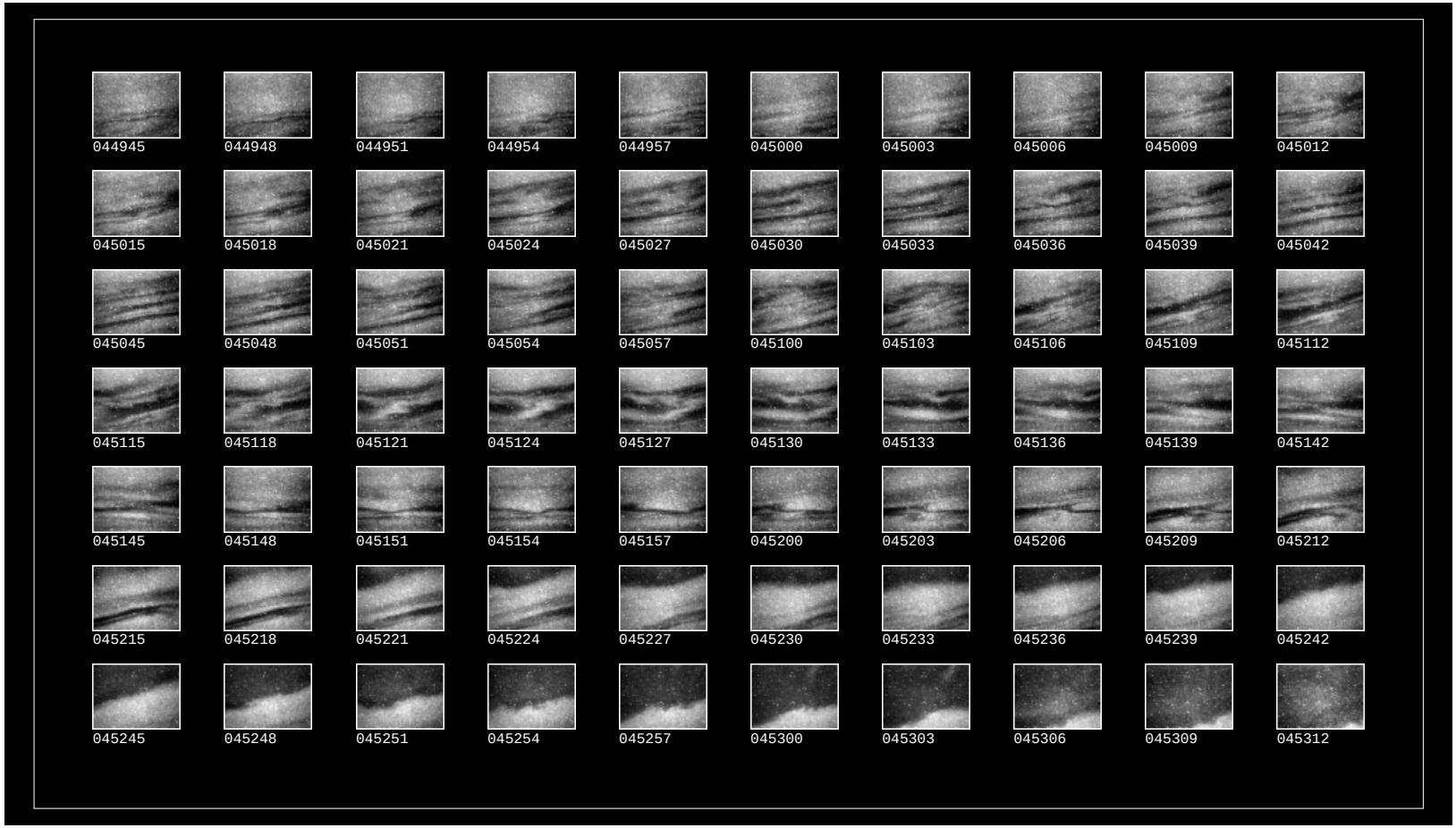

Figure 8.10: Black filamentary arc structures within westward drifting diffuse aurora, observed on March 4, 1995, 0449:45–0453:12 UT. The westward drift speed was $\sim$1 km s^{-1}.

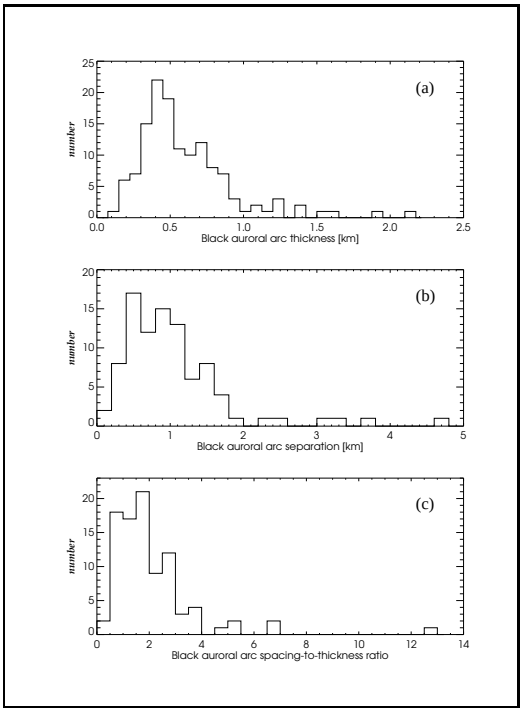

Figure 8.11: (a) Distribution of the thickness of 135 black arcs observed during the field trip. (b) Thickness of 92 emitting diffuse surfaces separating black arcs in the cases of multiple arcs. (c) Black auroral arc spacing-to-thickness ratio. An altitude of 105 km has been assumed.

idea of diffuse *vs.* discrete aurora has to be discarded, or must at least be used with some caution.

8.2.3 Vortex Formation on Black Arcs

Whereas the formation of small-scale ripples along black arcs was observed throughout the campaign, a full development into black vortex street arrays, i.e., black vortices spaced quasi-periodically along a black arc, was a comparatively rare phenomenon. Vortex street arrays have earlier been described by Davis [1978a], who also included the first known television photographs of the phenomenon. Black vortices appear similar to the "curls" described by Hallinan and Davis [1970], except that they show a clockwise rotation as viewed antiparallel to the magnetic field. Davis [1978a] attributed them to the Kelvin-Helmholtz instability acting on a sheet of positive space charge.

On March 6 the evolution of two rather impressive vortex street arrays were observed, as shown in Figures 8.14 through 8.17. The event depicted in Figure 8.14 took place within relatively homogeneous IBC I aurora. A vortex street structure was seen around 0559:28 UT, but individual vortices were not properly resolved, presumably because of a considerable height extent of emissions combined with an off-zenith observation angle. The presence of auroral rays diverging away from the vortices may be an indication that the vortex street array was located at a very high altitude. These vortices subsequently died away, and the black arc drifted equatorward. As this 700-m-thick black arc entered magnetic zenith, new vortices started forming,

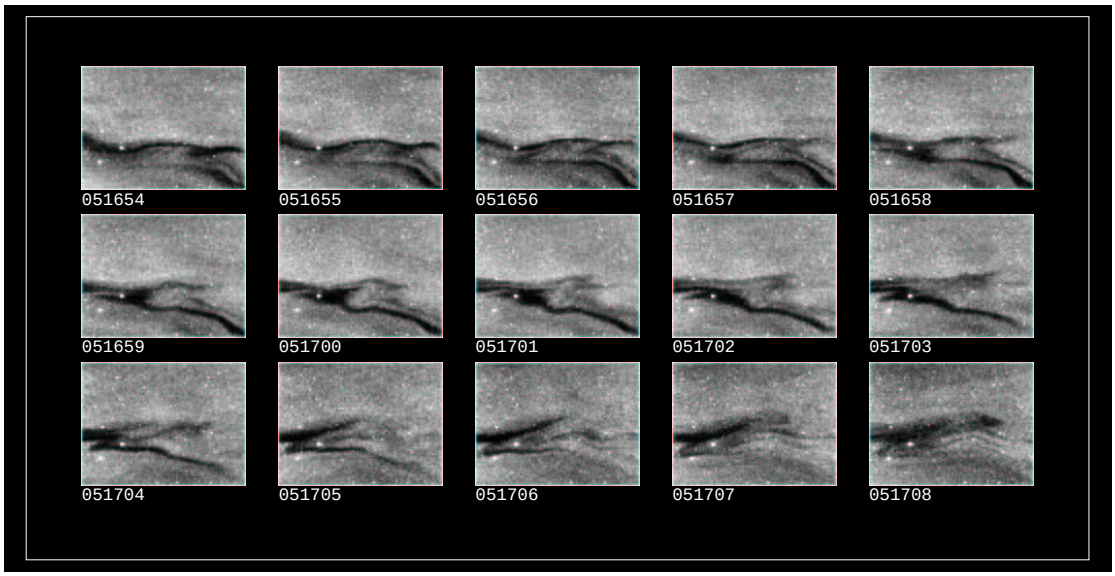

Figure 8.12: Dynamic filamentary black arcs observed on March 1, 1995, 0516:54–0517:08 UT.

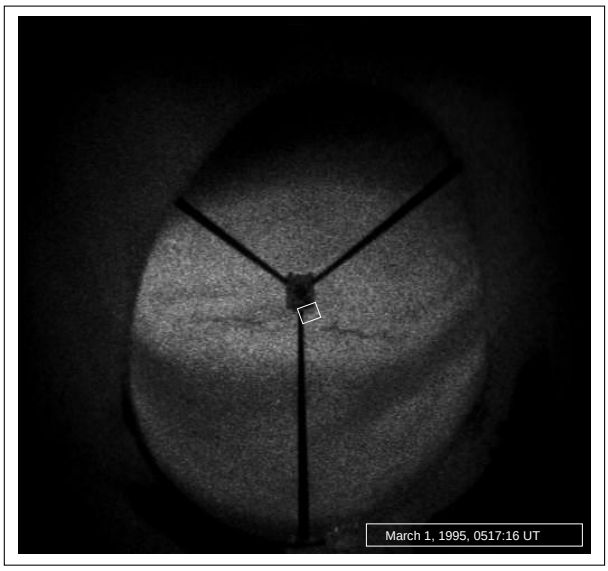

Figure 8.13: All-sky camera view (557.7 nm) of the scene of Figure 8.12. The field of view in that figure is indicated here by a white box. *All-sky footage is courtesy of the Institute of Space and Atmospheric Studies, University of Saskatchewan.*

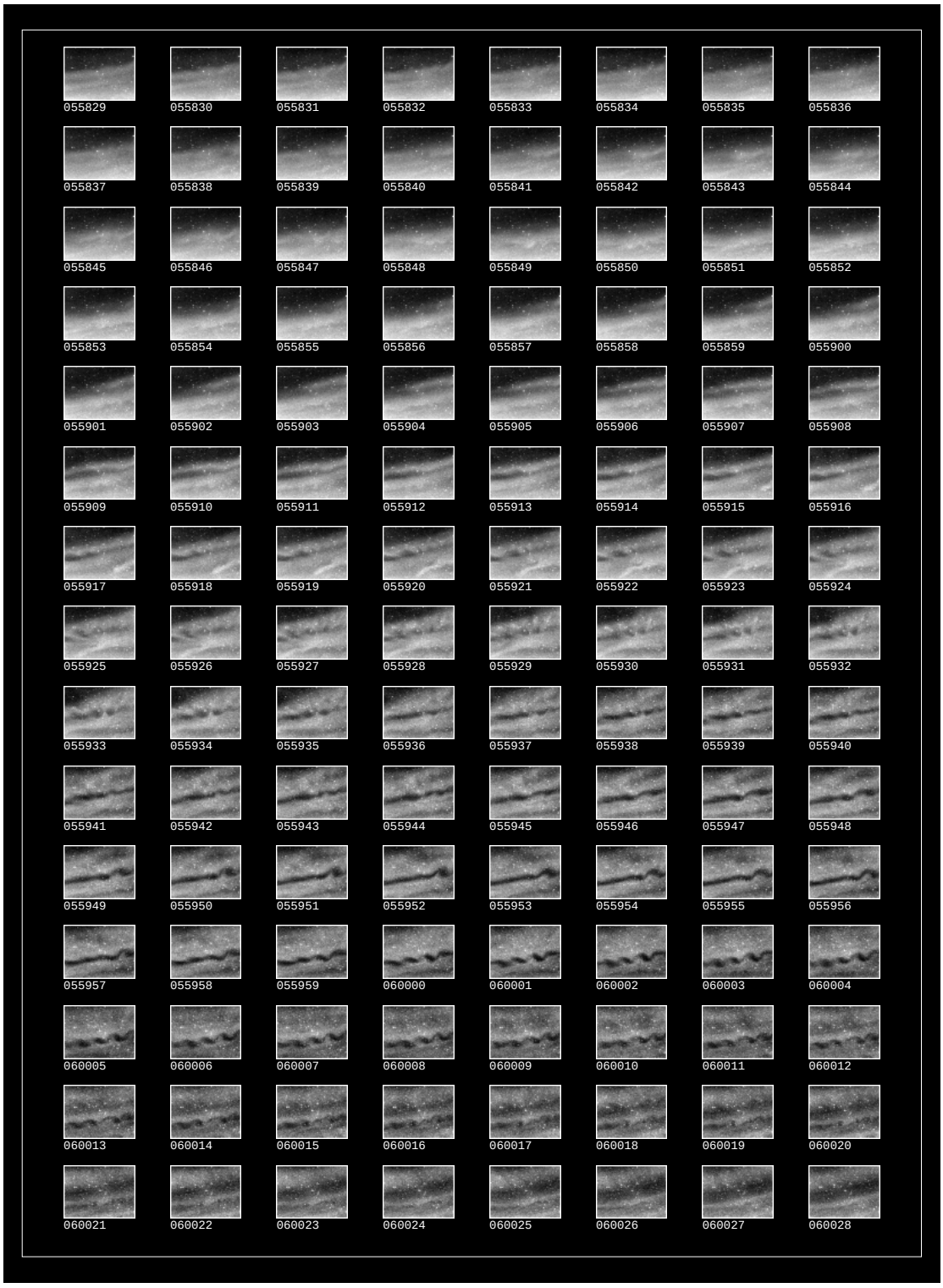

Figure 8.14: Vortex street arrays observed March 6, 1995, 0558:29–0600:28 UT.

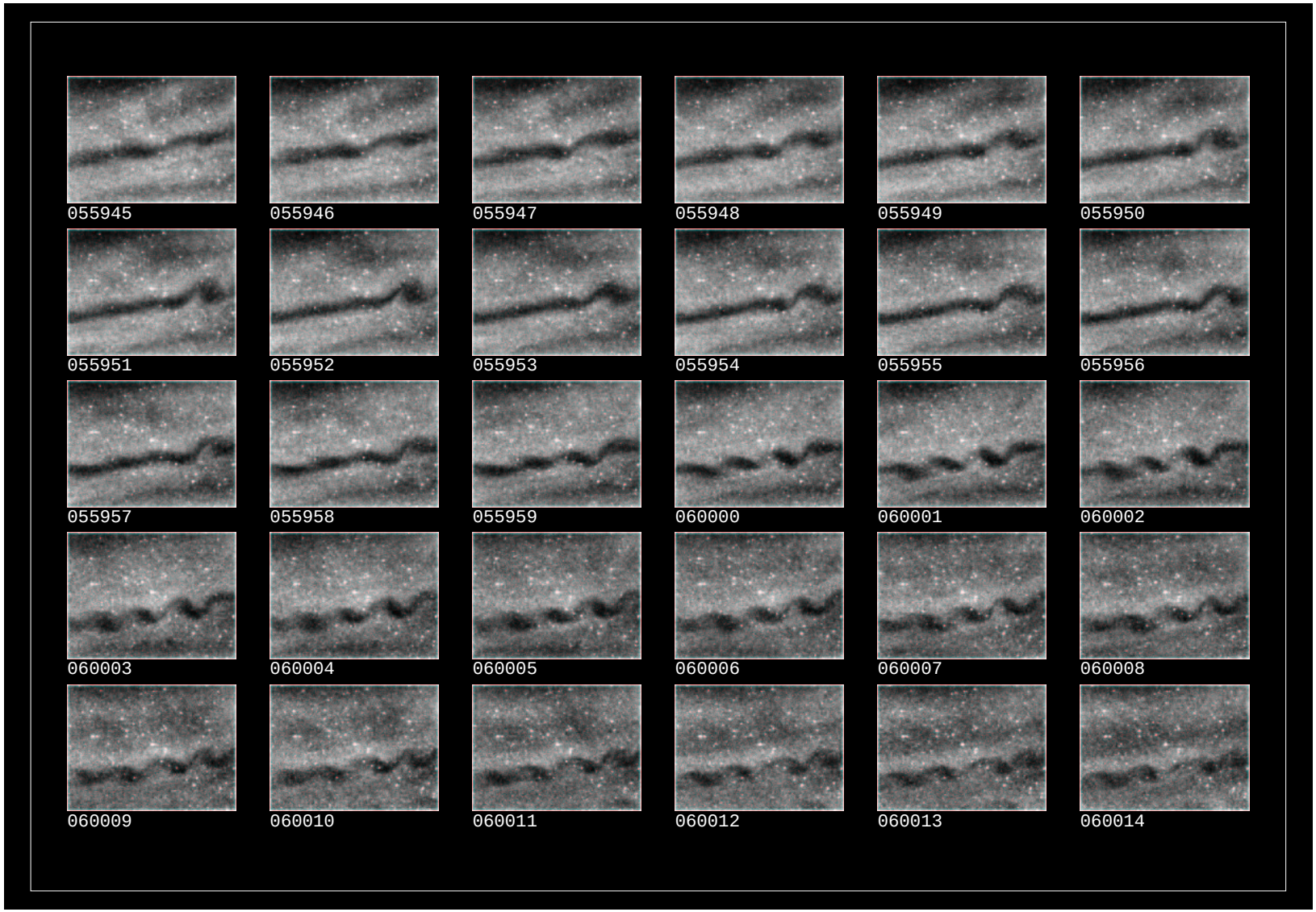

Figure 8.15: Portion of Figure 8.14 reproduced in greater spatial detail.

as seen in Figure 8.14 from about 0559:58 UT and shown again in greater spatial detail in Figure 8.15. This event did not appear to be subject to the perspective effect of the event that occurred 30 s prior, nor was it accompanied by auroral rays. The vortex street array drifted westward at an apparent speed of $\sim$300 m s^{-1}, and the vortex pitch ("wavelength") was about 3.3 km. If the vortices are considered elliptically shaped, they can be described as having a major axis dimension of 1.8 km and a minor axis dimension of 1.2 km. Vortices were seen in this case to have extremely long lifetimes in comparison with the highly transient auroral "curls" of Hallinan and Davis [1970], which are the topic of Chapter 10. Note the presence of a second black arc adjacent to, and equatorward of, this black arc. As can be seen around 0559:50 UT, this faint arc also showed evidence of vortex activity. Careful examination of the original videotape reveals that this black vortex was traveling eastward. If these two parallel black arcs are assumed to comprise one multiple black arc containing two vortex systems of oppositely directed velocities, the motions turn out to be clockwise with respect to the center of the multiple arc. This finding is in contrast to the case of auroral "curls," in which the motions are, without observed exception, counterclockwise with respect to the center of the multiple arc [Hallinan and Davis, 1970]. The scenario of Figure 8.14 is seen in context in the all-sky camera image of Figure 8.19a. The white box indicates the narrow field of view of Figure 8.14. The vortex street, not properly resolved by the all-sky camera, is seen to occur at the very poleward edge of the auroral distribution. This was indeed found to be a common location of black vortex streets. They were thus also normally found poleward of the region of the eastward traveling black objects described earlier.

Figure 8.16 depicts an event that took place in postbreakup diffuse aurora, 1 hour 20 min prior to the above event. Again we observe the clockwise rotational sense consistently seen in black auroral vortices. In this case the vortex street array drifted eastward at a speed of about 850 m s^{-1}, with a wavelength of about 3.6 km and physical dimensions similar to those of the above mentioned event. Bright discrete flickering features were observed shortly before and after this event, and auroral rays were seen propagating eastward along the edge of the northern slab of diffuse aurora immediately prior to the formation of vortices. The equatorward emitting surface was in this case considerably brighter than the poleward one, and vortices were seen to be fairly distorted (see, Figure 8.17) in comparison with the near "picture-perfect" vortices of Figure 8.15. Just as in the case of the event of Figure 8.14, this event was found at the poleward edge of the auroral distribution.

Further, three extremely transient examples were observed on March 4 between 0600 and 0700 UT (not shown), within diffuse aurora exhibiting considerable shearing behavior. Wavelengths were about 2.5 km, and vortices were roughly circular with diameters of $\sim$1 km. Vortex street lifetimes were in these cases only a few seconds.

Finally, Figure 8.18 shows the formation of black vortices at the interface between bright and diffuse discrete[1] aurora during breakup. The bright arc seen in the figure actually comprised two discrete auroral arcs of considerable height extent seen at an off-zenith angle. Auroral "curls" were moving rapidly along these two adjacent arcs, motions being counterclockwise with respect to the center of the multiple

[1] This terminology is described at the end of Chapter 1.

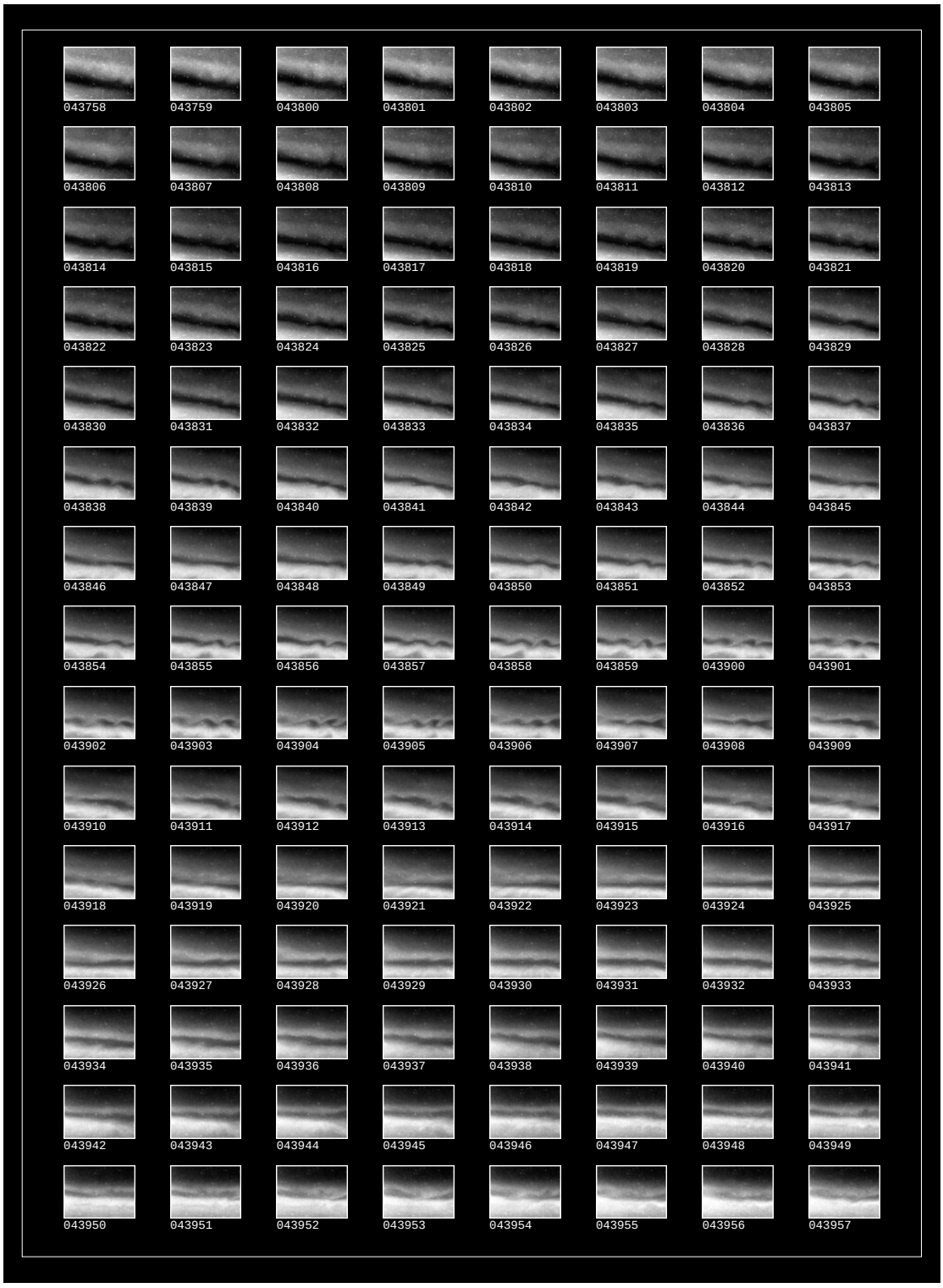

Figure 8.16: Vortex street array observed March 6, 1995, 0437:58–0439:57 UT.

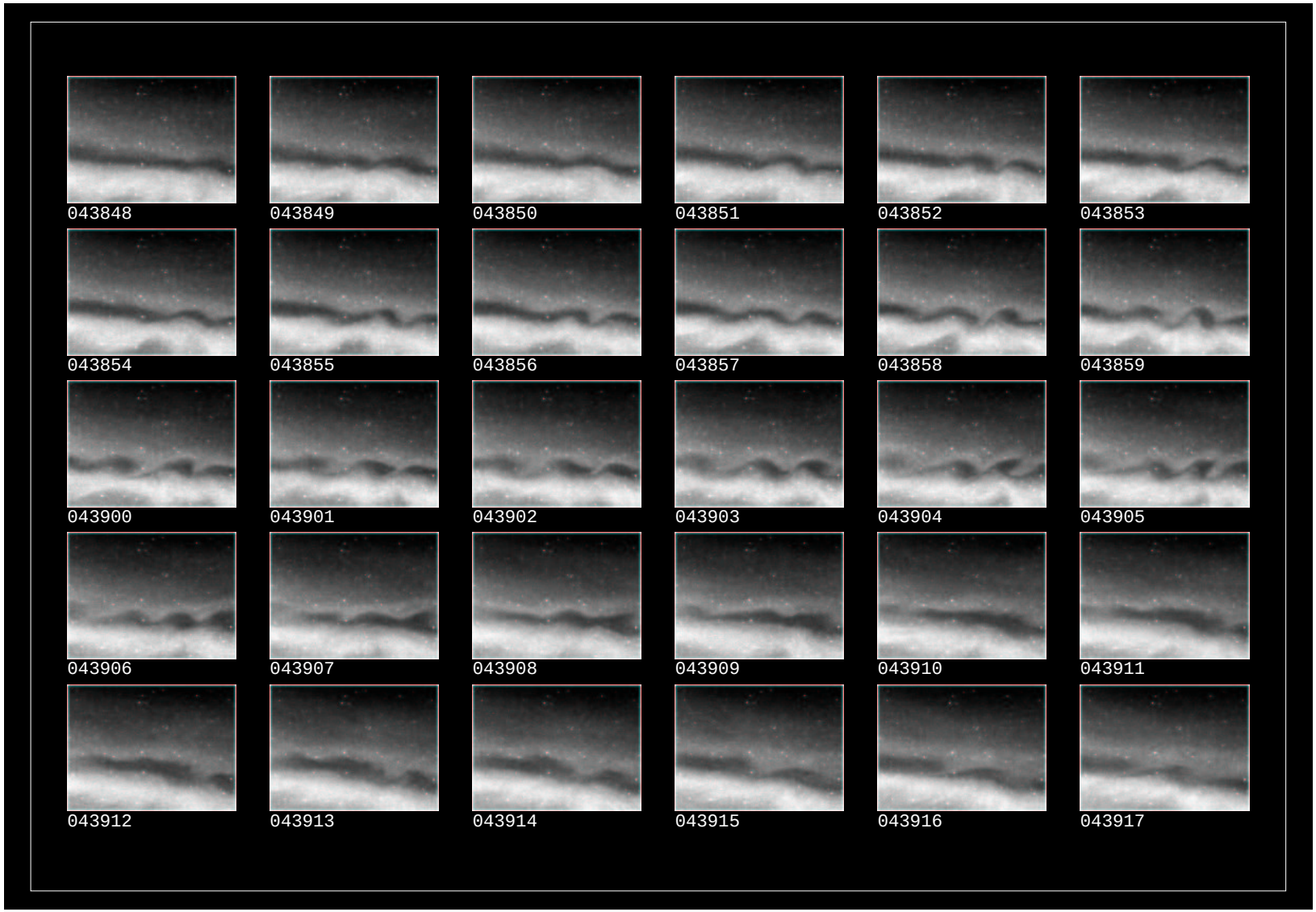

Figure 8.17: Portion of Figure 8.16 reproduced in greater spatial detail.

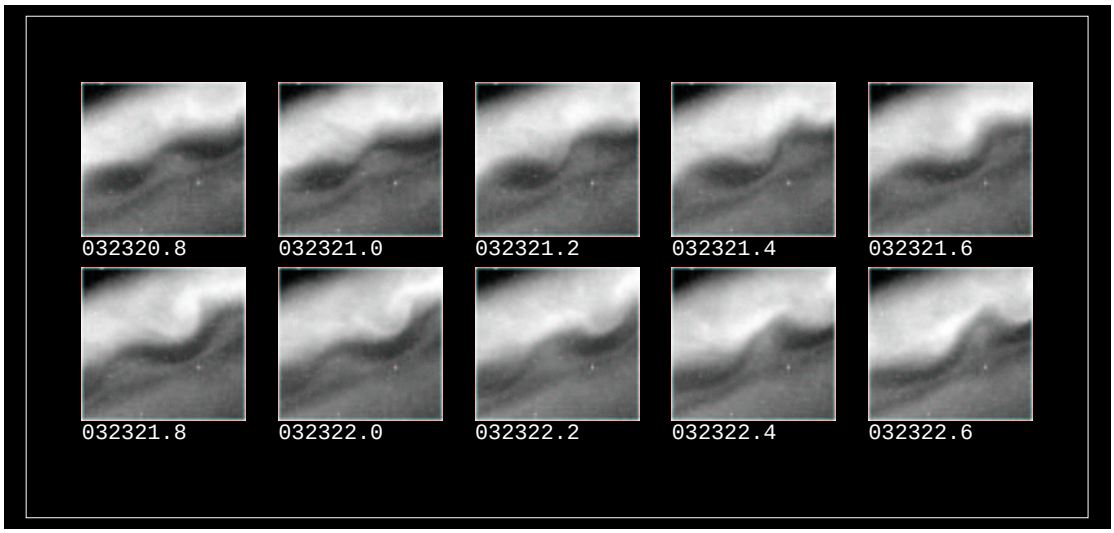

Figure 8.18: Black vortex formation at the interface between discrete and diffuse aurora during auroral breakup, seen on March 1, 1995, at around 0323:22 UT. The temporal resolution is 0.2 s, and the (cropped) field of view is 5.9° by 5.5°.

Date	Time, UT	λ, km	Major Axis, km	Minor Axis, km	Velocity
March 6, 1995	0600:02	3.3	1.8	1.2	$\sim$0.3 km s^{-1} W
March 6, 1995	0559:29	2.5	...	...	$\sim$no drift
March 6, 1995	0439:06	3.6	1.9	0.8	$\sim$0.85 km s^{-1} E
March 4, 1995	0648:00	2.5	1.0	0.5	$\sim$1.5 km s^{-1} W
March 4, 1995	0645:40	2.7	1.3	0.6	$\sim$no drift
March 4, 1995	0603:15	2.3	1.0	1.0	$\sim$5.0 km s^{-1} E
March 1, 1995	0323:21	6.0	3.6	1.8	$\sim$4.0 km s^{-1} W

Table 8.2: Observed characteristics of black vortices. Columns are date, time, vortex pitch, vortex dimensions (major and minor axis lengths, assuming an elliptical shape), and vortex street array drift velocity.

discrete arc. The diffuse aurora appeared as parallel diffuse arcs immediately equatorward of the active bright arcs prior to vortex formation (see, Figure 8.9h). A logarithmic intensity mapping had to be performed on these images to be able to show both the bright and the diffuse forms. The actual difference in brightness between the more active and the diffuse aurora was thus much greater than what is conveyed by the figure. The event is seen in a wider context in the all-sky camera image of Figure 8.19b, where the white box indicates the smaller field of view. Note that the two counterstreaming bright arcs appear to the all-sky camera as one contiguous bright arc across zenith. Table 8.2 summarizes some of the physical characteristics of the black vortex street arrays observed during the campaign.

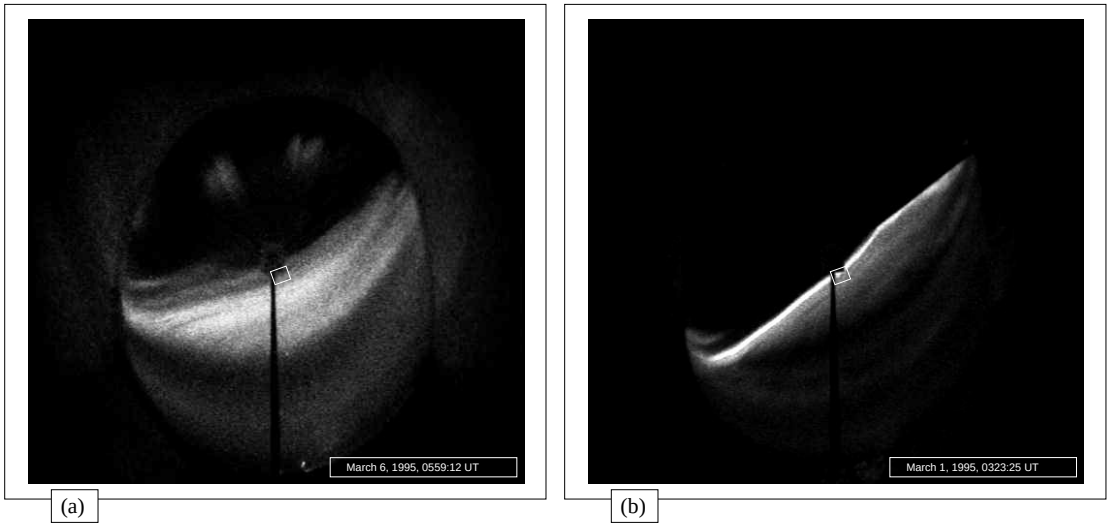

Figure 8.19: (a) All-sky camera view (557.7 nm) of the scene of Figure 8.14. (b) All-sky camera view (557.7 nm) of the scene of Figure 8.18. The much narrower field of view of the PAI is indicated by a white box in the images. *All-sky footage is courtesy of the Institute of Space and Atmospheric Studies, University of Saskatchewan.*

8.3 Discussion

Black aurora appears to be a common feature of the midnight sector during the recovery phase. Black auroral arcs are seen to form vortices with a rotational sense opposite that of "curls" in bright auroral arcs, generally thought to be associated with an excess of negative space charge. This fact, combined with the small scale size of many black auroral forms ($<$1 km) and the gyroradius of protons ($\sim$100 m), suggests that the corresponding geomagnetic flux tube may contain an excess of positive charge, as was also pointed out by Royrvik [1976].

The frequently observed phenomenon of dual-layer pulsations involves two apparently overlapping groups of aurora, comprising a pulsating auroral patch or veil superimposed on a diffuse background that sometimes develops internal structure. Whenever it was possible to determine the drift vector of the background, its major component was found to be directed eastward, i.e., opposite that of the premidnight foreground. This finding agrees with the results of Royrvik and Davis [1977], who found the drift in the background portion of dual-layer pulsating aurora to always be toward the east. This pattern is suggestive of a close connection between such background aurora and eastward drifting patches and arc segments. Note that in most cases, dual-layer pulsations did not occur simultaneously with the passage of black objects through the field of view, making it virtually impossible to determine explicitly whether a black object was embedded in the background or foreground layer.

Forms existing in a state intermediate between that of a black arc and an eastward drifting string of black patches were observed on a few occasions in the background region during foreground "off" states, suggesting a connection between black patches, black arc segments, and black arcs. This is further supported

by the above mentioned observations of patches and arc segments tied to underlying dark arc structures, as well as by Royrvik [1976], who observed eastward drifting black patches "interconnecting" to form east-west aligned black bands. (Note the analogy to ordinary aurora, where pulsating arcs are often seen to be formed by a recombination of patches and arc segments in the late recovery phase of an auroral substorm.) In comparing the histograms of Figure 8.4d and Figure 8.11a, however, it appears that black arcs tended to be somewhat thinner than black patches and arc segments.

The premidnight diffuse auroral oval thus appears to be caused not only by westward drifting, often pulsating, auroral patches, veils, and arc segments, but also by a diffuse background emission that sometimes develops an internal structure exhibiting eastward drift. These two kinds of auroras, corresponding to the foreground and background layers, may be caused by unrelated precipitation mechanisms, resulting in particles of different energy and thus in different altitudes of emission. Triangulation of discrete features has indicated that the altitude of the foreground emission is in the range 90–107 km and that the background emission may be somewhere in the range 120–240 km [Brown et al., 1976; Royrvik and Davis, 1977; Davis, 1978a; Stenbaek-Nielsen and Hallinan, 1979]. Because it is clearly impossible to determine the altitude of emission in each case, a 105 km altitude has been assumed throughout. Derived linear dimensions and drift speeds therefore may be seriously underestimated, especially in the case of eastward drifting black patches and arc segments, if indeed these are located in the background emission. In the case of black arcs and vortices, estimated quantities may be more realistic, as these typically were found embedded in the lower-altitude, typically westward drifting, foreground emission.

Throughout the campaign, auroral patches, veils, and arc segments were seen drifting westward in the dusk sectors with a typical speed of $\sim$1 km s^{-1}, except for brief periods during which the drift reversed due to the development of a large-scale (counterclockwise) vorticity within the diffuse aurora. In an earlier study of auroral patches and arc segments at Rabbit Lake, La Ronge, and Park Site [Nakamura and Oguti, 1987] it was concluded that the drift of such auroral structures was due to convection electric fields in the magnetosphere. Velocities in that study were found to be in the range 50–2,000 m s^{-1}, drifts being westward in the dusk sectors and switching to an eastward drift at local midnight.

The drift velocity of black patches and arc segments measured in this work has a magnitude comparable to that associated with ordinary aurora subject to convection drift but is oppositely directed. There were never any indications that these eastward drifts were due simply to temporary drift reversals associated with large-scale vorticities. Significantly, no westward drifting black patches and arc segments were observed. By using simultaneous all-sky camera observations, it was established that the eastward drifting black objects often resided somewhat poleward of, or overlapped with, the main (strictly westward drifting, diffuse, often pulsating) auroral distribution.

In many ways the black aurora is analogous to a negative of normal aurora. Further studies of the black aurora therefore may provide a fresh new approach to unlocking some of the mysteries pertaining to the surrounding diffuse emission. Clearly, coordinated efforts of ground-based and space-based instrumentation are required for a fuller insight into the phenomenon.

Chapter 9

Asymmetric Multiple Auroral Arcs

High-resolution optical observations by the Portable Auroral Imager show a frequent occurrence of asymmetric multiple small-scale auroral arc structures during auroral substorms. Whereas the classical multiple arc array tends to exhibit a fairly symmetrical configuration, with parallel motions within individual discrete arcs being opposite in direction across the center of the arc array, the multiple arcs to be discussed herein are distinguished by the presence of discrete arcs strictly equatorward of the two bright counter-streaming arcs that would ordinarily define the center of the arc array. The intensity of these parallel equatorward-lying arcs were in most cases found to decrease rapidly in the equatorward direction. By considering the topology of the structures and the spacing between arcs, observations are found to be consistent with recent theories suggesting inertial Alfvén waves as a possible cause of fine-scale auroral arcs. Nevertheless, a number of other mechanisms are plausible, some of which are briefly touched upon in the discussion section.

9.1 Introduction

There are a number of spatial scales associated with the latitudinal extent of visible auroral phenomena. The spatial scale of the phenomenon to be discussed herein corresponds to that of the "small-scale arcs" of Hallinan and Davis [1970], also termed "breakup arcs" by Goertz [1981]. This is the smallest-known spatial scale in the visible aurora, on the order of 100 m—resolved only by a high-resolution imager carefully aligned to the direction of the local magnetic field. Remarkably, auroral fine-scale structures are still largely unexplained [Borovsky, 1995].

Fine-scale auroral arcs frequently appear as closely-spaced arrays, or multiple arc systems. The dynamical characteristics of the thin linear structures involved suggest that the name "arc" be applied to the thinnest features observed and the name "multiple arc" to an observed ensemble, a practice already observed by Carl Störmer many years ago. When the individual arcs comprising a multiple arc exhibit sufficient internal structure to allow imaging instrumentation to detect parallel motions, such motions are invariably found to be opposite in direction across the center of the arc array, with drifts being westward south of the

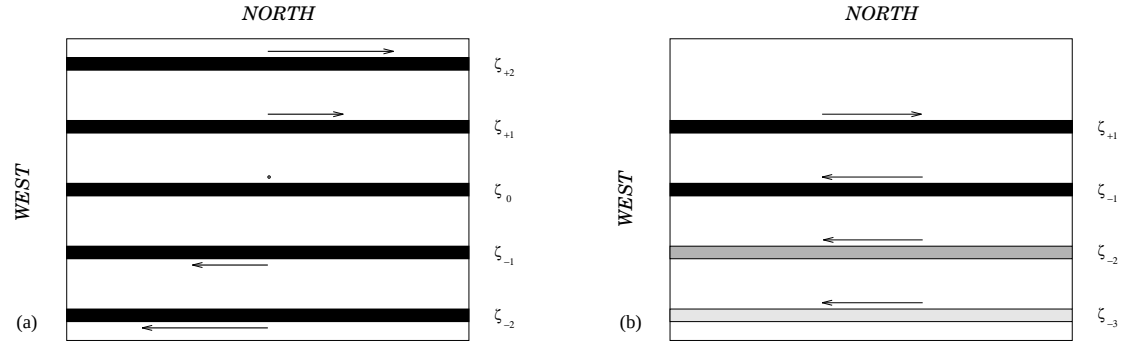

Figure 9.1: (a) The relative motion between closely spaced auroral arcs comprising the "classic" multiple arc as seen looking parallel to the magnetic field [Davis, 1978a]. (b) The configuration and relative motion of the asymmetric multiple arc events discussed in this chapter.

multiple arc center and eastward north of the center. Figure 9.1a (after Davis [1978a]) depicts this symmetric situation. For convenience, a labeling scheme for the discrete arcs comprising a multiple arc system has here been introduced. The greek letter *zeta* (ζ) is used, with arcs north of the multiple arc center labeled using positive subscripts (ζ_{+1}, ζ_{+2}, ...), subscript increasing in value in the poleward direction. Similarly, negative subscripts of ζ denote arcs south of the center (ζ_{-1}, ζ_{-2}, ...), the absolute value of the subscript increasing in the equatorward direction. The middle arc in the figure of Davis [1978a]—the arc with no apparent internal drift motion—is here named ζ_0.

During winter 1995 and 1997 field trips to Rabbit Lake, the Portable Auroral Imager observed during substorms several instances of a highly asymmetric version of the above described "classic" multiple arc system. The common feature of these asymmetric systems was the absence of arc ζ_0 as well as all arcs north of ζ_{+1}, typically accompanied by a decrease in arc emission rates away from ζ_{-1} in the equatorward direction. Arcs equatorward of ζ_{-1} will hereafter be referred to as "secondary arcs," without necessarily having made any inferences as to their origin or relationship to the "primary arcs," ζ_{+1} and ζ_{-1}. The situation is illustrated in Figure 9.1b. It is considered significant that the opposite configuration, i.e., secondary arcs occurring on the poleward side instead of on the equatorward side, never was observed. The study of such arc systems may provide information about how energy is transferred to auroral electrons. Further, the separation of arcs within multiple arcs may provide a lower limit on how close the source regions may be. Some characteristics of the observed systems will be reviewed, and possible causative mechanisms will be considered.

The PAI's primary field of view during the campaigns considered here was 7.4° by 5.5°, yielding a spatial resolution of somewhat better than 100 m at 105 km altitude. No optical filtering was performed. As before, an altitude of auroral emissions of 105 km will be assumed throughout.

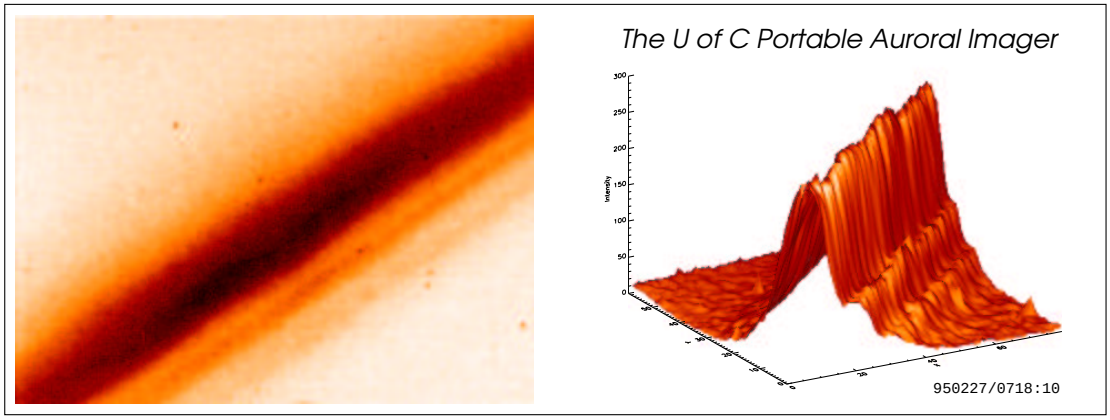

Figure 9.2: Asymmetric multiple arc event. Secondary arcs occur on the equatorward side only. The dark spots are stars; pseudo-colors have been added. The right hand side of the panel shows the event in a representation wherein the relative image intensity is plotted along the vertical axis.

9.2 Observations

Figure 9.2 shows an example of an asymmetric multiple arc system event. This particular event was observed on February 27, 1995, at 0718 UT. The arc system was roughly geomagnetic east-west aligned, with secondary arcs on the equatorward side. The wide northernmost "arc" seen in the picture is in actual fact the counter-streaming arcs ζ_{+1} and ζ_{-1}, both of considerable height extent, seen at an off-zenith observation angle. This is evident from viewing the original video footage. In this particular case, secondary arcs out to ζ_{-3} were seen. These secondary arcs appeared to have a more limited height extent than $\zeta_{+1}-\zeta_{-1}$, a trait common to all observed events. Figure 9.3a shows an all-sky camera image of the same event. The PAI's field of view is indicated with a white box. Note that the all-sky camera cannot resolve the two counterstreaming bands comprising this seemingly single, very long and thin, bright auroral band stretching across the zenith. Figure 9.3b shows the same impressive band, as it appeared 40 s later. Asymmetric auroral arcs appeared to be associated mainly with such very bright discrete arcs or bands.

Table 9.1 lists some characteristics of the 22 such asymmetric multiple arc events that were observed. Note that all events were fairly transient, as the multiple arc configuration would exist for only 5–30 s before it would break down or evanesce.

The column labeled *n* indicates the subscript of the southernmost arc of the event (ζ_n). It is possible that in some cases the finite extent of the field of view was a factor in limiting the number of secondary arcs that could be counted. The imager's restricted ability to resolve discrete features under low-contrast conditions ($\sim$1 kR features on an airglow background) may also have constituted a limitation.

The next column shows the spacing between arcs within each observed multiple arc system. The counter-streaming curtains ζ_{+1} and ζ_{-1} were usually subject to fairly violent motions involving the formation of "curls" [Hallinan and Davis, 1970] along arcs, making the measurement of arc separations and widths difficult. Measuring the distances between ζ_{-2}, ζ_{-3}, and ζ_{-4}, as they drifted through the magnetic zenith,

Date	Time, UT	*n*	Spacing, km	Width, m	Perp. speed, m s^{-1}	Par. speed, km s^{-1}
February 27, 1995	0615	-3	1.0	350	0	30
February 27, 1995	0718	-3	1.0	370	250	30
February 28, 1995	0355	-3	1.6	600	0	10
March 1, 1995	0321	-3	1.6	750	320	···
March 1, 1995	0323	-4	2.5	1100	270	···
March 1, 1995	0323	-4	1.6	700	270	20
March 1, 1995	0413	-3	1.2	460	0	···
March 4, 1995	0602	-3	2.0	700	270	10
March 6, 1995	0402	-3	1.6	550	0	···
March 6, 1995	0402	-3	0.9	350	0	···
March 6, 1995	0444	-2	2.0	800	0	···
March 6, 1995	0531	-3	2.0	780	430	···
March 6, 1997	0317	-3	1.1	530	0	20
March 6, 1997	0324	-4	1.1	490	1700	10
March 6, 1997	0523	-6	1.0	610	0	70
March 6, 1997	0546	-3	1.8	530	1800	···
March 6, 1997	0547	-3	1.4	510	1600	5
March 7, 1997	0602	-2	1.1	510	1000	15
March 12, 1997	0600	-5	1.2	530	550	···
March 12, 1997	0605	-4	1.1	540	870	5
March 15, 1997	0710	-3	2.4	1300	1400	15
March 15, 1997	0730	-3	1.3	710	0	20

Table 9.1: Observed characteristics of 22 asymmetric multiple arc events. Columns are date, time, the ζ-index *n* (see text) of the southernmost arc of the event, arc spacing, approximate arc width, the equatorward drift speed of the arc system, and the parallel drift speed of features embedded within main arcs.

was more easily accomplished owing to less spatial distortions. Secondary arcs appeared evenly spaced within each event, the measured distances constituting column four of Table 9.1. The resulting histogram is shown in Figure 9.4a. The mean value was 1.5 km. Whenever it was possible to estimate the distance between the secondary arc ζ_{-2} and the distorted main arc ζ_{-1}, it was found to be somewhat larger than the distance between secondary arcs.

Secondary arcs within each event all appeared to have similar widths. The fifth column of Table 9.1 lists the measured widths of such arcs as seen in, or near, the magnetic zenith. These were obtained by measuring the approximate linear widths of ζ_{-2} and/or ζ_{-3} on high-resolution hardcopies of digitized video frames. A more rigorous definition of arc widths, e.g., by fitting to Gaussian intensity profiles, was generally not possible because of low emission rates and the resulting adverse signal to noise ratio. The tabulated values should thus be taken as estimates only. These are presented in the form of a histogram in Figure 9.4b. The mean secondary arc width was about 650 m. Although it was hard to define the widths of main arcs, the general impression was that these were broader in extent than secondary arcs.

The quantity in the sixth column of Table 9.1 is the estimated perpendicular (equatorward) speed of the multiple arc system ($\zeta_{+1}-\zeta_{-1}$) relative to the camera field of view. The average speed was about

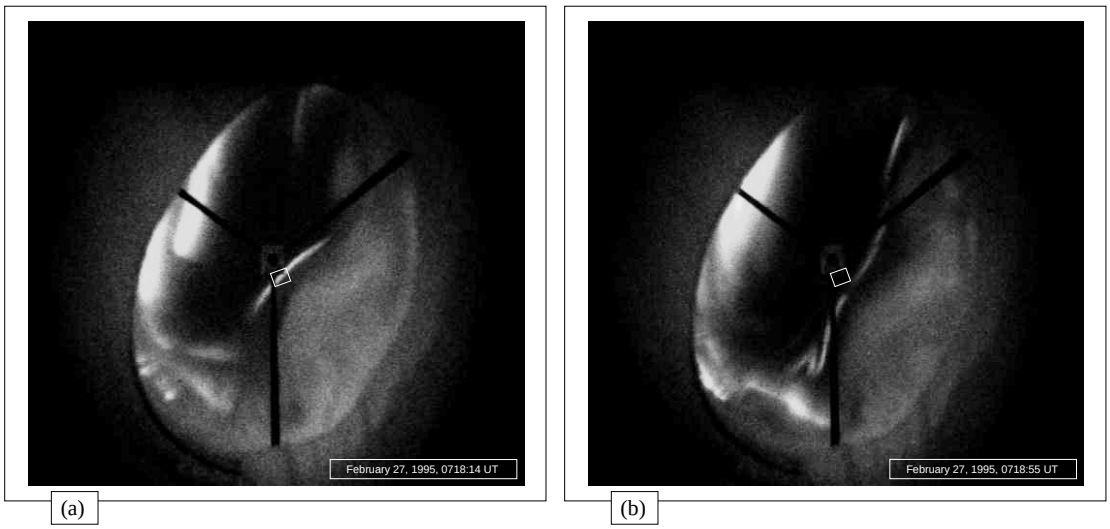

Figure 9.3: (a) All-sky camera image (557.7 nm) which puts the event of Figure 9.2 into context. (b) View of the same thin arc 40 s later, after it had left the PAI's field of view. The white box indicates the field of view of the PAI. *All-sky footage is courtesy of the Institute of Space and Atmospheric Studies, University of Saskatchewan.*

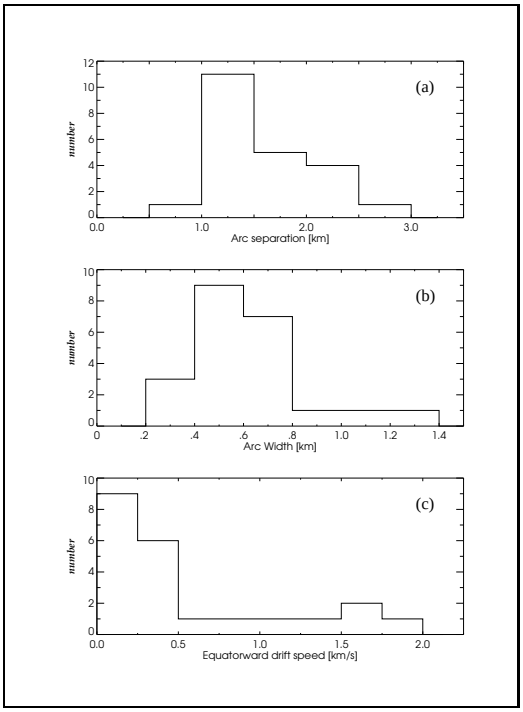

Figure 9.4: Histograms showing the distribution of the (a) arc separation, (b) arc width, and (c) equatorward drift speed of the 22 observed asymmetric multiple arc events.

500 m s^{-1}. This data is shown in the histogram of Figure 9.4c. In some cases all arcs within the system would appear to drift at the same speed, in other cases secondary arcs drifted at a somewhat lower speed, eventually being swallowed up by a faster-drifting $\zeta_{+1}-\zeta_{-1}$ system. In one case arcs would "switch off" and reappear further equatorward, in which case an equivalent linear speed was estimated for the purpose of Table 9.1.

The speed of motions parallel to ζ_{+1} and ζ_{-1}, shown in the last column of the table, could only be determined for about half of the events observed. These were found to be distributed in the range 5–70 km s^{-1}, with a mean value of approximately 20 km s^{-1}. Such apparent velocities were measured using easily identifiable structures within the arcs. It is noteworthy that the plasma producing these larger-scale structures at times appeared to drift faster than the structures themselves, the impression being one of a rapidly moving plasma conspiring to form slower moving features embedded within. This phenomenon, which has apparently not been described before, will be studied more closely in Chapter 10. Motions were consistently eastward for ζ_{+1} and westward for ζ_{-1}. No marked increase in the westward drift speed within secondary arcs with distance away from ζ_{-1} was identified, although a lack of discrete features within secondary arcs generally prohibited the accurate measurement and comparison of such motions.

From looking at Figure 9.2 it might be argued that the asymmetric nature of these arc systems could be due simply to perspective effects, in that (a) a corresponding set of secondary arcs might exist north of ζ_{+1}, though obscured by the off-zenith $\zeta_{+1}-\zeta_{-1}$ system, and (b) the decrease in arc intensity as one moves equatorward away from ζ_{-1} might be due to the fact that, in the present case, ζ_{-2} is almost exactly in the zenith, while ζ_{-3} is somewhat equatorward of zenith. As to the first objection, while it is true that one cannot preclude the existence of secondary arcs north of ζ_{+1} at the time of the snapshot, it is also true that any such arcs consistently vanished prior to $\zeta_{+1}-\zeta_{-1}$ drifting sufficiently equatorward to allow visual inspection. As to the second objection, during the course of the 22 observed events, many of which were equatorward-drifting, a variety of configurations of asymmetric multiple arc systems with respect to the local zenith were observed with this particular intensity characteristic surviving throughout, suggesting that the often observed intensity decrease in the equatorward direction is indeed real.

However, such perspective effects, as well as the spatial deformations commonly occurring on auroral arcs, did prohibit a sound assessment of simultaneous arc intensities across the arc system. Arc intensity ratios appeared to vary considerably from event to event. Figure 9.5 illustrates this spread by depicting four examples of asymmetric multiple arcs in the same panel. The event of Figure 9.5a is, of course, identical to the event already depicted in Figure 9.2. Intensity ratios are seen to vary from cases with a very rapid decrease in arc intensity in the equatorward direction, such as in the event of Figure 9.5a, to cases involving a barely perceptible decrease in arc intensity beyond ζ_{-2}, as shown in Figure 9.5b. The event of Figure 9.5a was exceptionally well-behaved and well-defined, making it possible to estimate the intensity of secondary arcs with respect to ζ_{-1}. The resulting ratio was estimated at $1{:}\frac{1}{3}{:}\frac{1}{6}$ (in "white light"). The secondary arcs of the event depicted in Figure 9.5b consisted of ∼IBC I aurora, while the $\zeta_{+1}-\zeta_{-1}$ system was formed by IBC III or IV aurora, forcing the imager into saturation. A logarithmic intensity re-mapping thus had to be performed for secondary arcs to be at all visible in the figure. Secondary arcs out to ζ_{-4} are seen in this event.

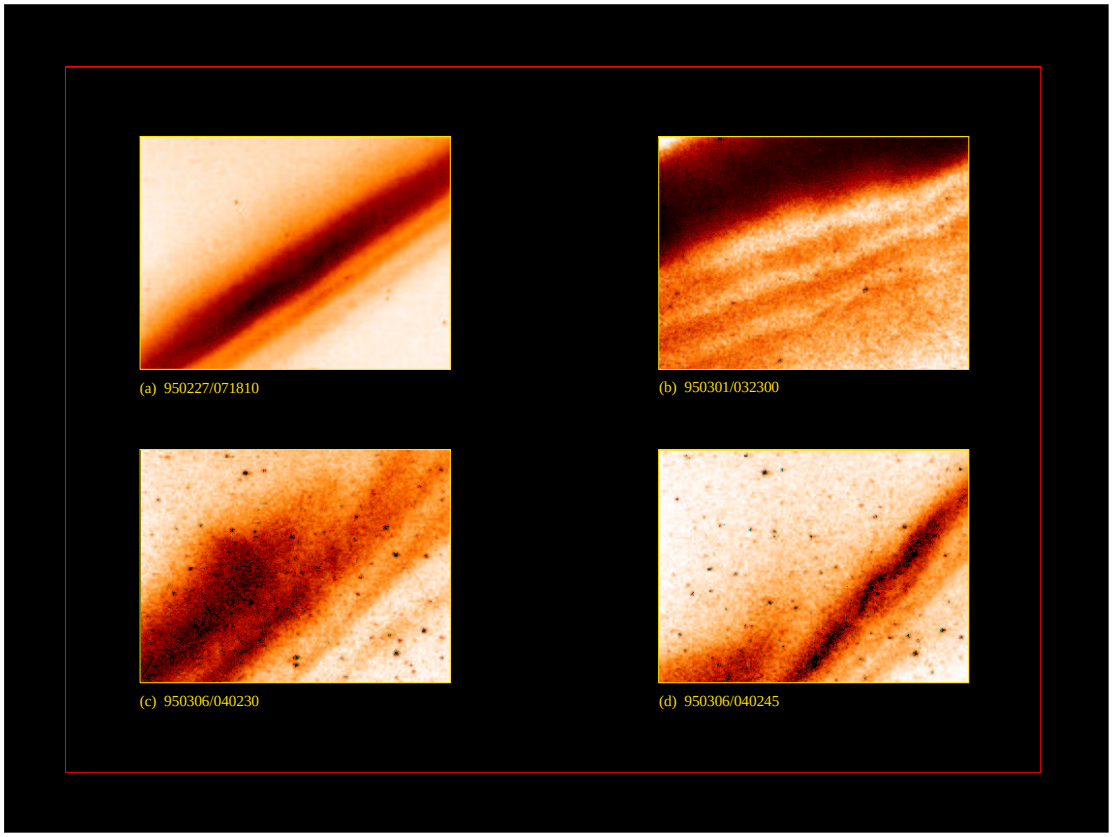

Figure 9.5: Four examples of asymmetric multiple arc events. Pseudo-colors have been added.

(Interestingly, the event of Figure 9.5b is closely associated with the event depicted earlier in Figures 8.18 and 8.19b.) In the events of Figure 9.5a and 9.5b, the bright poleward "arc" is in actual fact arcs ζ_{+1} and ζ_{-1}, both of considerable height extent, seen at an off-zenith observation angle.

Finally, Figures 9.5c and 9.5d demonstrate the dynamic nature of some events. These two events took place within 15 s of each other and might be considered two different stages of the same event. In Figure 9.5c the two northernmost features constitute the $\zeta_{+1}-\zeta_{-1}$ system. Arcs ζ_{-2} and ζ_{-3}, which materialized south of $\zeta_{+1}-\zeta_{-1}$ a few seconds prior to this snapshot, are also seen. As the system drifted equatorward ζ_{+1} began to disappear while ζ_{-1} appeared to split up into two arcs, the newly formed arc becoming to the system a new ζ_{+1}. The initial stages of this splitting process can be seen in the top right hand corner of Figure 9.5c. A subsequent split of ζ_{-2} into two arcs, and the disappearance of ζ_{-3}, resulted in the situation of Figure 9.5d, wherein the bright northernmost system is the new $\zeta_{+1}-\zeta_{-1}$ system mentioned above, with the ζ_{-2} and ζ_{-3} being the result of the splitting of the old ζ_{-2}. Remnants of the original ζ_{+1} can be seen in the lower left hand corner. Notice that the inter-arc distances in the event of Figure 9.5d is about half those of the event in Figure 9.5c.

9.3 Discussion

There have been a number of speculations that Alfvén waves might be the source of some auroral arcs and structures. Here we shall consider three scenarios: multiple reflections of Alfvén waves from a moving source [Lysak, 1985], electron inertia conics [Stasiewicz et al., 1997], and mode conversion in standing Alfvén waves or field line resonances (FLRs) [Samson et al., 1996; Wei et al., 1994; Streltsov and Lotko, 1996]. To a first order the observational features which must be explained are the predictable asymmetry of the auroral arc structures, the extremely linear topology of the arcs, the spacing of the arcs, and the apparent equatorward propagation of the arcs. We also prefer models which are as complete as possible and have a minimum of *a priori* assumptions. Though a plausible scenario, the moving magnetospheric source model with multiple ionospheric reflections developed by Lysak [1985] requires the *a priori* assumption of a localized source of magnetospheric Alfvén waves. Furthermore, this model makes no predictions of asymmetry in the formation of arcs, or of arc spacing. The electron inertia conic model of Stasiewicz et al. [1997] requires the *a priori* assumption of the existence of strong localized current channels which radiates dispersive inertial Alfvén waves, with "cone-shaped" propagation structures formed by these waves. Single resonance cones cannot explain the linear topology of our asymmetric arcs structures, and so a second *a priori* assumption of a spatially uniform, thin current sheet is required for the conic model. Furthermore, the dispersive cones are rotationally symmetric indicating that no spatial asymmetry is commonly expected for conic sources, including arcs produced from sheet currents. Consequently, this model might have difficulties in explaining the asymmetries of the equatorward decreasing arc intensities and apparent equatorward velocities in all our examples.

We now turn to the third model which is based on mode conversion in field line resonances. There have been a number of speculations that shear Alfvén waves might be associated with auroral arcs [e.g., Goertz, 1984]. One manifestation of these shear Alfvén waves are the ULF (1–4 mHz) FLRs which have been suggested as the source for some types of auroral arcs [Samson et al., 1996]. The FLR model is in a sense somewhat more complete than some other models in that the field aligned current sheets and field topologies evolve self-consistently, as a natural consequence of the absorption of energy in the resonance layer, and need not be assumed *a priori* (J.C. Samson, private communication, 1997). Furthermore, nonlinear ponderomotive forces in the FLR can produce density cavities at the altitude of the accelerator region [Rankin et al., 1995]. If these shear Alfvén waves have a latitudinal scale size of the order of several electron inertia lengths, $\lambda_e = (m_e/\mu_0 n e^2)^{1/2}$, or less, then mode conversion to inertial Alfvén waves might take place [Goertz, 1984; Wei et al., 1994; Streltsov and Lotko, 1996]. Figure 9.6 shows a plot of the mapped separation (dashed) of auroral arcs along a field line with an ionospheric latitude of 66°, along with the calculated electron inertia length along this field line. The above measured average arc separation of 1.5 km is used, and the electron number density n along the field line is modeled as [Borovsky, 1993a],

$$n = 0.18\,(10^5 \exp[-(r - 1.05R_E)/0.1R_E] + 5((r/R_E) - 1)^{-1.5})\ \mathrm{cm}^{-3}. \tag{9.1}$$

Note that the mapped arc separations first cross the calculated electron inertia length between 2 and 3 R_E.

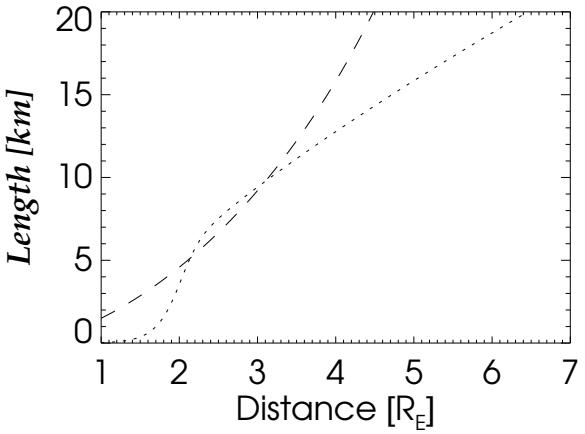

Figure 9.6: Mapped arc separation (dashed) and calculated electron inertia length along the same field line *vs.* distance.

Altitudes of 2–3 R_E above the auroral ionosphere are the most likely regions for mode conversion to occur. If the observed arcs were formed due to some type of electron inertia process, for example through mode conversion, then the arc separations mapped along the field lines should indeed be at some point comparable to the electron inertia length. (If the mapped spacing had been everywhere much larger than the electron inertia length, then inertial Alfvén waves could likely have been ruled out, and we would have had to look for some other possible accelerator mechanism.)

To describe the mode conversion configuration for inertial Alfvén waves, we use the very simple model outlined by Goertz [1984], as more sophisticated models are beyond the scope of this thesis. First we note that if we are looking at mode conversion at low altitudes, the process is intrinsically asymmetric. In this cold plasma the inertial Alfvén waves propagate in the direction of decreasing density or increasing Alfvén velocity. This is reflected in decreasing amplitudes of the electric fields in the direction of increasing Alfvén velocity (see Figure 9.7, discussed below). Bearing this in mind, our mode conversion scenario predicts that these multiple arcs must occur in regions with plasma densities that have poleward gradients. Following Goertz [1984], assuming a gradient with a scale size $1/K$ in the x direction we obtain the equation for the perpendicular electric field,

$$\lambda_e^2 \frac{d^2 E_x}{dx^2} - K x E_x = 0 \; . \tag{9.2}$$

This mode conversion equation is an Airy differential equation, the solution of which is of the general type shown in Figure 9.7. A comparison of Figures 9.7 and 9.2 emphasizes the similarities of the asymmetric topologies of the discrete arcs and the mode conversion electric fields. The wavelengths near the position of the resonance are given by,

$$\lambda_x \approx (3\pi)^{\frac{2}{3}} (\lambda_e^2 / K)^{\frac{1}{3}} \; . \tag{9.3}$$

Using Equation 9.3 and the measured arcs separations of 1 to 2 km we estimate that the spatial scale size of the perpendicular density gradient, $1/K$, in the accelerator region is less than 1 km if the density in the accelerator region is given by the profile in Figure 9.6, ranging to about 4–5 km if the densities are ten times those

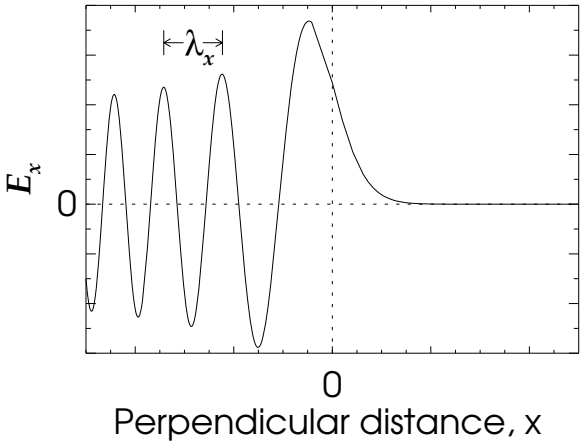

Figure 9.7: Numerical solution of the mode conversion equation, Equation 9.2.

plotted in Figure 9.6. These numbers are comparable to the scale sizes of gradients in some observed density cavities [Stasiewicz et al., 1997]. We have thus used the two observational features of spacing and topology to support an argument for Alfvén waves (as opposed to other possible mechanisms, such as double layers, anomalous resistivity, etc.) as a plausible explanation of the observed asymmetric multiple arcs. Further combined ground-based observations with high spatial resolution and wider angle all-sky images should help to establish whether mode conversion in ULF FLRs is a likely scenario for the formation of this common, but previously unreported substorm-related phenomenon. On a final note, it is interesting to note that electric-field signatures very similar to those of Figure 9.7 may actually also be discerned in S3-3 electric-field data (see, Figure 1 of Mozer [1981]).

Chapter 10

Small-Scale Spatially Periodic Distortions of Auroral Forms

High-resolution television observations by the Portable Auroral Imager of the small-scale spatially periodic distortions of auroral forms known as "curls" are presented. During winter 1995 and 1997 field trips to Rabbit Lake a large amount of video data containing auroral curls was acquired. Analysis of this data set has led to much improved insight into the properties of these features. Observed spatial and temporal characteristics of 440 curls and curl system events are presented, with results compared to those of earlier surveys wherever applicable. Curl systems appeared to have a preferred wavelength of about 3 km, significantly lower than what has been previously reported. The horizontal motions of curls along arcs were found to lie mainly in the range 0–30 km s^{-1}, although curls with apparent speeds approaching 100 km s^{-1} were also seen. Curl speed was found to be positively correlated with auroral emission rate. Curl lifetimes of 0.1–46 s were observed, the preferred values being in the range 0.25–0.75 s. This result differs significantly from earlier reports on curl lifetimes. The preferred areal extent of curls appeared to be around 0.5 km^2, but curls as small as 0.08 km^2 and as large as 22 km^2 were observed. The filaments connecting tightly wound curls were often extremely thin, in the range 100–300 m, rivaling the width of the thinnest features ever seen in the aurora. Striking parallels between the characteristics of these $\sim$1 km scale size curls and the characteristics of the $\sim$100 km scale size auroral "spirals" observed by the Freja UV imager are pointed out and discussed in terms of shear-driven instabilities. In addition, observations of the interesting new phenomena of "auroral kinks" and "spinning auroral patches" are briefly described.

10.1 Introduction

There are several latitudinal spatial scales associated with auroral arcs, varying from the 10–100 km wide band system, which often appears as one single broad arc when viewed from space, down to the smallest building block, the 0.1–1 km thin curtain [Davis, 1978a; Borovsky, 1993b]. Auroral features are subject to a

wide variety of perturbations; the particular type of perturbation experienced is often a function of the spatial and temporal scale sizes involved. The study of perturbed auroral arcs has the potential of yielding much valuable information on the instabilities causing such distortions and thus also on the production mechanisms responsible for the arcs.

Johnson [1996] has performed a survey of 109 auroral arcs as seen from the Freja satellite. Many of these large-scale arcs, of the order of 10–100 km wide, were seen to exhibit the formation of spirals spaced quasiperiodically along the arc, shown to be consistent with the Kelvin-Helmholtz instability acting on a current sheet. Such data may shed much needed light on the larger-scale processes occurring in the equatorial plasma sheet region but are of limited usefulness in making inferences regarding the production mechanisms of the thinnest of auroral arcs, whose origin is considered to be in the upper atmosphere, in the acceleration region, or somewhere in between [Borovsky, 1995]. Freja E field data acquired during arc crossings show evidence of considerable fine structure within the $\sim$100 km scale size arc, indicating the presence of multiple current sheets within one apparent single arc, whose auroral signatures could not be resolved by the Freja UV imager [Johnson, 1996].

Ground-based studies reveal that the 0.1–1 km thin curtains comprising the large-scale arcs and spirals seen from space are often themselves subject to smaller-scale geometric distortions that are quasiperiodic along the arc. The all-sky photograph in Figure 2 of Hallinan and Davis [1970] captures this situation in a most magnificent manner. The type of small-scale spatially periodic auroral arc distortion most commonly seen is the vortex-like "curl" formation first studied in depth by Hallinan and Davis [1970]. By using image orthicon cameras in the northern and southern hemispheres, they were able to study 104 examples of such small-scale auroral vortices, all of which were found to have a counterclockwise rotational shape and motion as viewed antiparallel to the Earth's magnetic field.

In view of the increasing focus within the auroral community on the largely unexplained phenomenon of fine-scale auroral arcs (see, e.g., Borovsky [1995], Stasiewicz et al. [1997], as well as Chapter 9 of this thesis), we have attempted to improve upon the earlier survey by Hallinan and Davis [1970]. This has been made possible by the current availability of low-light level imagers superior to earlier imaging instrumentation both in sensitivity and linearity, as well as by the availability of powerful image processing workstations. In addition, this present survey in a sense complements the survey of Johnson [1996]. While that survey dealt with spatial distortions of arcs in the 10–100 km spatial scale regime, this present survey fills the gap by focusing on periodic perturbations in the 0.1–10 km regime. The spatial scale of the phenomena to be discussed herein thus corresponds to that of the "breakup arcs" of Goertz [1981]. Some main results are reviewed below. Wherever applicable, results are compared to those of Hallinan and Davis [1970]. In addition, some interesting parallels between our present results and those of Johnson [1996] are pointed out.

During the 14 nights of observation considered here, the Portable Auroral Imager was operated the first 11 nights using the 105 mm, f/1.8 Nikon 35-mm camera lens and was operated the last 3 nights using the 50 mm, f/1.4 Cosmicar television lens. The 105 mm lens gave the imager a 7.4° by 5.5° field of view, resulting in a coverage of 10.1 km by 13.5 km and an experientially estimated spatial resolution of about 50 m at 105 km altitude for the kind of bright features being studied here. The 50 mm lens provided a field

of view of 16° by 12°, corresponding to about 30 km by 20 km linear coverage at 105 km altitude and an estimated spatial resolution of 100 m.

No optical filtering was performed during these observing sessions, allowing the detection of features with intensities approaching those of airglow. Absolute intensity measurements of auroral features were thus not made. The thinness of curtains associated with breakup conditions, their rapid movement through magnetic zenith, and their often turbulent distortions would have made such a task very difficult. However, a rough intensity classification has been implemented in this chapter. On the basis of a visual assessment of the aurora as it appears on the video screen, features are roughly classified into the intensity categories of "IBC I/II or less" and "IBC III/IV or more." In the following, the first category will be referred to as "weak" aurora, and the latter will be referred to as "bright" aurora. This type of classification is, admittedly, rather crude but is, nevertheless, found to provide some valuable insight into the behavior and nature of the small-scale periodic distortions here under scrutiny.

10.2 Observations

During the winter 1995 and 1997 field trips to Rabbit Lake a large amount of footage of short-scale auroral phenomena was acquired. The resulting database was surveyed for auroral arcs exhibiting small-scale vortical perturbations. Such perturbations will hereafter be referred to as "curls," and curls spaced quasiperiodically along an arc will be referred to as a "curl system" in accordance with the terminology of Hallinan and Davis [1970]. In multiple arcs, curl systems often coexist on adjacent arcs, producing what is commonly known as a "vortex street array." Curl systems in the equatorward portion of a multiple arc often have oppositely directed horizontal velocities as compared to curl systems in the poleward portion of the multiple arc, motions invariably being counterclockwise with respect to the multiple arc center [e.g., Davis, 1978a].

The data presented in this chapter were acquired on the nights of February 27 to March 1, 1995, March 3 to March 6, 1995, March 6 to March 7, 1997, and March 12 to March 17, 1997. On each of these nights, the observing period was approximately 0200–0800 UT (evening sector). The vast majority of curl systems were found within breakup aurora and westward traveling surges. However, such features were also found within the more diffuse aurora, which often tends to exhibit some shear behavior.

A total of 440 examples of arcs with curls or curl systems were found in the data, five of which are shown in Figure 10.1. Figure 10.1a shows snapshots of four (events 1 – 4) different curl systems. Event 4 in Figure 10.1a demonstrates how a small curl system, seen here as a sequence of rays, can itself suffer a perturbation so as to form a larger-scale curl system. This is somewhat analogous to the situation in Figure 2 of Hallinan and Davis [1970], except on a much smaller spatial and temporal scale. Figure 10.1b depicts the spatial and temporal evolution of a curl system. The event is shown here with a temporal resolution of 0.5 s. The rotational shape and motion of curl systems were consistently found to be counterclockwise as viewed antiparallel to the Earth's magnetic field, in full agreement with the observations of Hallinan and

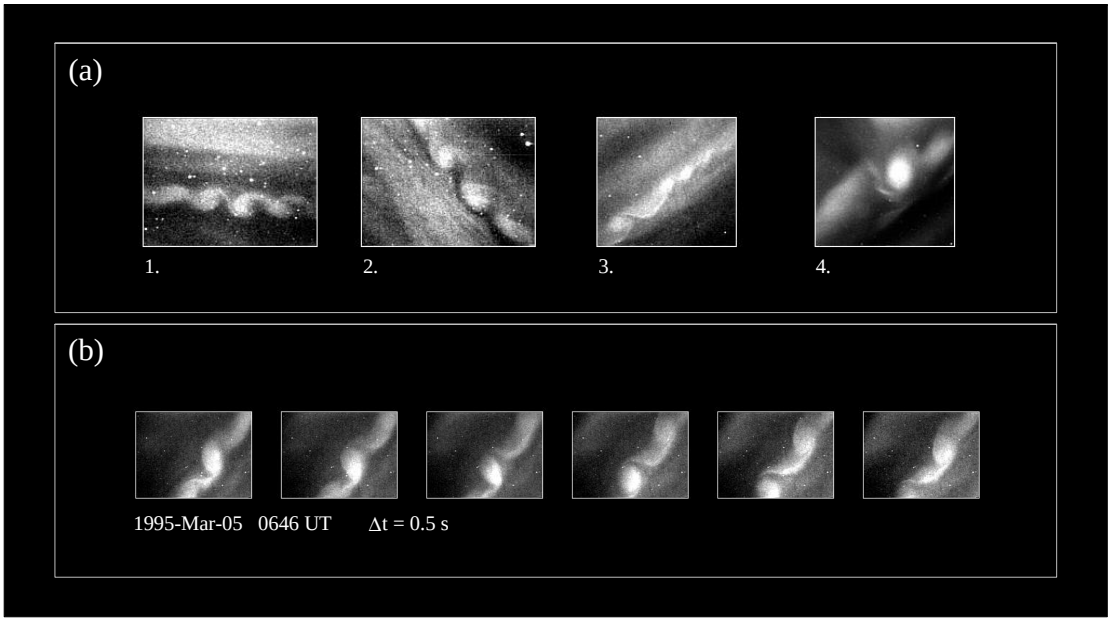

Figure 10.1: (a) Four examples of curl system events. (b) The evolution of a curl system. The extent of the field of view in these frames is 10.1 km by 13.5 km at an altitude of 105 km, with the exception of events 3 and 4 of Figure 1a, whose field of view is 10.1 km by 10.8 km because of windowing applied during image digitization. In all images presented in this chapter, north is up and west is to the right. The magnetic zenith is close to the center of the frames. The white spots are stars.

Davis [1970].

For each observed curl system event, the following quantities were estimated when the feature was in or within a few degrees of the local magnetic zenith: curl system wavelength (vortex pitch), curl velocity in the direction of the arc (relative to the imager's field of view), curl dimensions, width of arc prior to curl development, width of the thin threads connecting the tightly wound curls of a curl system, curl lifetime, and curl intensity (based on the rough classification scheme described in the previous section). An altitude of emission of 105 km will be assumed throughout the chapter. Note that Hallinan and Davis [1970] assumed a 100 km lower border altitude, so a correction factor has been applied wherever data are compared. The next four sections describe some of the properties of the observed curls and curl systems.

10.2.1 Wavelength

Curls typically had a near-elliptical symmetry although many heavily distorted curls were also found. Owing to their obvious quasiperiodicity it was usually not a problem to define a representative wavelength for each curl system. Figure 10.2a shows the distribution of the measured spacing between curl centers for 415 curl systems. Studying the histogram of Figure 10.2a, wavelengths are seen to generally be in the range 1–9 km, as also found by Hallinan and Davis [1970]. However, the present distribution is positively skewed, while the distribution in the case of the 83 curl systems studied by Hallinan and Davis [1970] appears negatively skewed (see, their Figure 4). Consequently, while they measured a typical value of about 6 km,

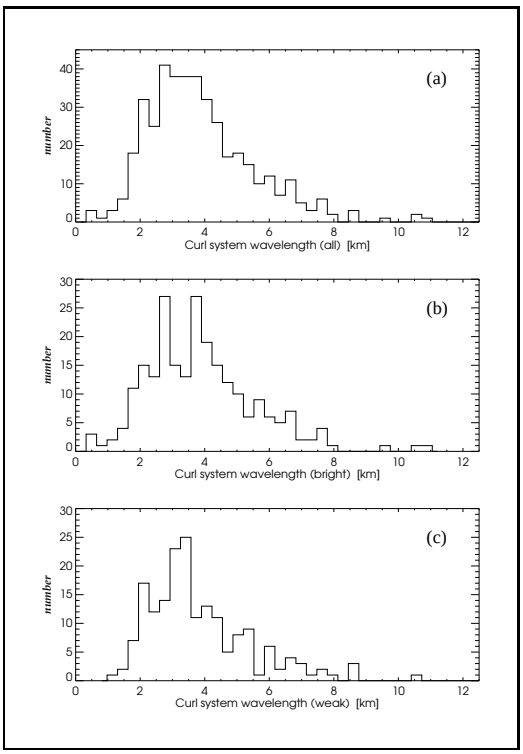

Figure 10.2: Histogram showing the distribution of curl system wavelengths. (a) All curl systems. (b) Curl systems in "bright" (see text) aurora. (c) Curl systems in "weak" (see text) aurora.

this present survey indicates a significantly lower preferred value of about 3 km, with a mean of 4 km.

Of the 415 observed curl systems, 232 were associated with bright aurora (as defined in Chapter 10.1), and 183 were associated with weak aurora. The corresponding wavelength distributions are shown in Figures 10.2b and 10.2c, respectively. The distributions for weak and bright auroral curl systems appear to be similar, both having a mean of 4 km. The maximum wavelength observed was 18 km. This curl system was found in weak aurora, and its wavelength was approximately twice the maximum wavelength observed in bright aurora.

Curl systems were generally very active and fast moving features, effectively lowering the imager's spatial resolution because of the presence of slow auroral emissions. The estimated limiting resolution for curl system wavelength determination purposes was thus about 0.5 km in bright aurora and about 1.0 km in weak aurora. The falloff in the distribution for wavelengths less than about 2 km is thus not considered to be because of instrumental limitations. In spite of difficulties associated with defining vortex centers and in determining widths within rapidly moving features, measured distances in this chapter are considered to be accurate to within an estimated 10–20%.

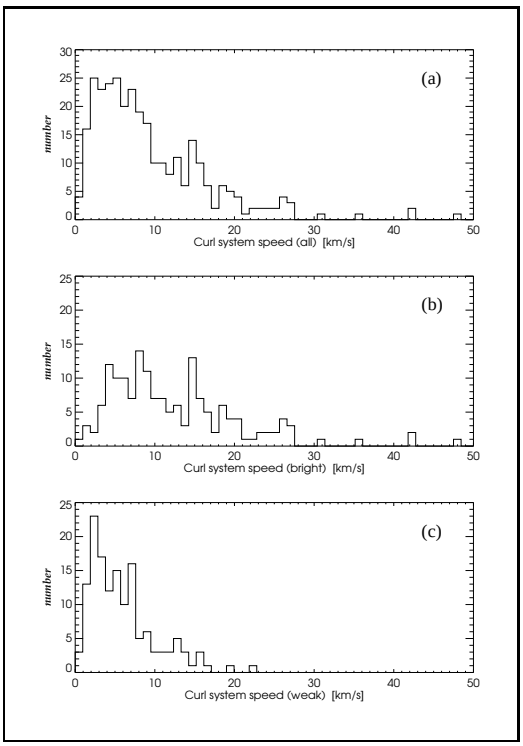

Figure 10.3: The distribution of measured apparent parallel horizontal speeds of curl systems. (a) All curl systems. (b) Curl systems in bright aurora. (c) Curl systems in weak aurora.

10.2.2 Speed

Curls are often seen to rapidly evolve on auroral arcs while simultaneously exhibiting extremely swift horizontal east-west aligned motions along arcs, often in opposing directions on adjacent arcs. Velocities display a wide variability from curl system to curl system, even within the same vortex street array. Figure 10.3a shows the distribution of measured apparent horizontal speed of 311 curl systems of nonzero (for reasons to be explained below) velocity. Speeds were found to lie in the range 0–90 km s^{-1}, with a mean of 10 km s^{-1} and preferred speeds in the range 2–8 km s^{-1}. This is a result similar to that of Hallinan and Davis [1970], who measured the speed of 24 curl systems, although the highest curl speed measured in that survey was only about 23 km s^{-1}.

Of the 311 curl systems whose speed could be determined, 167 were associated with bright aurora, and 144 were associated with weak aurora. An interesting trend emerges when plotting the corresponding speed distributions separately, as done in Figures 10.3b and 10.3c. There appears to be a marked skew in the speed distribution for weak auroral curl systems toward lower speeds as compared to the distribution for bright features, a qualitative result that will not come as a surprise to anyone having spent some time observing the aurora at this spatial scale. (As a digression, it is interesting to note that Maggs and Davis [1968] found a similar relationship between structural thickness and auroral brightness, supporting the idea that the mechanisms producing the aurora tend to become more spatially localized as their effectiveness

increases.) The mean of the distribution for bright features shown in Figure 10.3b is 13 km s^{-1}, while that of the distribution for weak features is about 6 km s^{-1}. The 90 km s^{-1} maximum speed measured during the survey was, not surprisingly, associated with very bright auroral activity. The maximum speed measured for a curl system in weak aurora was 23 km s^{-1}.

In addition to the 311 moving curl systems just discussed, there were 122 curl systems of zero velocity, not shown in the same histogram for obvious reasons. This additional preferred speed of 0 km s^{-1} is a significant new finding. In view of the distributions of Figures 10.3b and 10.3c, it might come as a surprise that as many as 80 of these 122 stationary curl systems were associated with bright aurora. A partial explanation, based on a closer scrutiny of the curl systems involved, will be given in the discussion section.

10.2.3 Lifetime

It is well known that auroral curls are of a highly transient nature. Hallinan and Davis [1970] determined the total lifetime of curls from 28 curl systems and obtained values in the range 0.4–2.2 s, with an average value of 1.3 s. This number has been frequently quoted in the past by authors in need of an estimate of typical curl lifetimes. In the present study, total curl lifetimes for 301 curls from 301 different curl systems have been determined. The resulting distribution is shown in Figure 10.4a. In addition to the counts shown here, there were 11 more counts in the range 8-46 s. Total lifetimes were thus found to reside in the range 0.1–46 s, a significantly wider range than what has been previously reported. The preferred value appeared to be 0.25–0.75 s, with a mean of 2.3 s.

Of the 301 curls studied, 196 were associated with bright aurora, and the remaining 105 were associated with weak aurora. From the corresponding distributions, shown in Figures 10.4b and 10.4c, it becomes clear that the shorter lifetimes are preferred by the brighter, often more dynamic aurora. In the case of bright aurora, lifetimes were found to be in the range 0.1–9.0 s with a mean of 0.9 s, and for weak aurora curl lifetimes were in the range 0.1–46 s, with a mean of 4.8 s.

In addition to these 301 curl events, a significant number of events were encountered wherein the movement of the curl through the finite field of view did not allow the observer to see the curl's birth and/or decay, preventing a proper estimate of total lifetime. The actual duration of stay within the field of view for 105 such curls was measured, however, providing at least a lower boundary on their lifetimes. Figure 10.4d shows the resulting distribution, with shaded areas representing the contribution from curls in weak aurora. The abscissa should be read as "curls with lifetime greater than... ." Note that bright curls tended to stay within the field of view for a much shorter duration than weak curls, again reflecting the difference in speed between curls in bright and weak aurora.

A scatterplot of curl system speed *vs.* total curl lifetime for 191 curl system events, shown in Figure 10.5, suggests no significant correlation between curl system speed and curl lifetime. A somewhat weaker statement can be made, however, namely, that subsecond lifetimes appear to be preferred by curls of horizontal speed greater than about 4 km s^{-1}. The finite field of view of the imager permits only certain combinations of lifetimes and velocities to be measured. The limitations imposed by the fields of view of

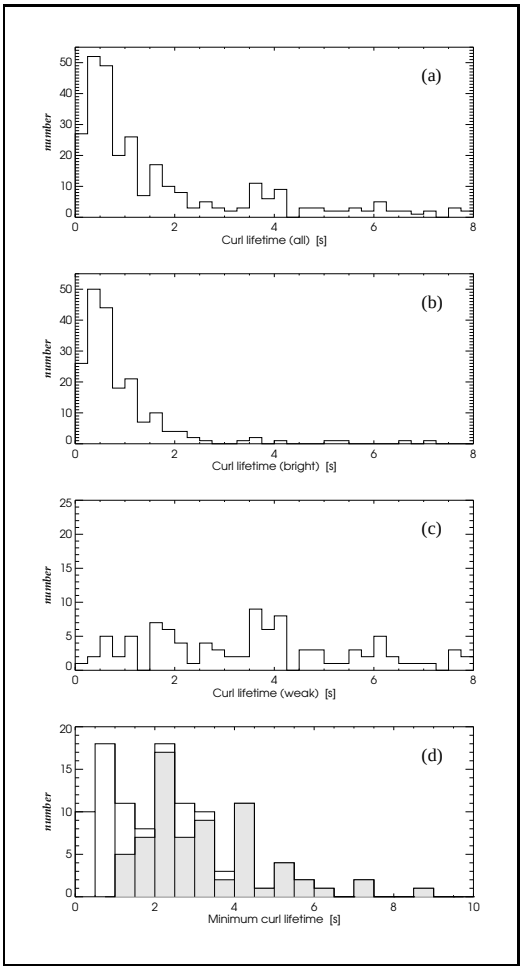

Figure 10.4: Distribution of curl lifetimes. (a) All curl systems. (b) Curl systems in bright aurora. (c) Curl systems in weak aurora. (d) Lower limit on lifetime of curls formed by bright (nonshaded area of the histogram) and weak (shaded area of the histogram) aurora that traversed the field of view (see text).

the two lenses used in this survey are indicated in Figure 10.5 by dashed lines. About 20% of the points populating the scatterplot were observed through the larger field of view.

Figure 10.6 shows the longest-lived event observed during this entire survey. It occurred on March 14, 1997, 0542 UT. The event is shown here with a temporal resolution of 1.0 s. The temporal progression in Figure 10.6 is left-to-right and top-to-bottom. Note the presence of relatively sharp intensity gradients as well as the presence of what might be described as black aurora (see, Chapter 8). The first frame in the sequence of Figure 10.6 is an all-sky camera image that gives the context of the curl event. The location of the field of view of the remaining frames in Figure 10.6 is located slightly below the center of the all-sky camera frame, at the equatorward edge of the distinct east-west aligned arc that is seen stretching across zenith just south of some very active equatorward drifting breakup aurora. Note that this diffuse east-west aligned arc appeared in the narrow field of view as a diffuse surface on the poleward side of the frames. It is a significant finding that curls are not all highly transient but that more stable and long-lived events do exist. This may be of

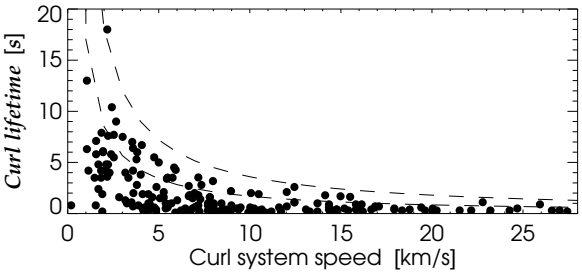

Figure 10.5: Scatterplot of curl system speed *vs.* curl lifetime. Dashed lines indicate the limitations imposed by the field of view of the two lenses used during these campaigns (105 mm and 50 mm focal lengths, with the 50 mm lens providing the widest field of view here).

significance when trying to interpret in terms of auroral curls data from a moving space-borne instrument, as done by Marklund et al. [1994]. Such stable, long-lifetime curl system events associated with weak aurora have also been seen in the black aurora, as shown in Chapter 8.

10.2.4 Dimensions

Curl dimensions were determined by estimating the curl's minor and major axes as it attained an approximately elliptical shape. Figure 10.7a depicts the distribution of estimated curl area for 421 curls seen close to the magnetic zenith. Of these curls, 243 were associated with bright aurora, and 178 were associated with weak aurora. The corresponding distributions are shown in Figures 10.7b and 10.7c, respectively. The areal distributions for weak and bright auroral curls appear similar, both having a mean of 2.3 km^2 and a preferred areal extent of $\sim$0.5 km^2. Both the largest and smallest curl observed were associated with bright aurora. The largest feature seen had an area of 22 km^2, and the smallest observed curl had an estimated area of 0.08 km^2. The largest observed feature in weak aurora was 11 km^2, and the smallest was about 0.2 km^2, possibly owing to the lower limiting resolution in weak aurora. No correlation was found between curl area and curl speed, neither was there any statistically significant correlation between curl area and curl lifetime.

During the dynamic conditions giving rise to curl formation, a variety of orientations of minor and major axes relative to geomagnetic north-south were seen. The major axis was frequently seen to be north-south aligned (with the minor axis seen to be east-west aligned), as the curl developed as a result of a counterclockwise rotation of a segment of an otherwise east-west aligned arc. Figures 10.7d and 10.7e show the measured dimensions of minor and major axes, respectively, for the 421 observed curl events. Preferred minor axis dimension is $\sim$1 km, while the preferred major axis dimension appears to be $\sim$2 km. Figure 10.7f shows the distribution of curl aspect ratios, suggesting a preferred ratio in the vicinity of $\sim$1:2.

Tightly wound auroral curls within a fully developed curl system are often interconnected by extremely thin auroral threads, whose thinness often rivals the thinnest features ever seen in the aurora. Examples of such fine-scale features are shown in Figure 10.8 in examples 1 – 6. Figure 10.9 depicts the distribution of the measured width of 259 thin filaments. The mean of the distribution is about 270 m, and the preferred "thinness" appears to be in the range 100–300 m. The limiting resolution during these measurements was

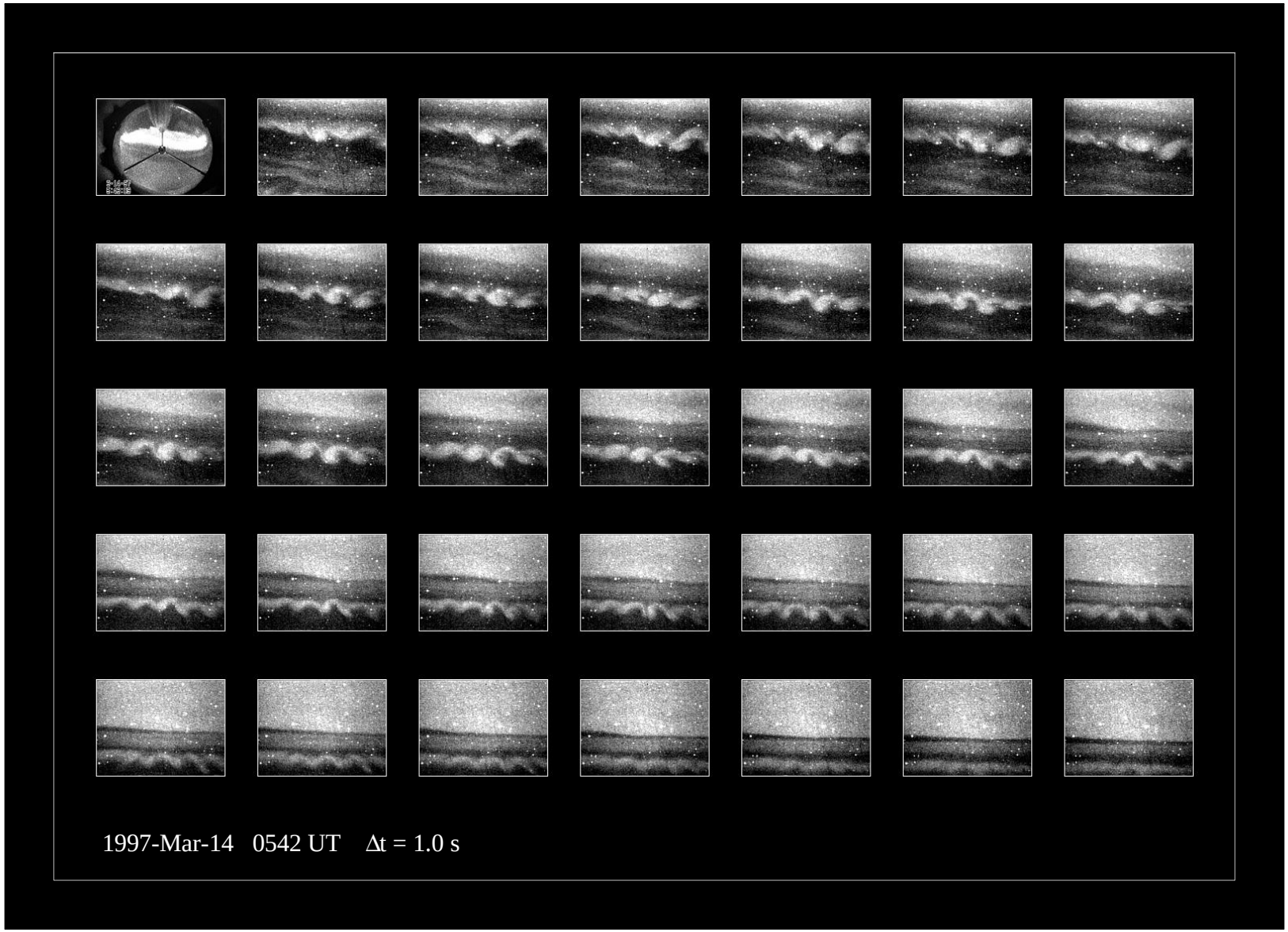

Figure 10.6: Example of extremely long-lived curl system event associated with weak aurora. The extent of the field of view is 10.1 km by 13.5 km at an altitude of 105 km. *All-sky footage is courtesy of the Institute of Space and Atmospheric Studies, University of Saskatchewan.*

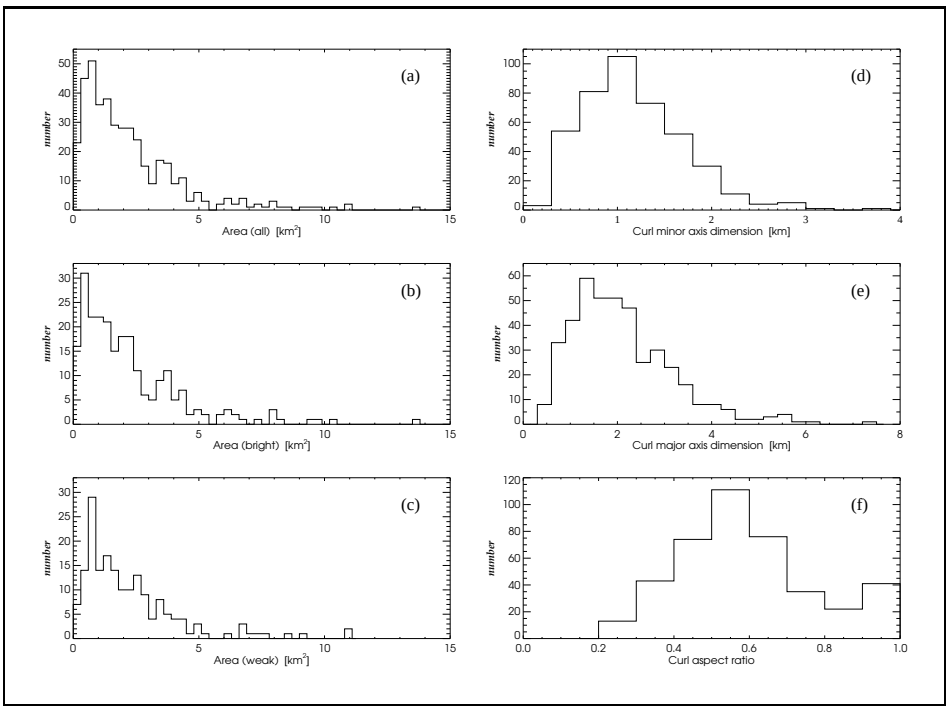

Figure 10.7: (a) Distribution of estimated area of all curl systems. (b) Estimated area of curl systems in bright aurora. (c) Estimated area of curl systems in weak aurora. (d) Distribution of curl minor axis dimensions (assuming an elliptically shaped curl). (e) Distribution of curl major axis dimensions. (f) Distribution of curl aspect ratios.

less than 100 m, as only specimens with no significant perpendicular motion were studied. Note again that an altitude of 105 km has been assumed throughout for both bright and weak auroral curls.

10.3 Discussion

A plasma characteristic commonly invoked for understanding a number of ionospheric observations of vortical structure is the existence of shear regions within the plasma [e.g., Lotko and Shen, 1991]. The presence of a shear, that is, a spatial inhomogeneity of mass motion, provides a source of energy from which instabilities can grow. The relationship between the width of the distorted arc and the wavelength of the distortion is important because it provides one of the conditions for the growth of these types of distortions. From the theoretical development of the charge and current sheet instabilities (see, e.g., the review of Hallinan and Davis [1970]), vortical forms undergo maximum growth when the width of the shear layer ($2a$) and the wavenumber of the perturbation ($k = 2\pi/\lambda$) are related by,

$$ka = \text{constant}, \tag{10.1}$$

where the constant represents the value for optimal wave growth. On the basis of a numerical analysis in the linear regime, Walker [1981] quotes an effective range of 0.5–0.8 for this constant, with 0.6 being a typical

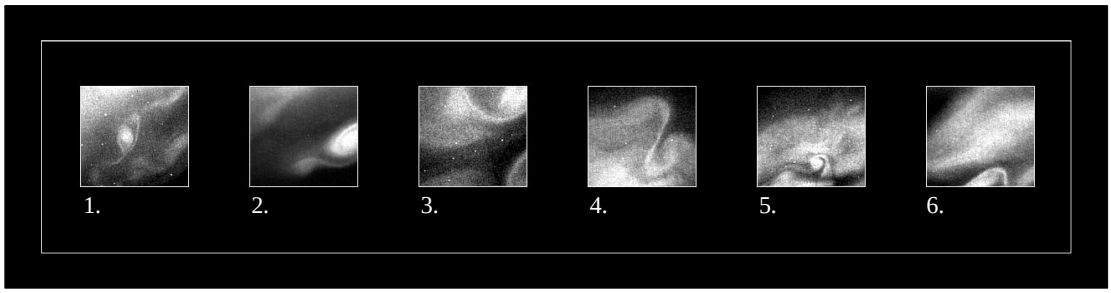

Figure 10.8: Six examples of the very thin filaments that often connect curls within a fully developed curl system. The field of view is 10.1 km by 10.8 km at an altitude of 105 km.

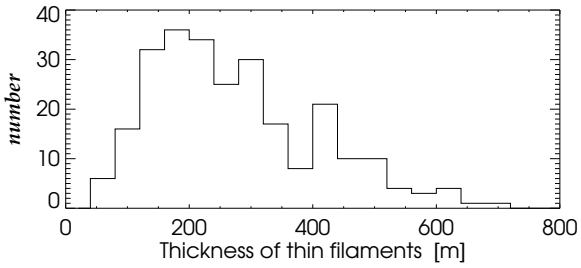

Figure 10.9: Distribution of thicknesses of fine-scale threads connecting curls within curl systems.

value. Note that ka is dimensionless, eliminating the auroral altitude assumption.

Wavenumbers are in our case easily obtained from the earlier wavelength measurements, while the widths of the arcs are taken to be $2a$, in agreement with Murphree et al. [1994]. The widths of 132 arcs on which curls subsequently developed were estimated. Only arcs composed of bright aurora were used, as these permitted a more precise determination of arc widths. The resulting data are presented in Figure 10.10a as a scatterplot of wavelength *vs.* arc width. The distribution of the resulting values of the product ka is shown in Figure 10.10b. This distribution, indeed, peaks in the range predicted by Walker [1981] and has a mean value of $ka = 0.71$. The scatterplot of Figure 10.10a indicates that a relationship between the two parameters may exist. Fitting a line (shown in Figure 10.10a) through the data points by linear regression yields a relationship given by,

$$\text{width [km]} = (0.17 \pm 0.01) \times \lambda\text{[km]} + 0.17 \pm 0.06, \tag{10.2}$$

where the errors associated with the slope and *y* intercept are their standard deviations from the scatter in the data. The correlation of this relationship is 0.8, confirming that the width of the distorted arc is a linear function of the wavelength of the distortion. Ignoring the *y* intercept on grounds that this value is probably below the limiting resolution (caused in large part by the presence of slow auroral emissions), Equation 10.2 gives a value for the constant of Equation 10.1 of,

$$ka = 0.52 \pm 0.04. \tag{10.3}$$

The correlation seen here is thus indicative of some type of shear process, commonly discussed in terms of the

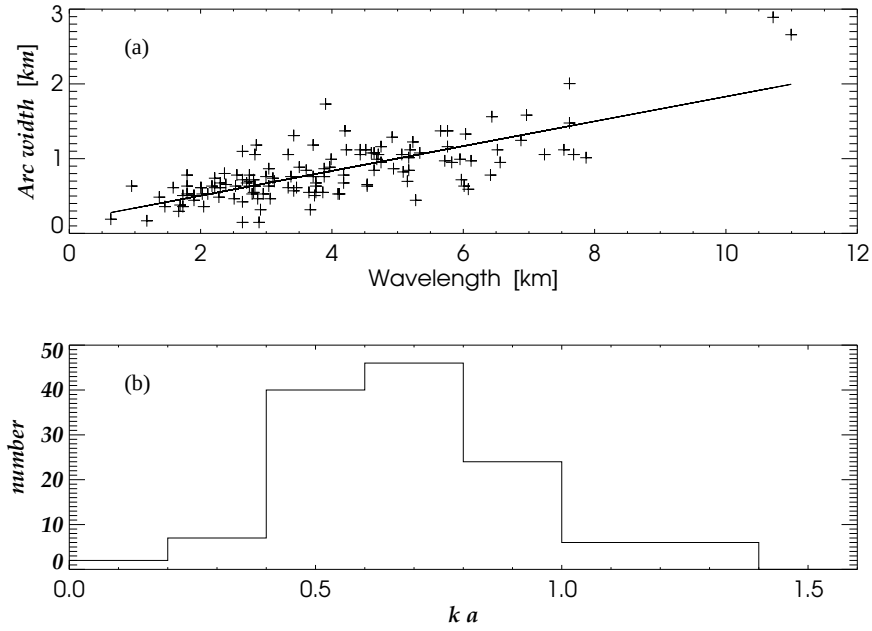

Figure 10.10: (a) Scatterplot of curl system wavelength *vs.* arc width. (b) The resulting distribution of the product of the wavenumber with the width of the shear layer, ka.

Kelvin-Helmholtz instability, as the source of curls. Further, the rotational sense can at this spatial scale be attributed to the Kelvin-Helmholtz instability acting on a negatively charged charge sheet, as already pointed out by Hallinan and Davis [1970]. Note that the rotational sense of curls is opposite from what is seen in the case of vortex streets in the black aurora, considered to be due to the Kelvin-Helmholtz instability acting on a positive space-charge sheet [e.g., Marklund et al., 1994].

It is interesting to note that Johnson [1996], in improving upon the survey of Murphree et al. [1994] of large-scale auroral vortices ("spirals") with wavelengths of the order of 100 km, obtained a distribution qualitatively very similar to that of Figure 10.10. Figure 10.11a (after Johnson [1996]) shows a 77-point scatterplot of perturbation wavelengths *vs.* corresponding latitudinal arc widths as measured by the Freja UV imager. Figure 10.11b (M.L. Johnson, private communication, 1997) shows the corresponding distribution of values of the product ka. The distribution of ka peaks also in this case in the general range predicted by Walker [1981], with the mean here being at $ka = 0.75$. Johnson [1996] obtained a correlation of 0.7 for the data, with a fitted value for the constant of Equation 10.1 of,

$$ka = 0.50 \pm 0.06, \tag{10.4}$$

a value statistically consistent with that of Equation 10.3, which was obtained for curl systems with wavelengths of the order of only 1 km.

Spirals are large scale ($\lambda \sim 100$ km) and reversible and have a clockwise rotational sense as seen antiparallel to the Earth's magnetic field [Hallinan, 1976; Johnson, 1996]. They are commonly interpreted in terms of the Kelvin-Helmholtz instability as manifesting because of the magnetic shear associated with

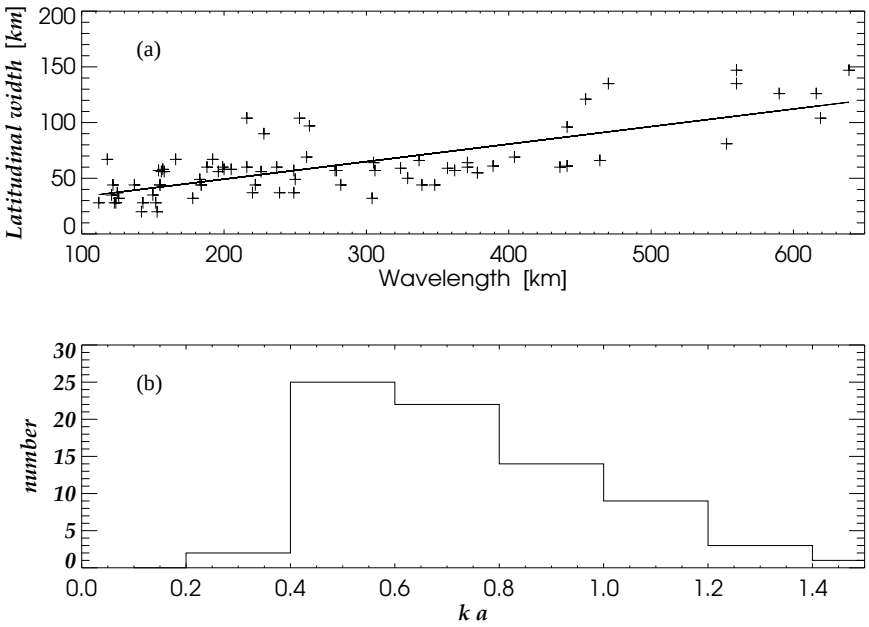

Figure 10.11: (a) Scatterplot of spiral system wavelength *vs.* latitudinal arc width, as measured from space using the Freja UV imager (after Johnson [1996]). (b) The resulting distribution of the product of the wavenumber with the width of the shear layer, ka.

upward current sheets (a view by no means shared by all investigators [e.g., Lysak et al., 1995]). Curls, conversely, are very small-scale ($\lambda \sim$ 1–10 km) and irreversible, having a counterclockwise rotational sense. They are usually considered indicative of the counterclockwise shear which can result from the $\mathbf{E} \times \mathbf{B}$ drifts surrounding a sheet of negative charge. Their scale size is thus limited because of the generally thin nature of charge sheets, keeping total potentials within reasonable bounds [Hallinan, 1976]. Because of the marked differences between these two phenomena, it is somewhat surprising to find such good agreement between the functional dependencies of wavenumber upon shear layer width. These apparent consistencies across several orders of magnitude of scale size may be indicative of some very robust and scalable underlying physics.

We return finally to an issue brought up in Chapter 10.2.2 on curl speed. Data suggest that the horizontal motion of a curl system along an arc tends to be more rapid for a curl system composed of bright aurora than for a curl system composed of weak aurora. In addition to the 311 curl systems whose speed is plotted in Figure 10.3a, as many as 122 curl systems of zero velocity were observed. Surprisingly, the majority of these stationary systems were found to be associated with bright aurora, not weak aurora. A closer examination of these zero-velocity curl systems yields a partial explanation. The majority of these zero-velocity systems appeared to belong to a somewhat different class of small-scale quasiperiodic perturbations. This kind of feature appeared to come into existence as a result of two parallel, closely spaced, counterstreaming auroral arcs conspiring together to develop "kinks" (for lack of a better term), which are quasiperiodic along the arc set. The two arcs responsible were in some cases adjacent, linear counterstreaming arcs that approached each other, often to a point where they appeared to the imager as one single arc, and subsequently developed

kinks. In other instances, two counterstreaming curl systems were seen drifting toward each other, apparently merging and forming one single new curl system with larger curls (kinks). In most cases, however, it was not possible to observe an actual merging of two physically separate arcs, leaving open the possibility that what was originally one single arc may have developed an internal counterstreaming, effectively splitting it up into two counterstreaming layers. Kinks consistently developed with a counterclockwise rotational sense, just like curls, and the resulting "kink systems" were almost indistinguishable from the more conventional curl systems (which develop on single auroral arcs, arcs without internal counterstreaming). A kink system could only be identified as such when the two adjacent (seemingly merged) arcs responsible for the kink system exhibited sufficient internal structure to allow imaging instrumentation to detect the presence of counterstreaming motions within the system. This counterstreaming could be seen in the video footage as an extremely rapid (of the order of 10–100 km s^{-1}) drift of plasma elements eastward along the poleward edge of the stable east-west aligned kink system and westward along the equatorward edge of the same system. There is thus both a microscopic aspect (high velocities and large shear) and a macroscopic aspect (large, stable kinks) to these systems. Note that when talking about the (usually zero) velocity of a kink system, it is always the macroscopic velocity that is referred to. The violent counterstreaming at the microscopic level appeared to have a stabilizing effect on the macroscopically formed kinks, which not only had an approximately zero apparent horizontal velocity but were also seen to have somewhat longer lifetimes than ordinary curl systems.

Six examples of kink systems are shown in Figure 10.12. Figure 10.12a shows snapshots (1 – 5) of five such systems. The filaments connecting kinks within kink systems were often extremely thin, in spite of the high velocity-shear experienced across these narrow channels. Figure 10.12b shows the evolution of a kink system event. It is depicted here with a temporal resolution of 33 ms, a less than optimum resolution considering the lack of optical filtering, but one which, nevertheless, demonstrates the dynamic, yet stable nature of these events. While the duration of this event was only about 1 s, it was not uncommon for events to appear stationary within the field of view for several seconds. Note that the locations of the (macroscopic) perturbations appear fixed relative to magnetic field lines rather than relative to any given plasma volume element, a situation opposite to that of curl systems. Kink systems with a low, nonzero speed were also seen, but it was in most cases impossible to determine whether a moving periodic structure was a kink system or simply an ordinary curl system. Thus no systematic ordering of the surveyed periodic structures into the classifications of curl systems and kink systems was attempted; they have in this survey been treated together as one. Kink systems appear to be very common, although seemingly more common among zero or very low velocity systems. It is very possible that significant portions of what has above been labeled as and discussed as curl systems were in actual fact kink systems. Likewise, it is possible that some of the curl systems studied by Hallinan and Davis [1970], many of which had zero velocity, may have been kink systems.

A peculiar consequence of kink systems are the detached, spinning vortices ("spinning auroral patches") frequently observed during these campaigns. Detached vortices appear at the end of the kink system's lifetime when the thin threads connecting kinks disappear (or become too thin to be resolved or else become so weak that their intensities fall below the threshold of detection of the imager). As the kinks

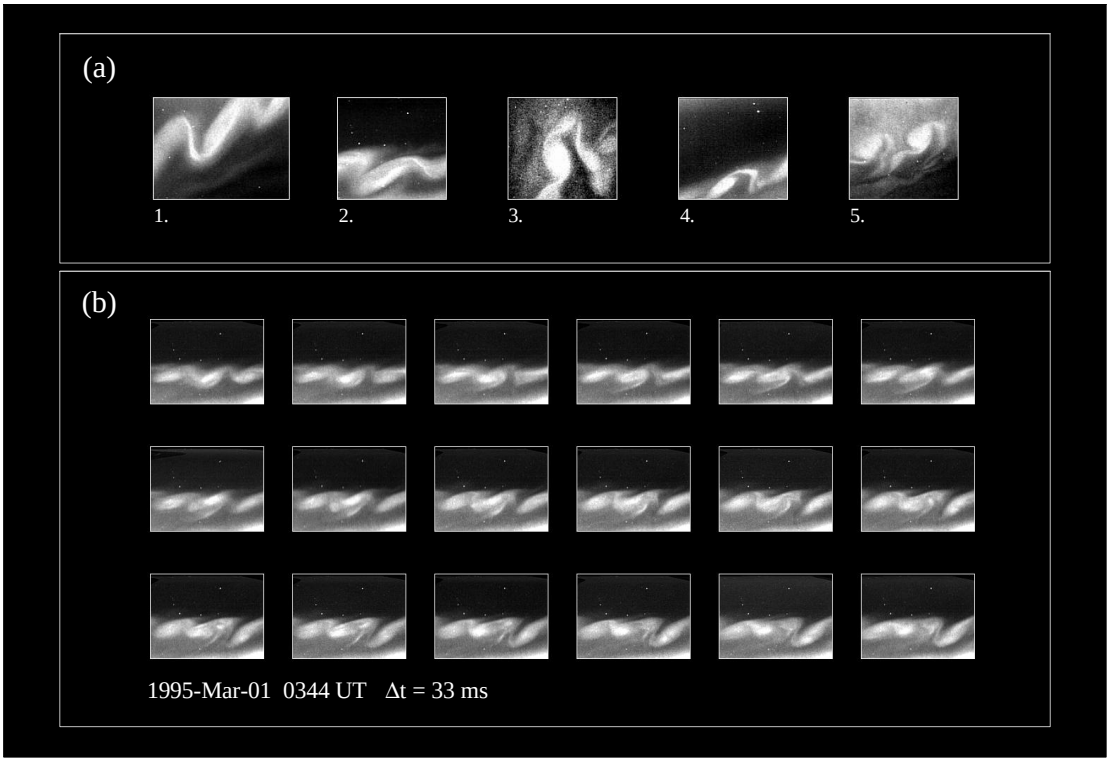

Figure 10.12: Examples of kink systems. (a) Snapshots of five auroral kink events. (b) The evolution of an east-west aligned kink system. The field of view of these frames is 10.1 km by 13.5 km at a 105 km altitude, with the exception of images 2 – 5 of Figure 12a, whose field of view is 10.1 km by 10.8 km because of windowing applied during image digitization.

were originally formed by rapidly counterstreaming arcs, they now in their seemingly detached state have a spinning appearance. They were often seen to go through several full revolutions in the counterclockwise direction, with a lifetime of the order of several seconds before they would dissipate. The dimensions of these spinning auroral patches seemed to be consistent with the data of Figure 10.7a. The phenomena described herein as kink systems and spinning auroral patches have, to our knowledge, not been previously reported.

Chapter 11

Conclusion

This dissertation has been divided into two major parts: Instrumentation and Observations. Yet, these two parts are in a sense inseparably tied together, as the process of scientific discovery is intimately tied to that of the development of appropriate instrumentation. It has been demonstrated how a novel imaging system yielding useful scientific data can be designed and constructed on a limited budget (CAD 50,000) by applying knowledge of auroral physics and proficiency in the fields of electro-optics, electronics, and computer science. It was during -50°C arctic winter field conditions discovered that in addition to these skills, a certain amount of hobbyism and an ability to improvise are required as well.

Low-light-level imaging design involves the evaluation of a number of variables that affect overall system performance. Some factors that must be considered include lens speed and focal length, filter transmission, spectral response and diameter of the image intensifier photocathode, CCD characteristics, and the performance of the video processing and recording circuitry. Performance-wise, the Portable Auroral Imager provides some significant improvements over earlier documented auroral TV camera systems [e.g., Frey et al., 1996b; Borovsky et al., 1991; Oguti, 1975; Maggs and Davis, 1968]. Specifically, the photocathode used on the PAI is considerably more sensitive to a wider range of frequencies than previous photocathodes due to a new GaAs photocathode composite with improved spectral responsivity (see, Figure 2.5). Further, the use of a third-generation intensifier tube results in improved spatial resolution, as well as in a considerable increase in the expected intensifier lifetime [Roaux et al., 1985]. Using a full-frame CCD sensor instead of an interline transfer CCD further contributes to an improved system sensitivity and resolution [Barbe and Campana, 1977]. The ICCD is a highly linear detector [Rougeot and Girard, 1988; Janesick et al., 1987], ensuring that structures are observed in a dynamically robust manner; the results of Maggs and Davis [1968] have at times been dismissed on grounds that the dynamic range or contrast response of their image-orthicon detector may have caused them to measure widths of optical-brightness variations of only a few percent within much-thicker auroral arcs [Davis, 1978a]. By adopting S-VHS instead of ordinary VHS recording technology preservation of data integrity has been greatly improved. The wider bandwidth of the S-VHS video signal yields more than 400 lines of horizontal resolution, as opposed to the 270 lines of the more widely used VHS

video standard [Johnston et al., 1991]. Furthermore, by using time code equipment locked to GPS time, accurate time-stamping of each individual video frame is ensured, at a precision level consistent with that of the video camera's own internal time base. Finally, the portability of the PAI is, to our knowledge, unprecedented in that all field items fit into a small set of foam-fitted aluminum cases. Easy transportability and configurability greatly improve the instrument's value and flexibility as a support instrument, fielded and operated by a single person, e.g., for the purpose of footprint support of high-resolution satellite experiments.

A wide variety of observations of small-scale auroral phenomena made by the PAI has been presented. Each of the four surveys presented in Chapters 7 to 10 contains some unique observations and discoveries pertaining to the smallest and least explored spatial and temporal scales in the aurora. Chapter 7 presents observations of the thinnest forms ever observed in the aurora. Chapter 8 presents the first comprehensive survey of the various phenomena associated with the interesting concept of "black aurora." Further, Chapter 9 discusses observations of the previously unreported phenomenon of "asymmetric multiple arcs." Associated with this substorm-related phenomenon are auroral forms that move with speeds approaching 100 km s^{-1}. Speeds of auroral forms of this order of magnitude are to our knowledge not previously reported. Finally, Chapter 10 improves considerably upon the much quoted, but somewhat limited survey of Hallinan and Davis [1970]. A variety of interesting and previously unknown features of the phenomenon of auroral "curls" are noted in this chapter. It has throughout this dissertation been pointed out and demonstrated that terms like "arc," "discrete," and "diffuse," when applied to the aurora, are very dependent on the scale size involved and must thus be used with extreme caution. Note finally that it is beyond the scope of this thesis to provide actual explanations of the various observed phenomena—although possible mechanisms have been alluded to in some places. It is left up to the theoreticians to provide a more complete explanation.

For completeness, it should be mentioned that subsequent to condensed versions of the surveys contained in Chapters 8 to 10 were published [see, Trondsen and Cogger, 1997; Trondsen et al., 1997; Trondsen and Cogger, 1998], other investigators began to follow up. For example, building upon the results of Trondsen and Cogger [1997], Kimball and Hallinan [1998a] presented a morphological study of black vortex streets, significantly improving upon the existing statistics. Further, Kimball and Hallinan [1998b] studied the black auroral patches specifically in relation to other types of aurora. Possible origins of the asymmetric multiple auroral arcs first reported by Trondsen et al. [1997] have been discussed in more detail by Streltsov et al. [1998]. Note also that theories addressing the sub-100-m spatial scale regime have lately begun to emerge [e.g., Lanchester et al., 1997].

Someone has said that the average Ph.D. thesis amounts to little more than transferring old bones from one graveyard to another. However, it is the hope of this author that at least some of the original observations made herein may be of use to the auroral community. Also, the reader is encouraged to improve upon the instrument concept presented. The underlying principles and assumptions have hopefully been clearly stated so as to facilitate such a process. The quantity and quality of emerging theories notwithstanding, progress within the field of auroral microphysics is in the author's opinion intimately tied to, and ultimately limited by, progress in the field of optical instrumentation.

Appendix A

Determining the Geocentric Latitude and Longitude of an Image Pixel

Geographic and geomagnetic field line grids are established for the PAI by using background stars as reference points. Using such star data in conjunction with an ephemerides program, the topocentric azimuth and elevation of each pixel in the image is easily obtained. This information can then be used to determine the geocentric latitude and longitude of each pixel at a given altitude. This geographic latitude and longitude may, in turn, be used to calculate the geomagnetic latitude and longitude of the pixel, by employing any one of the many popular geomagnetic field models that are available.

The process of calculating the geocentric latitude and longitude of a pixel (or, rather, of an event observed by the pixel) based on its topocentric azimuth Φ and elevation α is as follows. First, a geocentric polar angle Ψ needs to be assigned to the pixel. Figure A.1 shows the underlying geometry. Using simple trigonometry, the following relations emerge,

$$(R_E + h)\cos\Psi = R_E + t\cos\theta, \tag{A.1}$$

$$(R_E + h)\sin\Psi = t\sin\theta. \tag{A.2}$$

By combining these two equations, the geocentric polar angle Ψ of the observed event is obtained as,

$$\Psi = \theta - \sin^{-1}\left(\frac{R_E \sin\theta}{R_E + h}\right), \tag{A.3}$$

where h is the desired altitude (in our case 105 km, the altitude of auroral emission), and R_E is the radius of the Earth. The zenith angle θ is simply $90^\circ - \alpha$. We are thus in possession of the geocentric polar coordinates (Ψ, Φ) of each image pixel, as related to the local zenith.

Assume now that the PAI is located at the equator, on the Greenwich (0°) meridian. The next step involves calculating the Cartesian coordinates of the event which has geocentric polar coordinates (Ψ, Φ). These can then subsequently be rotated to the actual latitude and longitude of the observing site. The resulting

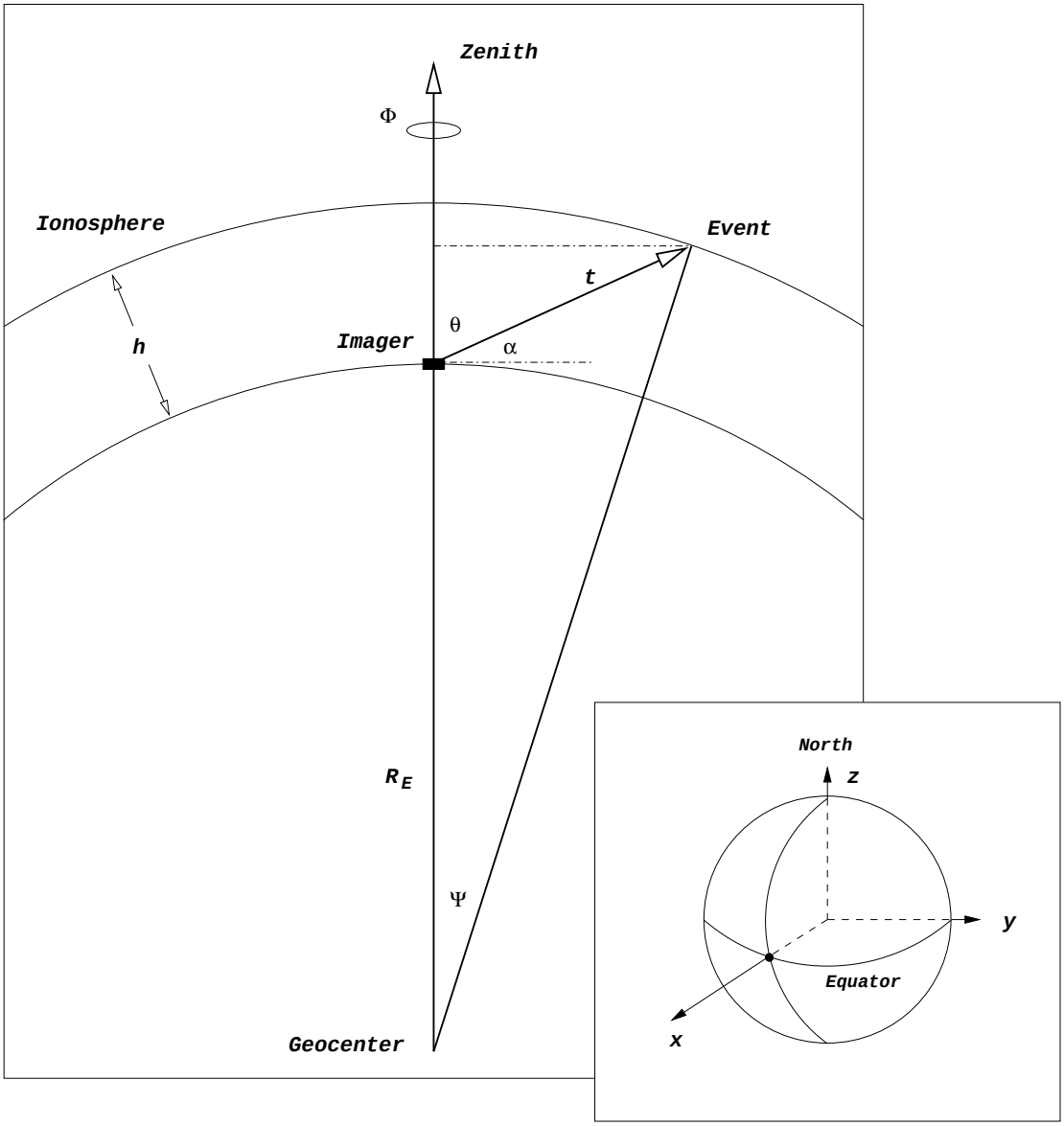

Figure A.1: Geometry underlying the geometric mapping of PAI image pixels.

Cartesian coordinates can then finally be converted to geocentric latitude and longitude, yielding the desired quantities.

Let α and β be geocentric longitude and latitude, respectively. Further, let ($\hat{x}$, $\hat{y}$, $\hat{z}$) be a Cartesian unit vector, where *z* is north, and *x* passes through $\alpha = \beta = 0°$, as shown in the insert of Figure A.1. The conversion matrix from geocentric to Cartesian coordinates is,

$$\begin{bmatrix} \hat{x} \\ \hat{y} \\ \hat{z} \end{bmatrix} = \begin{bmatrix} \cos\beta\ \cos\alpha \\ \cos\beta\ \sin\alpha \\ \sin\beta \end{bmatrix}. \tag{A.4}$$

We need to obtain the inverse relations. These are easily found to be,

$$\alpha = \tan^{-1}(\frac{y}{x}) \quad \text{for} \quad 0 \leq \alpha \leq 2\pi, \tag{A.5}$$

$$\beta = \sin^{-1}(z) \quad \text{for} \quad |\beta| \leq \frac{\pi}{2}. \tag{A.6}$$

Since we assume that the PAI is located at $\alpha = \beta = 0°$, the zenith is along the *x* axis. The Cartesian coordinates of an event having geocentric polar coordinates (Ψ, Φ) are,

$$\begin{bmatrix} \hat{x} \\ \hat{y} \\ \hat{z} \end{bmatrix} = \begin{bmatrix} \cos\Psi \\ \sin\Psi\ \cos\Phi \\ \sin\Psi\ \sin\Phi \end{bmatrix}. \tag{A.7}$$

(Note that due to our choice of coordinate system, the azimuthal angle about the zenith, Φ, is zero to the east. This must be kept in mind when azimuthal data output by an ephemerides program, which assume a zero azimuth to the north, are used.) Next, we need to rotate the imager over to the real observing site location (α, β). Starting at the equator Greenwich meridian ($\alpha = \beta = 0°$), we proceed to rotate by an amount α around the *z* axis. This must then be followed by a rotation around the *y* axis of the geocentric coordinate system by an amount $-\beta$. Note that these rotations are done according to the right hand rule. Subsequent to these rotations, the Cartesian coordinates of the event are,

$$\begin{bmatrix} \hat{x} \\ \hat{y} \\ \hat{z} \end{bmatrix} = R_y(-\beta)\, R_z(\alpha) \begin{bmatrix} \cos\Psi \\ \sin\Psi\ \cos\Phi \\ \sin\Psi\ \sin\Phi \end{bmatrix}, \tag{A.8}$$

where $R_y(-\beta)$ and $R_z(\alpha)$ are the rotational matrices about the *y* and *z* axes, respectively. Finally, the latitude and longitude values of each pixel may be found by using the inverse relations derived earlier, found in Equations A.5 and A.6. This converts from Cartesian coordinates to values of geocentric latitude and longitude. Based on azimuth and elevation data of a given pixel, and by assuming an altitude of emission and a site location, the corresponding geographic latitude and longitude have thus been derived. These can be used as input to geomagnetic field models to obtain geomagnetic latitudes and longitudes, as was done in generating Figure 8.1.

It now only remains to obtain the the rotational matrix $R = R_y(-\beta)R_z(\alpha)$ of Equation A.8. The rotational matrices R_x, R_y, and R_z are well-known. They are, in terms of the Euler angle, η,

$$R_x(\eta) = \begin{bmatrix} 1 & 0 & 0 \\ 0 & \cos\eta & -\sin\eta \\ 0 & \sin\eta & \cos\eta \end{bmatrix}, \tag{A.9}$$

$$R_y(\eta) = \begin{bmatrix} \cos\eta & 0 & \sin\eta \\ 0 & 1 & 0 \\ -\sin\eta & 0 & \cos\eta \end{bmatrix}, \tag{A.10}$$

and,

$$R_z(\eta) = \begin{bmatrix} \cos\eta & -\sin\eta & 0 \\ \sin\eta & \cos\eta & 0 \\ 0 & 0 & 1 \end{bmatrix}. \tag{A.11}$$

Only Equations A.10 and A.11 are needed in our case. The desired matrix R is thus,

$$R = R_y(-\beta)\, R_z(\alpha) = \begin{bmatrix} \cos\alpha\cos\beta & -\sin\alpha\cos\beta & -\sin\beta \\ \sin\alpha & \cos\alpha & 0 \\ \cos\alpha\sin\beta & -\sin\alpha\sin\beta & \cos\beta \end{bmatrix}. \tag{A.12}$$

This matrix may now be used directly in solving Equation A.8.

Bibliography

Albrecht, C., Noise sources in image intensifying devices, in *Diagnostic Radiologic Instrumentation*, edited by R. D. Moseley and J. H. Rust, pp. 291–311, Charles C. Thomas Ltd., 2600 South First Street, Springfield, Illinois 62794, USA, 1965.

Allen, K. B., A guide to specifying the components of an intensified solid state television camera, *Proceedings of SPIE*, *1072*, 64–69, 1989.

Baker, D. J., Rayleigh, the unit for light radiance, *Applied Optics*, *13*, 2160–2163, 1974.

Bankov, L., N. Bankov, A. Bochev, I. Kutiev, L. Todorieva, E. M. Dubinin, I. M. Podgorny, and Y. N. Potanin, Suprathermal electrons in small-scale field-aligned currents, *Geophysical Research Letters*, *13*, 105–108, 1986.

Barbe, D. F., and S. B. Campana, Imaging arrays using the charge-coupled concept, in *Advances in Image Pickup and Display*, vol. 3, pp. 171–296, Academic Press, New York, 1977.

Baumgardner, J., B. Flynn, and M. Mendillo, Monochromatic imaging instrumentation for applications in aeronomy of the Earth and planets, *Proceedings of SPIE*, *1745*, 199–205, 1992.

Beach, R., G. R. Cresswell, T. N. Davis, T. J. Hallinan, and L. R. Sweet, Flickering, a 10-cps fluctuation within bright auroras, *Planetary and Space Science*, *16*, 1525–1529, 1968.

Beauvais, Y., J. Chautemps, and P. deGroot, LLL TV imaging with GaAs photocathode/CCD detector, in *Advances in Electronics and Electron Physics*, vol. 64A, pp. 267–274, Academic Press, New York, 1985.

Belon, A. E., G. J. Romick, and M. H. Rees, The energy spectrum of primary auroral electrons determined from auroral luminosity profiles, *Planetary and Space Science*, *14*, 597, 1966.

Bennett, E. L., M. Temerin, and F. S. Mozer, The distribution of auroral electrostatic shocks below 8000-km altitude, *Journal of Geophysical Research*, *88*, 7107, 1983.

Benson, K. B., ed., *Television Engineering Handbook*, McGraw-Hill, 1985.

Borovsky, J. E., Auroral arc thicknesses as predicted by various theories, *Journal of Geophysical Research*, *98*, 6101–6138, 1993a.

Borovsky, J. E., Optical measurements of the fine structure of auroral arcs, in *Auroral Plasma Dynamics*, edited by R. Lysak, vol. 80 of *Geophys. Monogr. Ser.*, pp. 25–30, American Geophysical Union, Washington, D. C., 1993b.

Borovsky, J. E., Fine-scale structures in auroral arcs: An unexplained phenomenon, in *Space Plasmas: Coupling Between Small and Medium Scale Processes*, edited by M. Ashour-Abdalla, T. Chang, and P. Dusenbery, vol. 86 of *Geophys. Monogr. Ser.*, pp. 255–267, American Geophysical Union, Washington, D. C., 1995.

Borovsky, J. E., D. M. Suszcynsky, M. I. Buchwald, and H. V. DeHaven, Measuring the thicknesses of auroral curtains, *Arctic*, *44*, 231–238, 1991.

Boyd, R. W., *Radiometry and the Detection of Optical Radiation*, John Wiley and Sons, New York, 1983.

Bracewell, R. N., *Two-Dimensional Imaging*, Prentice-Hall, Inc., New Jersey, 1995.

Broadfoot, A. L., and K. R. Kendall, The airglow spectrum, 3100–10000 Å, *Journal of Geophysical Research*, *73*, 426–428, 1968.

Broadfoot, A. L., and B. R. Sandel, Application of the intensified CCD to airglow and auroral measurements, *Applied Optics*, *31*, 3097–3108, 1992.

Brown, N. B., T. N. Davis, T. J. Hallinan, and H. C. Stenbaek-Nielsen, Altitude of pulsating aurora determined by a new instrumental technique, *Geophysical Research Letters*, *3*, 403–404, 1976.

Caudle, D. E., Low light level imaging systems application considerations and calculations, *Proceedings of SPIE*, *1346*, 54–63, 1990.

Chamberlain, J. W., *Physics of the Aurora and Airglow*, Academic Press, New York, 1961.

Coltman, J. W., Scintillation limitations to resolving power in imaging devices, *Journal of the Optical Society of America*, *44*, 468–471, 1954.

Csorba, I. P., Recent advancements in the field of image intensification: The generation 3 wafer tube, *Applied Optics*, *18*, 2440–2444, 1979.

Csorba, I. P., *Image Tubes*, Howard W. Sams & Co., Inc., 4300 West 62nd Street, Indianapolis, Indiana 46268, USA, 1985.

Currie, B. W., Auroral heights over west-central Canada, *Canadian Journal of Physics*, *33*, 773–779, 1955.

Davis, T. N., The application of image orthicon techniques to auroral observation, *Space Science Reviews*, *6*, 222—247, 1966.

Davis, T. N., Observed microstructure of auroral forms, *Journal of Geomagnetism and Geoelectricity*, *30*, 371–380, 1978a.

Davis, T. N., Observed characteristics of auroral forms, *Space Science Reviews*, *22*, 77–113, 1978b.

deVries, H., The quantum character of light and its bearing upon the threshold of vision, differential sensitivity, and visual acuity of the eye, *Physica*, pp. 553–564, 1943.

Eather, R. H., Low light level imaging design, *Scientific Report No. 1, AFGL-TR-82-0308*, Air Force Geophysics Laboratory, USAF, Hanscom AFB, Massachusetts 01731, USA, 1982.

Elphinstone, R. D., J. S. Murphree, and L. L. Cogger, What is a global auroral substorm?, *Reviews of Geophysics*, *34*, 169–232, 1996.

Engstrom, R. W., *Photomultiplier Handbook*, RCA Corp., RCA, Solid State Division, Lancaster, Pennsylvania 17604, USA, 1985.

Evans, S., Horizontal movements of visual auroral features, *Journal of Atmospheric and Terrestrial Physics*, *16*, 191–193, 1959.

Fink, D. G., *Principles of Television Engineering*, McGraw-Hill, New York, 1947.

Frank, L. A., and K. L. Ackerson, Observations of charged particle precipitation into the auroral zone, *Journal of Geophysical Research*, *76*, 3612, 1971.

Frey, H. U., G. Haerendel, D. Knudsen, S. Buchert, and O. H. Bauer, Optical and radar observations of the motion of auroral arcs, *Journal of Atmospheric and Terrestrial Physics*, *58*, 57–69, 1996a.

Frey, H. U., W. Lieb, O. H. Bauer, H. Höfner, and G. Haerendel, CCD-camera system for stereoscopic optical observations of the aurora, *Proceedings of SPIE*, *2863*, 460–466, 1996b.

Gartlein, C. W., Unlocking secrets of northern lights, *Nat. Geograph. Mag.*, p. 673, 1947.

Goertz, C. K., Discrete breakup arcs and kinetic Alfvén waves, in *Physics of Auroral Arc Formation*, edited by S.-I. Akasofu and J. R. Kan, vol. 25 of *Geophys. Monogr. Ser.*, pp. 451–455, American Geophysical Union, Washington, D. C., 1981.

Goertz, C. K., Kinetic Alfvén waves on auroral field lines, *Planetary and Space Science*, *32*, 1387–1392, 1984.

Gonzales, R. C., and P. A. Wintz, *Digital Image Processing*, Addision-Wesley, Reading, Massachusetts, USA, 1987.

Gorney, D. J., A. Clarke, D. Croley, J. Fennell, J. Luhmann, and P. Mizera, The distribution of ion beams and conics below 8000 km, *Journal of Geophysical Research*, *86*, 83, 1981.

Gustafsson, G., N. E. Papitashvili, and V. O. Papitashvili, A revised Corrected Geomagnetic Coordinate System for epochs 1985 and 1990, *Journal of Atmospheric and Terrestrial Physics*, *54*, 1609–1631, 1992.

Haerendel, G., B. U. Olipitz, S. Buchert, O. H. Bauer, E. Rieger, and C. LaHoz, Optical and radar observations of auroral arcs with emphasis on small-scale structures, *Journal of Atmospheric and Terrestrial Physics*, *58*, 71–83, 1996.

Hallinan, T. J., Auroral spirals, 2, theory, *Journal of Geophysical Research*, *81*, 3959–3965, 1976.

Hallinan, T. J., and T. N. Davis, Small-scale auroral arc distortions, *Planetary and Space Science*, *18*, 1735–1744, 1970.

Hertel, R. J., Signal and noise properties of proximity focused image tubes, *Proceedings of SPIE*, *1155*, 332–343, 1989.

Hitachi, Ltd., *Instruction Manual. Hitachi S-VHS Professional VCR, VL-S100*, Hitachi, Ltd., Tokyo, Japan, 1989.

Horowitz, P., and W. Hill, *The Art of Electronics*, Cambridge University Press, New York, 1989.

Hunten, D. M., F. E. Roach, and J. W. Chamberlain, A photometric unit for the airglow and aurora, *Journal of Atmospheric and Terrestrial Physics*, *8*, 345–346, 1956.

ITT Defense, F4162 – 18 mm proximity focused image intensifier tube Gallium Arsenide response, *ITT Electro-Optical Products data sheet*, ITT Electro-Optical Products Division, 7635 Plantation Road, Roanoke, Virginia 24019, USA, 1990.

ITT Defense, *Preliminary Installation and Operations Manual, ITT Model F4588 LLLTV Camera*, ITT Electro-Optical Products Division, 7635 Plantation Road, Roanoke, Virginia 24019, USA, 1993.

Janesick, J. R., T. Elliott, S. Collins, M. Blouke, and J. Freeman, Scientific Charge-Coupled Devices, *Optical Engineering*, *26*, 692–714, 1987.

Johnson, C. B., S. B. Patton, and E. Bender, High resolution microchannel plate image tube development, *Proceedings of SPIE*, *1449*, 2–12, 1991.

Johnson, M. L., Survey and analysis of auroral arcs in the dusk and midnight sectors, Master's thesis, University of Calgary, Calgary, Alberta, Canada, 1996.

Johnston, W. E., R. D., and B. L. Tierney, Acquisition of digital images from video tape, in *Pattern Recognition and Image Processing in Physics: Proceedings of the Thirty-Seventh Scottish Universities' Summer School in Physics, Dundee, August, 1990*, edited by R. A. Vaughan, pp. 273–282, Adam Hilger, Bristol, England, 1991.

Kan, J. R., and L. C. Lee, Formation of auroral arcs and inverted V precipitations: An overview, in *Physics of Auroral Arc Formation*, edited by S.-I. Akasofu and J. R. Kan, vol. 25 of *Geophys. Monogr. Ser.*, pp. 206–217, American Geophysical Union, Washington, D. C., 1981.

Kimball, J., and T. J. Hallinan, A morphological study of black vortex streets, *Journal of Geophysical Research*, *103*, 14,683, 1998a.

Kimball, J., and T. J. Hallinan, Observations of black auroral patches and of their relationship to other types of aurora, *Journal of Geophysical Research*, *103*, 14,671, 1998b.

Lanchester, B. S., M. H. Rees, D. Lummerzheim, H. U. Frey, and K. U. Kaila, Large fluxes of auroral electrons in filaments of 100 m width, *Journal of Geophysical Research*, *102*, 9741–9748, 1997.

Lavin, H. P., System analysis, in *Photoelectronic Imaging Devices*, edited by L. M. Bieberman and S. Nudelman, vol. 1, pp. 333–374, Plenum Press, New York, 1971.

Legault, R. R., Visual detection process for electrooptical images: Man – the final stage of an electrooptical imaging system, in *Photoelectronic Imaging Devices*, edited by L. M. Bieberman and S. Nudelman, vol. 1, pp. 69–87, Plenum Press, New York, 1971.

Lin, C. S., and R. A. Hoffman, Characteristics of the inverted V event, *Journal of Geophysical Research*, *84*, 1514, 1979.

Linde, P., Preprocessing of CCD images, in *Observational Astrophysics – Methods and Techniques in Optical Astronomy, Proceedings of Nordisk Forskerkursus, Copenhagen University Observatory*, edited by R. F. Nielsen, Astronomisk Forlag, Esbjerg, Denmark, 1987.

Lotko, W., and M.-M. Shen, On large-scale rotational motions and energetics of auroral shear layers, *Journal of Geophysical Research*, *96*, 9549–9565, 1991.

Lynch, T. F., Intensified TV cameras as instrumentation and measurement systems, *Application note*, ITT Electro-Optical Products Division, Fort Wayne, Indiana, USA, 1989.

Lysak, R. L., Auroral electrodynamics with current and voltage generators, *Journal of Geophysical Research*, *90*, 4178–4190, 1985.

Lysak, R. L., Y. Song, and J. C. Grieger, Coupling of the magnetopause to the ionosphere by means of Alfvén waves and field-aligned currents, in *Physics of the Magnetopause*, edited by P. Song, B. U. V. Sonnerup, and M. F. Thomsen, vol. 90 of *Geophys. Monogr. Ser.*, pp. 385–393, American Geophysical Union, Washington, D. C., 1995.

Maggs, J. E., and T. N. Davis, Measurements of the thicknesses of auroral structures, *Planetary and Space Science*, *16*, 205–209, 1968.

Marklund, G., L. Blomberg, C.-G. Fälthammar, and P.-A. Lindqvist, On intense diverging electric fields associated with black aurora, *Geophysical Research Letters*, *21*, 1859–1862, 1994.

Marklund, G., L. Blomberg, C.-G. Fälthammar, P.-A. Lindqvist, and L. Eliasson, On the occurrence and characteristics of intense low-altitude electric fields observed by Freja, *Annales Geophysicae*, *13*, 704–712, 1995.

McIlwain, C. E., Direct measurement of particles producing visible auroras, *Journal of Geophysical Research*, *65*, 2727–2747, 1960.

Meeus, J., *Astronomical Algorithms*, Willmann-Bell, Inc., P.O. Box 35025, Richmond, Virginia 23235, USA, 1991.

Mozer, F. S., The low altitude electric field structure of discrete auroral arcs, in *Physics of Auroral Arc Formation*, edited by S.-I. Akasofu and J. R. Kan, vol. 25 of *Geophys. Monogr. Ser.*, pp. 136–142, American Geophysical Union, Washington, D. C., 1981.

Murphree, J. S., M. L. Johnson, L. L. Cogger, and D. J. Hearn, Freja UV imager observations of spatially periodic auroral distortions, *Geophysical Research Letters*, *21*, 1887–1890, 1994.

Nakamura, R., and T. Oguti, Drifts of auroral structures and magnetospheric electric fields, *Journal of Geophysical Research*, *92*, 11,241–11,247, 1987.

Nicodemus, F. E., Radiance, *American Journal of Physics*, *31*, 368–377, 1963.

Oguti, T., *Metamorphoses of Aurora*, no. 12 in Memoirs of National Institute of Polar Research, National Institute of Polar Research, Tokyo, 1975.

Oguti, T., T.-I. Kitamura, and T. Watanabe, Global aurora dynamics campaign, 1985–1986, *Journal of Geomagnetism and Geoelectricity*, *40*, 485–504, 1988.

Omholt, A., *The Optical Aurora*, vol. 4 of *Physics and Chemistry in Space*, chap. 2.6, pp. 36–42, Springer-Verlag, New York, 1971.

Ono, T., M. Ejiri, and T. Hirasawa, Monochromatic auroral images observed at Syowa station, in Antarctica, *Journal of Geomagnetism and Geoelectricity*, *39*, 65–95, 1987.

Petitdidier, M., Calculated transmission profile of interference filters, *Applied Optics*, *22*, 1797–1799, 1983.

Pollehn, H. K., Performance and reliability of third-generation image intensifiers, in *Advances in Electronics and Electron Physics*, vol. 64A, pp. 61–69, Academic Press, New York, 1985.

Potemra, T., Birkeland currents in the Earth's magnetosphere, in *Plasma and the Universe*, edited by C.-G. Fälthammar, G. Arrhenius, B. R. De, N. Herlofson, D. A. Mendis, and Z. Kopal, p. 155, Kluwer Academic Publishers, Netherlands, 1988.

Rankin, R., P. Frycz, V. T. Tikhonchuk, and J. C. Samson, Ponderomotive saturation of magnetospheric field line resonances, *Geophysical Research Letters*, *22*, 1741–1744, 1995.

Reichenbach, S. E., S. K. Park, and R. Narayanswamy, Characterizing digital image acquisition devices, *Optical Engineering*, *30*, 170–177, 1991.

Reynolds, G. T., Thirty years of (image) intensified physics and biology, *Proceedings of SPIE*, *1161*, 104–124, 1989.

Richard, J. C., D. Riou, and M. Vittot, Low-light-level TV with image intensifier tubes and CCDs, in *Advances in Electronics and Electron Physics*, vol. 74, pp. 9–15, Academic Press, New York, 1988.

Roaux, E., J. C. Richard, and C. Piaget, Third-generation image intensifier, in *Advances in Electronics and Electron Physics*, vol. 64A, pp. 71–75, Academic Press, New York, 1985.

Rose, A., The sensitivity performance of the eye on an absolute scale, *Journal of the Optical Society of America*, *38*, 196–208, 1948.

Rose, A., *Vision: Human and Electronic*, Plenum Press, New York, 1973.

Rougeot, H., and P. Girard, Low light level TV with II/CCD coupled devices: Relative merits of different approaches, in *Advances in Electronics and Electron Physics*, vol. 74, pp. 17–25, Academic Press, New York, 1988.

Royrvik, O., Pulsating aurora: Local and global morphology, Ph.D. thesis, University of Alaska, Fairbanks, USA, 1976.

Royrvik, O., and T. N. Davis, Pulsating aurora: Local and global morphology, *Journal of Geophysical Research*, *82*, 4720–4740, 1977.

Sackinger, W. M., Noise performance of the channel electron multiplier, in *Photoelectronic Imaging Devices*, edited by L. M. Bieberman and S. Nudelman, vol. 1, pp. 177–191, Plenum Press, New York, 1971.

Samson, J. C., L. L. Cogger, and Q. Pao, Observations of field line resonances, auroral arcs, and auroral vortex structures, *Journal of Geophysical Research*, *101*, 17,373–17,383, 1996.

Sandel, B. R., and A. R. Broadfoot, Photoelectron counting with an image intensifier tube and self-scanned photodiode array, *Applied Optics*, *15*, 3111–3114, 1976.

Sawchuk, W., and C. D. Anger, A dual wavelength ground-based auroral scanner, *Planetary and Space Science*, *20*, 1935–1940, 1972.

Scott, F., and D. Frauenhofer, The modulation transfer function and methods of measurements, in *Photoelectronic Imaging Devices*, edited by L. M. Bieberman and S. Nudelman, vol. 1, pp. 291–306, Plenum Press, New York, 1971.

Smith, L., A computer controlled optical calibration system, Master's thesis, University of Calgary, Calgary, Alberta, Canada, 1981.

Smith, L. S., E. P. King, and L. L. Cogger, Image intensifier gain measurements, *Applied Optics*, *22*, 1268–1270, 1983.

Stasiewicz, K., G. Gustafsson, G. Marklund, P.-A. Lindqvist, J. Clemmons, and L. Zanetti, Cavity resonators and Alfvén resonance cones observed on Freja, *Journal of Geophysical Research*, *102*, 2565–2575, 1997.

Stenbaek-Nielsen, H. C., and T. J. Hallinan, Pulsating auroras: Evidence for noncollisional thermalization of precipitating electrons, *Journal of Geophysical Research*, *84*, 3257–3271, 1979.

Störmer, C., *The Polar Aurora*, Oxford University Press, London, 1955.

Streltsov, A., and W. Lotko, The fine structure of dispersive, nonradiative field line resonance layers, *Journal of Geophysical Research*, *101*, 5343–5358, 1996.

Streltsov, A. V., W. Lotko, J. R. Johnson, and C. Z. Cheng, Small-scale, dispersive field line resonances in the hot magnetospheric plasma, *Journal of Geophysical Research*, *103*, 26,559–26,572, 1998.

Texas Instruments, TC241 – 780- × 488-pixel CCD image sensor, *Texas Instruments specifications sheet*, Texas Instruments Inc., Image Sensor Technology Center, 7839 Churchill Way, M/S 3966, Dallas, Texas 75251, USA, 1990.

Texas Instruments, Interlace operation in TI Virtual-Phase CCD image sensors, *Texas Instruments technical note*, Texas Instruments Inc., Image Sensor Technology Center, 7839 Churchill Way, M/S 3966, Dallas, Texas 75251, USA, 1993.

Trondsen, T. S., The Portable Auroral Imager: Survey and recommendation, *Internal report*, Institute for Space Research, University of Calgary, 1992.

Trondsen, T. S., The Portable Auroral Imager: Instrument characterization and calibration — Lab Notes, *The PAI Documentation Set*, Institute for Space Research, University of Calgary, 1993.

Trondsen, T. S., The Portable Auroral Imager: Software: Program listings, *The PAI Documentation Set*, Institute for Space Research, University of Calgary, 1996.

Trondsen, T. S., and L. L. Cogger, High-resolution television observations of black aurora, *Journal of Geophysical Research*, *102*, 363–378, 1997.

Trondsen, T. S., and L. L. Cogger, A survey of small-scale spatially periodic distortions of auroral forms, *Journal of Geophysical Research*, *103*, 9405–9415, 1998.

Trondsen, T. S., L. L. Cogger, and J. C. Samson, Asymmetric multiple auroral arcs and inertial Alfvén waves, *Geophysical Research Letters*, *24*, 2945–2948, 1997.

Tyson, J. A., Low-light-level Charge-Coupled Device imaging in astronomy, *Journal of the Optical Society of America*, *3*, 2131–2138, 1986.

Vallance Jones, A., *Aurora*, D. Reidel Publishing Company, Dordrecht, Holland, 1974.

Van Geest, L. K., and K. W. J. Stoop, Super inverter image intensifier, in *Advances in Electronics and Electron Physics*, vol. 64A, pp. 93–100, Academic Press, New York, 1985.

Velichko, V. A., N. E. Molochuskin, V. P. Samsonov, and S. R. Smotritskiy, The orientation of rays with a short lifetime in the active corona of polar aurorae, *Geomagnetism and Aeronomy*, *25*, 729–731, 1985.

Walker, A. D. M., The Kelvin-Helmholtz instability in the low-latitude boundary layer, *Planetary and Space Science*, *29*, 1119–1133, 1981.

Wei, C. Q., J. C. Samson, R. Rankin, and P. Frycz, Electron inertial effects on geomagnetic field line resonances, *Journal of Geophysical Research*, *99*, 11,265–11,276, 1994.

Whitby, C. M., Performance prediction for night photography, *Proceedings of SPIE*, *33*, 171–180, 1972.

Williams, C. S., and O. A. Becklund, *Introduction to the Optical Transfer Function*, Wiley Series in Pure and Applied Optics, John Wiley and Sons, New York, 1989.

Zmek, W. P., Rules of thumb for planetary scopes – Part I, *Sky & Telescope*, *86*, 91–95, 1993.